National Library
of Canada

Bibliothèque nationale
du Canada

Canadian Theses Service

Service des thèses canadiennes

Ottawa, Canada
K1A 0N4

NOTICE

The quality of this microform is heavily dependent upon the quality of the original thesis submitted for microfilming. Every effort has been made to ensure the highest quality of reproduction possible.

If pages are missing, contact the university which granted the degree.

Some pages may have indistinct print especially if the original pages were typed with a poor typewriter ribbon or if the university sent us an inferior photocopy.

Previously copyrighted materials (journal articles, published tests, etc.) are not filmed.

Reproduction in full or in part of this microform is governed by the Canadian Copyright Act, R.S.C. 1970, c. C-30.

AVIS

La qualité de cette microforme dépend grandement de la qualité de la thèse soumise au microfilmage. Nous avons tout fait pour assurer une qualité supérieure de reproduction.

S'il manque des pages, veuillez communiquer avec l'université qui a conféré le grade.

La qualité d'impression de certaines pages peut laisser à désirer, surtout si les pages originales ont été dactylographiées à l'aide d'un ruban usé ou si l'université nous a fait parvenir une photocopie de qualité inférieure.

Les documents qui font déjà l'objet d'un droit d'auteur (articles de revue, tests publiés, etc.) ne sont pas microfilmés.

La reproduction, même partielle, de cette microforme est soumise à la Loi canadienne sur le droit d'auteur, SRC 1970, c. C-30.

NL-339 (r. 88/04)

Canada

THE PRODUCTION MECHANISM AND LIFETIMES OF CHARMED PARTICLES

THESIS SUBMITTED TO
THE SCHOOL OF GRADUATE STUDIES
IN PARTIAL FULFILLMENT OF THE REQUIREMENTS
FOR THE DEGREE OF
PH.D. IN PHYSICS

By
Søren Grandborg Frederiksen

University of Ottawa
July 1987

ISBN 0-315-40702-6

UNIVERSITÉ D'OTTAWA
UNIVERSITY OF OTTAWA

Introduction

The discovery of the J/ψ in 1974 [1], a resonance consisting of a charmed quark-antiquark pair was a major turning point in elementary particle physics. Predicted ten years earlier [2] to help explain the absence of strangeness changing neutral currents, the charm quark was expected to decay weakly into a strange quark [3]. The charm quark was also very important in the GIM (Glashow, Iliopoulos and Maiani) model [4] of weak interactions.

The J/ψ provided indirect evidence for the existence of charm. However, it was not until two years later with the discovery [5] of the D^0 that a particle with net charm was observed. A number of experiments subsequently looked for and discovered other charmed particles [6,7]. The main difficulties in studying charmed particles are their short lifetimes ($\tau \approx 10^{-13}$ sec.) and low production rates ($\sigma(\text{pp} \rightarrow c\bar{c} + X) \approx 80 \pm 60 \mu b$) [7]. The short lifetimes correspond to very short decay lengths, of the order of a few hundred microns for charmed particles with a few GeV/c momentum. Due to the short decay length, nuclear emulsion with its high spatial resolution is an ideal detector since it is possible to actually see the production and subsequent decay of the charm particle.

In 1977 a hybrid emulsion-spectrometer experiment (E-531) was set up in the wide-band neutrino beam at Fermilab. An advantage of the neutrinos is that they do not produce any tracks in the emulsion; therefore the background is very low and it is possible to leave the emulsion target in the beam for several months. Results using data collected from November 1978 to February 1979 (referred to as the first run) have already been published in numerous theses [8,9,10,11] and articles [12,13,14,15,16,17]. The exposure time was only about four months while the search for events in the emulsion and their subsequent analysis took several years. This thesis will discuss the data obtained in a second run of the experiment which collected data from November 1980 to May 1981, and will combine the data of the two runs together.

This experiment was one of the first to obtain a large enough number of charmed particles to measure the lifetimes accurately. It was also the first experiment able to study the production of charmed particles by neutrinos.

Acknowledgements

I would like to thank all those people involved with the entire E-531 collaboration without whose help this thesis would not possible.

I wish to especially thank my advisor Professor J. Hébert for his guidance and invaluable help, and his wife Dr. C.J.D. Hébert for reading my thesis and keeping me honest in the analysis of the data.

I also want to thank Ron Sidwell and Bill Reay for inviting me to help with the analyses of the data at O.S.U. and always being willing to help when I got stuck on a problem.

I want to thank Alain Gauthier, my partner and collaborator without whose help I would probably not have been able to finish so soon.

I wish to thank the Natural Sciences and Engineering Research Council for their financial support in the form scholarships.

Last, but certainly not least, I also want to thank my parents, Kjeld and Inge Frederiksen, and my brother and sister, Per and Henriette Frederiksen, who were always willing to give me any moral support that I needed.

Statement of Originality

My contributions to the collaboration were mainly in the analysis of the experimental data. I was responsible for the detailed study of about 25% of all the second run charm candidates. One event (1311-3060) was studied in more detail than the others; I measured the position and direction of the decay tracks in the emulsion and used these measurements in the analysis of the event. I used the Monte Carlo of the neutrino beam originally written by David Bailey, and modified and improved it for the second run. I also wrote the experiment Monte Carlo which was used to generate the event weights, and used it to compare with various distributions (Chapter 5). The cross section rates and limits discussed in Chapter 6, along with the distributions of various kinematic variables were also calculated by me.

Contents

List of Tables

List of Figures

Chapter 1

Theory

In the presently accepted models of Elementary Particle Physics all hadrons are composed of some basic point-like particles called quarks. These quarks along with the leptons (and the various anti-particles) are the fundamental constituents of all matter. The flavours of the quarks (or quark species) are the up (u), down (d), strange (s), charm (c), beauty (b) and truth (t); the leptons are the electron (e^-), muon (μ^-) and tau (τ^-) and their corresponding neutrinos. The properties of the quarks and leptons are summarized in Table 1. The leptons have all been "observed", but as yet no free quarks have been seen, the quarks are only found in groups as composite particles either as a meson or a baryon.

There are four known forces in nature and one of the main thrusts of present day particle theorists is to prove that these four forces are manifestations of a single force. The four forces are (in order of diminishing strength) the strong force, the electro-magnetic force, the weak force, and gravity. The strong force is the force responsible for the interaction of the quarks; the electro-magnetic force is the force between objects with charge; the weak force is the force responsible for (among other things) the decay of the neutron; finally, gravity which is a very weak force with infinite extent is the force between objects with mass.

Table 1: Quark and Lepton Properties

Quantum numbers		**Quarks**					
		d	u	s	c	b	t
Baryon number	B	$\frac{1}{3}$	$\frac{1}{3}$	$\frac{1}{3}$	$\frac{1}{3}$	$\frac{1}{3}$	$\frac{1}{3}$
Charge	Q	$-\frac{1}{3}$	$+\frac{2}{3}$	$-\frac{1}{3}$	$+\frac{2}{3}$	$-\frac{1}{3}$	$+\frac{2}{3}$
Isospin (third comp.)	I_Z	$-\frac{1}{2}$	$+\frac{1}{2}$	0	0	0	0
Strangeness	S	0	0	-1	0	0	0
Charm	C	0	0	0	$+1$	0	0
Beauty	B	0	0	0	0	-1	0
Truth	T	0	0	0	0	0	$+1$
		Leptons					
		e	ν_e	μ	ν_μ	τ	ν_τ
Charge	Q	-1	0	-1	0	-1	0
Electron Lepton Number	l_e	$+1$	$+1$	0	0	0	0
Muon Lepton Number	l_μ	0	0	$+1$	$+1$	0	0
Tau Lepton Number	l_τ	0	0	0	0	$+1$	$+1$

1.1 Quantum Chromodynamics

All quarks have a property referred to as colour. It can be thought of as a special type of charge which can have three different states called red, green and blue. This colour charge has some very special properties. When a specific colour and the corresponding anti-colour are present there is no net colour charge; similarly, when all three colours (red, green and blue) are present, there is again no net colour charge. The strong force is described by a non-Abelian SU(3) gauge theory called Quantum Chromodynamics (QCD), and is the force between different coloured objects. The mediators of the force are eight massless vector particles called gluons, in the same way that the photon is the force mediator for the electro-magnetic force in Quantum Electodynamics (QED). The gluon of QCD is different from the photon of QED because the gluons are themselves coloured and can be involved in a gluon-gluon interaction, while it is not possible to get a photon-photon interaction.

QCD depends only on the colour of the objects and not their flavour and thus the leptons, which have no colour charge, do not experience the strong force. QCD also conserves all the quantum numbers I_Z, S, C, B and T. This force is believed to be so strong that it is impossible to separate a quark from a hadron and one will only see quark combinations like $q\bar{q}$, qqq, $\bar{q}\bar{q}\bar{q}$ or any other combination where there is no net colour. The $q\bar{q}$ state does not have a net colour charge because the quark has one colour while the anti-quark has the corresponding anti-colour; for the qqq state the three colours red, green and blue are all present, again producing no net colour charge. This inability to observe free quarks is referred to as confinement

The combination of quark and anti-quark make up all the presently known mesons, some of which are shown in Table 2. The three quark combinations correspond to the baryons and are shown in Table 3.

1.2 Weak Force

The weak force was first seen in the decay of the neutron. Later when it was determined that the neutron was a composite particle, its decay was found to be due to the decay of a d quark into a u quark, an electron and an anti-electron-neutrino. As more and more particles were discovered it was found that a number of these also decayed via the weak force. Since the weak force is much weaker than the strong force, the weakly decaying particles live much longer than particles which decay via the strong force. The quark eigenstates "seen" by the weak force are different from those "seen" by the strong force, and one often talks about quark mixing.

The amount of mixing is given by the Kobayashi-Maskawa matrix formula [18]:

$$\begin{pmatrix} d' \\ s' \\ b' \end{pmatrix} = \begin{pmatrix} c_1 & -s_1c_3 & -s_1s_3 \\ s_1c_2 & c_1c_2c_3 - s_2s_3e^{i\delta} & c_1c_2s_3 + s_2c_3e^{i\delta} \\ s_1s_2 & c_1s_2c_3 + c_2s_3e^{i\delta} & c_1s_2s_3 - c_2c_3e^{i\delta} \end{pmatrix} \begin{pmatrix} d \\ s \\ b \end{pmatrix}$$

where $c_i = \cos\theta_i$ and $s_i = \sin\theta_i$ for $i = 1,2,3$. The four angles are determined experimentally (at present). The three θ angles correspond to the mixing of the quark states, while the fourth angle (δ) allows for CP violation.

Table 2: Mesons Constituents

Name	Combination	J	Isospin	I_3	Charge	Strangeness	Charm
π^+	$u\bar{d}$	0	1	+1	+1	0	0
π^-	$\bar{u}d$	0	1	−1	−1	0	0
π^0	$2^{-\frac{1}{2}}(u\bar{u} - d\bar{d})$	0	1	0	0	0	0
η^0	$2^{-\frac{1}{2}}(u\bar{u} + d\bar{d})$	0	0	0	0	0	0
ρ^+	$u\bar{d}$	1	1	+1	+1	0	0
ρ^-	$\bar{u}d$	1	1	−1	−1	0	0
ρ^0	$2^{-\frac{1}{2}}(u\bar{u} - d\bar{d})$	1	1	0	0	0	0
ω^0	$2^{-\frac{1}{2}}(u\bar{u} + d\bar{d})$	0	0	0	0	0	0
K^+	$u\bar{s}$	0	$\frac{1}{2}$	$+\frac{1}{2}$	+1	+1	0
K^0	$d\bar{s}$	0	$\frac{1}{2}$	$-\frac{1}{2}$	0	+1	0
K^-	$s\bar{u}$	0	$\frac{1}{2}$	$-\frac{1}{2}$	−1	−1	0
$\bar{K}^0$	$s\bar{d}$	0	$\frac{1}{2}$	$+\frac{1}{2}$	0	−1	0
η'	$s\bar{s}$	0	0	0	0	0	0
K^{*+}	$u\bar{s}$	1	$\frac{1}{2}$	$+\frac{1}{2}$	+1	+1	0
K^{*0}	$d\bar{s}$	1	$\frac{1}{2}$	$-\frac{1}{2}$	0	+1	0
K^{*-}	$s\bar{u}$	1	$\frac{1}{2}$	$-\frac{1}{2}$	−1	−1	0
$\bar{K}^{*0}$	$s\bar{d}$	1	$\frac{1}{2}$	$+\frac{1}{2}$	0	−1	0
ϕ	$s\bar{s}$	1	0	0	0	0	0
D^+	$c\bar{d}$	0	$\frac{1}{2}$	$-\frac{1}{2}$	+1	0	+1
D^0	$c\bar{u}$	0	$\frac{1}{2}$	$+\frac{1}{2}$	0	0	+1
D^-	$d\bar{c}$	0	$\frac{1}{2}$	$+\frac{1}{2}$	−1	0	−1
$\bar{D}^0$	$u\bar{c}$	0	$\frac{1}{2}$	$-\frac{1}{2}$	0	0	−1
η_c	$c\bar{c}$	0	0	0	0	0	0
D_s^+	$c\bar{s}$	0	0	0	+1	+1	+1
D_s^-	$s\bar{c}$	0	0	0	−1	−1	−1
D^{*+}	$c\bar{u}$	1	$\frac{1}{2}$	$-\frac{1}{2}$	+1	0	+1
D^{*0}	$c\bar{d}$	1	$\frac{1}{2}$	$+\frac{1}{2}$	0	0	+1
D^{*-}	$u\bar{c}$	1	$\frac{1}{2}$	$+\frac{1}{2}$	−1	0	−1
$\bar{D}^{*0}$	$d\bar{c}$	1	$\frac{1}{2}$	$-\frac{1}{2}$	0	0	−1
J/ψ	$c\bar{c}$	1	0	0	0	0	0
D_s^{*+}	$c\bar{s}$	1	0	0	+1	+1	+1
D_s^{*-}	$s\bar{c}$	1	0	0	−1	−1	−1

Table 3: Baryons Constituents

Name	Combination	J	Isospin	I_3	Charge	Strangeness	Charm
n	*udd*	$\frac{1}{2}$	$\frac{1}{2}$	$-\frac{1}{2}$	0	0	0
p	*uud*	$\frac{1}{2}$	$\frac{1}{2}$	$+\frac{1}{2}$	+1	0	0
Σ^-	*dds*	$\frac{1}{2}$	1	−1	−1	−1	0
Σ^0	*uds*	$\frac{1}{2}$	1	0	0	−1	0
Σ^+	*uus*	$\frac{1}{2}$	1	+1	+1	−1	0
Λ^0	*uds*	$\frac{1}{2}$	0	0	0	−1	0
Ξ^-	*dss*	$\frac{1}{2}$	$\frac{1}{2}$	$-\frac{1}{2}$	−1	−2	0
Ξ^+	*uss*	$\frac{1}{2}$	$\frac{1}{2}$	$+\frac{1}{2}$	+1	−2	0
Λ_c^+	*udc*	$\frac{1}{2}$	0	0	+1	0	+1

The GIM model [4] which uses only four quarks is simpler than the Kobayashi-Maskawa model and can be used for charmed-quark interactions. It is obtained from the K.M. theory by setting $\theta_2 = \theta_3 = 0$. In the GIM model the mixed quark states are given by:

$$\begin{pmatrix} d' \\ s' \end{pmatrix} = \begin{pmatrix} \cos\theta_c & \sin\theta_c \\ -\sin\theta_c & \cos\theta_c \end{pmatrix} \begin{pmatrix} d \\ s \end{pmatrix}$$

where θ_c is called the Cabibbo angle ($\theta_c = 13.4^\circ$).

1.3 The Standard Model

In the "standard" model of S. Glashow, A. Salam, and S. Weinberg, which has unified the electromagnetic and weak force, the coupling of the photon, $W^\pm$, and Z^0 is given by [19]:

$$\begin{aligned} \mathcal{L} \;=\; & \bar{\psi}\gamma^\mu [\, eQA_\mu + \frac{e}{\sqrt{2}\sin\theta_W}(\frac{1-\gamma_5}{2})\,(T^+W_\mu^+ + T^-W_\mu^-) \\ & + \frac{e}{\sin\theta_W\cos\theta_W}(\frac{1-\gamma_5}{2}T_3 - \sin^2\theta_W\, Q)\; Z_\mu]\psi \end{aligned}$$

where the ψ are quarks and/or leptons. Particles with a left-handed spin are usually put in doublets, while the right handed fermions are in singlets. They are grouped as follows:

$$\begin{pmatrix} u \\ d' \end{pmatrix}_L, \begin{pmatrix} c \\ s' \end{pmatrix}_L, \begin{pmatrix} t \\ b' \end{pmatrix}_L, \begin{pmatrix} \nu_e \\ e^- \end{pmatrix}_L, \begin{pmatrix} \nu_\mu \\ \mu^- \end{pmatrix}_L, \begin{pmatrix} \nu_\tau \\ \tau^- \end{pmatrix}_L$$

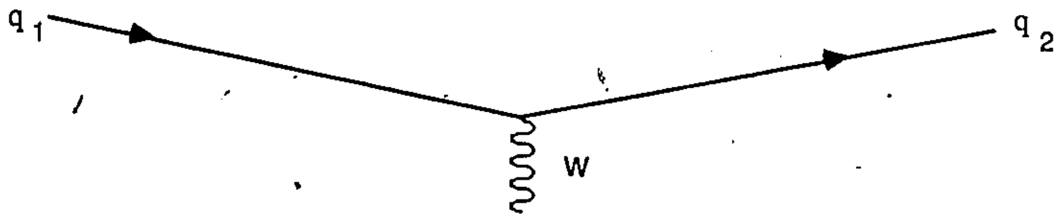

Figure 1: A qqW vertex.

$$u_R, d_R, c_R, s_R, t_R, b_R, e_R, \mu_R, \tau_R.$$

(there are no right handed neutrinos). The d', s', and b' weak eigenstates are mixtures of the down (d), strange (s), and bottom (b) mass eigen-states. The T^+ is a weak isospin raising operator which acts only on left-handed fermions; T_3 is the third component of the weak isospin (1/2 for ν_e, ,ν_μ, ν_τ, u, c, t, and $-1/2$ for e^-, μ^-, τ^-, d, s, b); Q is the electric charge (in units of proton charge); θ_W is the weak mixing angle ($\theta_W \simeq 28^o$); A_μ is the electromagnetic vector potential; W_μ is the weak vector potential. The right-handed particles do not participate in the weak interactions at all (their weak isospin equals zero).

Using the above theory it can be shown that there are no strangeness changing neutral currents, which is one reason why a charmed quark was postulated in the first place. A qqW vertex is shown in Fig. 1, the relative coupling strengths depend on the quark mixing and are as follows:

$q_1 \rightarrow q_2$	relative strength
$d \rightarrow u$	$\cos^2\theta_c$
$c \rightarrow s$	$\cos^2\theta_c$
$s \rightarrow u$	$\sin^2\theta_c$
$c \rightarrow d$	$\sin^2\theta_c$

In the GIM model charm quarks are produced by neutrinos by a number of different procedures as shown in Figure 2. The nucleon (proton and neutron) consists of valence up and down quarks surrounded by a "sea" of quark-antiquark pairs and gluons. This "sea" is produced by a cloud of virtual gluons which split up into a $q\bar{q}$ pair and which then combine again reproducing the gluon; this $q\bar{q}$ pair is present for a very short time given by the Heisenberg uncertainty principle. The charm quark is produced when an incoming neutrino interacts with either a down or a strange quark. Since the changing of a down quark into a charm quark is suppressed by a factor of $\sin^2\theta_c \simeq 0.05$, and the number of strange quarks in the "sea" is small, the charm production rate is small. In the first run of E531 charmed particles were produced in only 4% of the neutrino interactions. Once the charm quark has been produced it "dresses" itself with other quarks or antiquarks from the valence and "sea" quarks of the interaction nucleon.

1.4 Weak Decay of Particle

The weak decay of a charged lepton can be described quite easily with the aid of Figure 3 , which shows the decay of a τ^-. The lepton emits a W and a neutrino; the W then in turn decays into an electron or muon along with their corresponding neutrinos, or else into a quark and an anti-quark (if the mass is high enough). Using fairly standard techniques and ignoring the mass effects of the decay products, the leptonic decay width of the lepton is predicted to be:

$$\Gamma_l(l^- \rightarrow l'^- \bar{\nu}'\nu) = \frac{G_F^2 m_l^5}{192\pi^3}$$

where G_F is the Fermi coupling constant (1.16637×10^{-5} GeV^{-2}), and m_l is the mass of the decaying lepton.

In order to obtain the lifetime the leptonic branching ratio for a given lepton has to be known. The only possible first order decay mode of the muon is into an electron and thus the $\mu^- \rightarrow e^-$ branching ratio is 1.0. The τ^-, however, can decay into an electron, muon, and a $\bar{u}d$ pair; because there are three colours there are 3 possible $\bar{u}d$ pairs. Thus the electronic and muonic branching ratios $(B.R._l)$

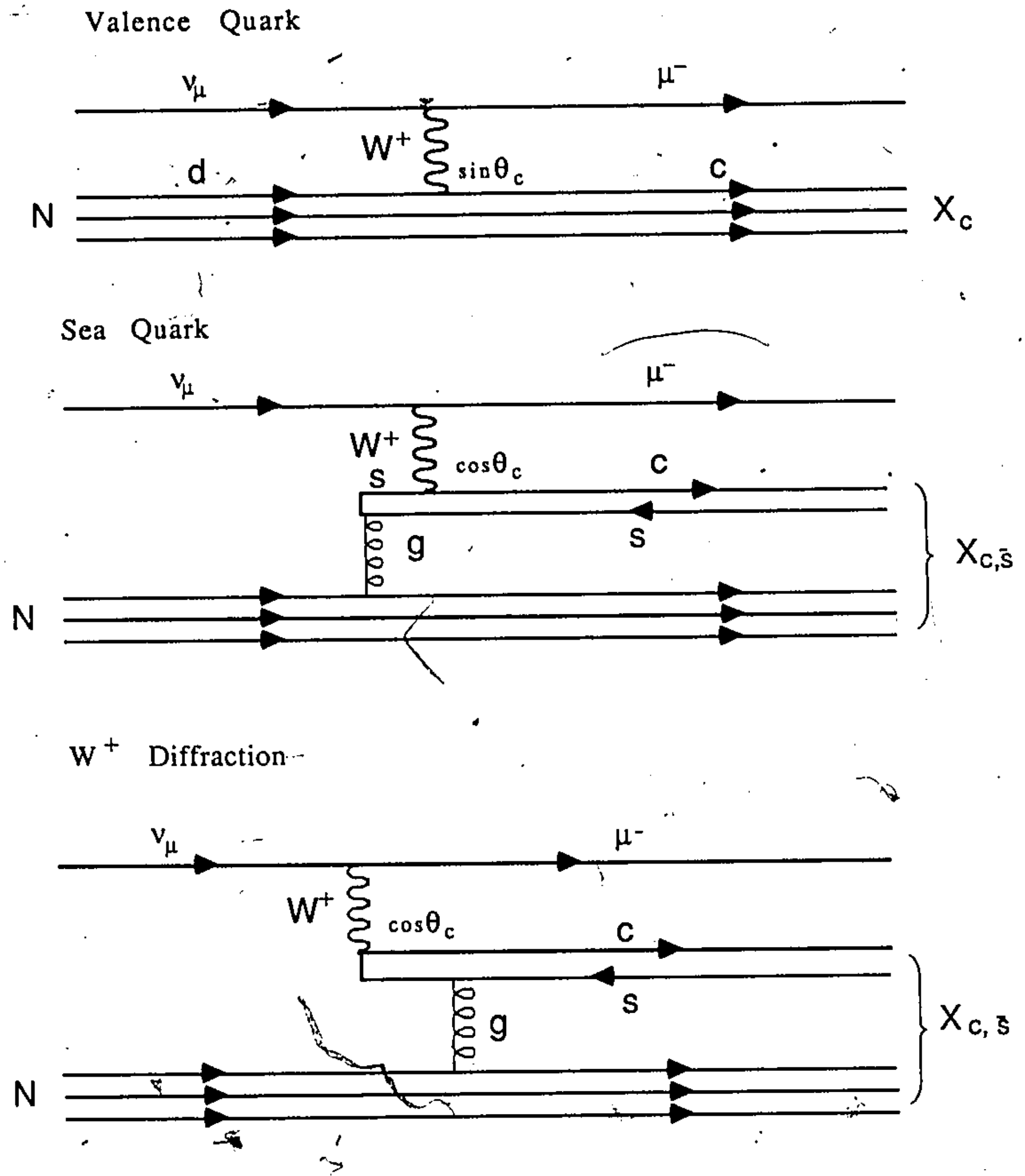

Figure 2: Charm production by neutrinos.

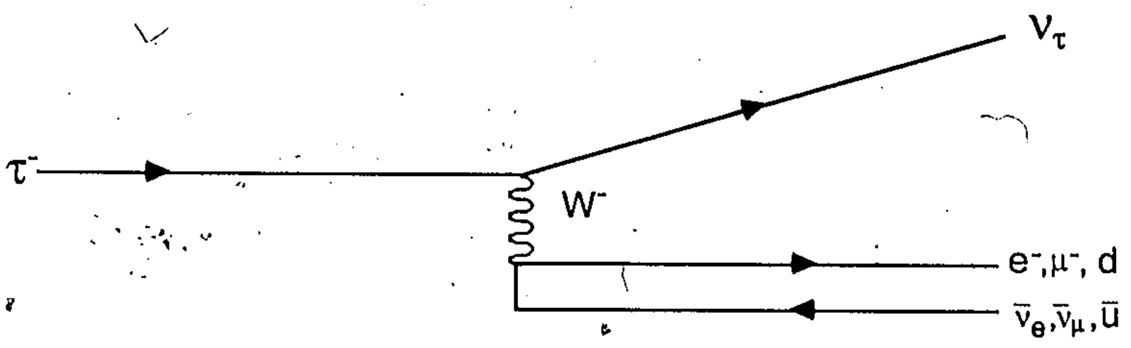

Figure 3: Decay of charged lepton.

of the τ are predicted to be 1/5. When the W breaks up into the quark pair the quarks fragment, pulling other quarks out of the vacuum. Since this involves the strong force the branching ratio is somewhat modified. Ignoring this effect and using $\Gamma_l = B.R_l \cdot \Gamma_{total}$ and $\tau = 1./\Gamma_{total}$ the lifetime of the tau lepton is predicted to be:

$$\tau_\tau = \frac{1}{5}\left(\frac{m_\mu}{m_\tau}\right)^5 \tau_\mu = \ 3.2 \times 10^{-13}\ s.$$

This is in excellent agreement with the experimentally measured tau lifetime of $(3.3 \pm 0.4) \times 10^{-13}$ seconds [19].

The same procedure can be used to calculate the lifetime of the charm. In order to do this calculation it has to be assumed that the non-charm quark in the charmed-particle does not interact with the charm quark and thus has no effect on the lifetime. This is called the spectator model because the non-charm quark is assumed to behave as a 'spectator'. It turns out that this model is not correct. However, it can be used to get the correct order of magnitude for the charmed-particle lifetimes. In this model the charm quark emits a W and changes into a strange (or down) quark, and the emitted W then decays as in the tau decay. The mass of the charm quark is not known very accurately. It can be estimated to be

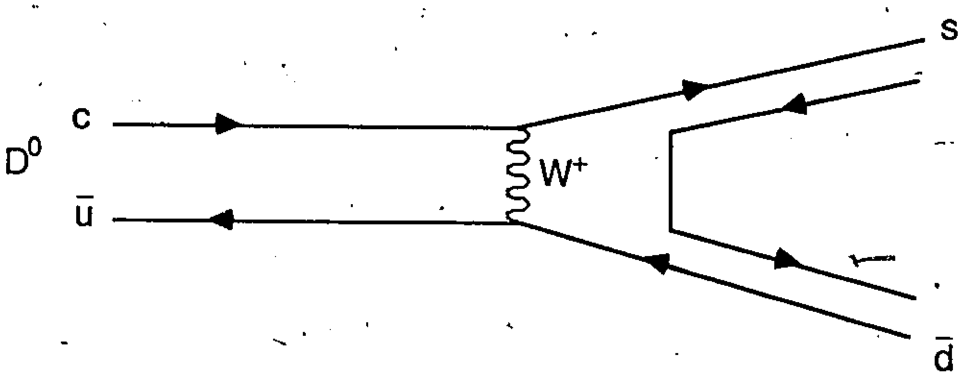

Figure 4: Decay of D^0 via the exchange diagram.

1.5 GeV/c^2 and thus the charm lifetime is predicted to be:

$$\tau_c = \frac{1}{5}\left(\frac{m_\mu}{m_c}\right)^5 \tau_\mu = 7.6 \times 10^{-13}\ s.$$

If the spectator model is correct, the lifetimes and semileptonic branching ratios would be the same for all charmed particles. However, the liftetimes and branching ratios have been found to differ by more than a factor of two. The non-charm quark must thus interact with the charm quark, modifying the charmed-particles lifetimes in some manner. One possible way for the non-charm quark to have an effect on the lifetimes is if the exchange diagram (Fig. 4) is non-negligible. In this type of interaction the emitted W does not 'decay' but changes the $\bar{u}$ quark of the D^0 into a $\bar{d}$ quark. This type of diagram is not possible for the $D^\pm$ because the emitted W^+ cannot interact with the $\bar{d}$ (in the D^+), and thus the D^0 will have an extra decay diagram that the $D^\pm$ does not have. Hence their lifetimes will differ, which is what is observed experimentally.

The Λ_c^+ also has a possible exchange diagram similar to the D^0, the $D_s^\pm$ does not have an exchange diagram but it is possible for it to decay via the annihilation diagram which is shown in Figure 5. The exact contributions of these diagrams are not known very accurately, but they would probably tend to decrease the particle lifetimes, as is observed experimentally.

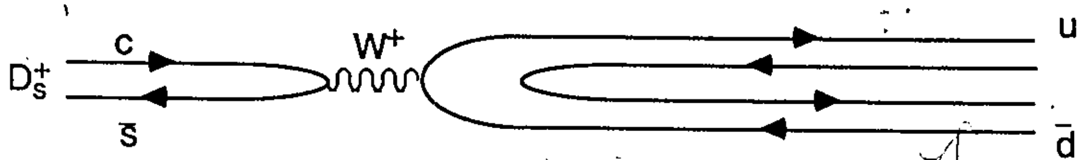

Figure 5: Decay of $D_s^\pm$ via the annihilation diagram.

Prior to 1982 very few experiments had actually measured the lifetimes of the charmed particles. E-531 was one of the first experiments to measure the lifetimes using relatively large statistics. The first run results of E-531, along with the measurements of a number of other experiments, are shown in Table 4. The references were taken from the 1984 Review of Particle Properties [21]. Our experiment shows a noticeable difference between the $D^\pm$ and D^0, $D_s^\pm$, and Λ_c^+ lifetimes. See also reference [32] for a review of the various charmed-particle lifetimes.

1.5 Kinematics of Neutrino Interactions

In the study of neutrino interactions there are a large number of observables which can be studied. There are, however, a few "standard" variables which are normally used to describe neutrino interactions [33]. The reaction shown by Figure 6 is

$$a + b \rightarrow c + X$$

where "a" is the incident neutrino, "b" is the target nucleon, "c" is the outgoing lepton (a charged lepton for charged current interactions and a neutrino for neutral current), and "X" represents the particle or particles produced in the interaction. The incoming lepton has a four-vector momentum of k and the outgoing lepton has a momentum k', the target had a momentum p while the sum of the "interaction particles" momentum is p'. The total momentum transferred by the exchange

Table 4: Comparison of Charmed-Particles Lifetimes Prior to 1982

Particle	Ref.	Events	Lifetime (10^{-13} s)
D^0	[12]	16	$2.3^{+0.8}_{-0.5}$
	[22]	—	< 8.0
	[23]	3	$0.53^{+0.57}_{-0.25}$
	[24]	3	$0.58^{+0.2}_{-0.8}$
	[25]	—	< 2.1
	[26]	3	$2.8^{+2.2}_{-1.3}$
	[27]	1	2.1
		1	5.9
	[28]	5	$3.1^{+2.0}_{-1.6}$
	[29]	11	$6.7^{+3.5}_{-2.0}$
$D^{\pm}$	[13]	11	$11.5^{+7.5}_{-3.5}$
	[22]	—	< 8.0
	[23]	4	$2.5^{+2.2}_{-1.1}$
	[24]	8	4.4
	[25]	—	$10.4^{+3.9}_{-2.9}$
	[26]	1	$2.2^{+2.3}_{-1.1}$
	[29]	9	$8.2^{+2.2}_{-2.5}$
	[30]	70	$9.5^{+3.1}_{-1.9}$
$D_s^{\pm}$	[13]	4	$1.9^{+1.3}_{-0.7}$
	[31]	1	1.4
Λ_c^+	[13]	8	$2.3^{+1.0}_{-0.6}$
	[24]	1	0.57

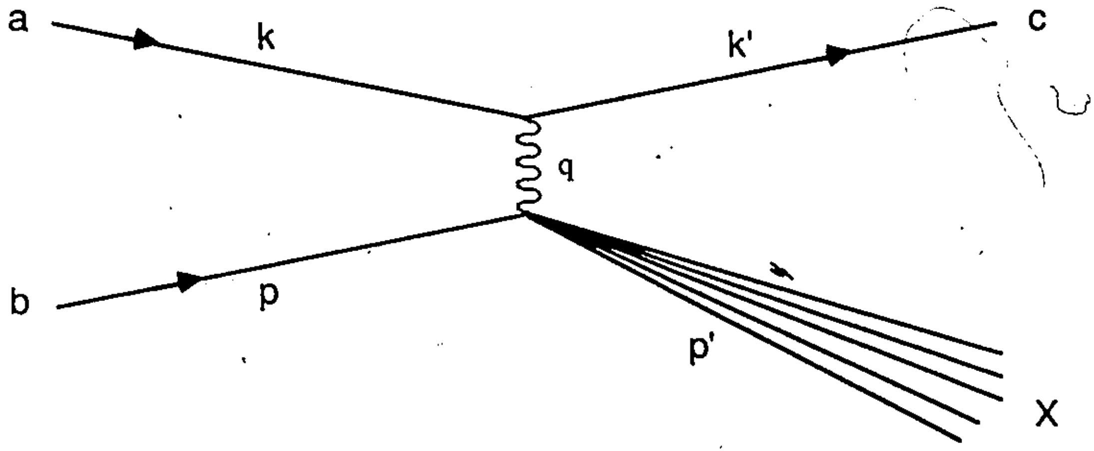

Figure 6: Neutrino interaction.

particle ($W^{\pm}$ or Z^0) is

$$q = k' - k$$

Because of tagging inefficiencies this experiment can mainly study charged current interactions, and in this discussion it will be assumed that the incoming neutrino is a muon neutrino, and the outgoing lepton a negative muon; the generalization to other neutrino species is very straight forward. The various variables used to describe neutrino interactions are defined as follows:

$$\begin{aligned} k &= (E_\nu, \vec{\mathbf{p}}_\nu) \\ k' &= (E_\mu, \vec{\mathbf{p}}_\mu) \\ p &= (m_N, \vec{0}) \\ p' &= (E_X, \vec{\mathbf{p}}_x) \end{aligned}$$

$$Q^2 = -q \cdot q = 2E_\nu E_\mu - 2P_\nu P_\mu \cos\theta - m_\nu^2 - m_\mu^2$$

$$\begin{aligned}
\nu &= E_h - m_N = E_\nu - E_\mu \\
x &= \frac{-q\cdot q}{2p\cdot q} = \frac{Q^2}{2m_N\nu} \\
y &= \frac{\nu}{E_\nu} \\
W^2 &= m_X^2 = m_N^2 + 2m_N\,\nu - Q^2
\end{aligned}$$

Inclusive reactions which produce a shower of hadrons are usually referred to as deep inelastic reactions.

The variable "Q^2" is referred to as the momentum transferred, "ν" is the energy transferred to the recoiling hadrons, while "W" is the invariant mass of the particles recoiling against the muon. In the quark model the struck nucleon is composed of a number of quarks and the neutrino interacts with one of the quarks. For large Q^2 the variable "x" is the fraction of the nucleon energy possessed by the struck quark. The variable "y" is the fraction of the available energy associated with the recoiling mass.

1.5.1 Quark Fragmentation

The various fragments recoiling against the muon can be divided up into two groups current fragments and target fragments with the difference between the two types shown in Figure 7. It is almost impossible to actually tell which fragments are current fragments and which are target fragments. However, one approach is to use the variable "Z", which is defined as

$$Z = \frac{E_i}{\nu}$$

where E_i is the energy of the ith outgoing fragment. Generally the particles with a high Z value correspond to the current fragment while the target fragments have a low Z. If one assumes that only d quarks participate in charged-current νN interactions (and the sea quarks are ignored) one has

$$\frac{\partial\sigma}{\partial x\,\partial Z} = \frac{\partial\sigma_{CC}^{\nu N}}{\partial x} D_u^h(Z,x)$$

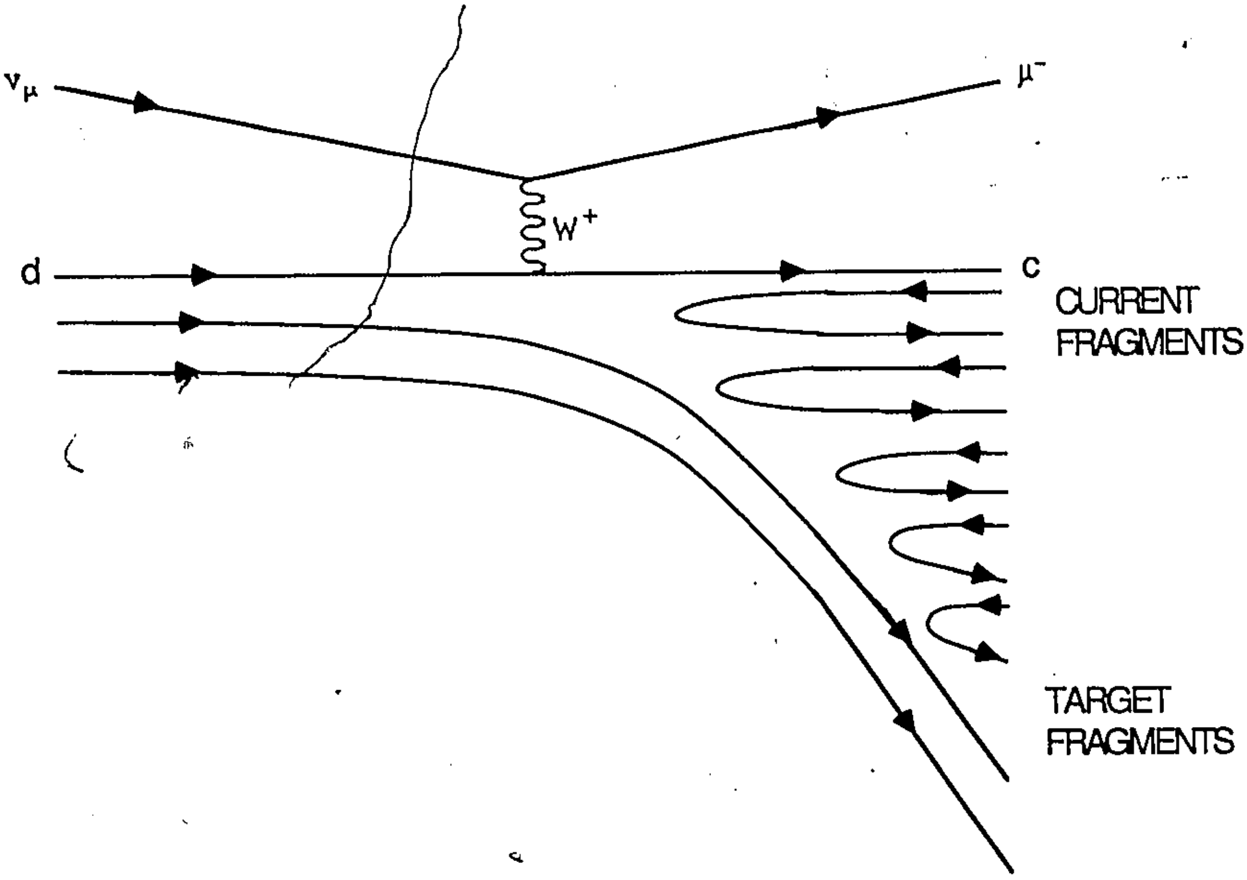

Figure 7: Fragmentation of quarks.

where $D_u^h(Z,x)$ is called the "fragmentation function" for the scattered u quark to become a hadron of type h. Making the hypothesis (called factorization) that the fragmentation of a quark does not depend on the previous history of the quark but only on its energy, the fragmentation function becomes

$$D_u^h(Z,x) \to D_u^h(Z)$$

Thus ideally it should be possible to measure the fragmentation of a quark by observing the distribution of particles in the final state. However, in this derivation it is assumed that there are no target fragments. The target fragments will distort the observed particle distribution. In order to separate the current and target fragments an emperical rule is that current fragments should have $Z > 0.2$. Different theories will give different fragmentation functions, and thus the particle Z distribution can be used to check on the validity of different theories. Due to the contamination from the target fragments, the Z distribution has a limited accuracy. Charmed-particles are known to be current fragments since they are produced in the initial interaction (they can be produced in the fragmentation process but this will be a second order effect, and because of mass constraints be extremely small and negligible); thus they are perfect for checking the theoretical fragmentation functions. A study of the target fragments is more difficult since the only thing that could tag them is the fact that they usually, but not always, have a low Z.

1.5.2 Feynman x

Another possible variable to use in the study of the neutrino interactions is Feynman x which is defined as

$$x_F = \frac{P_L^*}{P_L^*(\max)}$$

P_L^* is the projected momentum of a particle (in the center of mass of the recoiling hadrons) on the momentum vector pointing in the direction of motion of the center of mass (C.M.); $P_L^*(\max)$ is the maximum possible C.M. momentum that a track could have and still be consistent with conservation laws. The value of $P_L^*(\max)$ is obtained by assuming that there are only two hadrons in the interaction and they are produced in the "decay" of a particle of mass W, with this assumption

$$P_L^{*2}(\max) = \frac{W^4 + m_h^4 + m_r^4 - 2W^2m_h^2 - 2m_h^2m_r^2 - 2m_r^2W^2}{4W^2}$$

where m_h is the mass of the hadron being considered, and m_r is the mass of the recoiling hadron. m_r is set equal to zero if the hadron being considered is a baryon (e.g. proton or Λ_c^+), and m_r is set equal to the the nucleon mass (average of proton and neutron) if h is a meson. For events with a very large invariant mass $P_L^*(\max) \approx W/2$ and some experiments use a Feynman x definition given by

$$x_F = \frac{2P_L^*}{W}$$

It does not matter very much which definition is used since the two definitions give almost the same answer.

A negative x_F corresponds to a particle moving backwards in the center of mass system. An x_f value of +1 would correspond to particles being knocked very strongly in the forward direction while particles with $x_F = -1$ would correspond to particles that had not been involved in the initial collision and were almost at rest in the lab frame. Because most particles only have a small fraction of the maximum possible momentum and they can go in all directions with equal probability, the Feynman x distribution for most particles will be very peaked at $x_F = 0$.

Feynman x is meaningless for events involving the quasi-elastic production of a Λ_c^+. The quasi-elastic production of a Λ_c^+ is shown in Figure 8, in which the reaction $\nu_\mu n \rightarrow \mu^- \Lambda_c^+$ takes place. In this process no other particles are produced. However, in practice the neutron with which the incoming neutrino interacts is not a free neutron; there are other particles present to complicate the picture. After the neutron has been changed into a Λ_c^+, the original nucleus breaks up, producing a few extra particles. The produced Λ_c^+ will also travel through part of the nucleus interacting with some of the other nucleons via the strong force, and hence may produce a few more particles. Thus experimentally it is very difficult to tag a Λ_c^+ produced quasi-elastically. The usual signature is a Z value of 1.0 and only two energetic tracks coming from the primary interaction, namely the μ^- and the Λ_c^+. The remaining particles have very low momenta.

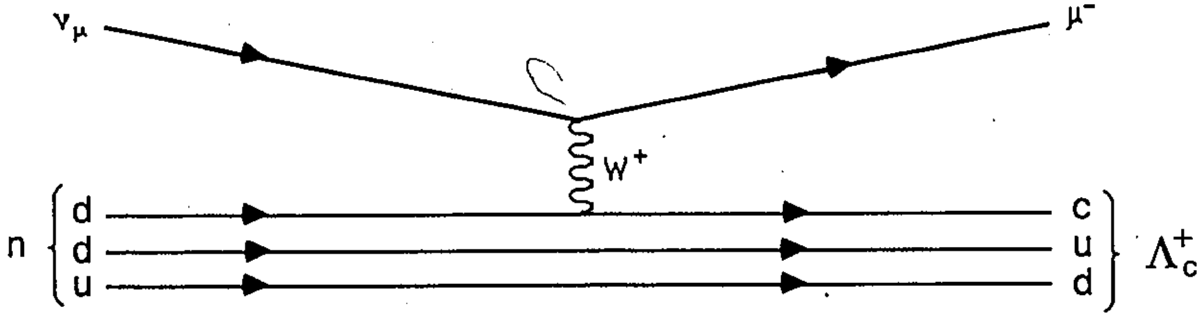

Figure 8: Quasi-elastic production of Λ_c^+.

1.5.3 Transverse Momenta

Two other variables that should be considered are p_{out} and $p_\perp$ [20]. The transverse momentum ($p_\perp$) of a particle is defined with respect to the direction of the recoiling hadronic system ($\vec{\mathbf{p}}_X$). p_{out} is the projection of a particle's momentum vector on a unit vector perpendicular to the plane defined by the incoming and outgoing leptons. Assuming that the target nucleus is completely at rest (no Fermi motion), the direction of the recoiling hadrons will lie in the same plane as the incoming neutrino and outgoing muon. Mathematically the two vectors are defined as:

$$\begin{aligned} p_\perp &\equiv |\vec{\mathbf{p}}_i - (\vec{\mathbf{p}}_i \cdot \hat{\mathbf{p}}_X)\hat{\mathbf{p}}_X| \\ p_{\text{out}} &\equiv \vec{\mathbf{p}}_i \cdot \frac{\vec{\mathbf{p}}_\nu \times \vec{\mathbf{p}}_\mu}{|\vec{\mathbf{p}}_\nu \times \vec{\mathbf{p}}_\mu|} \end{aligned}$$

The relative directions of the various momentum vectors are shown in Figure 9. If the hadrons are produced isotropically about $\vec{\mathbf{p}}_X$ then $< p_{\text{out}} >= \frac{2}{\pi} < p_\perp >$ and $< p_{\text{out}}^2 >= \frac{1}{2} < p_\perp^2 >$. The variable p_{out} is used by some experiments because it does not depend on the energies of the muon and neutrino, which can at times be very uncertain.

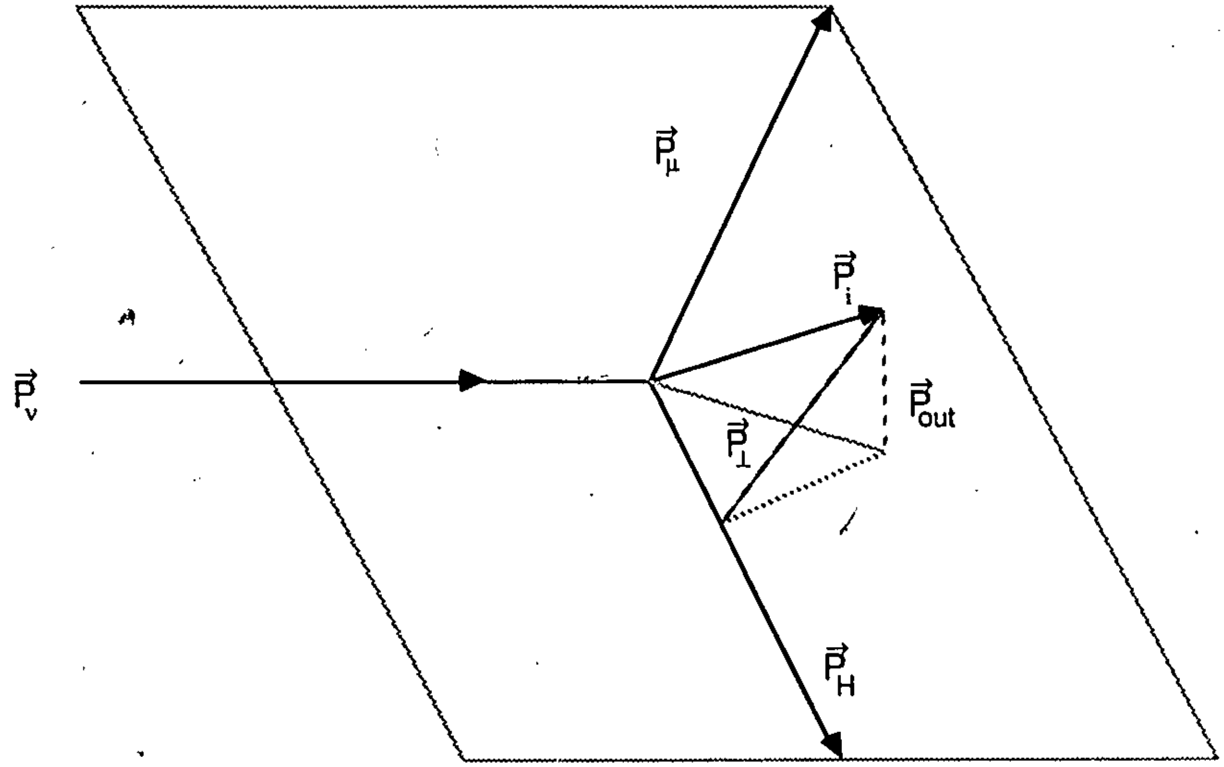

Figure 9: Definition of $p_\perp$ and p_{out}.

1.6 Cross Sections

The differential cross section of charged-current νN interactions in terms of Q^2 and ν may be written as [33]

$$\frac{d^2\sigma^{\nu N}}{dQ^2\,d\nu} = \frac{G_F^2}{2\pi}\frac{E_\mu}{E_\nu}\left\{\cos^2\frac{\theta}{2}W_2(Q^2,\nu) + 2\sin^2\frac{\theta}{2}W_1(Q^2,\nu) \pm \frac{E_\nu + E_\mu}{m_N}\sin^2\frac{\theta}{2}W_3^{\nu,\bar{\nu}}(Q^2,\nu)\right\}$$

The three $W_{1,2,3}$ terms are the structure functions where W_1 is due to magnetic scattering, W_2 is due to electric scattering, and W_3 is a parity violating term which arises because of the interference between the vector and axial currents (V-A interference). The + sign of the ± sign is used for νN interactions, while the − sign is for $\bar{\nu}N$ interactions.

Defining new form factors as follows:

$$\begin{aligned} F_1^{\nu,\bar{\nu}}(Q^2,x) &= W_1^{\nu,\bar{\nu}}(Q^2,\nu) \\ F_2^{\nu,\bar{\nu}}(Q^2,x) &= \nu W_2^{\nu,\bar{\nu}}(Q^2,\nu)/m_N \\ F_3^{\nu,\bar{\nu}}(Q^2,x) &= \nu W_3^{\nu,\bar{\nu}}(Q^2,\nu)/m_N \end{aligned}$$

and changing the variables used from Q^2 and ν to x and y the above becomes

$$\frac{d^2\sigma^{\nu N,\bar{\nu}N}}{dx\,dy} = \frac{G_F^2 m_N E_\nu}{\pi}\left\{(1 - y - \frac{m_N xy}{E_\nu})F_2^{\nu,\bar{\nu}} + y^2 x F_1^{\nu,\bar{\nu}} \pm y(1 - \frac{y}{2})xF_3^{\nu,\bar{\nu}}\right\}$$

In the limit $Q^2 >> m_N^2$ and $\nu >> m_N$, the form factors $F_i(Q^2,x)$ must be independent of Q^2 (called scaling limit) and thus:

$$F_i(Q^2,x) \rightarrow F_i(x)$$

At first there appear to be 12 different form factors (3 each for νn, νp, $\bar{\nu}n$, and $\bar{\nu}p$). However, if charge symmetry is assumed in strong interactions then

$$F_i^{\nu n} = F_i^{\bar{\nu}p} \quad \text{and} \quad \mathrm{F}_i^{\bar{\nu}n} = \mathrm{F}_i^{\nu p} \qquad \mathrm{i} = 1,2,3$$

This will leave six form factors which can be reduced to three if targets with equal numbers of protons and neutrons are used.

If in the cross section equation the small term $m_N xy/2E_\nu$ is ignored and the equation rearranged, then

$$\frac{d^2\sigma^{\nu N,\bar{\nu}N}}{dx\,dy} = \frac{G_F^2 m_N E_\nu}{\pi}\left\{(xF_1 \pm \frac{xF_3}{2}) + (F_2 - 2xF_1)(1-y) + (xF_1 \mp \frac{xF_3}{2})(1-y)^2\right\}$$

Using the Callan-Gross relationship:

$$F_2 - 2xF_1 = 0$$

the cross section formula becomes

$$\frac{d^2\sigma^{\nu N,\bar{\nu}N}}{dx\,dy} = \frac{G_F^2 m_N E_\nu}{\pi}\left\{(xF_1 \pm \frac{xF_3}{2}) + (xF_1 \mp \frac{xF_3}{2})(1-y)^2\right\}$$

Integrating the cross section formula over y gives:

$$\begin{aligned}
\frac{d\sigma^{\nu p}}{dx} &= \sigma_0 E_\nu\left\{\frac{2}{3}F_2^{\nu p}(x) + \frac{1}{3}xF_3^{\nu p}(x)\right\}\\
\frac{d\sigma^{\bar{\nu} p}}{dx} &= \sigma_0 E_\nu\left\{\frac{2}{3}F_2^{\bar{\nu} p}(x) - \frac{1}{3}xF_3^{\bar{\nu} p}(x)\right\}
\end{aligned}$$

These formulae predict that the total cross section should rise linearly with energy which is exactly what is observed experimentally.

The four independent structure functions may be written in terms of the quark and anti-quark distributions inside the nucleus (u, d, s, and c) as follows[34, page 277]:

$$\begin{aligned}
F_2^{\nu p}(x) &= 2x(\bar{u}(x) + d(x) + s(x) + \bar{c}(x))\\
F_2^{\bar{\nu} p}(x) &= 2x(u(x) + \bar{d}(x) + \bar{s}(x) + c(x))\\
xF_3^{\nu p}(x) &= 2x(-\bar{u}(x) + d(x) + s(x) - \bar{c}(x))\\
xF_3^{\bar{\nu} p}(x) &= 2x(u(x) - \bar{d}(x) - \bar{s}(x) + c(x))
\end{aligned}$$

The above are the structure functions for charged current interactions; for the neutral current interactions the structure functions are

$$\begin{aligned}
F_2^{\nu p} = {} & 2\rho^2 x\left\{\left[\frac{1}{4} - \frac{2}{3}\sin^2\theta_W + \frac{8}{9}\sin^4\theta_W\right]\left[u(x) + \bar{u}(x) + c(x) + \bar{c}(x)\right]\right.\\
& \left. + \left[\frac{1}{4} - \frac{1}{3}\sin^2\theta_W + \frac{2}{9}\sin^4\theta_W\right]\left[d(x) + \bar{d}(x) + s(x) + \bar{s}(x)\right]\right\}
\end{aligned}$$

$$\begin{aligned}
xF_3^{\nu p} &= 2\rho^2 x \left\{ \left[\frac{1}{4} - \frac{2}{3}\sin^2\theta_W\right] [u(x) - \bar{u}(x) + c(x) - \bar{c}(x)] \right. \\
&\quad \left. + \left[\frac{1}{4} - \frac{1}{3}\sin^2\theta_W\right] \left[d(x) - \bar{d}(x) + s(x) - \bar{s}(x)\right] \right\} \\
F_i^{\bar{\nu} p} &= F_i^{\nu p} \\
\rho &= \frac{m_W^2}{m_Z^2 \cos^2\theta_W}
\end{aligned}$$

The quark distributions are normalized to satisfy the following conditions

$$\begin{aligned}
\int_0^1 (u - \bar{u})dx &= \begin{cases} 2 & \text{protons} \\ 1 & \text{neutrons} \end{cases} \\
\int_0^1 (d - \bar{d})dx &= \begin{cases} 1 & \text{protons} \\ 2 & \text{neutrons} \end{cases} \\
\int_0^1 (s - \bar{s})dx &= \int_0^1 (c - \bar{c}) = 0
\end{aligned}$$

By measuring the cross sections as a function of x it is thus possible to measure the structure and thus in turn the quark and anti-quark distributions. There are a number of different theoretical predictions for the various quark and anti-quark distributions.

Chapter 2

Experimental Apparatus

This experiment, designated E-531 and designed to study charmed particle decays, was an international collaboration with participation from four countries and over 72 physicists. The people involved in the second run are listed in Appendix A. In designing the detector a number of important considerations had to be taken into account: the measurement of very short decays distances, along with an accurate determination of the momentum, particle type and direction of the decay products. These objectives were achieved by using a nuclear emulsion target, in which the charm decay length and particle directions were measured, followed by a spectrometer in which the products from the charmed-particle decays were identified and their momenta measured. The charmed particles were created by a beam of incoming neutrinos which were produced by the proton synchrotron at the Fermi National Accelerator Laboratory (Fermilab) in Batavia, Illinois, U.S.A. Two complete runs of the experiment were carried out, one from November 1978 to February 1979 and a second run from from November 1980 to June 1981.

Charmed particles are expected to be produced in about 8% of the neutrino interactions [35, p. 317], while dilepton data [36] suggested that charm particles are produced in up to 10% of neutrino interactions. The first run of our experiment was in agreement with these predictions, charm being produced in about 7% of the charged-current events [16]. Because neutrinos are neutral particles they have the advantage of not producing any emulsion tracks and so it was possible to leave the emulsion target sitting in the neutrino beam for several months. The long exposure time was necessary due to the low cross section ($E \times 0.67 \times 10^{-38}$ cm^2 /GeV) for neutrino interactions.

The detector is shown in Figure 10 with the incoming neutrino beam entering from the left; the coordinate system is a right handed coordinate system with the Z axis in the direction of the neutrino beam; the X axis is perpendicular to the beam direction and parallel to the ground; the Y axis is at a right angle to the ground. Part of the apparatus sat on a 3.5 ton 1.5 m x 2.75 m x 0.3m granite block to ensure that the relative position of the emulsion and drift chambers remained constant. The positions of the drift chambers were measured continuously with respect to the granite block using a Linear Variable Differential Transformer (LVDT) gauging system. To minimize thermal fluctuations the ambient temperature was maintained at $20 \pm 5°$C, and the emulsion was kept at $10.0 \pm 2.5°$C during the experiment.

2.1 Neutrino Beam

The proton synchroton at Fermi National Accelerator Laboratory (Fermilab) was able to accelerate protons up to a momentum of 500 GeV/c. Protons with a momentum of 350 GeV/c were used for the first run while 400 GeV/c protons were used for the second run of the experiment to produce the neutrino beam. The layout of the proton beam is shown in Figure 11 and the neutrino beam in Figure 12. Protons were extracted from the ring every 7 seconds with about 1.5×10^{13} protons per spill and they hit a BeO target one interaction length long (30 cm); the interactions in the BeO produced a large number of particles predominantly pions and kaons.

These pions and kaons then passed through a magnetic horn, 5.3 m downstream (direction of beam) of the target shown schematically in Figure 13. This horn generated a magnetic field which focused (defocused) particles with an angular distribution greater than 1.8 mrad by bending them toward (away) from the beam center. These particles passed through part of the horn itself and about 10 % of the particles interacted. Particles with a production angle between 1.3 and 1.8 mrad

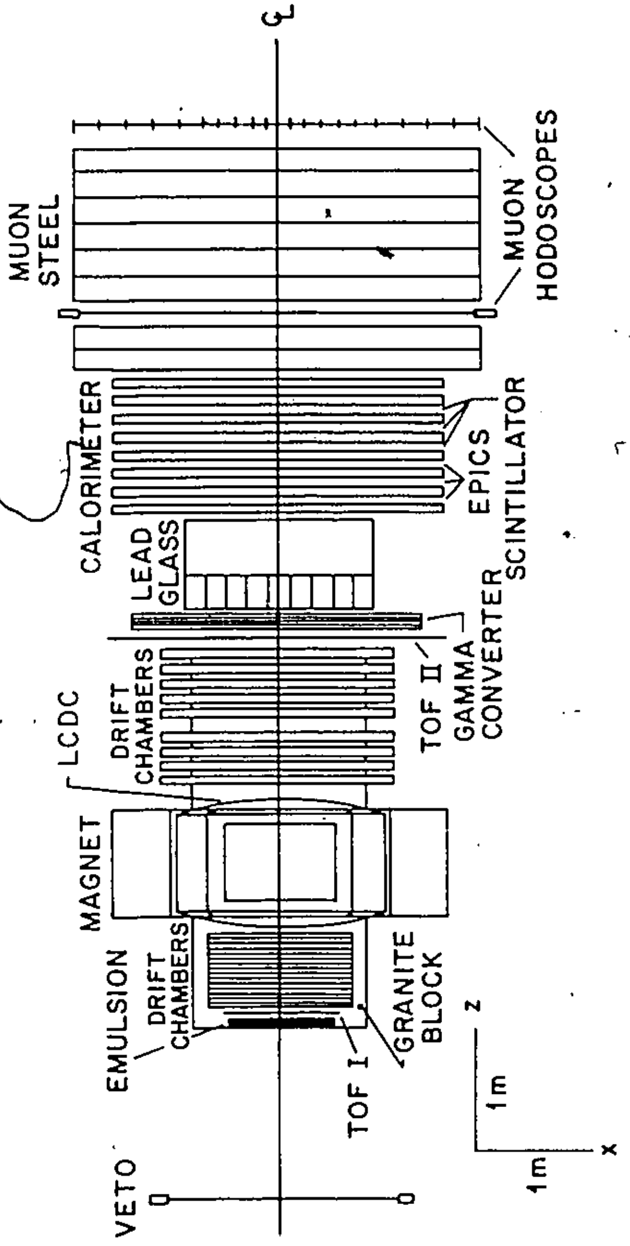

Figure 10: The E-531 spectrometer.

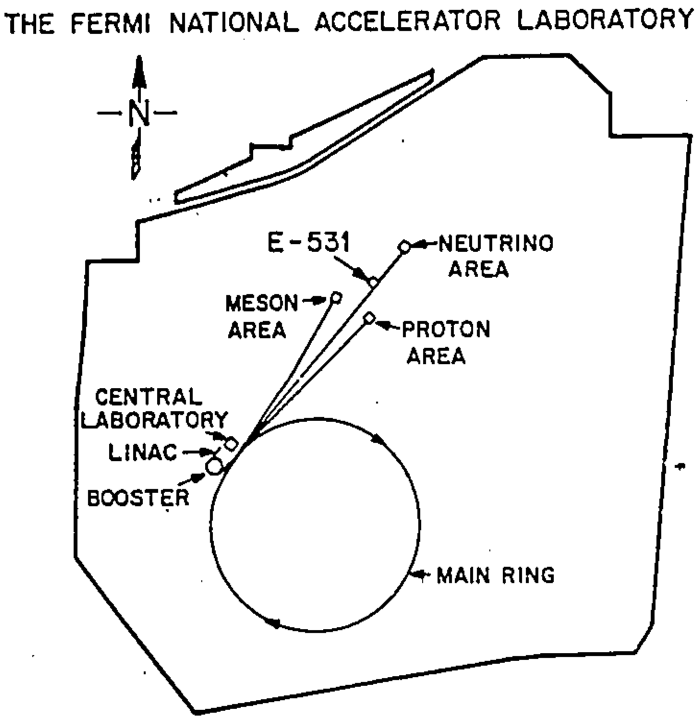

Figure 11: The Fermilab proton beam.

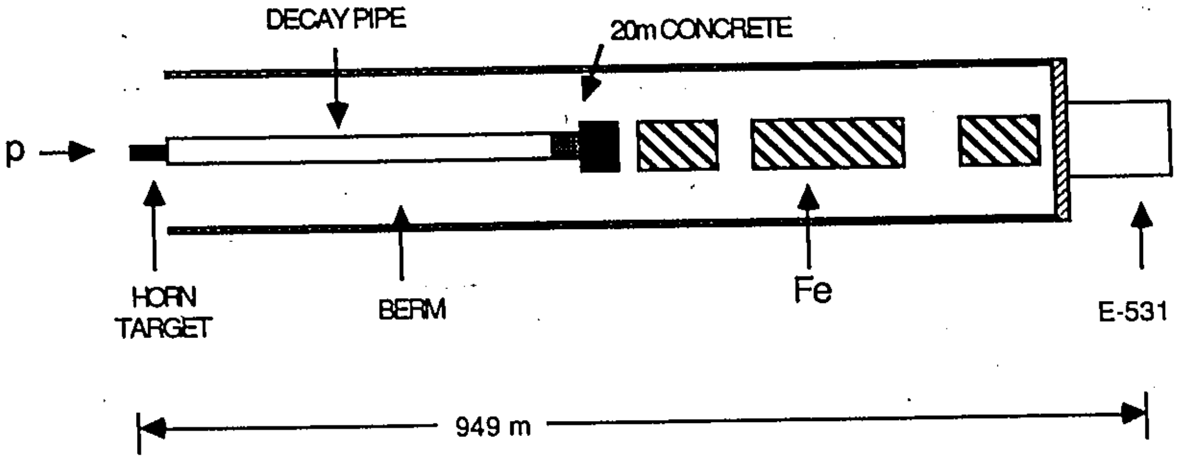

Figure 12: The neutrino beam.

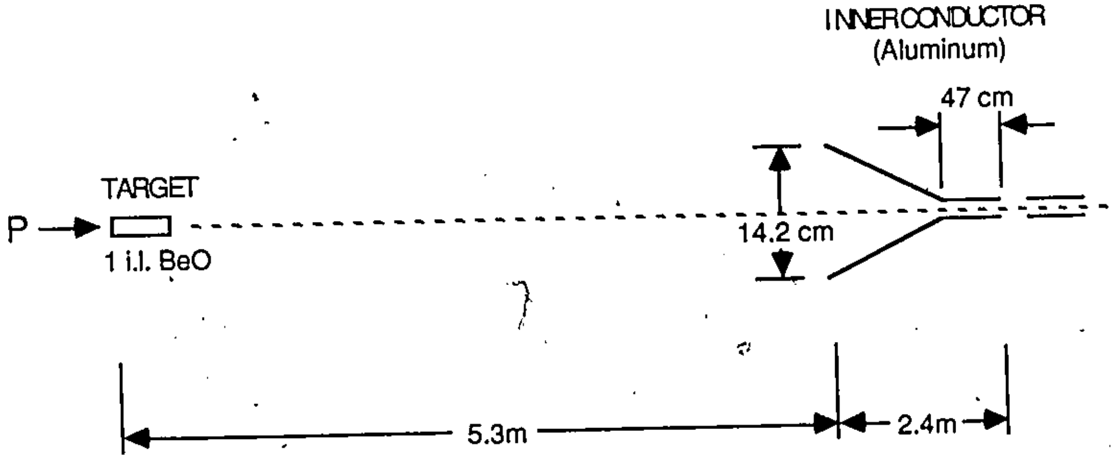

Figure 13: Schematic drawing of the single horn system.

Table 5: Decay Modes Producing Neutrino Beam

Particle Decay Mode	Branching Ratio
$\pi^+ \rightarrow \mu^+\nu_\mu$	100 %
$K^+ \rightarrow \mu^+\nu_\mu$	63.51 %
$K^+ \rightarrow \mu^+\nu_\mu\pi^0$	3.18 %
$K^+ \rightarrow e^+\nu_e\pi^0$	4.82 %
$K_L^0 \rightarrow e^+\nu_e\pi^-$	19.35 %
$K_L^0 \rightarrow \mu^+\nu_\mu\pi^-$	13.55 %
$\mu^+ \rightarrow e^+\nu_e\bar{\nu}_\mu$	100 %

were not bent but passed through part of the horn's aluminium collar and about half of these particles interacted, particles with an angle less than 1.3 mrad did not interact with anything. The horn current was set to 80 (85) kA for most of the first (second) run producing a transverse momentum kick of 0.171 (0.182) GeV/c to the particles. Positively charged particles were focused producing a beam of predominantly neutrinos. For part of the running time the horn current had the opposite sign thus focusing negatively charged particles and producing a beam of predominantly antineutrinos. It was found that 0.2 (1.5)% of all the first (second) run triggers occurred during these antineutrino runs.

The pions and kaons (and any protons that did not interact) passed through a long vacumn pipe, 410 m long and 0.91 m in diameter, about 10 % of the pions and 30 % of the kaons decayed in this region producing a number of neutrinos and charged particles; Table 5 shows the dominant decay modes which result in neutrinos. Particles which did not decay (the protons, and most of the decay products) were absorbed by concrete at the end of the decay pipe. A combination of concrete, earth and 14,000 tons of steel (during the first run there were only 8,000 tons) sat between the end of the decay pipe and our E-531 detector. The neutrinos were not stopped by the shielding and passed through our detector which was installed 949 m downstream of the BeO target. The shielding was not 100 % efficient and some muons were able to penetrate the shielding and reach our detector.

A Monte-Carlo of the neutrino beam, using the momentum and angular distributions of A.J. Malensek [37] for the pions and kaons, was used to predict the energy spectra and relative intensities of the various neutrinos. The relative pions and kaons distributions are known very well but the absolute number of particles is not known very well and thus it is possible to generate only relative energy spectra but not absolute distributions. The predicted spectra are shown in figure 14.

2.2 Veto Counter

Moving downstream through the apparatus the first thing encountered was the veto counter situated 1.3 m upstream of the emulsion target. It consisted of seven scintillation paddles with an Amperex 56AVP phototube on each end. Each paddle was 25.4 cm x 178 cm; the paddles were placed horizontally (parallel to the X axis). The total area of the paddles was 3.1 m^2(1.78 × 1.78). The purpose of the veto counter was to prevent the triggering of the detector on events caused by charged particles present in the neutrino beam. The timing of the counters was set such that neutrino interactions which produced backward going tracks did not veto the event.

It was estimated that the counters had an efficiency of 98 % for detecting charged particles [10]. During the first run the veto counter had an overall efficiency of $89 \pm 1\%$, the 11% inefficiency was due to dead time losses (5 ± 1 %), charged track detection inefficiency ($2 \pm 1\%$), and geometric losses ($3 \pm 1\%$); 13 ± 2 % of the real neutrino triggers were accidentally vetoed. For the second run the veto counter was rebuildt and the timing improved to give an efficiency of $97 \pm 1\%$, and only about 1 % of real neutrino triggers were vetoed.

2.3 Emulsion Target

Downstream of the veto counter was the emulsion stack, shown in Figures 15 and 16. The emulsion target consisted of 22.9 litres Fuji nuclear emulsion for the first run and 32.1 litres for the second run. During each run the emulsion was divided into

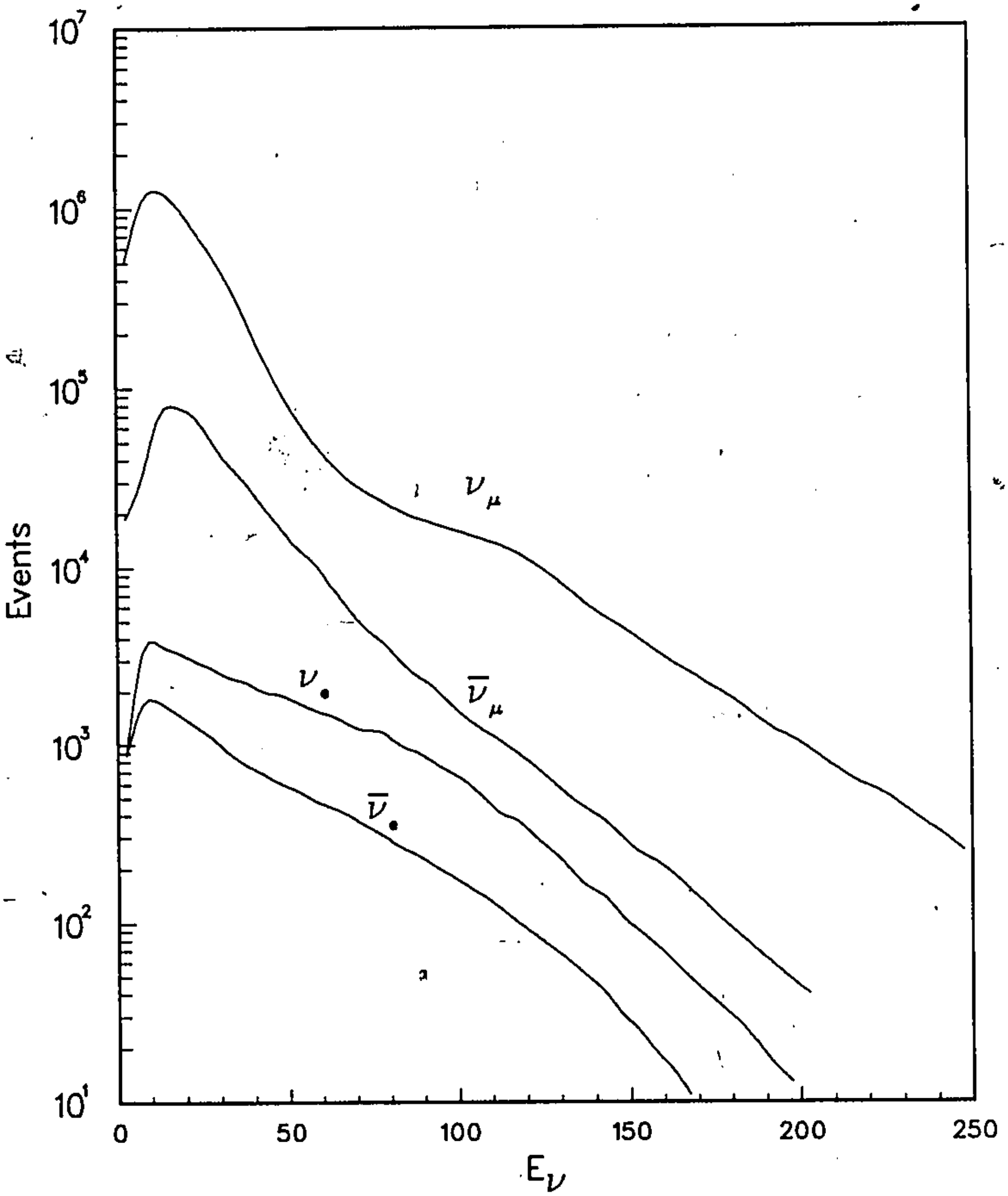

Figure 14: Neutrino energy spectra.

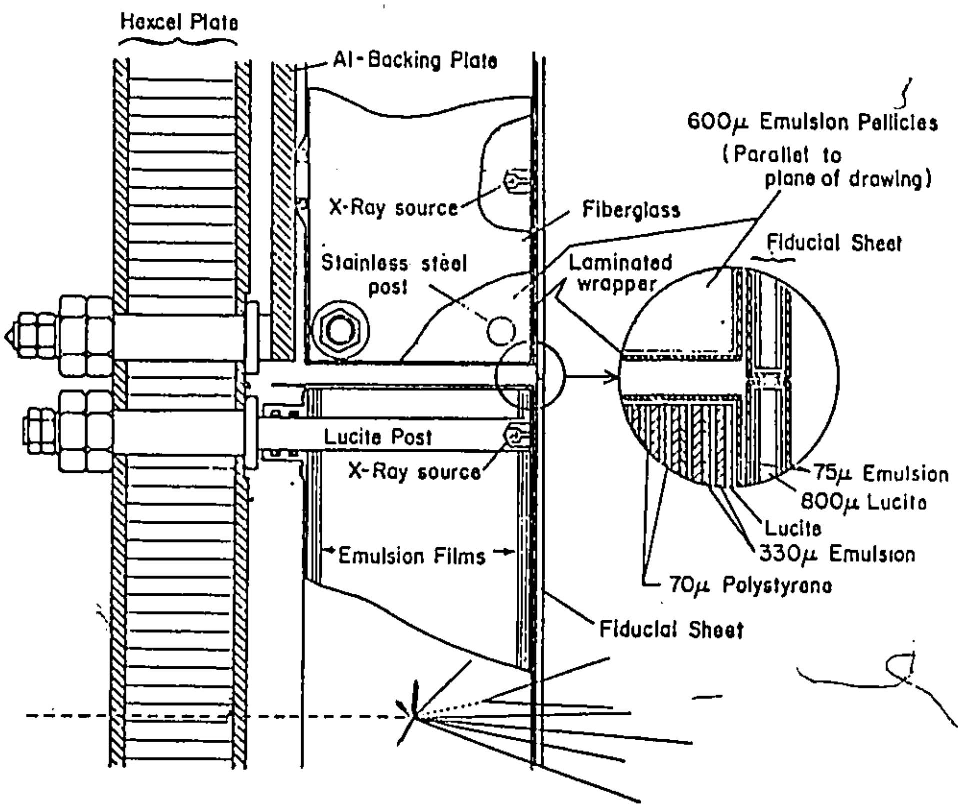

Figure 15: Emulsion modules.

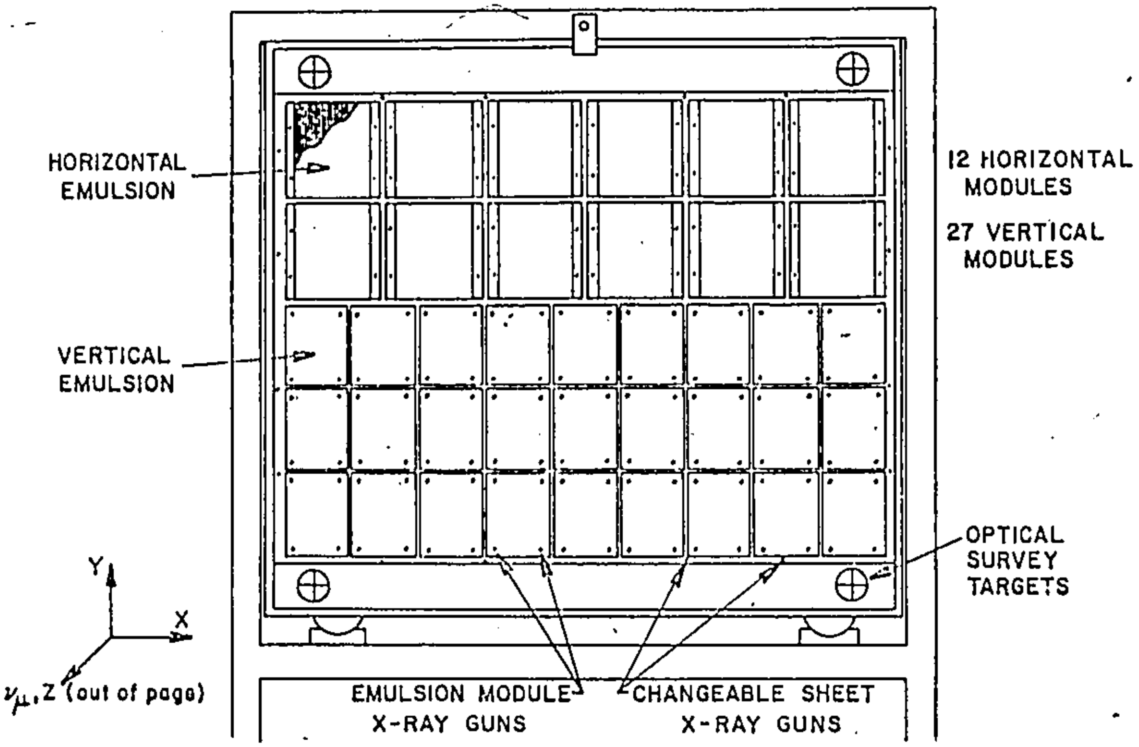

Figure 16: The emulsion target.

Table 6: Chemical Composition of Fuji ET-7B Emulsion

Element	% Weight
Iodine	0.3
Silver	45.4
Bromine	33.4
Sulphur	0.2
Oxygen	6.8
Nitrogen	3.1
Carbon	9.3
Hydrogen	1.5

42 modules, three modules were exchanged half way through the run so only 39 modules were exposed at any one time. The emulsion was 5 cm thick (in the direction of the beam) during the first run and 7 cm thick during the second run. The modules were mounted on the downstream side of an aluminum hexcel plate which was bolted to the granite block's surface. The composition of the Fuji ET-7B emulsion is shown in table 6 at a relative humidity of 68 %, and a density of 3.73 g/cm^3.

There were two types of modules: the upper half of the stack consisted of horizontal modules where the plane of the emulsion pellicles was parallel to the beam, while the bottom half consisted of vertical modules with the pellicles perpendicular to the beam direction. The 12 horizontal modules made up 40 % (21.9 litres) of the target. Each module consisted of 177 pellicles, 625 μm thick, and 14 cm × 5 (7) cm area. In each module the pellicles were pressed between two fiberglass-epoxy blocks, 15 mm thick using four stainless steel bolts in each corner. The 27 vertical emulsion modules contained 68 (97) pellicles, each pellicle consisted of 70 μm polystyrene film coated on each side with 330 μm of emulsion, and an area of 12 cm × 9.5 cm. They were placed on four Lucite guide posts and the pressure inside the covering envelope was reduced to half an atmosphere thus compressing the stack [15].

On the downstream side of the target there were two large fiducial sheet 91.5 cm

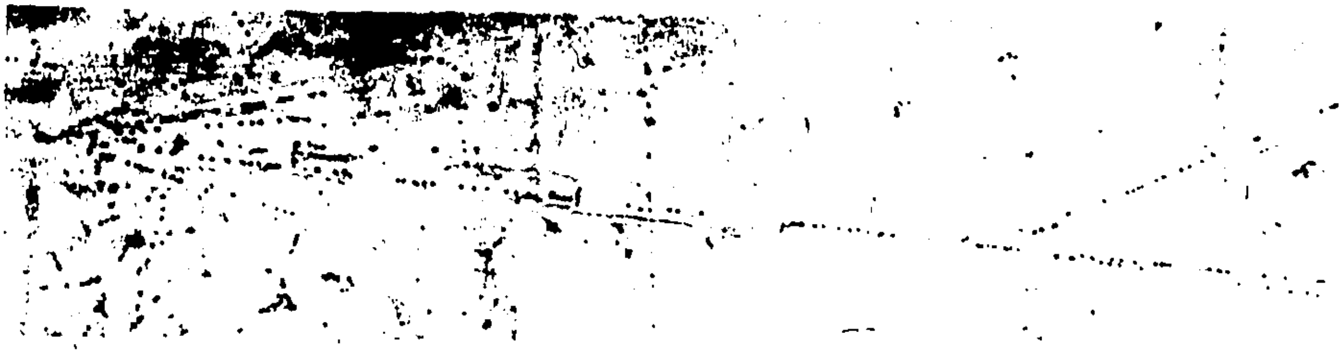

Figure 17: ν_μ interaction and charmed-particle decay.

× 40.0 cm, consisting of an 800 μm lucite base with 75 μm emulsion on both sides. One sheet was behind the horizontal modules and the other behind the vertical modules. These sheets were changed every few days during the first run and once a week during the second run. They facilitated the matching of spectrometer tracks with emulsion tracks (see Section 3.2).

The passage of a charged particle in the emulsion is shown by the development of silver grains along the particle path as shown in Figure 17 [9]. This figure shows a neutrino interaction followed by the decay of one of its charged particles. The number of grains per unit length along a track is proportional to the ionization (dE/dx) of the track, and the grain density for electrons (minimum ionizing tracks) was measured to be

$$I_0 = 28.4 \pm 0.7 \quad \text{grains per } 100\ \mu\text{m} \qquad \text{(horizontal)}$$
$$I_0 = 31.3 \pm 1.2 \quad \text{grains per } 100\ \mu\text{m} \qquad \text{(vertical)}$$

A "minimum ionizing track" is not truly a minumum ionizing particle but a track sitting on the "plateau" of the ionization curve (Section 3.2), the true minimum is below this "plateau". Shower tracks are particles that appear to be minimum

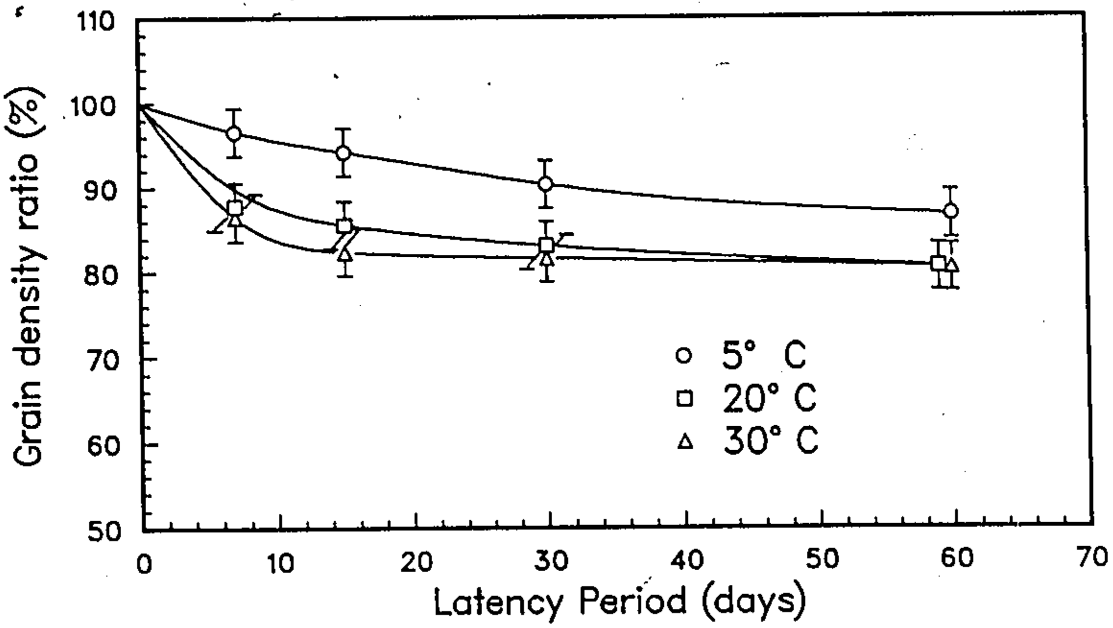

Figure 18: Fading of Fuji emulsion.

ionizing; grey tracks are particles that have an ionization > $1.4I_0$; black tracks are particles with an ionization > $4I_0$; heavy tracks refer to black and grey tracks. The emulsion was very resistant to the fading of images as shown by Figure 18 which was obtained by exposing a pellicle to a 1.5 GeV/c π^- beam. The pellicle was kept at a temperature of 10 $°C$ and a relative humidity of 50%, the same conditions which were maintained during the E-531 runs.

2.4 Time-of-Flight System

Situated 15.5 cm downstream of the emulsion stack was the Time-of-Flight I counter (TOF I) This consisted of a single piece of pilot F scintillator, 74×92 cm^2 and 1 cm thick, the light was transmitted through curved light guides to twelve phototubes as shown in Figure 19. The lucite light guides were 110 cm long and curved to ensure

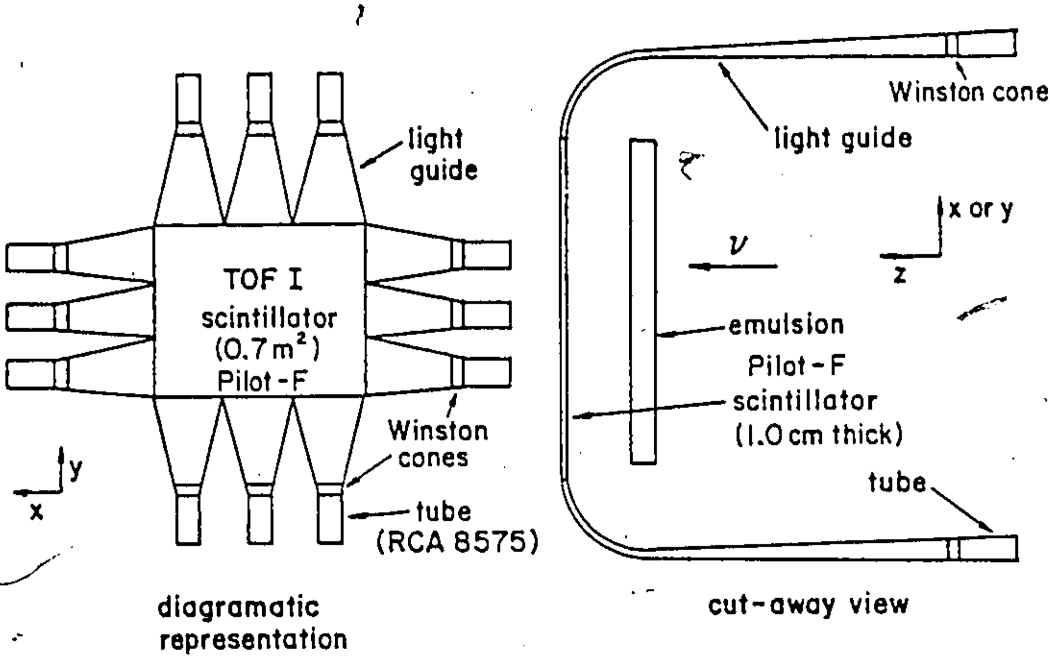

Figure 19: TOF I light guides.

that the phototubes were out of the magnet's fringe field. Each tube was encased in 1.5 cm thick iron pipe sections and 5 mm "mu" metal shields to protect them from the effects of the magnetic field. TOF I was used for the start time for all the Drift Chambers and the Time-to-Digital-Converters (TDC); in some cases it was also used to determine the start time for the Time-of-Flight of charged particles (Sec. 3.4). The online time resolution of the TOF I counter was 900 psec[10]; by using the muons that were present in the neutrino beam it was possible to improve the resolution to 450 psec. In the first (second) run a resolution of 250 (150) psec was obtained using the neutrino triggers and correcting for the overall geometry of the event. The poor resolution of the counter was due to the finite spot size (about 5 cm) of the interaction tracks in the TOF I counter.

A second TOF counter array (TOF II) was situated 2.7 m downstream of the TOF I on the other side of the magnet and drift chambers. The TOF II counter consisted of 16 scintillators 7 cm wide and 14 scintillators 10 cm wide, all the paddles being 2.5 cm thick and 1.5 m long. During the second run there were 18 wide scintillators with the 4 extra paddles added on the outside. The scintillator paddles were parallel to the Y axis with the narrow paddles clustered in the center of the TOF II plane and the wide paddles around the outside. There was also a 0.6 cm overlap of the narrow counters and 0.2 cm for the wide counters. The scintillators had a phototube on each end and were arranged as shown in Figure 20. Using the reconstructed tracks from the drift chambers, it was possible to obtain time-of-flight information whenever only one particle went through a given scintillator paddle. The time resolution of the TOF II array was 100 (140) psec for the narrow (wide) paddles during the first run. In the second run we were able to improve this resolution to 80 (106) psec.

The two arrays were also used as part of the trigger for the experiment; the neutrino interaction trigger consisting of ≥ 2.5 minimum ionizing particles in TOF I, two TOF II paddles on, and no veto counters on. For the first run there was the added restriction that the two TOF II paddles could not be adjacent.

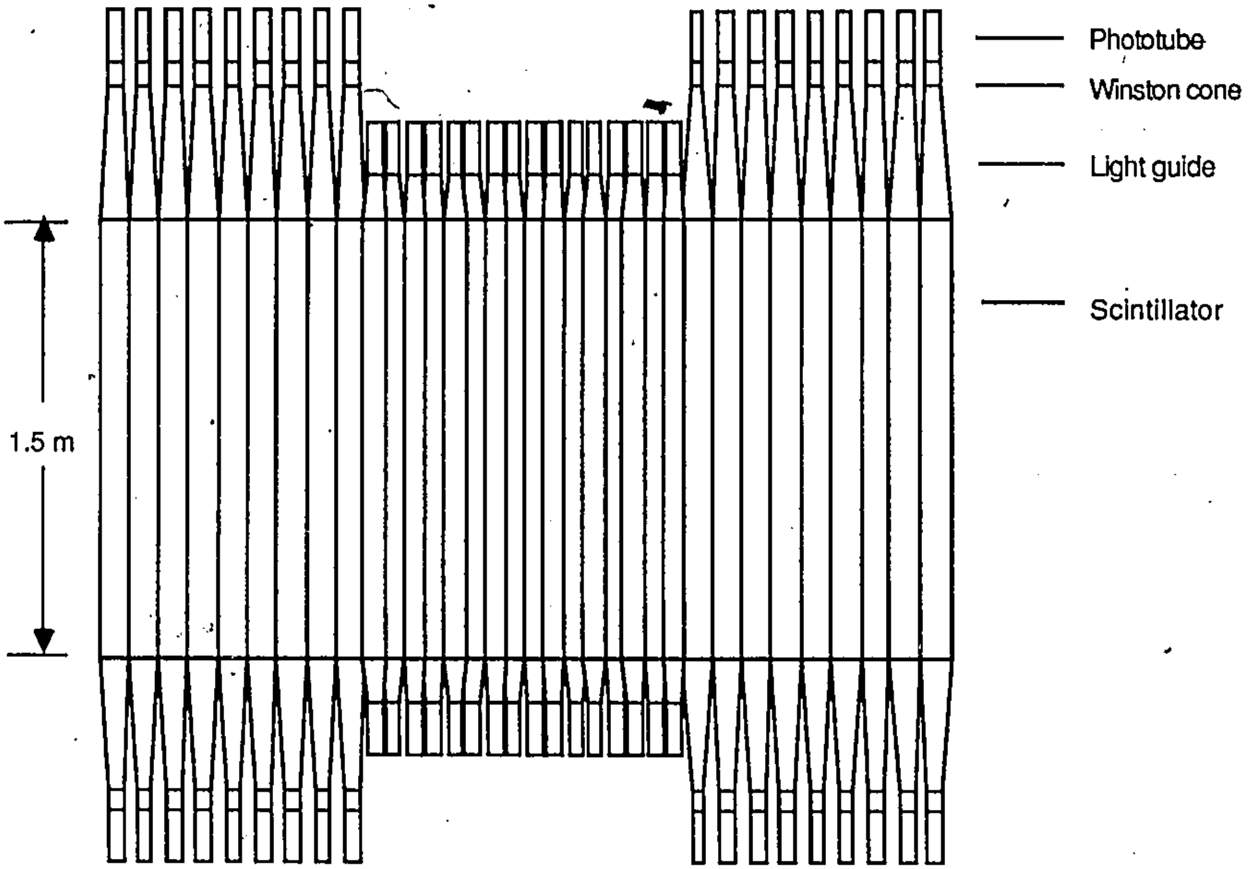

Figure 20: TOF II paddles.

2.5 Drift Chambers

The drift chambers and analyzing magnet [11] were used to determine the position of the decay vertex and the momenta of the particles. For the second (first) run of the experiment, there were a total of 24 (20) drift chambers, 15 (12) upstream of the magnet and 9 (8) downstream. Because of a rotation of the various planes with respect to each other, it was possible to reconstruct the events in three dimensions.

Upstream Chambers

The upstream drift chambers were divided into 3 planes with 5 (4 during first run) chambers in each plane, the 3 planes were offset from each other by 60° as shown in figure 21. These three planes were labelled X, U and V. The wires of the X chambers ran vertically and gave an X position for charged tracks. The U (V) chamber was rotated 60° clockwise (anti-clockwise), when looking downstream, with respect to the X chamber. The chambers were also shifted half a cell width from each other to help reduce the left-right ambiguity.

Each chamber had 32 sense wires, 4.0 cm apart (cell size), with field shaping wires between the sense wires as shown in Figure 22. The gas inside the chamber was a mixture of 50% argon and 50% ethane, contained by an aluminized mylar window which consisted of 25 μm Al on 50 μm mylar. The maximum operating voltage of the chamber was 3100 V, while the minimum voltage was 1700 V, giving an electric field of 700 V/cm. The active area of each chamber was $128 \times 128 = 1.7\text{m}^2$. The resolution of the chambers were found to be

$$\begin{aligned} \sigma_x &= 125\ \mu\text{m} \\ \sigma_\theta &= 0.6\ \text{mrad} \end{aligned}$$

Downstream Chambers

The downstream drift chambers were also divided into 3 planes with 5 (4) chambers in the X plane and 2 chambers in each of the other two. Because of their larger size these planes were rotated from each other by only 10°. For the downstream

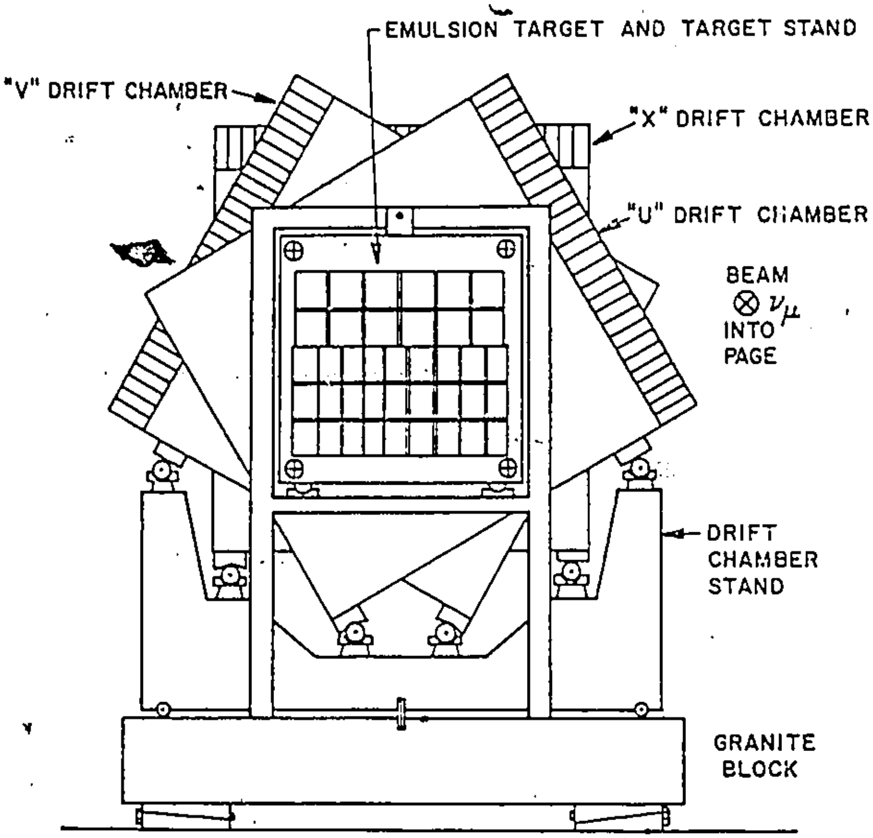

Figure 21: The drift chambers and emulsion target.

CELL CONFIGURATION AND
EQUIPOTENTIALS FOR UPSTREAM DRIFT CHAMBERS

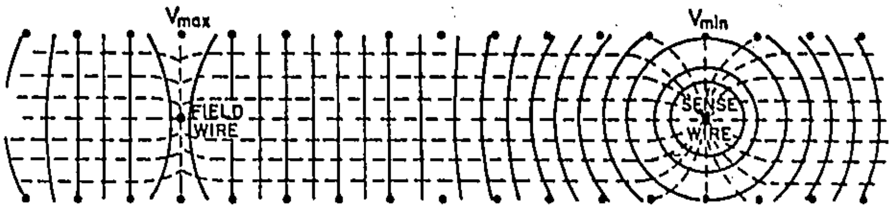

Sense wire: 20μm dia. Au-W wire
Field wire & cathode plane wires: 75μm dia. Cu-Be wire
Cell size = 4.0 cm V_{max} = 3.1 kV
2.0 mm cathode wire spacing V_{min} = 1.7 kV
7.0 mm cathode plane spacing E = 700V/cm

Figure 22: A drift chamber cell.

chambers the sense wires were 5.08 cm apart with field shaping wires between the sense wires. The gas mixture in the downstream chambers was the same as that in the upstream chambers, 50 % argon and 50% ethane, while the aluminized mylar gas window was 25 μm Al on 62.5 μm thick mylar. The maximum and minimum operating voltages were 3700 V and 1800 V, giving an electric field of 750 V/cm. The resolution of the chambers was found to be

$$\begin{aligned} \sigma_x &= 175\mu\text{m} \\ \sigma_\theta &= 0.8\text{mrad} \end{aligned}$$

2.5.1 Magnet

The SCM-104 magnet on loan to Fermilab from Argonne National Laboratory had a highly uniform field. When running at the nominal current of $2400A \pm 0.5\%$ it had a central field of 5.9 kgauss. The magnetic field strength was measured at a total of 50,000 points inside and outside the magnet gap and was used to map the magnetic field. For points far from the pole tip a polynomial parametrization was used for the spatial dependence of the field. It was found that this estimated field agreed with the measured field to within 5% . .

Tracks passing through the center of the magnet experienced a transverse momentum kick of

$$P_T = 0.03 \int B\, dl = 0.186\mathrm{GeV/c}$$

It was thus possible to measure the momentum of the produced particles from their curvature in the magnet gap, and tracks seen in both the upstream and downstream drift chambers (called up-down tracks) had a momentum resolution of

$$\sigma_P = [(0.013P)^2 + (0.005P^2)^2]^{1/2}$$

Due to the extra drift chambers the resolution for the second run was

$$\sigma_P = [(0.014P)^2 + (0.004P^2)^2]^{1/2}$$

Because of the magnet's fringe field, tracks which did not pass through the magnet gap were also bent and it was thus possible to get a momentum measurement for these tracks. Tracks which were seen only in the upstream drift chambers (up-only tracks) had a momentum resolution of

$$\begin{aligned}
\sigma_P &= 0.34P^2 && (\theta < 300 \text{ mrad} \\
\sigma_P &= 0.50P^2 && (300 \leq \theta < 600 \text{ mrad} \\
\sigma_P &= 0.75P^2 && (\theta \geq 600 \text{ mrad}
\end{aligned}$$

For the second run events, the resolution was improved to

$$\sigma_P = 0.08P^2$$

The momentum calibration was checked using the Time-of-Flight system and calculating the mass of the proton, as well as studying the 1/P distribution.

The calibration of the drift chambers was done continuously during the runs using muon triggered events. For the muons passing through the spectrometer a tuning program was run optimizing the following parameters[11]

1. Drift velocity in the chambers ($V_d = 50\mu\mathrm{m/nsec}$).

2. Position of the first wire in each drift chamber (used as a reference).
3. Non-linear drift velocity correction near the sense wires.
4. Sense wires offsets.
5. Finite propagation time along sense wires.
6. Angular correction (done once the track was reconstructed to first order).
7. Drift chamber stop time.

2.6 Large Cell Drift Chamber

During the first run of E-531 there was a large helium filled bag in the gap of the magnet; in the second run a Large Cell Drift Chamber (LCDC) was placed in the magnet gap. For a detailed description of the LCDC see Reference [38]. The LCDC helped to connect tracks reconstructed in the upstream and downstream drift chambers. It was initially designed to work as as a charged particle identifier using the relativistic rise in the ionization loss (dE/dx) of charged particles, unfortunately because of certain problem it could not be used as such.

The LCDC had two planes of 50 gold-plated tungsten anode wires 25.4μm in diameter (a total of 100 wires); each anode wire was surrounded by eight cathode wires. The two signal planes were parallel to the X axis. There were also three planes of high voltage wires (44 cm apart), one on each side of the signal planes which caused the charged tracks to "drift" to the signal planes. The chamber was surrounded by field shaping wires. A gas mixture of 80% argon and 20% carbon dioxide was used to fill the chamber.

2.7 Electromagnetic Calorimeter

Sitting downstream of the TOF II counters, about 3.1 m from the emulsion target was the electromagnetic calorimeter. The electromagnetic calorimeter was used to determine the position of the photons in the events and to identify the electrons and positrons produced in the interaction. It consisted of a gamma-ray converter system used to determine the shower positions very accurately, and was followed by a lead-glass block system to give an accurate energy measurement.

2.7.1 EPICS

The gamma-ray converter system, which was only installed for the second run of the experiment, consisted of a 1.59 cm thick lead sheet supported by a 0.95 cm aluminum sheet (about 2.9 radiation lengths total), followed by 3 planes of Extruded Proportional Ionization Chambers (EPICS). These EPIC planes consisted of square aluminum tubes 1.56 cm × 2.54 cm and 203 cm long, with a high voltage (2300 V), 2 mm gold plated tungsten wire running down the center of each cell. The 1.59 cm was in the direction of the beam, thus ideally the tubes had a position resolution of $2.54/\sqrt{12}$ cm in each plane. The three planes were rotated from each other by 60° (Fig. 23), the Y plane consisted of 80 tubes while the U and V planes had 96 tubes in each of them. With the three rotated planes it was possible to determine the X and Y coordinate of a hit. The pulse height of a tube was proportional to the number of particles passing through the tube. The X and Y coordinates of photons could be determined since they usually showered in the lead and aluminum sheet. Electrons/positrons also usually showered in the lead and aluminum sheets, producing a large number of particles which passed through the EPIC planes, the subsequent pulse being several times larger than a minimum ionizing pulse. This characteristic was one of the things used to identify electrons and positrons.

2.7.2 Lead Glass

The lead glass array (Figure 24) consisted of 68 blocks arranged in 8 rows, 9 blocks long with the corners removed. There were two types of blocks: most of the blocks were 11 radiation lengths long but 12 of the blocks (the shaded blocks in the figure) were 14 radiation lengths long; all the blocks were 19.3 cm × 19.3 cm square. The blocks were 2/3 to 1 interaction lengths long. A light guide and a 12.7 cm diameter

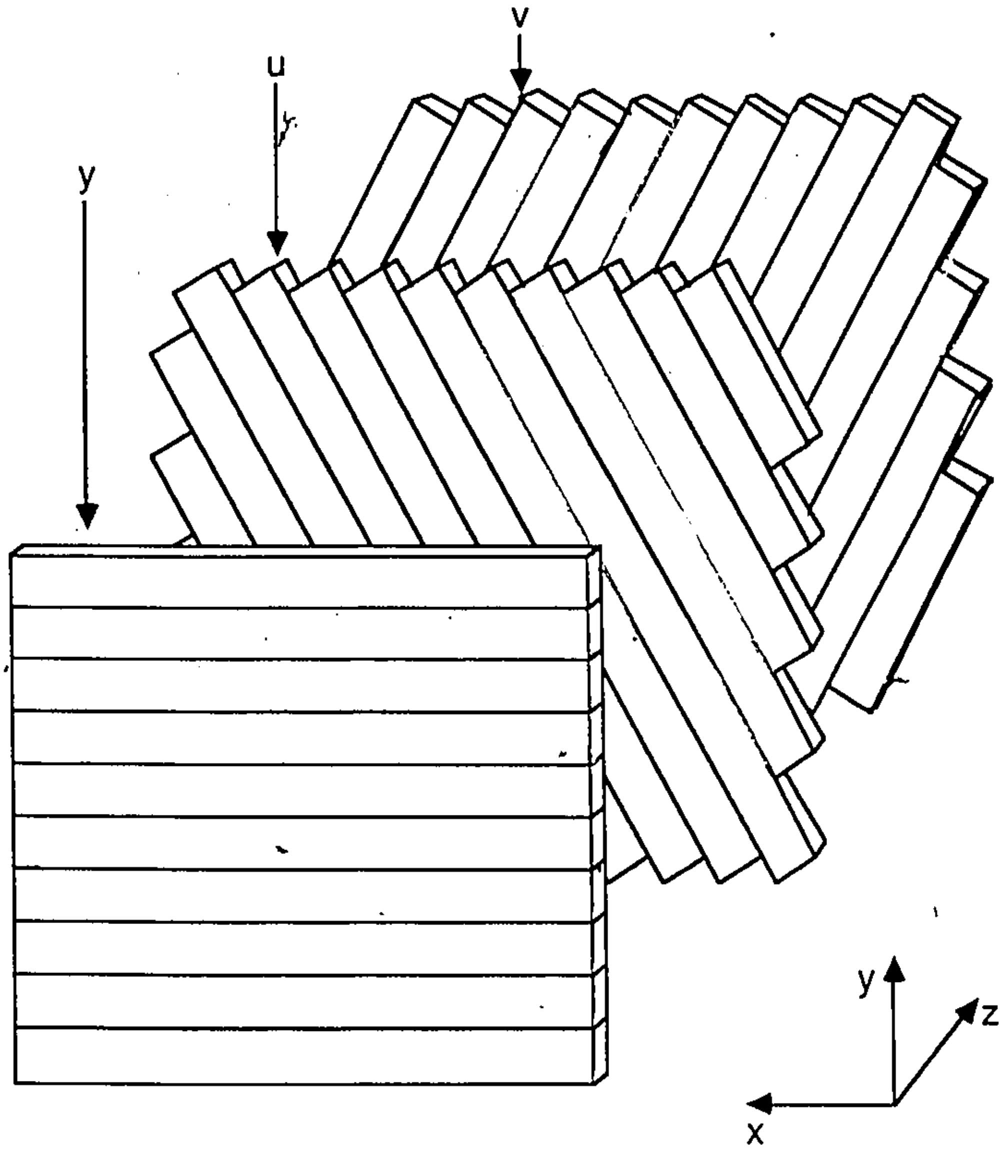

Figure 23: Extruded Proportional Ionization Chambers (EPIC).

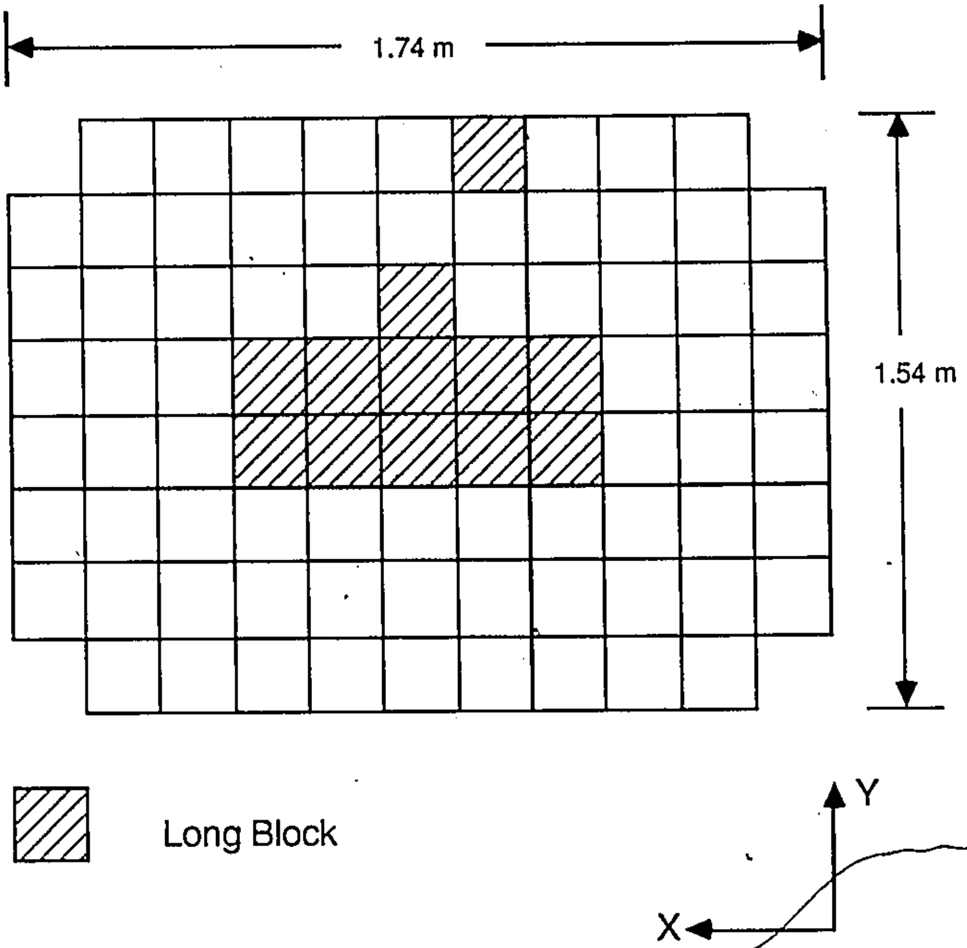

Figure 24: The lead glass array.

phototube was attached to the downstream end of each block.

Photons and electrons/positrons entering a lead glass block interacted and produced an electromagnetic shower (photon, electron, and positron cascade). The electrons/positrons produce a lot of Čerenkov light, the total amount of light is proportional to the number of particles which in turn is proportional to the energy of the initial particle. Thus, the signal produced by the phototube will be proportional to the energy of the incoming photon or electron/positron. Figure 25 shows the response of the two types of blocks to a beam of electrons from 5 to 30 GeV/c. The lead glass measured the energy of a gamma or electron/positron shower with a typical resolution of $\sigma(E) = 0.15\sqrt{E}$. In the second run the lead sheet and EPICS degraded the overall energy resolution slightly, and the net resolution was $\sigma(E) = 0.17\sqrt{E}$.

Minimum ionizing particles (other than electrons and positrons) will produce a signal of one value regardless of their energy. The energy that will be measured for these particles is:

$$\begin{aligned} \text{E(long block)} &= 400 \pm 30 \text{ MeV/(minimum ionizing particle)} \\ \text{E(short block)} &= 330 \pm 20 \text{ MeV/(minimum ionizing particle)} \end{aligned}$$

Some hadrons will interact in the lead glass and produce a signal larger than that due to a minimum ionizing track. Figure 26 shows the pulse height spectrum for a beam of negatively charged particles (pions and electrons), the minimum ionizing and electron peak are very obvious, the falling exponential is due to the interaction of the pions. Using this plot it is possible to show that there is a 10% probability that a charged track will deposit up to 1/3 of its energy in the lead glass.

2.8 Hadron Calorimeter

Situated about 4.1 m downstream of the emulsion target was the hadron calorimeter which measured the total hadronic energy in the event. It consisted of several planes of charged particle detectors, separated by 10 cm of steel (Figure 27). During the first run there were 5 planes of scintillators as the charged particle detectors, while

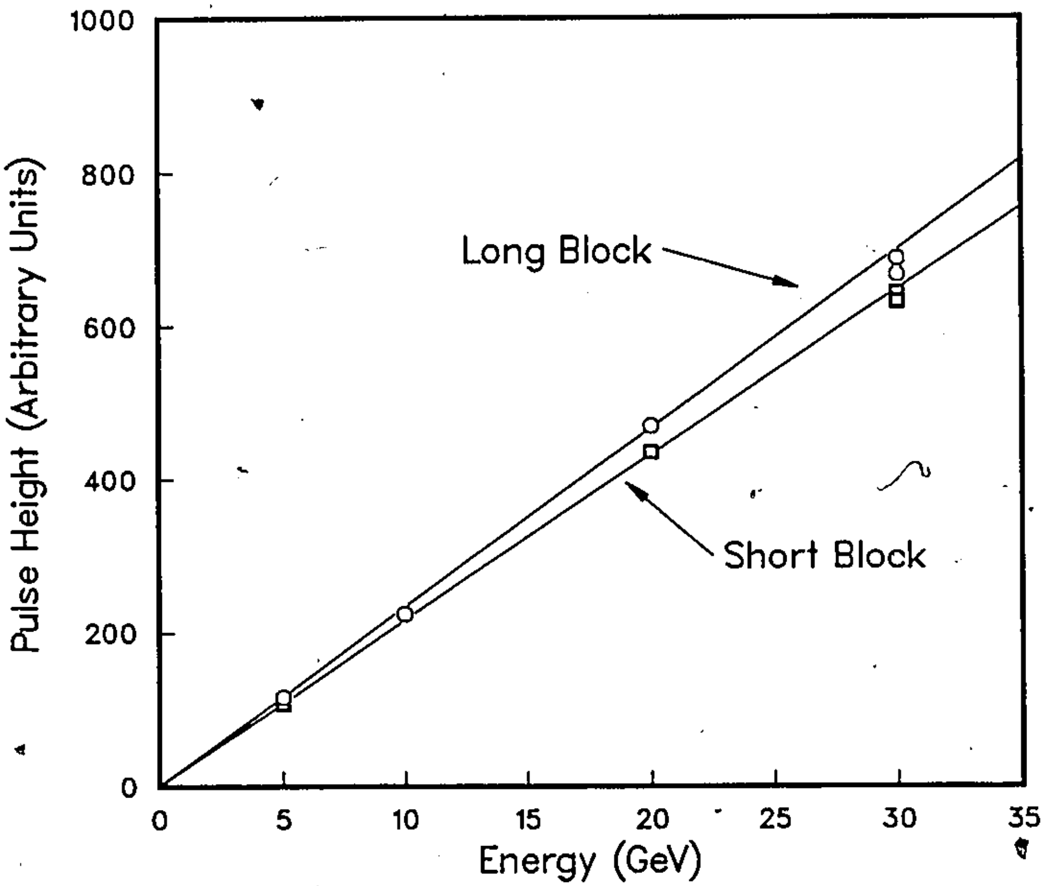

Figure 25: Lead glass pulse heights for electrons.

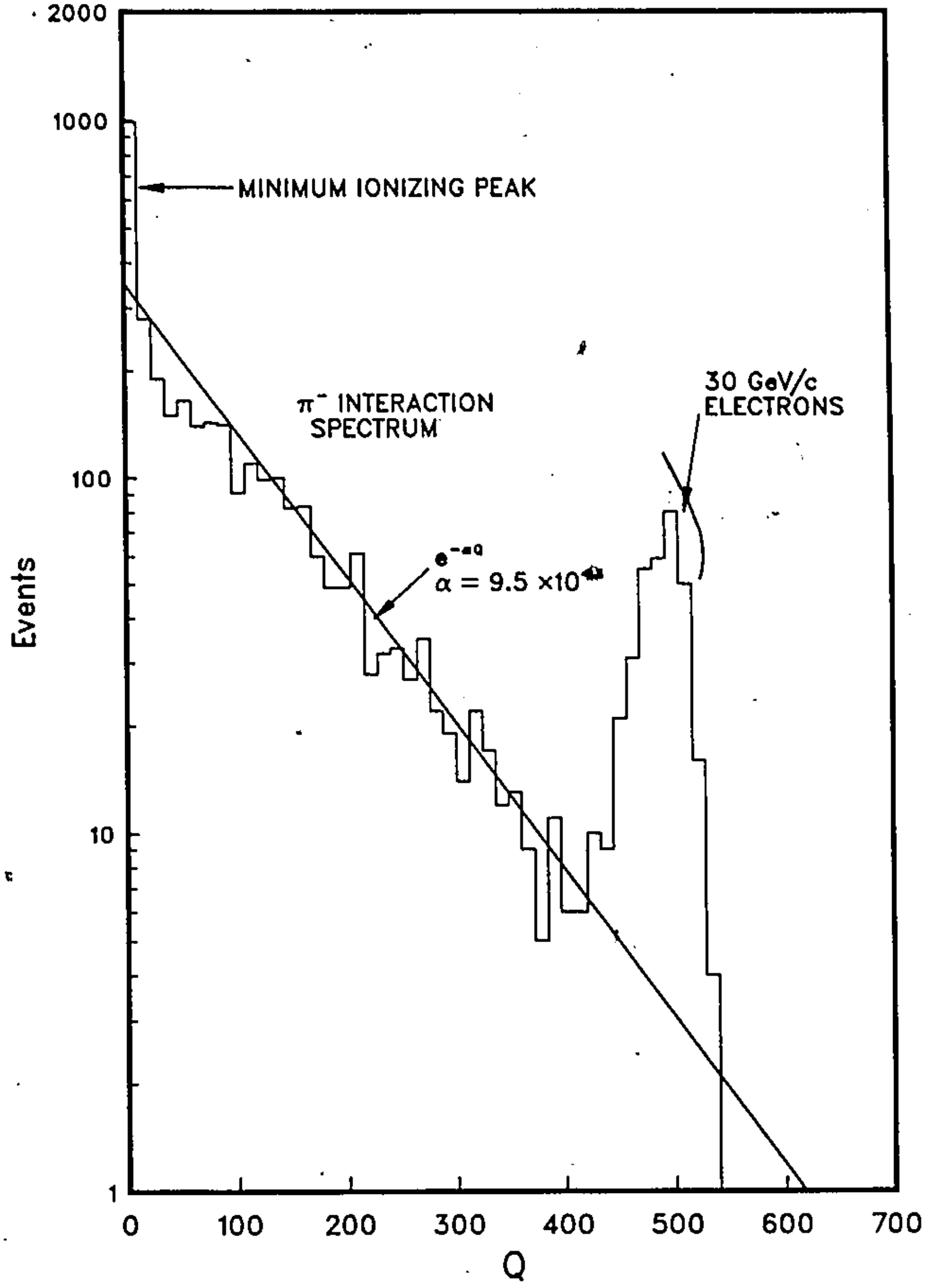

Figure 26: Lead glass pulse height spectrum for 30 GeV/c negative particles.

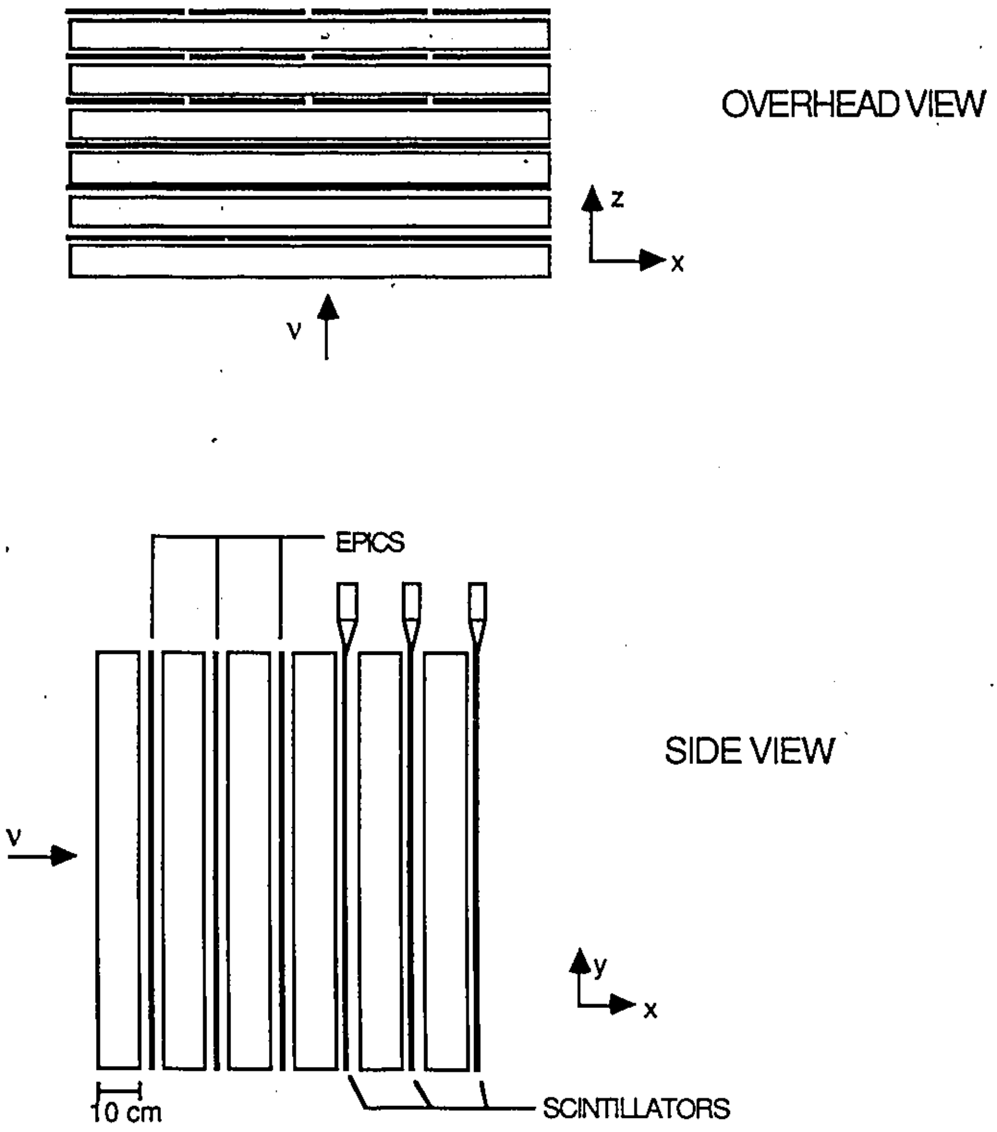

Figure 27: Hadron calorimeter

during the second run there were 3 planes of calorimeter EPICs followed by three planes of scintillators. The scintillator planes each consisted of four large scintillator paddles 1.3 cm thick, 76 cm wide and and 2.44 m long and were viewed by a single 12.7 cm diameter phototube on top of the paddle. The paddles were perpendicular to the beam direction and parallel to the Y axis. Because of their large size the paddles had a very poor position resolution and could only give the X coordinate of a hadronic shower. The calorimeter EPICs were built slightly differently from the electromagnetic EPICs; the casing was similar for the two EPIC types but the hadron calorimeter had 0.8 mm stainless steel wire instead. Another difference was that four calorimeter EPIC tubes were joined together to give one signal. The EPICs were all parallel to the X axis, and the X position was obtained by comparing the pulse heights at the end of each tube. The position resolution of the EPICs was determined to be

$$\begin{aligned} \Delta X &= 8.9 \text{ cm} \qquad E < 2.0 \text{ GeV} \\ \Delta X &= 6.4 \text{ cm} \qquad E > 2.0 \text{ GeV} \\ \Delta Y &= 10.2/\sqrt{12} \text{ cm} = 2.9 \text{ cm} \end{aligned}$$

The energy response and resolution of the calorimeter was [39]:

$$\begin{aligned} E_{\text{CAL}} &= \frac{N}{2a}(1+\sqrt{1+\frac{4ab}{N}}) \\ \sigma(E) &= 1.1\sqrt{E} \end{aligned}$$

where

N = the number of minimum ionizing particles observed in the calorimeter..

$a = 5.428$ /GeV

$b = 0.721$ GeV

No correction was made for the signal attenuation in the scintillator paddles which had an attenuation length of about 5 m.

Figure 28 shows the response of the hadron calorimeter to a singly minimum

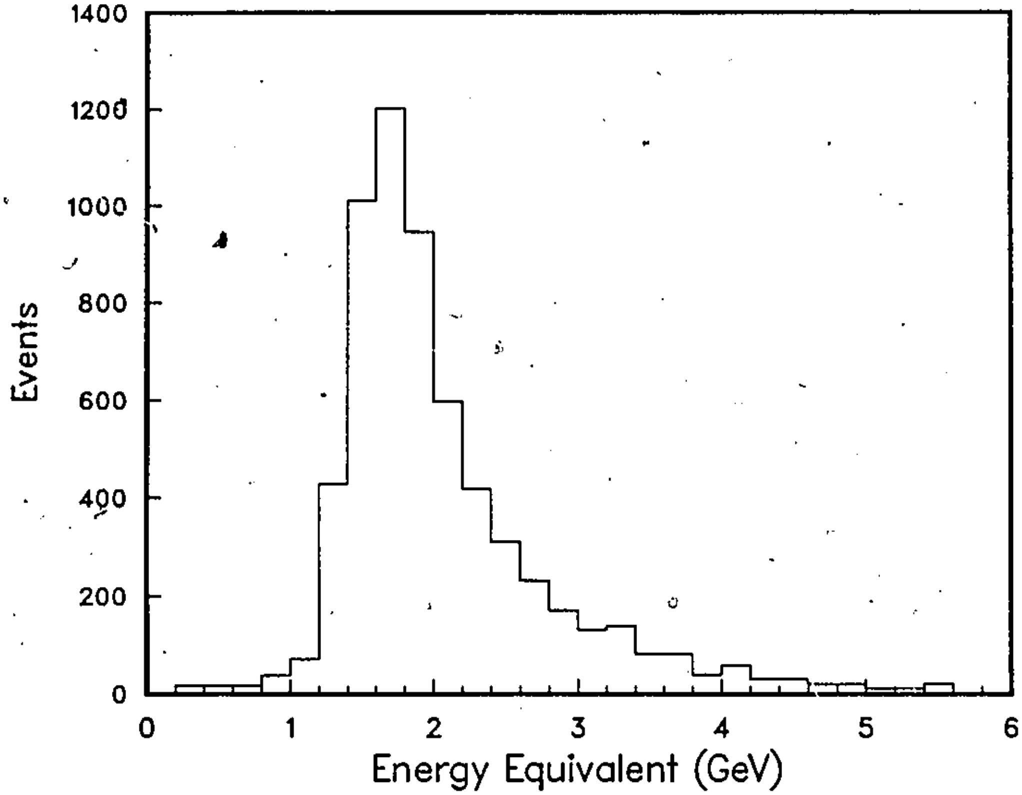

Figure 28: Energy distribution of muons passing through hadron calorimeter.

ionizing particle (muon) during the first run, the spectrum for first run events peaks at 1.75 GeV equivalent energy, while the second run spectrum has a similar shape but peaks at 2.0 GeV. The shift in the second run spectrum is due to the extra detection plane.

2.9 Muon Counters

The muon counters consisted of 36 scintillation paddles sitting downstream of 1.2 m (includes steel in the hadron calorimeter) followed by 1.1 m (2.3 total) of steel and 40 more counters (Figure 29). The first 36 paddles (referred to as the muon front paddles) were about 5.6 m downstream of the emulsion target and were set up parallel to the X axis. As shown in the figure they were divided into two rows of 18 each. The second set of paddles (muon back paddles) were also divided into two rows of 40 paddles each, with the paddles parallel to the Y axis. Any particle able to penetrate through the steel and produce a signal in the paddles was identified as a muon. The muon had to have a momentum of 1.9 GeV/c to reach the muon front counters and 3.4 GeV/c to reach the muon back counters.

There are three types of muon tags: "muon front-back" (MUFB), "muon front" (MUF), and "muon back" (MUB), depending on which muon plane was hit by the particle being considered. The detection efficiency for MUF, MUB and MUFB is[10] 95 ± 1 %, 94 ± 1%, and 89 ± 2% respectively. The inefficiency is due to timing and pulse height cuts and because of gaps between the paddles. A muon will not be tagged by either the MUF or MUB arrays 0.3% of the time, assuming it has sufficient energy and a proper angle to be tagged as a muon.

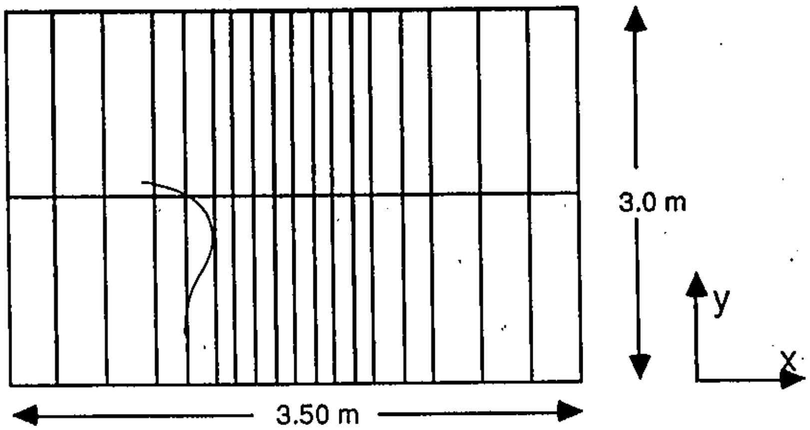

FRONT VIEW

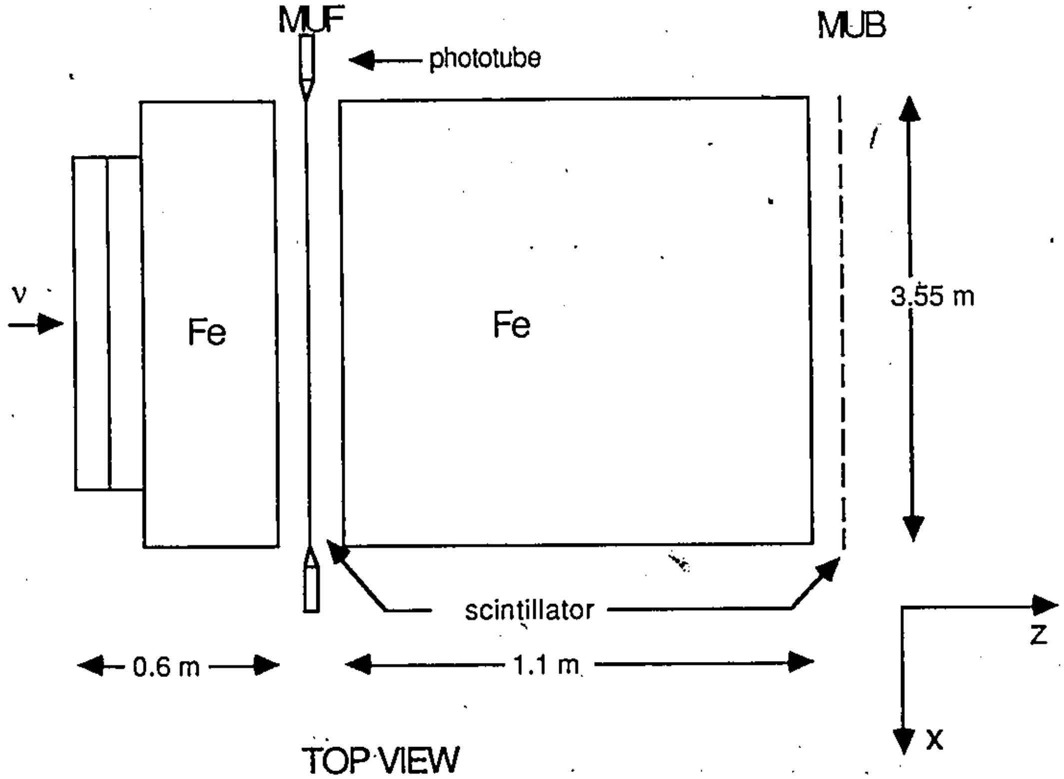

TOP VIEW

Figure 29: Muon steel.

Chapter 3

Fitting Events

The fitting of events involved a number of steps, and the events had to be treated on an individual basis. Numerous computer programs were run for different parts of the analysis. Using the data recorded on magnetic tape, an attempt was made to reconstruct all the tracks in the drift chambers and predict the position of the neutrino interaction. This information was then used in the search for the interactions in the emulsion. When an event was found a search for charm particle decay was also carried out, and if a decay was found the event was then reanalyzed in great detail.

3.1 Track Reconstruction

The first step in the study of a neutrino interaction was to run the track-finding program written by N.R. Stanton from Ohio State University. This program used the drift chambers data to reconstruct the tracks from the neutrino interaction. The program gave a prediction for the location of the neutrino interaction. It also calculated the momentum of the reconstructed tracks based on their curvature in the magnetic field.

The three dimensional reconstruction of a track was done [15] by first reconstructing tracks in the three offset planes. Given the position of a track in two of the planes it was possible to predict its location in the third plane. Comparing the predicted track location with the reconstructed tracks in that plane it was possible to resolve ambiguities among the tracks, and thus determine the track direction in three dimensions.

There were two slightly different procedures that were used when fitting the events. In the first procedure a trial vertex was estimated using the average of all the hits in the X, U, and V upstream drift chambers. Tracks were reconstructed in the downstream drift chambers and then projected back to the center of the magnet, this point and the trial vertex defined a "road" in which drift chamber hits were used to reconstruct upstream segments. The final tracks were chosen on a basis of their χ^2 and the number of hits used. An attempt was also made to identify some of the reconstructed tracks using the muon hodoscope (Sec. 3.7) A better vertex was made using the muon and a high momentum track. Using this improved vertex, the reconstruction of the tracks was then repeated. The final vertex was then determined using all the reconstructed tracks and a least squares fit.

The second procedure required the reconstruction of two or more stiff tracks (high momentum), which were then used to make a trial vertex. Tracks were then reconstructed as discussed above by using the downstream segments. Each reconstructed track was then given a weight based on: whether or not it was identified as a muon, the momentum of the track, its χ^2, and the number of hits. The tracks were then fitted to one or more vertices using these weights. An average drift chamber stop time was determined for the tracks. The improved stop time and vertex position were then used to get better fits to the reconstructed tracks.

The final fitting program used a combination of the two procedure to reconstruct all the tracks, and get a vertex position. In the first run the reconstruction process was estimated to have an efficiency of 85 % [15], estimated from the success rate of the program and by visually inspecting the drift chamber data. It was also estimated to have an efficiecncy of 75 % (80%) to reconstruct the individual tracks for first (second) run events for the first pass of the program (Sec. 3.3). This efficiency was estimated by visually inspecting a number of random charm candidate events and checking to see how many of the emulsion tracks were expected to be seen in the drift chamber, and how many were actually reconstructed.

3.2 Study of Events in the Emulsion

Those neutrino interactions which were sucessfully reconstructed were then searched for in the emulsion using all the available information. Two procedures called followback and volume scan were used to find the interactions. The followback procedure was used by all the scanning groups in the second run of the experiment, and by the groups scanning the vertical emulsion in the first run. The horizontal groups used the followback procedure for only 17 % of their events found in the first run, and the volume scan procedure for the rest of their events.

The followback procedure used the prediction for the slopes and coordinates of tracks in the downstream end of the emulsion modules. Tracks that matched the predictions of the drift chamber were searched for in the first emulsion pellicle, and when found were followed through the emulsion stack to the neutrino interaction. For the cases where it was not possible, or very difficult, to find any of the predicted tracks the tracks were looked for in the changeable sheet where they were easier to find due to the low background. When searching for the track matches an area ±1 mm was scanned around the predicted track position [15]. On average it took about one hour to hande a predicted event.

Tracks were searched for only if they passed the followback criteria which were that the track momentum $P \geq 400$ MeV/c and the track angle $\theta \leq 300$ mrad. When first searching for the neutrino interaction the followback criteria were usually much more restrictive, and the first track to be searched for was the most energetic one, usually the muon. In order for a track to be matched to the drift chamber prediction their angles had to agree within 8 mrad, and the position had to agree within 1 mm [15].

The efficiency for finding the primary interactions was independent of the Z position of the neutrino interaction. Figure 30 shows the efficiency for finding the neutrino interactions (ratio of the number of events found over the number of predicted events) as a function of the position of the interaction in the emulsion. Another check that the followback efficiency was flat consisted of looking at the number of gamma conversions found using the followback procedure as a

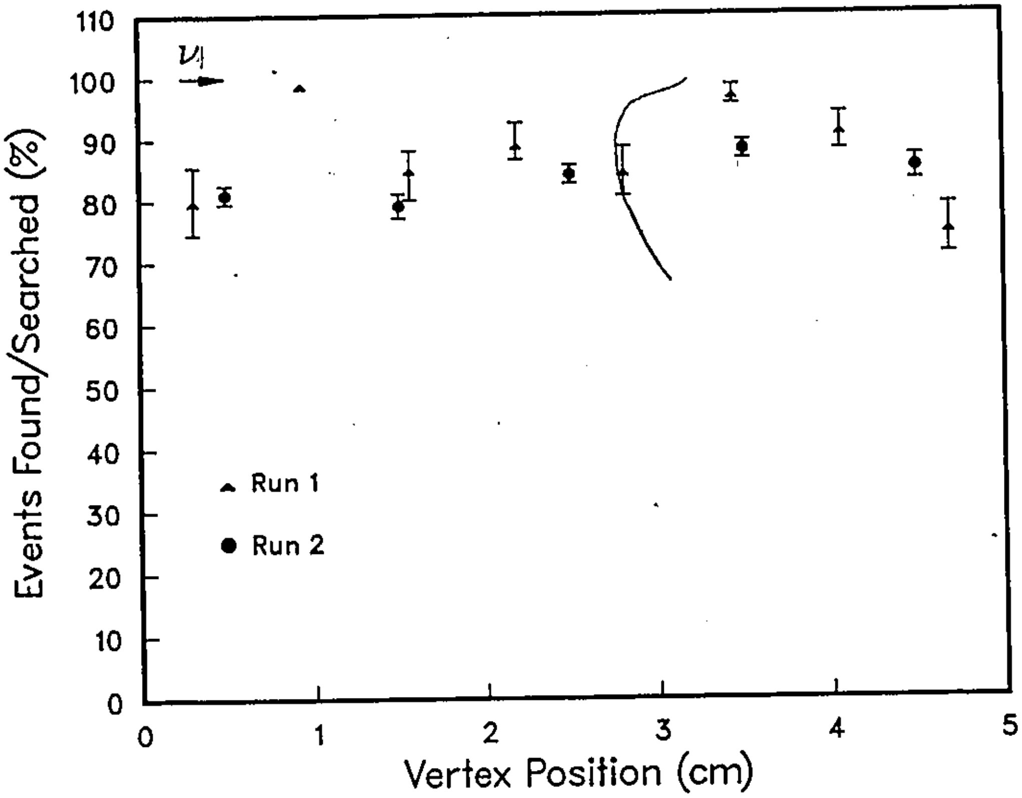

Figure 30: Event finding efficiency.

function of the conversion distance. The observed distribution was compared with the expected distribution and normalized to the total number of found conversions. This efficiency is shown in Figure 31. As can be seen from the two figures, the followback efficiency is independent of the position of the vertex. The average second run finding efficiency was 82 %; the apparent 18 % inefficiency was mostly a result of interactions that were predicted near the edge of the fiducial volume of the emulsion, but were actually outside. The fiducial volume of the emulsion is the volume defined by all the emulsion plates without the area 2 (5) mm from the vertical (horizontal) emulsion edges of each pellicle, and the same distance from the post holes.

The second method used to find the neutrino interactions was called the volume scan procedure. The neutrino interaction vertex was searched for in a $4 \times 4 \times 20$ mm^3 volume centered about the position predicted by the reconstruction program [15]. The 20 mm was in the Z direction which was usually the most uncertain coordinate. On average the total scanning time for an event using the volume scan procedure was about 4 hours. The average efficiency for event finding with the volume scan method was 42%. During the first run the horizontal group used a combination of volume scan and followback procedures to get a total event finding efficiency of 51%.

Decay Searches

Once a neutrino interaction had been found an attempt was then made to find any possible charmed-particle decays. Three procedure were used: followdown scanback, and volume scan. All three methods complemented each other, and the final efficiency for finding decays was very high.

All tracks from the primary vertex were followed through the emulsion for various distances (depending on the emission angle of the track) in order to search for decays and secondary interactions. This procedure was called the followdown procedure, and was used primarily to find charged-particle decays. The tracks were followed down 6 mm or the end of the emulsion if $\theta \leq 200$ mrad, and up to 3 mm at larger angles. Decays that were longer than the followed distances were found

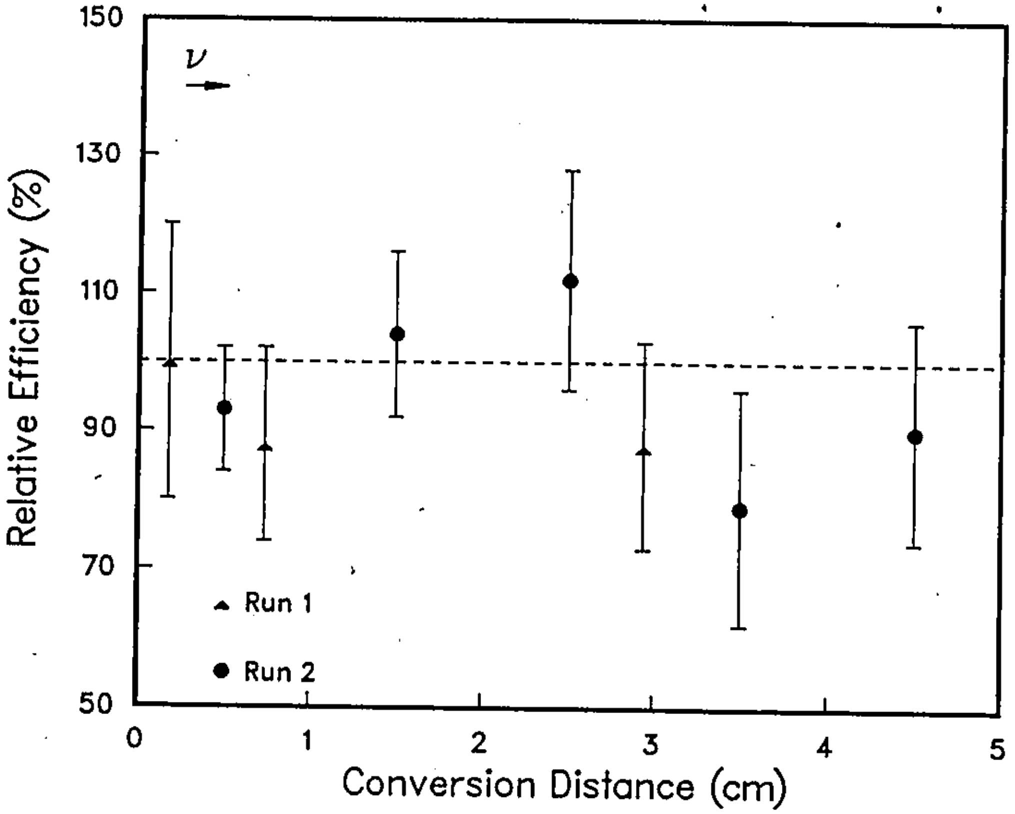

Figure 31: Gamma conversions relative finding efficiency.

using the followback/scanback technique. The efficiency for finding decays using the followdown techinque was almost 100 %.

The scanback procedure was equivalent to the followback procedure used to find neutrino interactions. It was applied to all unmatched drift chamber tracks (no 'equivalent' emulsion track from the found primary vertex) that passed the followback criteria. These tracks were found to originate from secondary interactions, e^+e^-pairs (gamma conversions), and decays. This procedure was used to find both charged and neutral interactions and decays. In some cases the decay or secondary interaction was found first and the decaying/interacting track was followed back to the neutrino interaction, or it was found when doing the scanback of another track (if the secondary vertex was due to a neutral particle). As has already been discussed the scanback/followback efficiency was independent of the Z position of the originating vertex and so the efficiency for finding decays using the scanback procedure is independent of the decay length.

A cylinder 200 μm in radius and 300 μm long downstream of the found neutrino vertex was volume scanned in the horizontal modules to look for possible decays. In the vertical modules a cylinder 200 μm in radius and about 1000 μm long was also volume scanned. The finding efficiency was estimated to be very low but was done in an attempt to find decays that could not be found by the scanback technique.

A vertex found in the emulsion is tagged as a decay vertex if it is downstream of the primary vertex, none of the tracks are black tracks, there is no recoil visible and the number of tracks is consistent with charge conservation. There are several types of neutral decay vertices called V's (or 2-prong), 4-prong, and 6-prong depending on whether there are 2, 4, or 6 tracks coming from the vertex. The charged vertices are kinks (or 1-prong), tridents (or 3-prong), and 5-prong decays corresponding to 1, 3, and 5 tracks from the vertex.

$p\beta$ Measurement

In some cases it might not be possible to reconstruct an emulsion track in the drift chamber because of geometric problems or an interaction in the emulsion. Sometimes the momentum resolution of a track will be very poor. For these tracks the $p\beta$ was usually measured in the emulsion using the multiple scattering of the track. Assuming a Gaussian distribution for the scattering of the track the angular distribution will have a width given by [19]:

$$\theta_0 = \frac{14.1\mathrm{MeV/c}}{p\beta} Z_{\mathrm{inc}} \sqrt{L/L_R} \left[1 + \frac{1}{9}\log_{10}(L/L_R)\right] \qquad \text{(radians)}$$

where p is the momentum in MeV/c, $\beta = v/c$ where v is the velocity of the particle, Z_{inc} is the charge number of the incident particle, L/L_R is the thickness of material the track has gone through in radiation lengths. L_R for the emulsion was 2.94 cm for the horizontal emulsion, and 3.20 cm for the vertical, the difference being due to the polystyrene sheets in the vertical emulsion. To eliminate measurement problems due to distortion of the emulsion, microscope stage noise, and temperature variations, the angular deviation of the track was often measured relative to a very energetic track (usually the muon). The $p\beta$ measurement was not very accurate for very energetic tracks, but was usually more accurate than the drift chamber for low momentum tracks observed only in the up stream drift chambers.

Particle Identification

It is also possible to identify some particles in the emulsion. Figure 32 shows the ionization of various particles as a function of $p\beta$. It was possible to measure the ionization of a track with a typical precision of 5 %, and using the momentum measured for a given track (from drift chambers or a $p\beta$ measurement) it was possible to identify low momentum particles. Protons and kaons could be separated for a momentum up to 1.2 GeV/c, and kaons could be separated from pions up to 700 MeV/c. In order to eliminate a possible identification for a given particle the expected and measured ionization had to differ by more than two standard deviations.

It was also possible to identify a particle from its range in the emulsion (distance travelled before stopping) if it had a low enough kinetic energy. The stopping of a pion was very obvious because as it slows down it becomes heavily ionizing and it then suddenly kinks, decaying into a muon and neutrino. The muon will travel about 600 μm and then decay into an electron and two neutrinos.

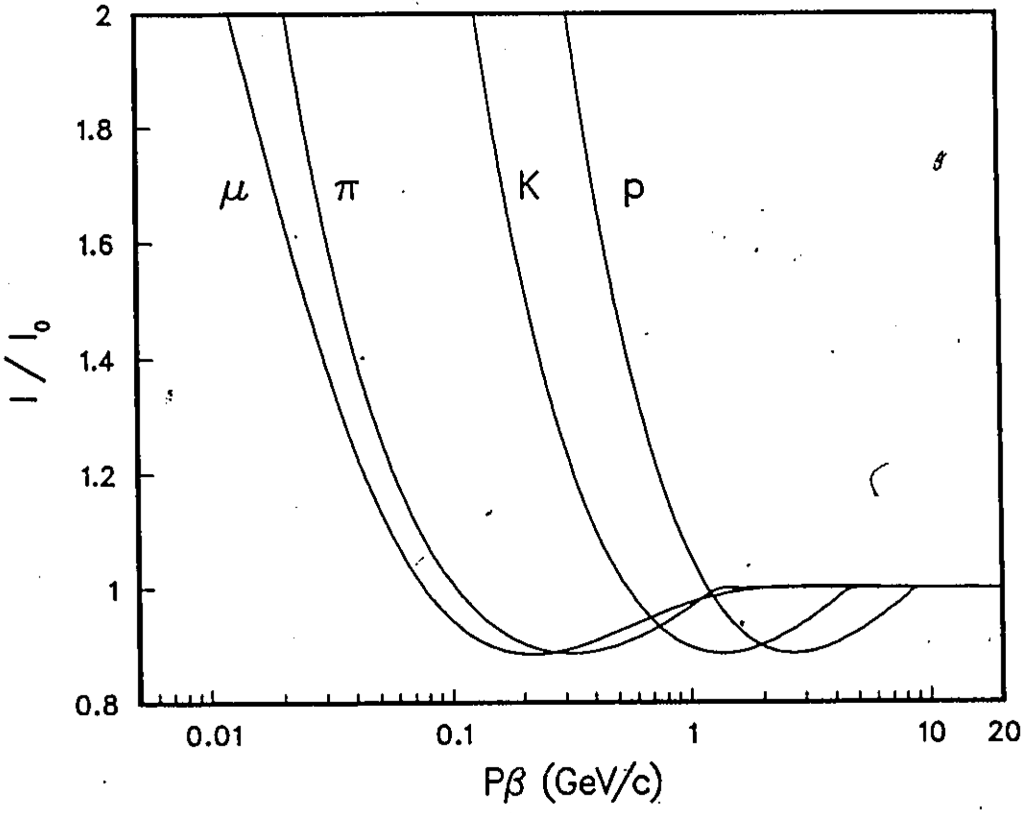

Figure 32: Ionization vs $p\beta$ for various particles.

3.3 The Second Reconstruction of the Tracks

Once a charm candidate (any decay) had been found the track-finding program was run again to look for tracks it might have missed the first time. Making use of the track measurements done in the emulsion, the program searched for drift chamber tracks to match the emulsion tracks. The second time through the program also reconstructed tracks that did not point back to the vertices found in the emulsion, this was done in order to look for the decays of Λ^0 or K_s^0 in the emulsion or drift chambers.

The first step in the fitting of an event was to visually inspect a projection showing the hits in the drift chambers and the reconstructed tracks of the track-finding program. These projections (Figure 33) were used to check that the reconstructed tracks were real tracks, and to ensure that no tracks were missed. The projections were also used to look for possible Vs which were due to the decay of a K_s^0 or a Λ^0 in the drift chamber. A V would be characterized by two tracks neither of which pointed towards the decay or interaction vertex, and which intersected in the first few drift chambers. The invariant mass of a possible V had to agree with the accepted mass of the possible neutral within 2.5 standard deviations.

3.4 Identifying Particles in the Spectrometer

The data from the Time-of-Flight system was used to identify the produced particles, with special emphasis put on the decay tracks. The various hits in the TOF paddles were compared with the predictions of the up-down tracks (tracks which were reconstructed in both the upstream and downstream drift chambers). By using the timing information, total path length, and particle momentum it was sometimes possible to determine what type of particle hit the TOF paddle.

The time given by the TOF II paddles is referred to as the stop time. The final time is corrected for the pulse height of the pulse in the paddle and the Y position of the hit (obtained from the drift chamber prediction) [10]. As a check on the hit in the paddle the Y position obtained by comparing the pulse height at the two ends

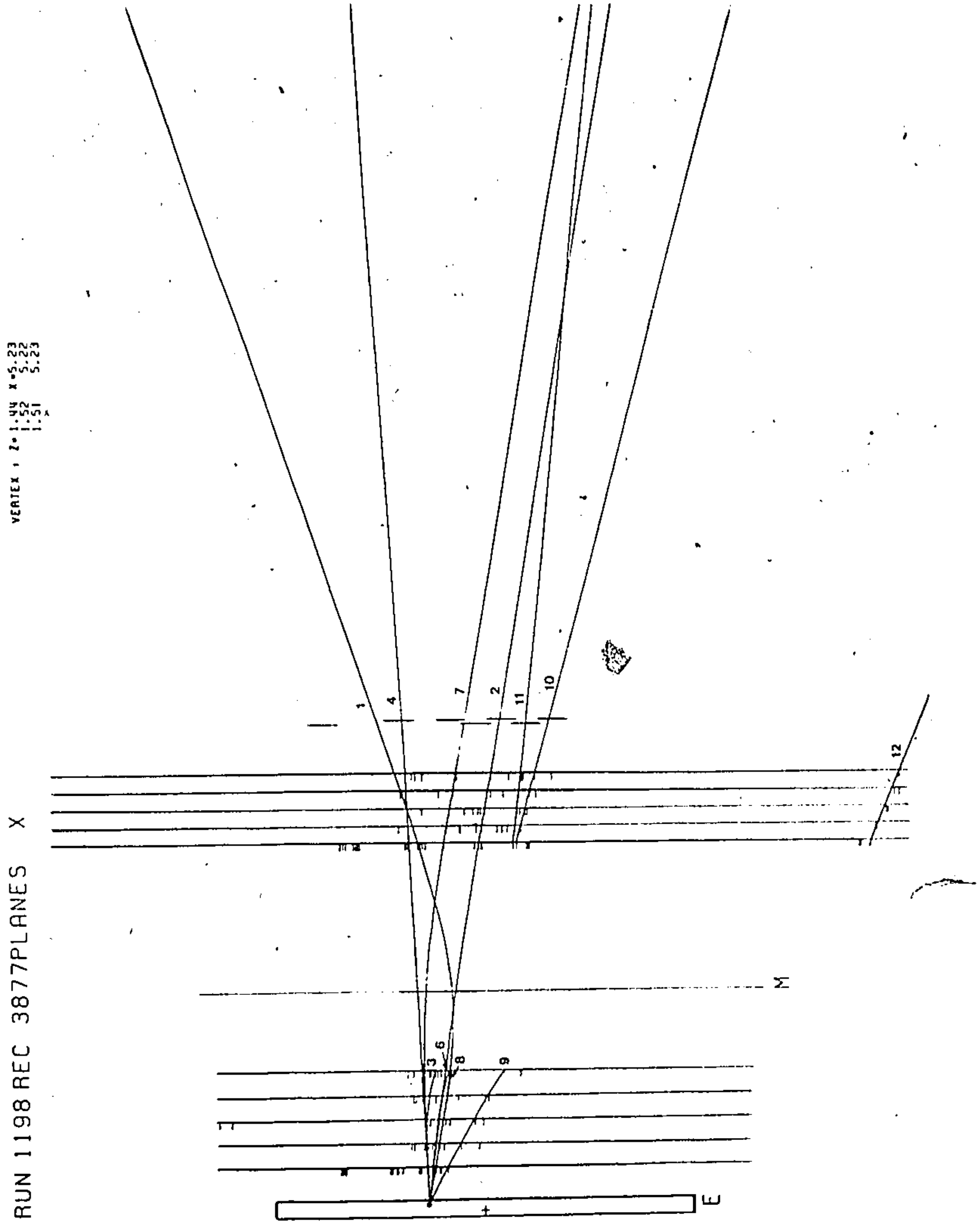

Figure 33: Reconstructed drift chamber tracks.

of the tube was compared with that obtained using the drift chamber information. The pulse height seen in the paddle also had to be consistent with a single track.

The total path length travelled by a track is given by:

$$L = \beta ct$$

where βc is the velocity of the track and

$$t = t_{\text{stop}} - t_{\text{start}}$$

The start time is obtained by using a track identified as a muon using the muon counters, or a very energetic track so that $\beta \simeq 1.0$, and fitting the above formula. If there are no muons identified or energetic tracks then the start time is obtained from the TOF I counter. The momentum of a track can be written as

$$P_{\text{track}} = \gamma\beta m$$

where $\gamma = 1/\sqrt{1-\beta^2}$, and m is the mass of the particle. By rearranging the above equations it is possible to obtain the following

$$m = P_{\text{track}}\sqrt{\frac{ct}{L}^{2} - 1}$$

The relation above can then be used to obtain the mass of the particle and thus its identity. Figure 34 shows the mass obtained using the TOF system for particles with a momentum less than 2 GeV/c.

As shown above the TOF system can be used to calculate a mass for the particle being considered. In practice the β of the track was calculated and then compared with that expected for various particles. In order for a particle to have a specific ID (identity or particle type) the calculated β had to agree with the expected value within 2 standard deviations.

It was only possible to use those paddles in which only one track was present. Attempts were made to try and correct the times and pulse heights when two tracks were present in a TOF II paddle but they were unsuccessful.

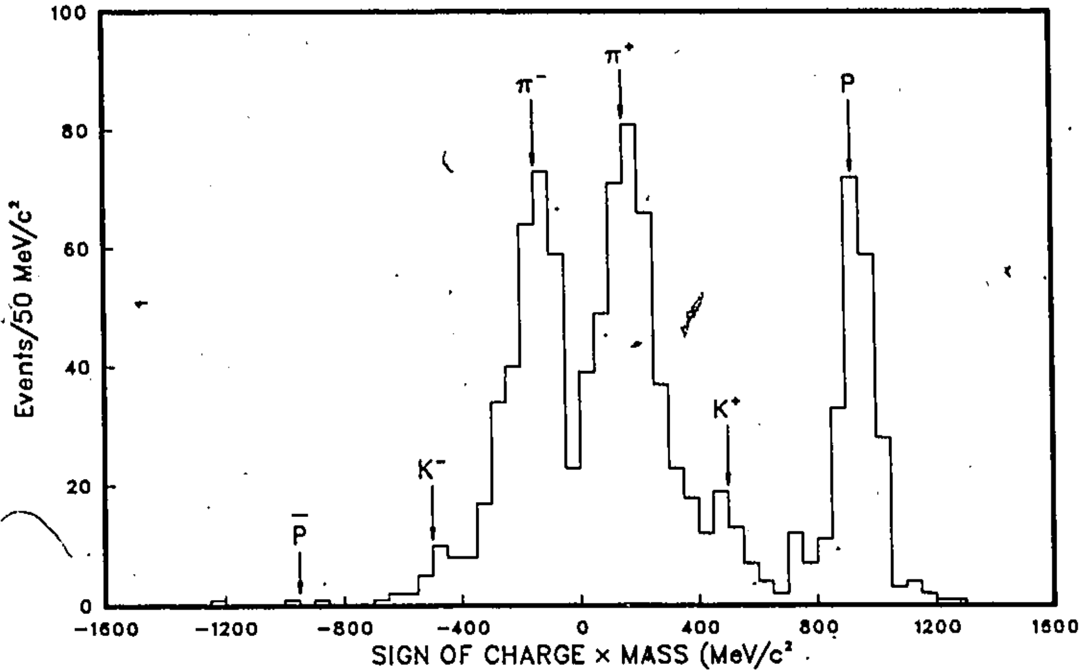

Figure 34: TOF mass spectrum.
The mass of the particle has been multiplied by its charge. A 2 GeV momentum cut has been applied

3.5 Electromagnetic Calorimeter

The EPICs and lead glass data were used to check whether or not any of the tracks were electrons (or positrons), and to determine the position and energy of the gammas (photons) in the event. Any track which deposits energy nearly equal to its momentum in the EPICs and lead glass was identified as an electron. In order to be tagged as an electron the ratio E/p had to be within 2.5 standard deviations of 1.0 (E is the deposited energy, and p is the momentum of the track). During the second run there was also the extra constraint that the tracks had to be several (> 3) times minimum ionizing in the EPICs. It was not possible to tag a track as an electron if its energy was below 1 GeV.

As already mentioned (Section 2.7.2), a charged particle will deposit about 350 MeV/c or up to 1/3 of its energy in the lead glass. Any excess energy which was not due to a drift chamber track was assumed to come from a gamma ray. The data from the EPICs and lead glass had to be checked carefully to ensure that all gammas were identified. During the first run the position of the gammas was assumed to be in the center of the lead glass block where the excess energy was observed. In the second run most gammas (about 90 %) converted in the lead sheet in front of the EPICs and thus it was possible to determine the position of the gamma using the EPICs. A gamma position was marked by the crossing of EPICs from the three rotated planes. The determination of the position was done with the aid of pictures (Figure 35 and 36) which shows the struck EPIC tubes and the energy in the lead glass blocks. A point with three EPICs crossing, some energy in the lead glass block at the same position, and no drift chamber track predicted to hit the EPICs/lead glass at that point, were the usual signature of a gamma. The gamma showers often spread a lot laterally and so a shower was usually marked by the crossing of several EPIC tupes from each plane.

Because the EPICs could be used to mark the position of the shower very accurately it was possible to correct the energy measured by the lead glass for geometric losses. Because the lead glass blocks were square and the phototubes round, not all the light from showers that were close to the corners of the blocks made it to

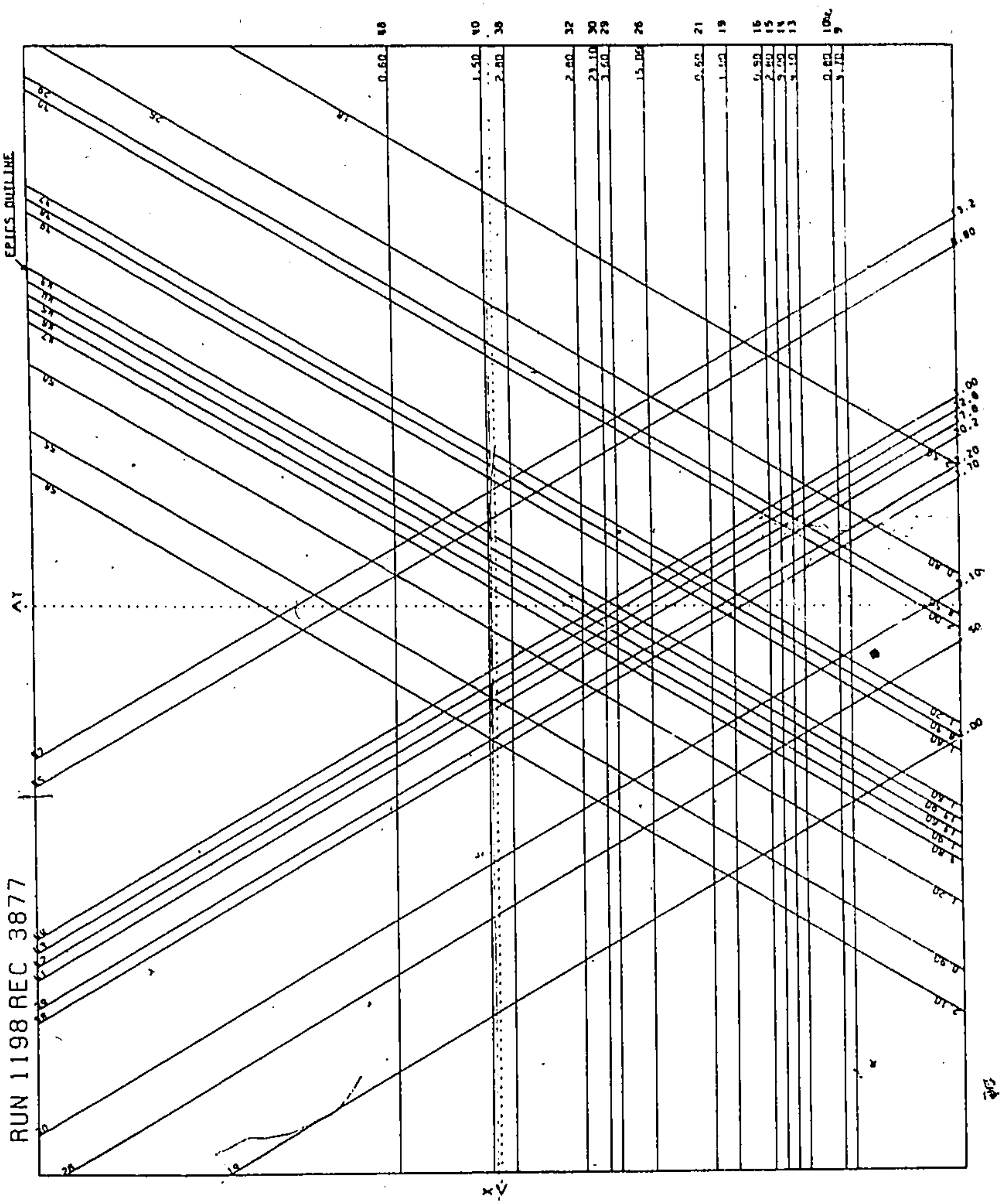

Figure 35: EPIC tubes with hits.

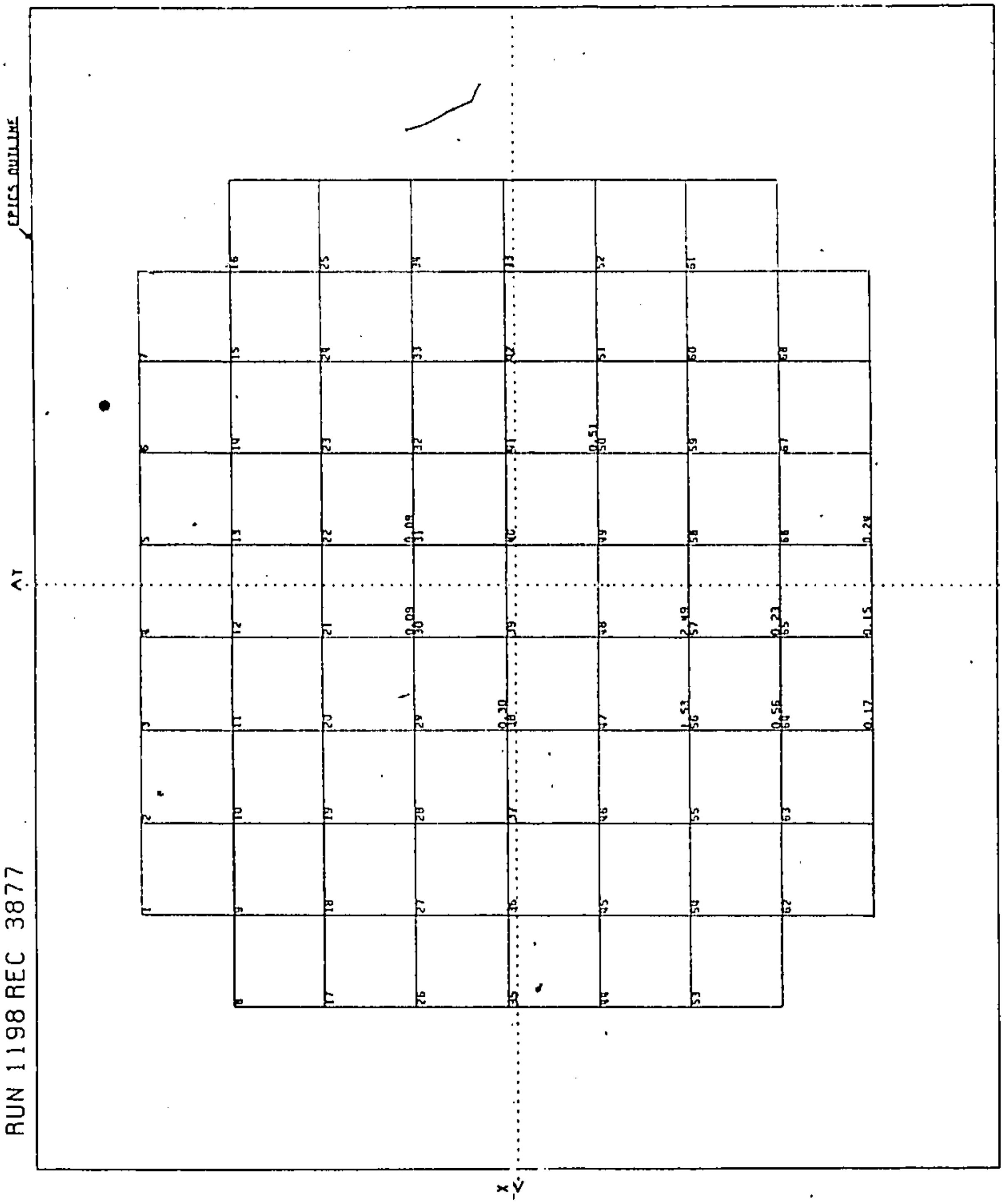

Figure 36: Energy deposited in lead glass.

the phototube. Also, showers close to the edge of the block deposited some energy into the neighbouring block. The following formula is used to correct the observed energy (E_{obs}) in the lead glass to get the "true" lead glass energy

$$E_{\mathrm{PbG}} = [1 + 0.08\left(\frac{r}{9.64}\right)^2]E_{\mathrm{obs}}$$

where r is the distance (in cm) of the shower from the center of the block.

As the shower develops in the lead sheet the electrons lose some energy due to ionization and this energy loss also has to be corrected for. On average the electrons will lose 0.02 GeV while traversing the lead sheet, since the pulse height (PH) in the EPICs reflects the number of electrons that were in the lead sheet, the total energy lost by the shower is given by $0.02 \cdot PH$, and thus the final energy of the shower is given by

$$E_{\mathrm{shower}} = E_{\mathrm{PbG}} + 0.02 \cdot PH$$

Any track that was identified as an electron in the electromagnetic calorimeter was assumed to come from a gamma conversion, unless it could be shown otherwise. Often the tracks identified as electrons or positrons were seen in the emulsion and found to come from gamma conversions in the emulsion. If the conversion point for the gamma was not known it was then assumed that it occurred one conversion length (9/7 radiation lengths) downstream of the vertex, or halfway between the vertex and the end of the emulsion, whichever was smaller. If the conversion was observed in the emulsion the energy of the electron and positron could be determined, either by observing them in the drift chambers or by multiple scattering measurements. It was usually very obvious when two drift chamber tracks were from a gamma conversion as the two tracks had almost identical exit angles and opposite charges; the invariant mass of the two tracks had to be less than 50 MeV/c^2. Any pair of drift chamber tracks meeting these requirements were assumed to be due to a gamma conversion, unless (for some reason) the emulsion data showed otherwise. The energies of the electron and positron were corrected for any bremsstrahlung energy that they might have lost traversing the emulsion. To correct for this loss the following formula was used

$$E_{\mathrm{initial}} = E_{\mathrm{observed}} e^{L/L_R}$$

Table 7: Errors on Initial Energy Versus Distance Travelled by Electrons

$E_{\mathrm{obs.}}$	0.50	1.00	1.50	2.00	2.50	3.00	4.00
Distance (cm)				(GeV)			
0.00	0.00	0.00	0.00	0.00	0.00	0.00	0.00
0.50	0.01	0.03	0.05	0.09	0.14	0.21	0.33
1.00	0.12	0.15	0.20	0.36	0.50	0.60	0.90
1.50	0.20	0.50	0.50	0.65	0.75	1.00	1.25
2.00	0.25	0.75	0.70	1.30	1.00	1.50	1.88
3.00	0.50	1.00	1.00	2.00	1.75	2.50	2.63
4.00	0.60	1.25	1.20	2.20	2.40	2.75	3.75
5.00	0.75	1.50	1.40	2.50	2.90	3.75	4.30

where L/L_R is thickness of emulsion that the particle travelled through in radiation lengths. The final energy of the gamma was then the sum of the electron and positron energies.

In order to use the gamma conversion in the fitting of the event it was very important that the uncertainties in the energy measurement be well understood. The Monte Carlo program EGS [40] was used to help understand the energy fluctuations in the observed energy of the electron and positron. A number of electrons of various energies were generated and passed through different thicknesses of emulsion; for a given final energy and emulsion thickness a plot was then made of the initial energy. For example, if the final energy of an electron was measured to be 1.0 GeV and it had travelled through 2.0 cm of emulsion, then a plot was made showing the energies of the electrons that resulted in a 1.0 GeV electron leaving the emulsion. These various plots were then examined and the initial energy of the electrons was found to be given by the formula shown above. The fluctuation in the initial energy was quite large and is shown in Table 7. The final electron energy uncertainty used depended on the initial energy, conversion distance, and measured momentum uncertainties.

As an example of how to use Table 7, assume that an electron has been observed to travel trough 2 cm of emulsion, and it is in a vertical module ($L_R = 2.94$ cm).

Further , assume that it has been observed in the drif chambers, and it has a measured momentum of 2.5 GeV/c. Thus, the initial energy of the track (at its 'origin') is given by

$$E_{\text{initial}} = (2.5\ \text{GeV}) \times e^{2/2.94} = 4.9\ \text{GeV}$$

The error on the initial energy is taken directly from the table, at 2 cm and an energy of 2.5 GeV, and it is 1.00 GeV. The initial energy of the electron is 4.9 ± 1.0. The final error used has to include this error (1.0 GeV), the uncertainty in the distance the electron travelled, and the uncertainty in the measured momentum.

Once the position and energy of all the gammas had been determined, an attempt then had to be made to find all the π^0 candidates. This was done by calculating the invariant mass of all the two gamma combinations possible, and those combinations that had a mass within 3 standard deviations or 60 MeV/c^2 (if the mass error was small) of the π^0 mass were used as a π^0. In an attempt to save computational time only the five π^0 which helped to balance the transverse momentum at the decay vertex were used when attempting to fit the decay (Section 3.8).

3.6 Hadron Calorimeter

The hadron calorimeter EPICs and paddles were used to determine the position and energy of the neutral hadrons produced. A comparison was made between the position of a hadron as given by the calorimeter EPICs and the extrapolated positions from the drift chamber tracks. Any calorimeter shower which could not be matched with a drift chamber track was assumed to be due to a neutral particle such as a neutron or K_L^0.

3.7 Muon Hodoscope

Muons were identified by their range in steel. As already mentioned it was possible to identify muons above 1.9 GeV because they were able to make it to the MUF paddles. It was also possible to identify muons with an energy lower than 1.9 GeV by studying their behavior in the hadron calorimeter. If a track was minimum ionizing in all the hadron planes (it did not produce a shower) and its range was consistent with a muon, it would be identified as a muon. Usually the tracks or a neighbouring track produced a shower and so no tracks were identified as muons using this procedure. However, it was usually possible to eliminate the muon as a possible ID for a track based on its behavior in the calorimeter steel.

When deciding whether or not a given muon paddle that registered a hit is associated with some reconstructed drift chamber track, the multiple scattering of the track had to be accounted for. Because of all the steel that the muons had to pass through before making it to the muon counters, it was possible for the muon to be scattered several centimeters (depending on the initial momentum). A muon paddle hit was associated with a track if the predicted hit was within 2.5σ of the observed hit, where σ is the expected multiple scattering for a track with the measured momentum.

3.8 Event Fitting

Once all the neutrals were found and the momentum and identity of the decay tracks had been determined, an attempt was made to fit kinematically the decay to some decay hypotheses consistent with the IDs. The fitting process was based on a procedure outlined in a CERN Easter School [41], which was incorporated into the fitting program [42]. When doing a fit there were a number (K) of constraint equations from energy and momentum balance at the decay vertex. The angles and momentum of all the charged tracks were measured in the emulsion and spectrometer; the angles of the neutral particles could be determined by the difference between their hit in the spectrometer and the decay vertex position. There were at least four constraint equations: one for each of the momentum coordinates (X, Y, and Z) and an equation from energy conservation. In order for the decay to be viable all the constraint equations must be valid. Not all the quantities were measured and thus it was possible to reduce the number of constraint equations. If there were J unmeasured quantities the number of constraints for a fit was n = K −

J. For a simple decay in which all the decay products were observed in the emulsion there were 4 constraint equations, and only one unknown (the charm momentum). This corresponds to a 3C fit. The number of constraint equations will not change if a neutral particle is included in the hypothesis as long as the particles' direction and energy can be measured directly. If one of the particles from the decay vertex also decay, such as a π^0, the number of constraint equations doubled, because there were also four constraint equations for this second decay. Thus when a π^0 was included in the decay there were a total of 8 constraint equations but four unknown quantities (charm momentum, and direction and momentum of π^0) which resulted in a 4C fit.

Usually the constraint equations for a given fit were not valid and it was necessary to vary the measured quantities in order to get valid constraint equations. This was done by a fitting program which varied the measured quantities according to their uncertainties and allowed the unmeasured quantities to be anything. It attempted to balance the energy and momentum of the decay while minimizing

$$\chi^2 = \sum_{i=1}^{N} \frac{(m_i - m_i^0)^2}{\sigma_i^2}$$

where there were N measured quantities, $m_i^0 \pm \sigma_i$ is the ith measured quantity, and m_i is the varied value. Once the program had completed the fit the confidence level could be calculated from the χ^2 value and the number of constraints. The fit was considered a "good fit" if the confidence level was greater than 1%.

For some events there were no "good fits" and the only possible fits were 0C or unconstrained fits. These were fits in which the momentum and direction of the neutral particle was left free and the number of constraint equations equalled the number of unknowns (if a charged-particle momentum was not known no solution was possible). Solving the constraint equations it was found that plotting the invariant mass of the decaying particle against the particle momentum resulted in a curve that looked like a distorted parabola. Thus for a given charmed-particle mass there were two possible momentum solutions for the neutral particle, if the minimum of the invariant mass plot was low enough. For 0C fits only the Cabibbo favored hypotheses were considered; Cabibbo unfavored hypotheses were ignored.

3.9 Fit of a Charged-Particle Decay

For the event 1198-3877 the track-finding program found a total of five drift chamber tracks. The event was predicted to be and subsequently found in one of the emulsion modules at the University of Ottawa. There were three shower tracks and one black track seen to come from the primary vertex. One of the shower tracks was matched to a 71 GeV/c negatively charged drift chamber track that was identified as a muon, indicating that this was a charged-current ν_μ interaction. While following one of the charged tracks leaving the neutrino interaction vertex, it was discovered that the track decayed into three particles (trident) after travelling 2280 μm . In the second reconstruction process, 11 drift chamber tracks were reconstructed in all.

There was a problem with the tracks found by the track reconstruction program. The three tracks coming from the decay vertex were all matched with positively charged drift chamber tracks. It was known from the ionization of the decaying particle that it was a singly charged particle. It turned out that one of the decay tracks was matched to an up-only track with a very large momentum uncertainty (almost 100%). This meant that the momentum and sign of the track were not well known. An attempt was then made to measure the pβ of the track in the emulsion; unfortunately, it was not possible to get an accurate measurement. Looking at a projection of the drift chamber tracks found by the reconstruction program (Fig. 33), it is obvious why the momentum resolution of the track was so poor. In the bending plane (X-plane), the track under consideration (D.C. track 8) travelled through a region where there are a lot of other tracks and it was quite possible for the track to be given the wrong sign. Looking at the drift chamber tracks picture, it was noticed that track 8 appears to go through the magnet gap and produces some hits in the first three downstream X chambers. The track missed the last two X chambers because of its large Y slope. Using the three hits in the X plane drift chambers, it was possible to determine the slope of the downstream segment of the track and thus determine its momentum and charge. It was found to be a negative track with a momentum of 5.65 ± 0.22 GeV/c. The measurements for all the found particles are summarized in Table 8.

Table 8: Summary of 1198-3877

	dx/dz	dy/dy	Momentum (GeV/c)	Charge	I/I_0	
EM-1	−0.054	+0.084	10.31 0.32	+1	—	
EM-2	+0.016	+0.021	71. 21.	−1	—	Muon
EM-3	−0.037 0.004	−0.155 0.006	—	+1	—	Charm Candidate
Decay Tracks						
EM-3-1	+0.011 0.003	−0.058 0.005	2.232 0.025	+1	0.94 0.06	
EM-3-2	−0.070 0.005	−0.230 0.010	5.65 0.22	−1	—	
EM-3-3	−0.214 0.015	−0.318 0.015	0.351 0.038	+1	0.87 0.05	Pion

The next step was to go through all the decay tracks to try and determine their identity. It was not possible to get any TOF information for decay track EM-3-1 because two tracks hit in the same TOF II paddle. The ionization measurement was not able to identify the track either. The track was consistent with a minimum ionizing track in 2 out of 3 EPIC planes (in the third plane a gamma candidate was using the same tube as the track). The lead glass block that the track hits had a total visible energy of 2.49 GeV. However, there were also two gamma candidates in the same block, and the track hit close to the edge of the block and there was no signal in the neighboring block. If the track was a positron all three EPIC planes would have been above minimum ionizing and there would also have been some energy deposited in the neighboring block, so this track was probably not an electron. A muon with this momentum would have made it to the MUF counter, but nothing was seen at the predicted position, so this track could not be a muon. Thus, track EM-3-1 was consistent with being a hadron.

EM-3-2 was the track that had to be reconstructed by "hand". It was not possible to get any TOF information for this track because it hit the same TOF II paddle as the above track (EM-3-1). The track momentum was too high for an ionization measurement to be of any use in identifying the track. The track deposited only 0.15 GeV in the lead glass, and there was no apparent EPIC crossing at its predicted position. Thus, this track is not an electron. Because of the large slope of the particle, it would not hit the muon paddles (MUF or MUB). However it should have been seen in the first three hadron calorimeter planes, and it would have been minimum ionizing if it was a muon. There was 3.6 GeV deposited in the first calorimeter plane, and nothing in any of the others (inconsistent with a muon), so this track could not be a muon.

The third decay (EM-3-3) was a low momentum track, and was only reconstructed in the upstream drift chambers. Because it was only seen in the upstream drift chambers, it was not possible to use the TOF system, the Electromagnetic Calorimeter, or Hadron Calorimeter to try and identify the particle. The ionization was measured for the track and was found to be consistent with only a muon or pion.

Table 9: Summary of Gammas in 1198-3877

#	dx/dz	dy/dz	Energy (GeV)
1	−0.027 0.008	−0.071 0.002	1.12 0.50
2	−0.008 0.005	−0.103 0.002	4.60 0.50
3	+0.095 0.008	−0.246 0.002	0.14 0.06
4	−0.135 0.005	−0.004 0.013	0.72 0.13
5	−0.103 0.008	−0.204 0.015	0.55 0.15
6	+0.022 0.002	−0.188 0.002	0.21 0.08

The transverse momentum of the three decay tracks with respect to the charmed-particle direction is 0.28 ± 0.06 GeV/c which implies that there is also a neutral particle coming from the decay.

Checking carefully through the lead glass and EPICs data (Fig. 35 and 36), it was possible to determine the energies and EPIC hits of the gammas produced in this event. The energies and calculated slopes for the six gammas are summarized in Table 9. There was a total of 20 gamma combinations which were consistent with a π^0. In the final fitting procedure, the 5 π^0 which balanced the transverse momentum the best were kept.

The fitting program was then run and all the possible decays, Cabibbo favored and singly Cabibbo unfavored, consistent with the IDs, were considered. The program found three fits where the confidence level was greater than 1%. Once a "good fit" was found the mass of the decaying particle was left free, thus reducing the number of constraints by one, and a second fit was attempted in which the program calculated the charm mass. For the decay hypothesis to be valid the initial and unconstrained-mass fits must have a confidence level greater than 1%, and the calculated mass must agree with the accepted mass within 2.5 standard deviations. All three fitted hypotheses had a fitted mass which agreed with the expected mass. It was not possible to tell what kind of a charmed particle this decay was, and the event was ambiguous among D^+, D_s^+, and Λ_c^+. The three hypotheses and their momentum are as follows

$$\begin{aligned} D^+ &\to \pi^+ K^- \pi^+ \pi^0 & P_c &= 15.5 \pm 0.5 \text{ GeV/c} \\ D_s^+ &\to K^+ K^- \pi^+ \pi^0 & P_c &= 15.5 \pm 0.5 \text{ GeV/c} \\ \Lambda_c^+ &\to p K^- \pi^+ \pi^0 & P_c &= 15.5 \pm 0.5 \text{ GeV/c} \end{aligned}$$

3.10 Fit of a Neutral-Particle Decay

Another event predicted and found in one of the University of Ottawa emulsion modules was event 1118-4569. For this event 9 tracks were reconstructed in the drift chambers. One of the tracks was followed back to the primary vertex. The primary vertex had 5 shower tracks and one black track. One of the shower tracks was identified as a negative muon with a momentum of 13 GeV/c. While carrying out the scanback procedure on the unmatched tracks a neutral 4-prong decay candidate and an e^+e^-pair were found. The decay vertex was 1589 μm downstream of the primary vertex. In the second reconstruction process, 10 drift chamber tracks were reconstructed in all (7 up-down, and 1 up-only). The data for all the tracks found in the emulsion are summarized in Table 10.

The various decay tracks were then checked carefully in an attempt to identify them. In this event the muon hit two TOF II paddles and it was possible to improve the resolution for the start time by combining the times from the two paddles. The track V-1 was identified as a kaon by the TOF. The track deposited only 0.33 GeV in the lead glass, and was minimum ionizing in only 2 out of the 3 EPIC planes which registered a hit, so it is not an electron. The track had sufficient energy to reach the MUF paddles, but no hit was registered at the predicted position, so it is not a muon. Track V-1 is, thus, identified as a K^-.

Track V-2 hits the same TOF paddle as another track and so it is not possible to obtain an ID using the TOF system. Since the track momentum is 1.8 GeV/c,

Table 10: Summary of 1118-4569

	dx/dz	dy/dy	Momentum (GeV/c)	Charge	I/I_0	
EM-1	−0.143 0.005	−0.073 0.005	3.23 0.04	+1	—	
EM-2	−0.076 0.004	+0.143 0.003	12.8 0.5	−1	—	Muon
EM-3	+0.285 0.005	−0.037 0.003	1.38 0.01	+1	—	Proton
EM-4	+0.034 0.005	+0.143 0.003	3.12 0.99	−1	—	
EM-5	+1.437	+1.206	—	—	—	
V-0	+0.073 0.005	−0.108 0.006	—	0	—	Charm Candidate
E1-0	+0.159 0.005	+0.129 0.006	—	0	—	e^+e^-pair
E1-1	+0.165 0.005	+0.129 0.005	0.30 0.03	+1	—	Positron
E1-2	+0.154 0.005	+0.130 0.005	—	−1	—	Electron
Decay Tracks						
V-1	+0.095 0.003	+0.011 0.001	2.18 0.02	−1	—	Kaon
V-2	+0.268 0.003	−0.255 0.002	1.84 0.02	+1	—	
V-3	−0.157 0.005	−0.150 0.005	1.74 0.02	−1	—	Pion
V-4	+0.166 0.002	−0.131 0.002	1.64 0.01	+1	—	Pion

an ID cannot be obtained by measuring its ionization in the emulsion. The track hits just outside the lead glass array and only 2 out of 3 EPIC planes register a hit. Both tubes are minimum ionizing and so this track is not a positron. The track should stop just before the MUF plane and be seen in all six calorimeter planes. It was not seen in any and so it cannot be a muon. Track V-2 is, therefore, a positive hadron.

The track V-3 has been identified by the TOF as an electron, muon or pion. The track hits a lead glass block in which there is 1.16 GeV visible energy, and the pulse heights in all three EPIC planes are about 4 times minimum ionizing. After applying the various corrections the energy deposited in the electromagnetic calorimeter is consistent with the track being an electron. Unfortunately, there is also another EPIC crossing over the same block, which appears to be due to a gamma, and the EPIC pulse heights are a little low for an electron. Also the shower has not spread very much laterally. There also appears to be some evidence for the track in the hadron calorimeter. If this track is an electron this would be a wrong sign semi-leptonic decay, which would be very rare, if not impossible. Taking all these things into account, it was not possible to uniquely identify this track as an electron, but the electron ID could not be eliminated either. If the track is a muon it should have been seen in all six hadron calorimeter planes. However there is some evidence for it in the first two planes but nothing downstream. Thus this track cannot be a muon. Hence, track V-3 is an electron or a π^-, and for the fitting procedure it was be assumed to be a pion.

The TOF system identified track V-4 as an electron, muon or pion. The track hit close to the border of two blocks and the total visible energy in the two blocks was 0.45 GeV, which is consistent with a hadron. In two 'unobstructed' EPIC planes the track was minimum ionizing (the third tube is also used by an electromagnetic shower), and thus it is not a positron. If this track is a muon it should have been seen in all six hadron calorimeter planes. There is some evidence for it in only the first two planes, so it is not a muon. Thus, track V-4 is a π^+.

The total transverse momentum of the four decay tracks with respect to the charmed-particle direction was calculated to be 0.17 ± 0.02 GeV/c which implies

Table 11: Summary of Gammas in 1118-4569

#	dx/dz	dy/dz	Energy (GeV)
1	+0.161	+0.129	0.45
	0.003	0.007	0.10
2	−0.028	+0.028	1.11
	0.004	0.004	0.16
3	+0.065	−0.057	0.99
	0.003	0.004	0.15
4	−0.076	−0.158	1.02
	0.005	0.002	0.15
5	−0.194	0.047	—
	0.008	0.015	

that there is at least one neutral paticle in the decay.

Checking through the lead glass and EPIC data carefully a total of 5 gamma candidates were found and they are listed in Table 11. Gamma number 5 corresponded to the crossing of several EPIC tubes but no energy in the lead glass block at the same location. Therefore only the direction of the gamma was known. There is some constraint on the energy of the gamma since it is very unlikely that a large-energy gamma would not be seen in the lead glass. The orientation of the e^+e^-pair was found to be inconsistent with the decay vertex position, and it was found to come from the primary vertex. A total of 11 gamma combinations were consistent with being from a π^0. The 5 π^0 which were able to reduce the transverse momentum closest to zero were kept in the final fitting procedure.

The fitting program attempted all possible decays consistent with the particle IDs. Since 3 of the 4 decay tracks had been identified, and this was a neutral decay the number of decay hypotheses actually tried was small. There was only one hypothesis that had a "good fit", and that was

$$D^0 \rightarrow K^-\pi^+\pi^-\pi^+\pi^0 \quad P_c = 8.5 \pm 0.2$$

Chapter 4

Lifetimes of Charmed Particles

All charmed-particle decay candidates were analyzed in great detail and whenever possible were assigned a momentum and a lifetime was then calculated. The individual events were then combined together to obtain lifetimes for the different charmed-particle species using a maximum likelihood estimation method. Before the calculation of the lifetimes could be done, a certain filtering of the events using various cuts and a calculation of the finding efficiencies were necessary. In the final analysis, the neutral and charged particle lifetimes were calculated slightly differently.

4.1 Cuts

When fitting some of the charm events, many difficulties were encountered which made the final fit uncertain. The uncertainty in the fits were usually very vague. There was usually no real justifiable reason to eliminate some events but it was "felt" that the fits were not very good. For these poor fits the problem was often that the events were unconstrained due to a missing neutral, or there was a charged track whose momentum could not be measured. In some cases the events were very complicated and so it was very difficult to sort out the event, while in others it seemed very simple but because of the low invariant mass of the charged particles, there were probably two neutrals in the decay. In an attempt to try to eliminate these various events a number of different cuts were tried and rejected.

One of the possible cuts was on the transverse momentum of tracks coming from the charm decay. The first cut was on the maximum P_T of the decay tracks: the momentum had to be less than 2.0 sigma above a certain maximum value which was determined from the type of decay involved. For example, for a neutral decay involving a V, the P_T had to be less than 2.0 sigma above 844 MeV/c. This is the maximum possible momentum a track can have in the decay $D^0 \rightarrow K^-\pi^+\pi^0$. Another possible cut was on the minimum mass of the $-1C$ curve (curve obtained in 0C fits when plotting the calculated mass against the particle momentum), using both a maximum and minimum possible value.

The only cut which had any real effect, and which was finally used was a cut on the Z position of the primary vertex. It was decided to cut the first 2.0 cm of the second run emulsion stack, thus reducing the second run emulsion thickness to 5.0 cm, the same as in the first run. It was found that if the Z cut was applied first, the other cuts that were considered did not have effect (no events were lost), thus the only cut needed was the one that used the Z position of the primary vertex. There were originally 54 neutral decay candidates found in the second run, from which 14 events were lost due to the Z cut. Four of the fourteen were constrained events (2 events had a D^{*0} fit, but it turned out that 3 of 4 unfittable events were lost. For the charged events, there were originally 50 decay candidates and again 14 events were lost due to the Z cut. Only one of the fourteen decays was constrained, and five out of 16 unfittable events were lost. Thus, the Z cut was found to eliminate predominantly poorly fit events and very few "good" events. The Z cut was applied to the entire data sample and all the quoted numbers include this cut, the only exception being the calculation of the efficiencies, which use the entire sample (without the Z cut) to increase the statistics.

4.2 Efficiency

The efficiency for finding the particle decays depends on the decay distance and event topology. It also varied from the first to the second run and from one laboratory to another. During the first run, events were found using the scanback, volume-scan, and the follow-down methods. All three methods were used to find charged decays while only the scanback and volume-scan methods could be used to find neutral decays. In the first run, institutions scanning the vertical emulsion modules used the scanback method while the horizontal groups used the volume-scan method; in the second run all groups used the scanback and volume-scan methods. The calculation of the scanback efficiency was done separately for the first and second runs. The calculation for the second run will be discussed below, the first run calculation was similar. The volume-scan efficiency was estimated from the ratio of the $\gamma \rightarrow e^+e^-$ pairs found by volume-scan over the number predicted. This efficiency was independent of the decay distance and was close to zero outside the scanning volume. It was not completely zero outside the scanning region because decays could be found "accidentally" while following a charged track. The final first run efficiencies are shown in Table 12, with the various types of efficiencies combined with a weight proportional to the number of events found by the different methods.

The term scanback efficiency actually refers to the combination of the efficiency for reconstructing the decay tracks in the drift chamber and the efficiency to follow these tracks back to the decay. The final scanback efficiency for a single track is

$$\epsilon_{SB} = \eta_{DC}\eta_{CS}\eta_{FB}$$

where

η_{DC} = The probability that the decay track will be observed in the drift chamber (that is it will be reconstructed and pass the scanning cuts).

η_{CS} = The probability that the candidate will be found in the changeable sheet.

η_{FB} = The probability to follow tracks in the changeable sheet back to its origin in the emulsion stack.

Table 12: First Run Particle Decay Finding Efficiency

	Region	Efficiency(%)
Charged	0– 2 μm	0 ± 8
	2– 5 μm	18 ± 8
	5–10 μm	50 ± 6
	10–30 μm	76 ± 4
	30–3000 μm	95 ± 5
	3000–6000 μm	85 ± 6
	6000–99999 μm	59 ± 13
Neutral	0– 2 μm	0 ± 8
	2– 5 μm	13.8 ± 7
	5–10 μm	35.1 ± 6
	10–30 μm	68.1 ± 5
	30–400 μm	82.0 ± 15
	400–1000 μm	73.3 ± 11
	1000–99999 μm	62.2 ± 5

For the case of an n prong decay the probability of observing m tracks is given by

$$ {}_nC_m\, \eta_{DC}^m \,(1-\eta_{DC})^{n-m} $$

Thus, if there are a total of N events with an n prong decay, the total number of events with m observed tracks is

$$ N\, {}_nC_m\, \eta_{DC}^m \,(1-\eta_{DC})^{n-m} = N_m \qquad \{m = 0, 1, \ldots, n\} $$

There are a total of $n+1$ equations with the constraint

$$ N = N_0 + N_1 + \ldots + N_n $$

Using these $n+1$ equations it is possible to solve for N, N_0 and η_{DC}. There are too many equations for events with $n > 2$ (it is over constrained). For the two prong case one has to solve the following three equations

$$ \begin{aligned} N_0 &= N(1-\eta_{DC})^2 \\ N_1 &= 2N\eta_{DC}(1-\eta_{DC}) \\ N_2 &= N\eta_{DC}^2 \end{aligned} $$

4.2.1 Neutral Decay Efficiency

Experimentally, the following has been measured for two prong decays:

$$ \begin{aligned} N_1 &= 13 \pm \sqrt{13} \\ N_2 &= 22 \pm \sqrt{22} \\ (N_0 &= 5 \pm \sqrt{5}) \end{aligned} $$

Solving for N, N_0, and η_{DC} one gets:

$$ \begin{aligned} N &= 37 \\ N_0 &= 2 \\ \eta_{DC} &= 0.77 \pm 0.06 \end{aligned} $$

The efficiency calculation for 4 prong events is a little more difficult since there are 5 equations with three unknowns. The five equations are:

$$\begin{aligned}
N_0 &= N(1-\eta_{DC})^4 \\
N_1 &= 4N\eta_{DC}(1-\eta_{DC})^3 \\
N_2 &= 6N\eta^2(1-\eta_{DC})^2 \\
N_3 &= 4N\eta_{DC}^3(1-\eta) \\
N_4{}' &= N\eta^4
\end{aligned}$$

It is possible to solve for the three unknowns using a graphical method. Because of statistical fluctuations in the number of events (N_m) it is possible to use a set of inequalities given by

$$N_m - \sqrt{N_m} \leq N\,{}_nC_m\,\eta_{DC}^m\,(1-\eta_{DC})^{n-m} \leq N_m + \sqrt{N_m}$$

By plotting this inequality for the $n+1$ equations in the $\eta_{DC} - N$ space it is possible to determine the region in which all the equations overlap and solve for two of the unknowns. After using the graphical method to determine N and η_{DC}, N_0 can be determined using $N_0 = N(1-\eta_{DC})^4$. Experimentally we have for the four prong events:

$$\begin{aligned}
N_0 &= 0 \\
N_1 &= 3 \\
N_2 &= 6 \\
N_3 &= 4 \\
N_4 &= 1
\end{aligned}$$

Using these numbers the following was obtained:

$$\begin{aligned}
N &= 17.5 \\
N_0 &= 1.0 \\
\eta_{DC} &= 0.51 \pm 0.10
\end{aligned}$$

Table 13: Track Finding Efficiency

Institution	Number of Events	Number of e^+e^-	$\eta_{CS} \cdot \eta_{FB}$
NG	1583	195	0.941
OOO	620	58	0.719
KB	587	37	0.482
OT(V)	260	43	1.117
OT(H)	105	14	1.017

NG: Nagoya, Aichi and Toho.
OOO: Osaka and Okayama.
KB Kobe and Korea.
OT(V): Ottawa (Vertical Emulsion).
OT(H): Ottawa (Horizontal Emulsion).

There was also one four prong event in which one of the tracks interacted and produced two shower tracks, and so it was possible to scanback five tracks in all. Only two tracks passed the scanning cuts and were reconstructed, giving an efficiency of $2/5 = 0.40 \pm 0.34$. Combining this with the 0.51 ± 0.10 gives

$$\eta_{DC} = 0.50 \pm 0.10$$

The value of η_{CS} was estimated by the Nagoya group. Using 148 "good" tracks from charm events, they were able to find 142 tracks in the changeable sheet, giving $\eta_{CS} = 142/148 = 0.96 \pm 0.02$. The η_{FB} was calculated by trying to followback 420 tracks to their origin. A total of 412 tracks could be followed back giving $\eta_{FB} = 412/420 = 0.98 \pm 0.01$. The η_{CS} and η_{FB} product for the other institutions was scaled relative to the Nagoya data using the number of e^+e^-pairs found. The fraction of e^+e^-pairs and corresponding $\eta_{CS}\eta_{FB}$ products are shown in Table 13 for the various institutions.

To get the final scanback efficiency for the different institutions the two prong and four prong efficiencies had to be combined. The individual efficiencies were calculated using

$$\begin{aligned} \varepsilon_V &= 1 - (1 - \varepsilon_{SB-2})^2 = 0.92 \pm 0.03 \\ \varepsilon_4 &= 1 - (1 - \varepsilon_{SB-4})^2 = 0.92 \pm 0.05 \end{aligned}$$

(where the above values are the efficiencies for Nagoya). The V and 4-prong efficiencies were then combined using a weight based on the V/4-prong ratio obtained from Mark II [43, Table 4.6]. Finally using the ratio of the number of e^+e^-pairs found by the volume scan method to the number predicted a volume scan efficiency was determined for the various institutions. The volume scan and scanback efficiencies were then combined together to get an overall efficiency for finding the decays. The efficiencies for the different institutions as a function of decay lengths are shown in Table 14.

4.2.2 Charged Efficiency

To calculate the scanback efficiency to find charged-particle decays a method similar to that used for the neutral particles was used. Using a sample of charged particles that could be found using the scanback method the following numbers were obtained

$$\begin{aligned} N_0 &= 8 \\ N_1 &= 9 \\ N_2 &= 12 \\ N_3 &= 8 \end{aligned}$$

There were also three events where one of the decay tracks interacted and for these 1 out of 4 tracks were found. Using the graphical method to obtain an efficiency which is then combined with that found for the three events with an interacting track gives:

$$\eta_{DC}(\text{trident}) = 0.54 \pm 0.02$$

There is also one 5-prong event with 2 out of 5 tracks able to be scanbacked, giving

$$\eta_{DC}(\text{5-prong}) = 0.40 \pm 0.33$$

The overall scanback efficiency determined for charged particle decays (using Mark II ratios for 3-prong to 5-prong [43] and η_{SB} and η_{CS} already found) for Nagoya is

$$\epsilon_{SB} = 0.89 \pm 0.03 = 89 \pm 3\%$$

Table 14: Neutral-Particle Decay Finding Efficiency

Decay Type	Region	Efficiency(%)
NG	0–15 μm	0 ±
	15–30 μm	71 ±
	30–1000 μm	95 ± 2
	1000–99999 μm	92 ± 2
OOO	0–3 μm	0 ±
	3–10 μm	63 ±
	10–300 μm	84 ± 6
	300–99999 μm	81 ± 7
KB	0–3 μm	0 ±
	3–10 μm	50 ±
	10–300 μm	67 ± 8
	300–99999 μm	62 ± 8
OT(V)	0–15 μm	0 ±
	15–30 μm	74 ±
	30–1000 μm	98 ± 3
	1000–99999 μm	97 ± 4
OT(H)	0–3 μm	0 ±
	3–10 μm	72 ±
	10–300 μm	96 ± 8
	300–99999 μm	96 ± 8

The followdown efficiency was estimated in the first run and determined to be 95 ± 5% [11]. Thus the final charged decay finding efficiency found by combining the followdown and scanback efficiencies are given in Table 15.

4.2.3 Kink Efficiency

Multiprong charged decays are usually fairly easy to observe. However single prong (kinks) decays are much more difficult to observe. The efficiency for finding kink decays depends on the geometry of the decay, its decay length and whether it occurred in the vertical or horizontal emulsion. It also depends on whether the track was scanned back or followed down. For most of this discussion it will be assumed that the track was found and followed with an efficiency of 100%, and any scanback or followdown inefficiencies will be included towards the end.

Once a kink candidate had been found the transverse momentum of the kink was used to decide whether or not it would be considered as a charm kink. Only kinks with a P_T 'kick' of 400 MeV/c or more were considered to be charm candidates. This cut was used to eliminate kinks due to multiple scattering and strange particle decays.

Vertical Emulsion

In order to observe a kink in the vertical emulsion the tracks have to be measured very carefully. In the vertical emulsion it is the projection of the tracks on the X-Y plane that is actually observed. As the track is followed, its position when leaving and entering the emulsion plate and at the plastic sheet boundaries are fitted on a micro-gauge (mesh)[44]. If there is a sudden change in the projected length of the track, or a change in the direction of the track, it will be considered as a kink decay. There is, however, a mimimum change below which a kink will not be detected since the change could be due to distortion, multiple scattering or fluctuations in the emulsion thickness. Assuming that the decay length of the track is longer than about 125 μm then the minimum angle below which a kink cannot be observed is

Table 15: Charged-Particle Decay Finding Efficiency

Institution	Region	Efficiency(%)	
NG	0–15 μm	0 ±	$0.0 < \theta \leq 0.2$
	15–30 μm	75 ±	
	30–1000 μm	100 ± 0.4	
	1000–6000 μm	99 ± 1	
	6000–99999 μm	89 ± 3	
	0–15 μm	0 ±	$0.2 < \theta$
	15–30 μm	75 ±	
	30–1000 μm	100 ± 0.4	
	1000–3000 μm	99 ± 1	
	3000–99999 μm	89 ± 3	
OOO	0–3 μm	0 ±	$0.0 < \theta \leq 0.2$
	3–10 μm	74 ±	
	10–300 μm	99 ± 1	
	300–6000 μm	99 ± 1	
	6000–99999 μm	78 ± 7	
	0–3 μm	0 ±	$0.2 < \theta$
	3–10 μm	74 ±	
	10–300 μm	99 ± 1	
	300–3000 μm	99 ± 1	
	3000–99999 μm	78 ± 7	
KB	0–3 μm	0 ±	$0.0 < \theta \leq 0.2$
	3–10 μm	74 ±	
	10–300 μm	98 ± 2	
	300–6000 μm	98 ± 2	
	6000–99999 μm	60 ± 8	
	0–3 μm	0 ±	$0.2 < \theta$
	3–10 μm	74 ±	
	10–300 μm	98 ± 2	
	300–3000 μm	98 ± 2	
	3000–99999 μm	60 ± 8	
OT(V)	0–15 μm	0 ±	
	15–30 μm	75 ±	
	30–1000 μm	100 ± 0.3	
	1000–6000 μm	100 ± 0.4	
	6000–99999 μm	94 ± 5	
OT(H)	0–3 μm	0 ±	
	3–10 μm	75 ±	
	10–300 μm	100 ± 0.6	
	300–6000 μm	100 ± 0.6	
	6000–99999 μm	91 ± 9	

given by

$$\begin{aligned}
\Delta\theta_{\perp c} &= 0.02\tan\theta + 0.024 \\
\Delta\theta_{\parallel c} &= 0.2\tan\theta + 0.024
\end{aligned}$$

where θ is the azimuthal angle of the decay track, $\Delta\theta_{\perp c}$ is the critical angle perpendicular to the projected direction of the track and $\Delta\theta_{\parallel c}$ is the critical angle in the same direction as the track projection. If the decay length is less than 125 μm then the critical angles are given by

$$\begin{aligned}
\Delta\theta_{\perp c} &= 0.02\tan\theta + \frac{3}{l} \\
\Delta\theta_{\parallel c} &= 0.15\frac{165}{l}\tan\theta + \frac{3}{l}
\end{aligned}$$

where l is the "visible" decay length of the track or, in other words the total path length in the emulsion, ignoring any distance travelled in the plastic sheet.

Horizontal Emulsion

When searching for kinks in the horizontal emulsion only the projection of the track in the Y-Z plane is used, and if the kink occurs entirely in the X-Z plane it will be difficult to see. The reason for this difficulty is due to the fact that the plane of the emulsion plates is in the Y-Z plane and the X-Z plane is "observed" by moving in depth through the emulsion. For the efficiency calculation it will be assumed that such a kink would not be seen. This will not affect the calculation much since most kinks are observable in both planes.

The kink efficiency is calculated differently for kinks very close to the primary vertex (within 20 μm) and for those far away [45]. For kinks close to the primary vertex, the efficiency depends on the product $l \cdot \Delta\theta$, where l is the decay length and $\Delta\theta$ is the kink angle. The efficiency as a function of this product is shown in Figure 37.

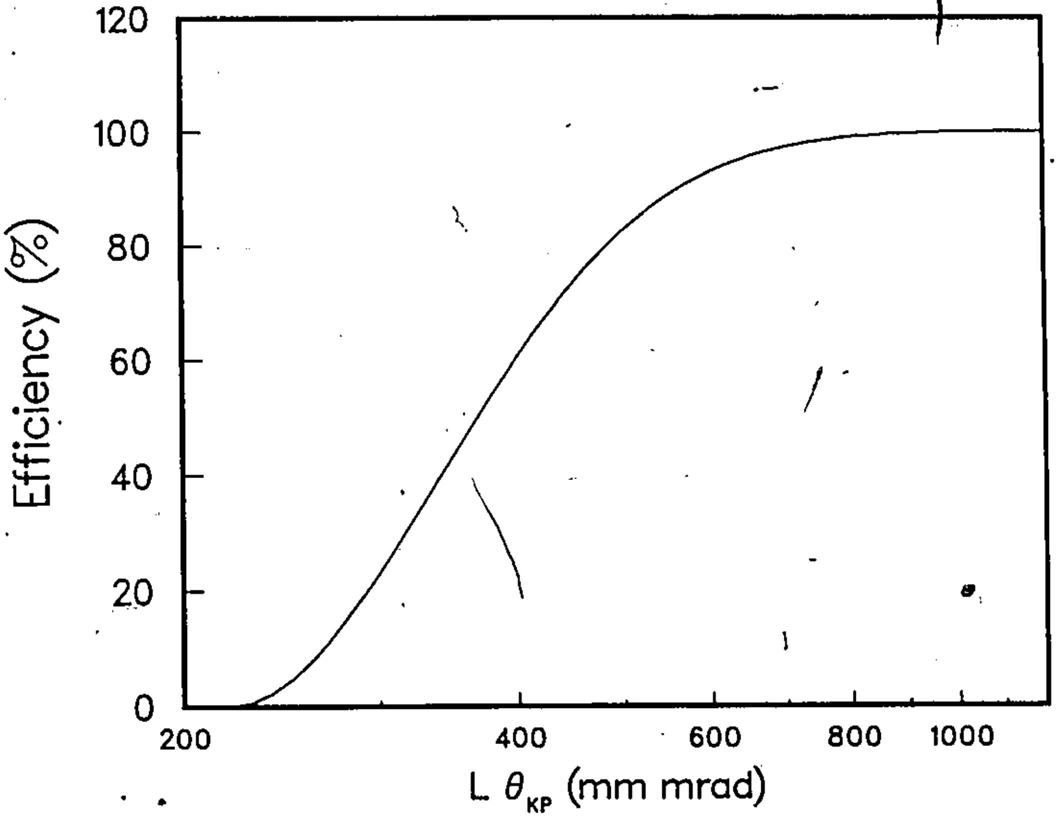

Figure 37: Kink finding efficiency for short decays.

For decays greater than 20 μm , the efficiency for detecting kinks is independent of the decay length. As long as the observed kink angle is greater than one degree (0.017 radians), it will be tagged as a kink. Because of fluctuations in the measurement of an angle, it is possible to tag an event with a kink angle less than 0.017 and miss one with an an angle larger than this. Ideally the efficiency would be zero up to 0.017 radians and 100 %for larger angles, but because of the measurement fluctuation there is, however, a much smoother transition as shown in Figure 38; the efficiency is not zero below 0.017 radians, and less than 100% just above.

Kink Efficiency as a Function of Decay Length

By using the data from the multiprong charmed-particle decays, it is possible to calculate the kink-finding efficiency as a function of only the decay length. In order to get an efficiency dependent on the decay length, the decaying-particle angle and kink-angle dependence have to be integrated out. The following assumptions were made: the angular distribution of the decaying particle is the same for the multiprong and single prong decays, the kink-angle distribution is the same as the distribution of the angles the decay tracks, from multiprong decays, make with the decaying-particle direction. By using the data from multiprong decays and integrating over the decaying-particle angular distribution and the kink angle, an efficiency dependent only on the decay length was obtained. This efficiency was then combined with the scanback and followdown efficiencies to get an overall kink-finding efficiency as shown in Table 16.

4.3 Log Likelihood Method

The lifetimes of the charmed-particles species were determined using the method of maximum likelihood [46]. The maximum likelihood method was used since it is one of the most powerful methods for determining unknown parameters. In order to use the maximum likelihood method the probability of observing a decay has to

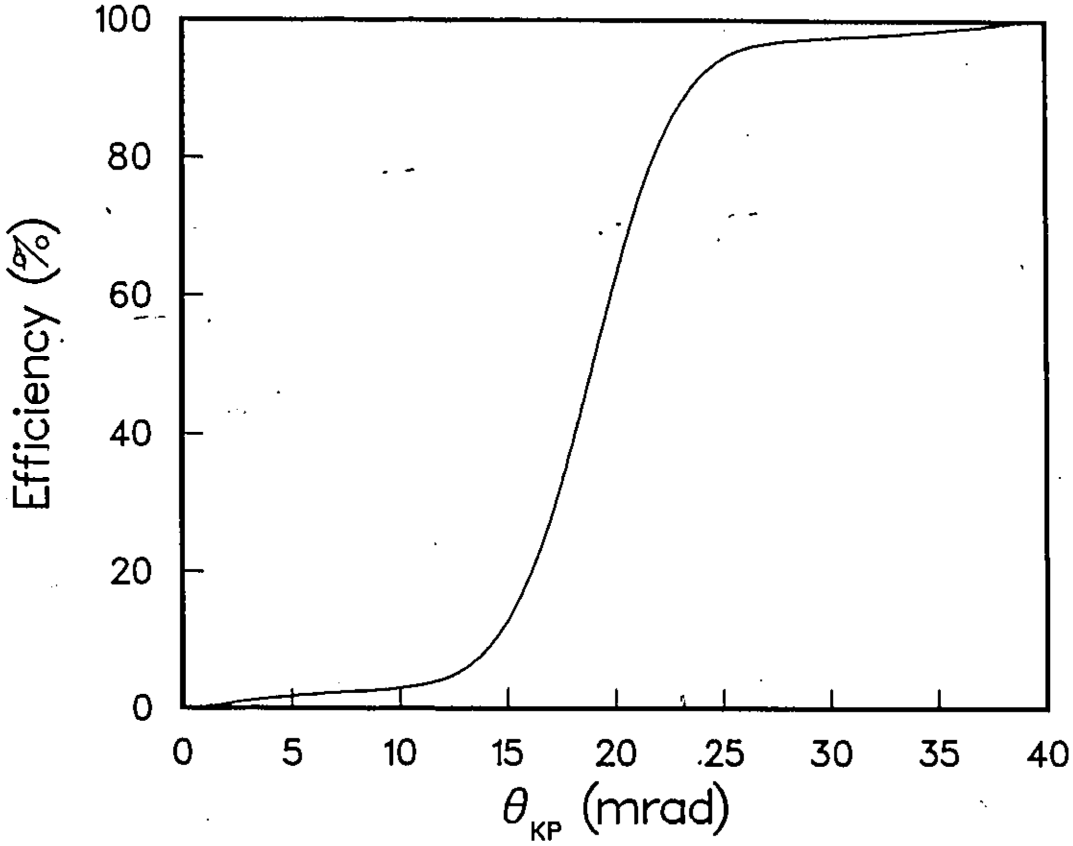

Figure 38: Kink finding efficiency for long decays.

Table 16: Kink Finding Efficiency

Emulsion Type	Region	Efficiency(%)
Vertical	0–25 μm	0
	25–30 μm	41
	30–35 μm	55
	35–55 μm	66
	55–85 μm	77
	85–185 μm	86
	185–1000 μm	91
	1000–6000 μm	90
	6000–99999 μm	81
Horizontal	0–5 μm	0
	5–10 μm	41
	10–15 μm	74
	15–20 μm	83
	20–300 μm	87
	300–6000 μm	87
	6000–99999 μm	53

be calculated. The probability density function (p.d.f.) is given by:

$$\text{p.d.f.}(t_i : \tau) = \frac{1}{\tau}e^{-t_i/\tau}$$

and is the probability that a particle with a lifetime τ will be seen to decay with a measured lifetime of t_i. Because, the efficiency for finding decays is not 100%, the p.d.f. will be modified to

$$\text{p.d.f.}(t_i : \tau) = \frac{1}{\tau}\frac{\varepsilon(l_i)e^{-t_i/\tau}}{A(P_i, \tau)}$$

where $\varepsilon(l_i)$ is the decay finding efficiency as a function of the decay length of the ith particle, and $A(P_i, \tau)$ is a normalization factor which depends on the charm momentum (P_i) and lifetime. $A(P_i, \tau)$ is given by:

$$A(P_i, \tau) = \int_0^\infty \frac{1}{\tau}\varepsilon(z(t))e^{-t/\tau}dt$$

$$z(t) = \beta\gamma ct = \frac{P_i}{m_i}ct$$

It is not possible to observe a particle decay very close to the primary vertex, because there are a number of tracks and it gets very confusing. It is also not possible to observe decays outside the emulsion (in theory it would be possible to see them in the drift chambers, but in practice a search was not done). Thus the efficiency is zero very close to the primary vertex and also outside the emulsion. This will modify the normalization factor, giving

$$A(P_i, \tau) = \int_{l_{sc}}^{l_{pp}} \frac{1}{\tau}\varepsilon(z(t))e^{-t/\tau}dt$$

where l_{sc} is the short distance cut-off (shortest decay length that is observable), and l_{pp} is the potential path (distance from from primary vertex to the end of the emulsion, in the direction of the charmed particle).

Given a total of N decays the likelihood function for all the decays is given by

$$\begin{aligned} L(\tau) &= \prod_{i=1}^{N} \text{p.d.f.}(t_i : \tau) \\ &= \prod_{i=1}^{N} \frac{1}{\tau}\frac{\varepsilon(l_i)e^{-t_i/\tau}}{A(P_i, \tau)} \end{aligned}$$

The best estimate for the particle lifetime is then the value of τ which maximizes the likelihood function.

For computational purposes it is easier to maximize the log of the likelihood function since the product now becomes a sum. The function that has to be maximized is now

$$\ln(L(\tau)) = \sum_{i=1}^{N} \left\{ \ln(\varepsilon(l_i)) - A(P_i, \tau) - \frac{t_i}{\tau} \right\}$$

The maximization of this formula is quite straight forward on a computer, the value of the log of the likelihood function is calculated as a function of the lifetime (τ) and the maximum value found. The one and two standard deviation (S.D.) limits are at the points where

$$\begin{aligned} L(\tau) &= L(\tau_{\max})e^{-1/2} \\ L(\tau) &= L(\tau_{\max})e^{-2} \end{aligned}$$

respectively. Thus, the 1 and 2 S.D. values correspond to the points where the maximum of the log likelihood function has been reduced by 0.5 and 2.0, respectively.

4.4 Neutral Decays

A total of 75 neutral decays were found (after the Z cut) in the emulsion fiducial volume, and they were all analyzed as previously described. These 75 events were comprised of 58 events that could be fitted to a D^0, and 15 events that could be fitted to a K_s^0 or Λ^0. The remaining two events could not be fitted to any known particles. However, from the P_T balance or some other argument, it was known these two decays were not strange particles. One of the events was considered to be an unfittable D^0 events; the other event had an identified proton as a decay product and was considered to be a neutral-charmed baryon, and is discussed in more detail in reference [11]. These two "unfittable" events were used for the charm production rate calculations, but were ignored when calculating the D^0 lifetime.

The 15 strange particles were all V decays and were comprised of 6 K_s^0, 8 Λ^0, and 1 event that could be either a K_s^0 or Λ^0. Using the same method as was used

Table 17: Neutral-Particle Decays

	Run 1	Run 2	Total
2-prong	10	26	36
4-prong	7	13	20
6-prong	2	0	2

to estimate the charm-finding efficiencies (Sec. 4.2.1), the strange particle finding efficiency was estimated to be 27%. Because of some doubt whether or not the efficiency calculation is valid when the efficiency is not close to 1, the efficiency was also calculated using a Monte Carlo method. A fairly simple Monte Carlo was written which generated strange particles with the momentum spectrum observed by a bubble chamber experiment [47]. The strange particle production rates used were those of reference [48] and [49]. The particles are allowed to decay using an exponential form and the tracks reconstructed randomly in the drift chambers using an 80% efficiency. Because strange particles have a long lifetime ($\sim 10^{-10}$ sec.), only low momentum particles decay in the emulsion (distorting the observed spectrum noticeably), and thus very few tracks pass the scanning criteria. The final finding efficiency is estimated to be 35% fairly close to that calculated above. A total of 470 K_s^0 and Λ^0 were expected to be produced, and of these 320 were expected to decay into V's. Sixty-two strange decays are expected to be "observable" in the emulsion and 22 decays should be found. This agrees very closely with the 24 strange decays found in all events, charmed and uncharmed.

The 58 D^0 decay candidates included 36 two-prong, 20 four-prong and two six-prong decays. The individual numbers for the first and second runs are shown in table 17. Forty-two of these decays had a fit with a confidence level greater than 1% and were thus classified as constrained. If there was more than one acceptable fit, the decay hypothesis to be used was chosen on the basis of the relative fit confidence level for the hypotheses and the number of neutrals (the events with the lowest number of neutrals were always used). If both Cabibbo-favored and -unfavored hypotheses were possible the Cabibbo-favored hypotheses were kept, since experimentally Cabibbo-favored decays are about 20 times more likely than unfavored decays [19]. If it was not possible to pick one hypothesis over another, all equally valid hypotheses were kept and given equal weights in the lifetime calculations. For the remaining sixteen unconstrained events, all Cabibbo favored hypotheses with an unobservable neutral particle, a minimum invariant mass consistent with a D^0, and track IDs consistent with the spectrometer information were used. In all but two cases the various hypotheses had equal weights, the exceptions were two events in which the different hypotheses were weighted according to their relative time-of-flight (TOF) confidence levels. For most of the unconstrained hypotheses two D^0 momentum solutions were possible. In some cases one solution could be eliminated because no neutral was seen at the predicted position. If neither solution could be eliminated, both were weighted equally.

An additional fitting constraint that was used for the D^0 events was a fit to the decay of the $D^{*\pm}$. The $D^{*\pm}$ decays into a $D^0/\bar{D}^0$ and a charged pion $49 \pm 8\%$ of the time. Figure 39 shows the difference between the invariant mass of the $D^0\pi^+$ ($\bar{D}^0\pi^-$) and the D^0using all our D^0 candidates, most of the mass combinations are off scale, and there is a peak at 145 ± 1 MeV/c^2, which agrees with the accepted $D^{*+} - D^0$ mass difference [19]. There is very little background (in fact the two event at about 155 MeV/c^2 are possibly a couple of D^{*+} but we were unable to fit them as such), and thus the $D^{*\pm}$ mass is a very good constraint.

Initially 38 events were classified as being constrained, leaving twenty unconstrained events. With the D^{*+} constraint the number of unconstrained events was reduced from twenty to sixteen, and the number of constrained events increased to 42. The 38 constrained D^0's had a weighted average mass of 1865 ± 6 MeV/c^2.

4.5 D^0 Lifetime Calculation

The D^0 lifetime was calculated using the maximum-likelihood estimattion method. Using the 58 events a lifetime of $4.3^{+0.7}_{-0.5}\,^{+0.1}_{-0.2} \times 10^{-13}$ seconds was determined [42,50,51]. The first error is a statistical error and the second error is a systematic error. The

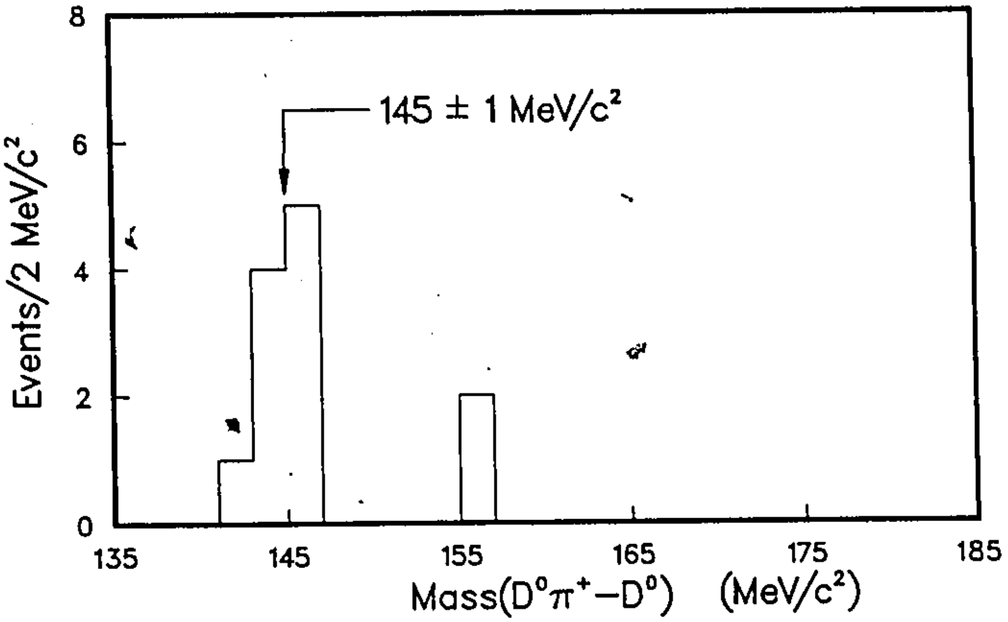

Figure 39: $D^0\pi^+$ ($\bar{D}^0\pi^-$) and D^0 invariant mass difference.

statistical error was obtained by checking at which values the log likelihood has been reduced by 0.5; the systematic error was obtained by varying the finding efficiencies, and by studying the effect of adding a second neutral (using a Monte Carlo method) to the unconstrained events. The differential decay-time distribution (dN/dt) is shown in Figure 40, where each event has been given a weight which was based on the short- and long-distance cutoffs, the finding efficiency, and the hypotheses weight.

A study was done of the possible lifetime measurement shift due to the association of a wrong π^0 with the charmed-particle decay, resulting in a wrong D^0 momentum solution. It was estimated that a constrained fit was obtained using a wrong π^0 in about 4% of the time, and resulted in a shift of less than 1% for the measured lifetime. These numbers were obtained by using the gammas from one event and the charged and charmed particles from another and then checking to see how often a good constrained fit was obtained.

When we first published the D^0 lifetime, we had three semileptonic decays which had a lifetime three times longer than the lifetime using the hadronic decays. These events were unconstrained (because of the missing neutrino) and their momenta were uncertain up to a factor of 2. It was also possible that the D^0 sample contained some contamination from some other neutral particle, and so it was decided to use only the hadronic decays for the lifetime measurement. With the inclusion of the second run data the lifetime of the semileptonic decays was calculated to be $4.9^{+2.9}_{-1.6} \times 10^{-13}$ seconds, in excellent agreement with the lifetime of the hadronic decays, and so the final calculated lifetime contains all the D^0 candidates.

4.6 Charged Particles Decays

A total of 62 charged-particle decay candidates were found in the emulsion. In a procedure similar to that used for the neutral events kinematic fits were tried for all the Cabibbo-favored and singly Cabibbo-unfavored decay modes of the $D_s^\pm$, $D^\pm$, and Λ_c^+. The filtering of the final fits was done slightly differently from that done for the neutral events. As for the neutral particles the filtering of the constrained fits

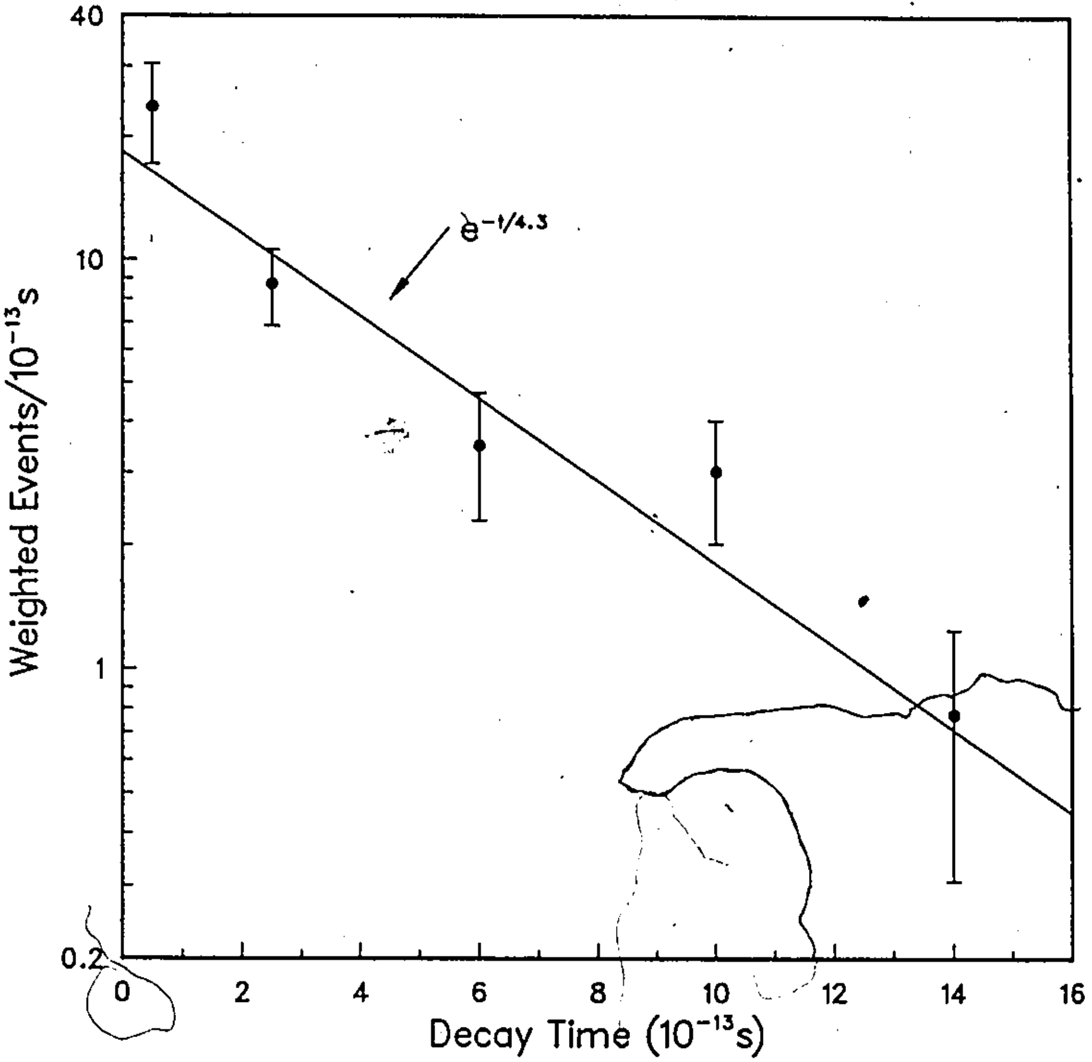

Figure 40: dN/dt for D^0 decays.

was done using the charmed-particle mass, the confidence level, and the quality and quantity of the neutrals used. For each charmed-particle species the best possible constrained fit was kept; in those cases where both Cabibbo-favored and -unfavored decays were possible, only the Cabibbo favored decay was kept. Thus it was possible in one event to have a Cabibbo-favored D^{+} decay and a Cabibbo-unfavored D_s^{+} decay. If only unconstrained events were possible then only Cabibbo-favored decays consistent with an unobservable neutral were kept. The fits for the various charmed-particle species had to be all constrained or all unconstrained.

Fourteen (5 kinks, 9 tridents) of the 62 charged-particle decay candidates could not be fitted to any charmed particles. These "unfittable" events had very poorly constrained fits, the kink events did not have any good constrained fits, or the decay was underconstrained (more unknowns than constraints). The remaining 48 decays (7 kinks and 41 tridents) were divided up as follows: 6 decays were fitted as $D_s^{\pm}$, 13 as Λ_c^{+}, 1 decay was fitted as a D^{-}, 27 decays were ambiguous among $D^{\pm}$, $D_s^{\pm}$, and Λ_c^{+}, and one decay was ambiguous among D_s^{+} and Λ_c^{+}.

4.6.1 The $D_s^{\pm}$ and Λ_c^{+} Lifetimes

Using the maximum-likelihood estimation method the $D_s^{\pm}$ was calculated to have a lifetime of $2.6^{+1.6}_{-0.9} \times 10^{-13}$ seconds [42,52,53]. To ensure that there were no biases in the lifetime calculation only the 6 events fitted as an $D_s^{\pm}$ were used in the calculation. These six events had a weighted average mass of 1980 ± 15 MeV/c^2.

The Λ_c^{+} lifetime was calculated using only the 13 events that were fitted to a Λ_c^{+}. All the Λ_c^{+} events had an identified proton in the final state; this meant that a proton was identified as coming from the charged-particle decay, or from a Λ^0 which appeared to come from the decay. The final lifetime was found to be $2.0^{+0.7}_{-0.5} \times 10^{-13}$ seconds [42,52,53], and the eight fully constrained decays were found to have an average mass of 2266 ± 13 MeV/c^2. Including the ambiguous D_s^{+}–Λ_c^{+} event had very little effect on either lifetime.

4.6.2 The $D^{\pm}$ Lifetime

The 28 remaining decays were all consistent with a $D^{\pm}$ hypothesis and the majority of them were probably $D^{\pm}$. However, the $D_s^{\pm}$ and Λ_c^{+} hypotheses could not be eliminated from most of the decays, and thus it was not possible to obtain a pure $D^{\pm}$ sample. Making the assumption that all these decays were $D^{\pm}$ and using the maximum-likelihood, estimation method a lifetime of $9.4^{+2.4}_{-1.8} \times 10^{-13}$ seconds was obtained. Thus, the $D^{\pm}$ lifetime is much longer than the $D_s^{\pm}$ and Λ_c^{+} lifetimes. The average mass of all the constrained fits is 1882 ± 12 MeV/c^2.

In order to calculate the $D^{\pm}$ lifetime correctly the $D_s^{\pm}$ and Λ_c^{+} "contamination" has to be corrected for. Because the $D^{\pm}$ has a lifetime that seems to be so much longer than the short lived contamination, it is possible to correct for this using a two parameter fit. The $D^{\pm}$ lifetime can be calculated using a two-dimensional likelihood function given by

$$L(\tau, f) = \prod_{i=1}^{N} \left[f \frac{1}{\tau} \frac{\varepsilon(l_i) e^{-t_i^{D^{\pm}}/\tau}}{A(P_i, \tau)} + (1-f) \frac{1}{\tau_X} \frac{\varepsilon(l_i) e^{-t_i^{X}/\tau_X}}{A_X(P_i, \tau_X)} \right]$$

where f is the fraction of the events that are $D^{\pm}$, $t_i^{D^{\pm}}$ is the measured lifetimes for the $D^{\pm}$, t_i^{X} is the average measured lifetimes for the $D_s^{\pm}$and Λ_c^{+}solutions, τ_X is the average of the measured $D_s^{\pm}$and Λ_c^{+}lifetimes ($2.1 \pm 0.5 \times 10^{-13}$ sec.), the A's are normalization factors, and the ε efficiencies.

Using the above likelihood function it was determined that the $D^{\pm}$ has a lifetime of $11.1^{+4.4}_{-2.9} \times 10^{-13}$ seconds and there was a short lived contamination of $4.8^{+5.0}_{-5.6}$ events in the 28 ambiguous decays [42,52,53]. Figure 41 shows the weighted differential lifetime (dN/dt) plot. Each decay had a weight based on the cutoff distances, finding efficiency, and hypothesis weight. The solid curve corresponds to the results of the two-parameter fit and the dashed curve is for the one-parameter fit. Both curves appear to be equally valid, but the two-parameter fit reflects more accurately the effect of the short lived contamination.

Table 18 summarizes all the charmed-particles lifetime results. All these results are in excellent agreement with the results of the Tagged Photon Spectrometer Collaboration which are also shown in Table 18. This is a very recent experiment

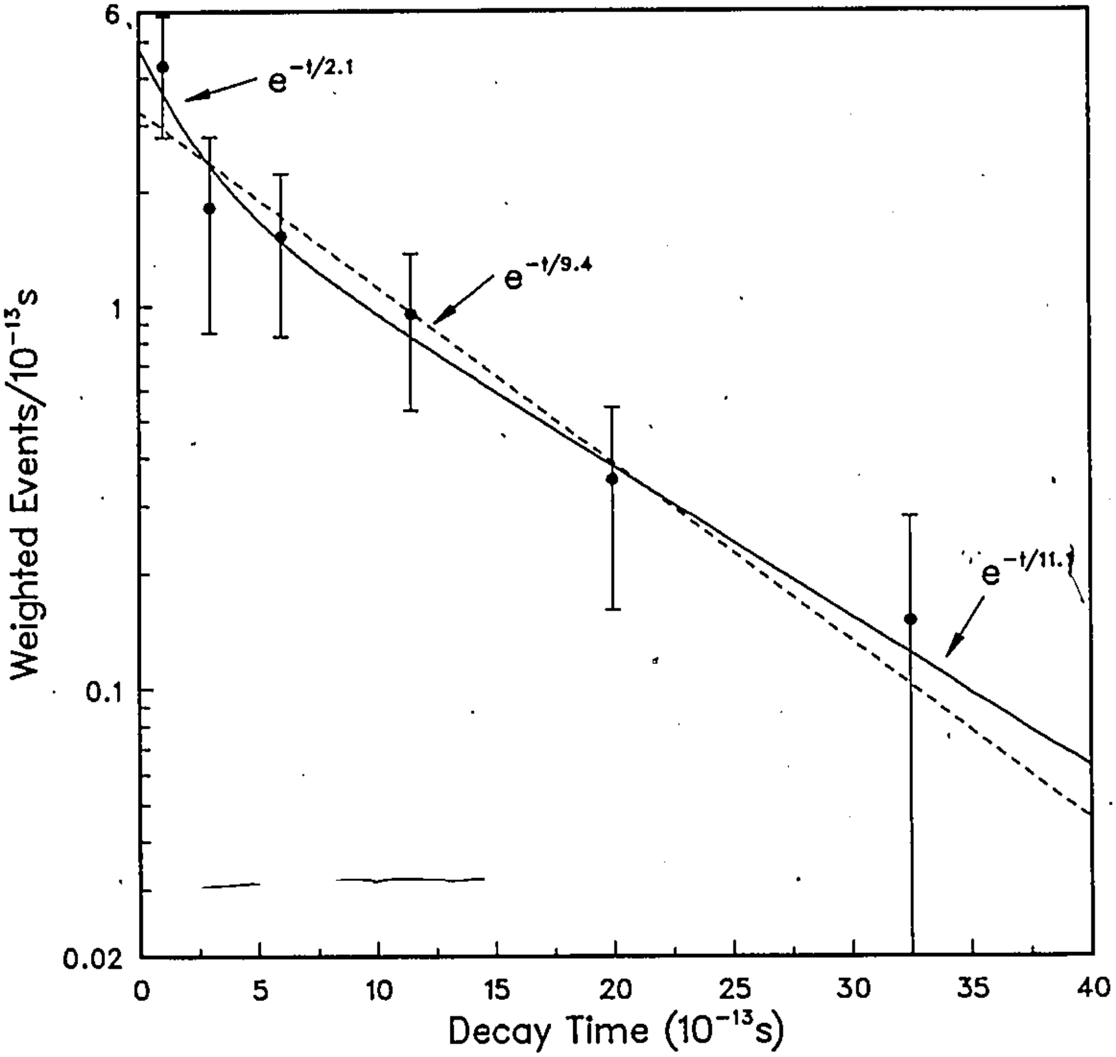

Figure 41: dN/dt For Ambiguous Events.

Table 18: Charmed-Particles Lifetimes

Particle	Lifetime ($\times 10^{-13}$ seconds) E-531	TPS	Ref.
D^0	$4.3^{+0.7}_{-0.5}{}^{+0.1}_{-0.2}$	$4.35 \pm 0.15 \pm 0.10$	[54]
$D_s^\pm$	$2.6^{+1.6}_{-0.9}$	$4.8^{+0.6}_{-0.5} \pm 0.2$	[55]
Λ_c^+	$2.0^{+0.7}_{-0.5}$	$2.0^{+0.5}_{-0.4} \pm 0.3$	[56]
$D^\pm$	$11.1^{+4.4}_{-2.9}$	$10.6 \pm 0.5 \pm 0.3$	[54]

that has the largest statistics of all the charm-lifetime experiments; for other recent experiments see Ref. [57].

4.7 Semileptonic Decay Rates

Using the above results the ratio of the $D^\pm$ to D^0 lifetimes is $2.6^{+1.1}_{-0.8}$. This ratio was found using a two-parameter likelihood function, the two parameters being the two lifetimes. A two-parameter fit was used to ensure that the uncertainty in the ratio was calculated correctly, since it did not make any difference to the value calculated whether a two-parameter fit was used or a straight ratio taken. The ratio is not equal to 1.0, as was expected from the spectator model, and this model is not correct. This ratio is in excellent agreement with Mark III who measured the lifetime ratio using the ratios of the semileptonic branching ratios and they found [58] $\tau^+/\tau^0 = 2.3^{+0.5-0.1}_{-0.4-0.1}$.

As was discussed in Section 1.4, the semileptonic decay rates of the various charmed particles should still be equal. Using the electron semileptonic branching ratios for the $D^\pm$ and D^0[58] and the Λ_c^+[59] and our measured lifetimes, the following semileptonic decay rates were calculated

$$\begin{aligned} \Gamma(D^0/\bar{D}^0 \rightarrow e^\pm X) &= (1.7 \pm 0.5) \times 10^{11}\ \mathrm{s}^{-1} \\ \Gamma(D^\pm \rightarrow e^\pm X) &= (1.5^{+0.4}_{-0.6}) \times 10^{11}\ \mathrm{s}^{-1} \end{aligned}$$

$$\Gamma(\Lambda_c^+ \to e^+X) \ = \ (2.3^{+1.0}_{-1.2}) \times 10^{11}\ \mathrm{s}^{-1}$$

The three rates all agree with each other within their uncertainties as was expected, indicating that the W-boson radiation contributes equally to the three decay rates.

The D^0 is believed to have a shorter lifetime than the $D^\pm$ because the W-exchange process is non-negligible. Recently the $D^0 \to \bar{K}^0\phi$ branching ratio was measured to be $(0.99 \pm 0.32 \pm 0.17)\%$ [60]; Mark III also measured this branching ratio [61] and obtained a comparable number (with larger errors), and the also measured the branching ratio for $D^0 \to \bar{K}^0K^+K^-_{\mathrm{non}-\bar{K}^0\phi}$ to be $(1.1^{+0.4+0.3}_{-0.3-0.2})\%$. Both these rates are much larger than would have been expected if the W-exchange process was negligible. Thus, it appears that the idea that the W-exchange process is non-negligible is valid.

4.8 Charmed-Particles Weight

The charmed particles are all assigned a weight that is inversely proportional to the probability that the decay would have been found. This probability is equal to the efficiency for finding the particle decay given its momentum, direction and measured decay time, as well as the short and long distance cutoffs. This efficiency factor was actually given by the normalization constant from the likelihood function and is

$$\epsilon = \int_{t_{sc}}^{t_{pp}} \frac{1}{\tau}\varepsilon(z(t))\mathrm{e}^{-\frac{t}{\tau}}dt$$

Each event is then given a weight given by:

$$W = \frac{1}{\epsilon}$$

The D^0 events are also given an extra weight of $1/(1\text{-}B_0)$ where $B_0 = 9.1 \pm 1.9\%$ and is the branching ratio for D^0 into all neutral hadrons [62], since these events would not be found by our experiment.

The charm kink candidates also had an extra weight to account for those events lost due to the 400 MeV/c P_T cut. A small Monte Carlo program was used, which generated a number of random charmed particle and allowed them to decay and then checked to see how many charmed particles passed the P_T cut. Each event was then given a extra 'kink weight' which depended on particle momentum, decay hypotheses, and which type of emulsion module (horizontal or vertical) it was in. The average kink weight was about 2.

Chapter 5

Studying Neutrino Interactions

In order to fully understand the behavior of the spectrometer and all the efficiencies, a Monte Carlo was written which simulated the response of the spectrometer to various types of interactions. This Monte Carlo was used to calculate the triggering and reconstruction efficiencies of the spectrometer. Two different Monte Carlos were used for the first and second run. The first run Monte Carlo is described in reference [10], while the second run Monte Carlo is described below. The two programs gave similar results under the first run conditions, the main difference between the two was the neutrino energy spectra that were used. The various finding and triggering efficiencies were the same for the two Monte Carlos.

5.1 Monte Carlo of Experiment

As has already been mentioned a Monte Carlo program which generated the expected neutrino energy spectrum was written. The generated spectra were then used to randomly generate the type and energy of an incoming neutrino. The quark-lepton interaction was then generated using the Monte Carlo program LEPTO[1], version 4.3, and the final quark fragmentation was done using Lund Monte Carlo

---

[1] A series of routines which randomly generated the Bjorken-x and y of a neutrino interaction, and initialised a number of variables which were then used by the Lund Monte Carlo. These routines were written by Gunnar Ingelman of DESY

routines [63]. The produced particles were then tracked through the entire spectrometer and allowed to interact in the various detectors. The response of the different detectors was also checked.

5.1.1 The Neutrino Interactions

The energy of the incoming neutrino was generated using the Monte Carlo predicted interaction spectra. These spectra were obtained using the results of the neutrino-beam Monte Carlo program (Section 2.1) which gave a prediction for the neutrino energy spectrum ($N(E_\nu)_{\text{energy}}$). The interaction spectra were obtained by

$$
\begin{aligned}
N(E_\nu)_{\text{interaction}} &= 0.67 \cdot E_\nu \cdot N(E_\nu)_{\text{energy}} \\
N(E_{\bar{\nu}})_{\text{interaction}} &= 0.34 \cdot E_{\bar{\nu}} \cdot N(E_{\bar{\nu}})_{\text{energy}}
\end{aligned}
$$

The multiplication of the energy spectra by $E_\nu(E_{\bar{\nu}})$ results from the total cross-section's linear rise with energy (Section 1.6). The two constants were obtained experimentally [19, page 84]. The relative number of ν_μ, $\bar{\nu}_\mu$, ν_e , and $\bar{\nu}_e$ were predicted by the beam Monte Carlo. The program used a neutral-current to charged-current ratio of 0.30 (0.38) for (anti-) neutrino interactions [65, page 341] when deciding if the interaction was neutral or charged current.

With the neutrino energy determined, the program randomly calculated the Bjorken-x and y of the interaction. The Bjorken-x distribution used for the sea and valence quarks and gluons was that of Glück, Hoffmann, and Reya (GHR) [66]. The y distribution was flat for neutrino interactions and given by $(1-y)^2$ for antineutrino interactions. The program also decided whether the incoming lepton interacted with a neutron or a proton based on the composition of the emulsion (nuclei present), and the relative structure functions of the two nucleons. On average the leptons interacted twice as often with the neutrons as with the protons. This was because the majority of the incoming leptons were neutrinos which will interact with a d quark but not an u quark, the neutron has twice as many d quarks as the proton, and emulsion is approximately an isoscalar target (equal number of neutrons and protons).

Once the neutrino energy, x and y had been chosen, all other relevant variables were then fixed (Section 1.5). Thus, the direction and energy of the scattered lepton and recoiling quark could be determined. All the relevant data were then passed to the Lund Monte Carlo routines which proceeded to do the fragmentation of the scattered quark. The fragmentation procedure is fairly complicated and is described in detail in reference [63].

5.1.2 Particle Tracking

Once all the particles from the neutrino interaction had been determined, the program then followed all the particles (charged and neutral) through the spectrometer. All the charged particles were multiple scattered and their energies decreased due to ionization losses while traversing the solid parts (emulsion, lead sheet, lead glass and steel) of the spectrometer. The charged particles were given a transverse momentum kick of 186 MeV/c when passing through the magnet gap. The program usually checked the response of the various detectors to a single ionizing particle instead of a 'global' response. For example, in the hadron calorimeter the energy deposited by a shower was determined by summing up the effect of the individual tracks in a hadronic shower instead of the simpler procedure of generating a random energy using $\delta E = 1.1\sqrt{E}$.

The interaction lengths of the particles were inversely proportional to their cross sections which were calculated using a GEANT[2] routine [64]. While travelling through all solid parts of the spectrometer, the distance the particle would travel before interacting was randomly calculated using the particle interaction length. The interaction of the particle with part of the spectrometer was 'done' by the TATINA routines, a subset of the GEANT routines. These routines would randomly generate a direction and momentum for particles from the interaction and these particles were then in turn followed through the rest of the spectrometer.

A decay distance was calculated for all unstable particles based on their momentum and lifetime. The lifetimes used were those of the Particle Data Group

---

[2] This is another standard set of CERN Monte Carlo routines used in the study of particle detectors

[19], except for the charmed-particle for which our measured lifetimes were used. If the track was found to decay before interacting, the Lund routines were used to calculate the momentum and direction of the decay products. The Lund routines used branching ratios based on theoretical considerations and, when available, the measured branching ratios from the 1984 Review of Particle Properties [21]. As for interactions, all the decay products were followed through the rest of the spectrometer.

Using the conversion length of photons, the program randomly decided where all the photons converted and then followed the resultant electrons and positrons through the spectrometer. Once a photon had converted in the lead sheet (in front of the lead glass) it was assumed that an electromagnetic shower developed and the number of particles in the shower leaving the lead sheet and entering the lead glass depended on the initial energy and on the total thickness of lead passed through. If the photon did not convert until it entered the lead glass, it was naturally assumed that the shower developed only in the lead glass. The energy resolution was assumed to be given by $0.15\sqrt{E}$ for showers entering the lead glass. Showers which started farther in the lead glass (from unconverted photons entering the lead glass, or from photons from secondary interactions in the lead glass) had a correspondingly poorer resolution. For first run events there was no lead sheet; photons leaving the emulsion would convert only in the lead glass.

The pulse heights of all the particles entering the EPICs and scintillator paddles were randomly generated using the distribution observed experimentally for muons (minimum ionizing particles) in the electromagnetic EPICs. The scintillator distribution was widened to compensate for their poorer resolution. The particles passing through the ionization counters were from the initial neutrino interaction, electromagnetic showers or secondary interactions in the solid parts of the spectrometer.

5.1.3 Event Tagging

The program checked through all the generated events and tagged those that would have triggered the spectrometer. It then checked through all the tracks to see if they were reconstructed, and it was assumed that if at least two tracks were reconstructed one of which was up-down (there had to be at least two up-down in the first run) then the entire event was reconstructed and would be searched for in the emulsion. Next the program checked to see if the primary vertex of an interaction would be found using the measured followback efficiency. The Monte Carlo also checked the efficiency for finding charmed-particle decays (for those in which a charmed particle was produced) to compare with the efficiencies calculated using the data.

5.1.4 Tests of Monte Carlo

To check that the Monte Carlo was working correctly a number of tests were done, in which certain predictions of the Monte Carlo were compared with those observed experimentally. Figure 42 shows the Monte Carlo predicted response of the lead glass to a beam of 30 GeV/c beam of negative particle (pions and electrons). This spectrum should be compared with that of Figure 26, and as can be seen the two distributions have very simialr shapes. The response of the hadron calorimeter to tracks of various energies are shown in Figure 43 which shows a scatter plot of the measured energy of a track versus its momentum. Figure 43(a) shows the prediction of the Monte Carlo (the track momenta were generated randomly between 0 and 20 GeV/c) while Figure 43(b) shows the observed plot. As can be seen the two plots look very similar. Finally, Figure 44 shows the response of the hadron calorimeter to a beam of muons; the solid line corresponds to the Monte Carlo prediction, while the dotted line corresponds to that observed experimentally. The agreement between the two appears to be quite good. Thus, the predictions of the Monte Carlo appear to agree with those observed experimentally.

The only main disagreement between the Monte Carlo and the experimental results are in the finding efficiency. The Monte Carlo predicts that about 97% of the reconstructed events (the exact number depends on the neutrino type) should be found. Experimentally only 82% are found. The experimental inefficiency is due to events whose primary vertex is outside the fiducial volume of the emulsion, but whose predicted position (due to position fluctuations) is inside the fiducial volume. This effect is not included in the Monte Carlo program, which explains

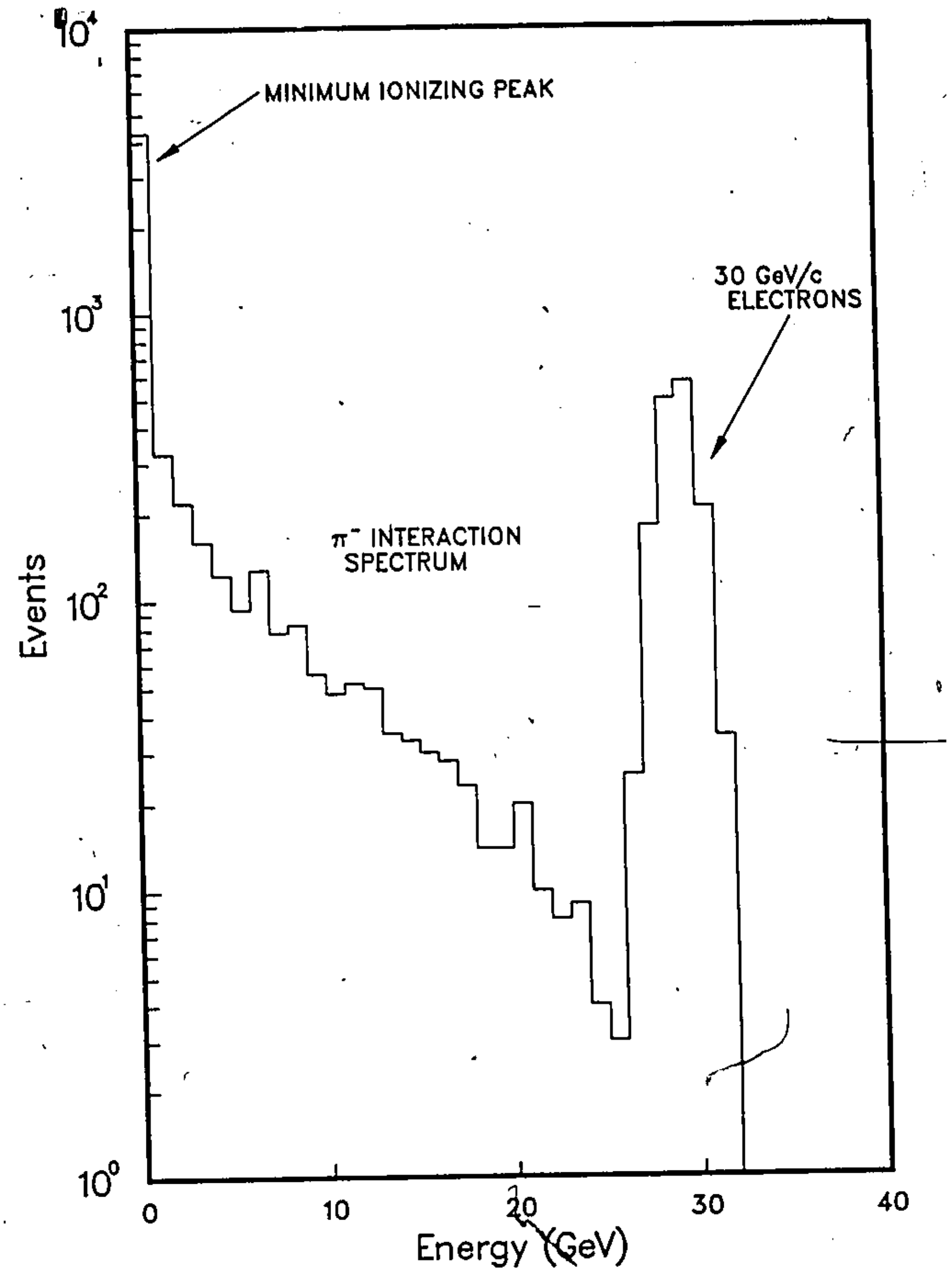

Figure 42: Monte Carlo pulse height spectrum in lead glass.

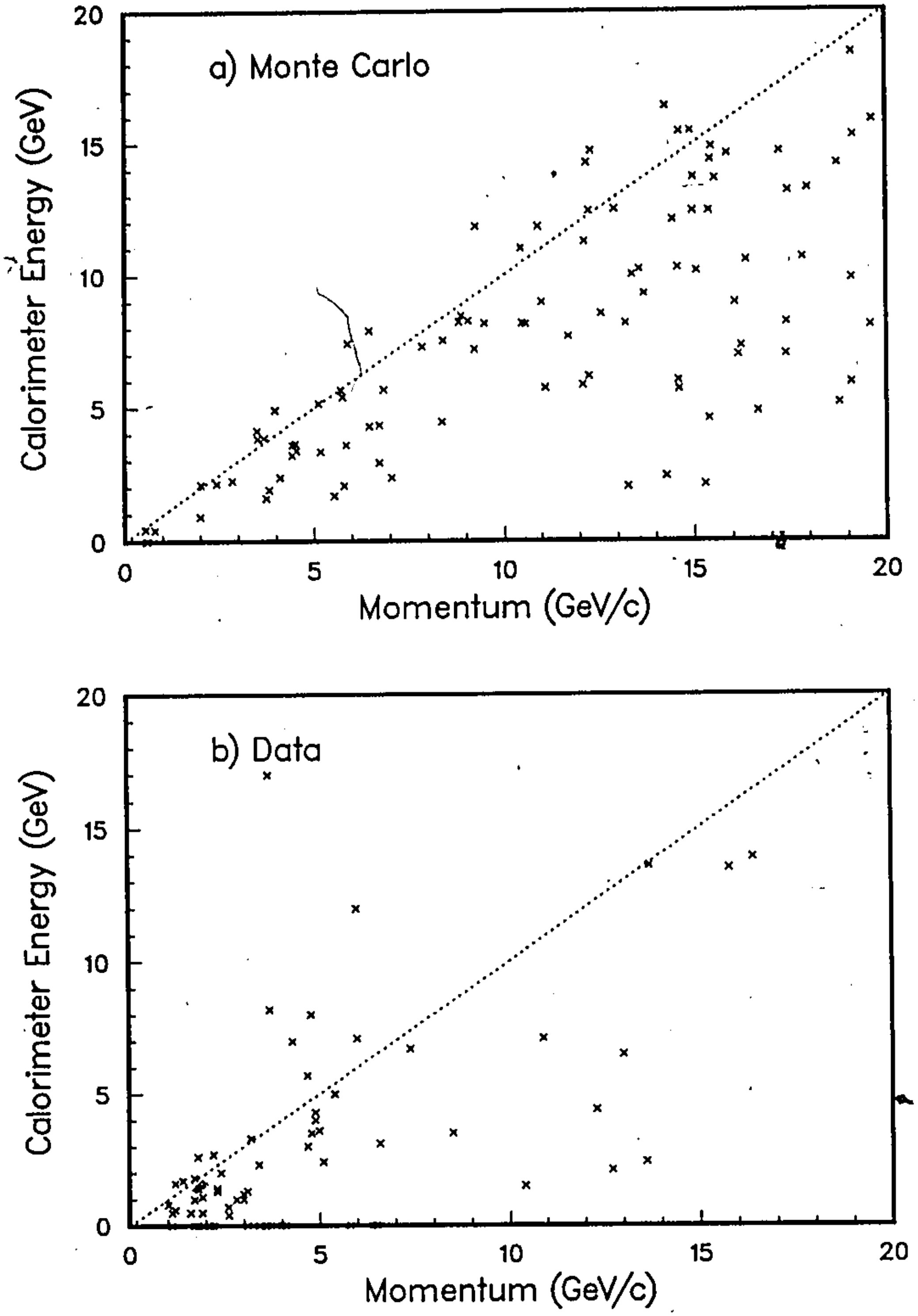

Figure 43: Response of calorimeter to various hadrons.

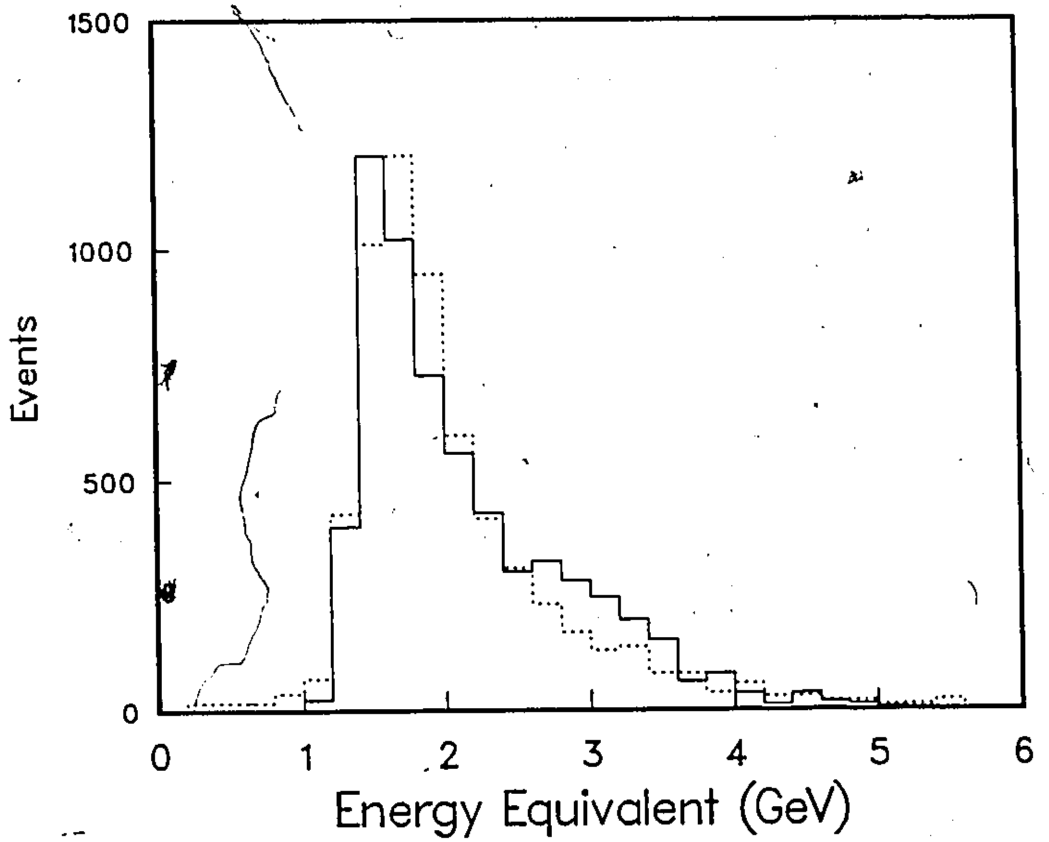

Figure 44: Response of calorimeter to minimum ionizing particles.

the discrepancy. It is assumed that this inefficiency is the same for all events, and since in all cases only efficiency ratios will be important this disagreement can be ignored.

5.1.5 Lund Defaults

The Lund Monte Carlo is a very powerful program and has been tested quite extensively. One of its advantages is the large number of adjustable parameters; these parameters can be modified to optimize the agreement between the Monte Carlo and the experiment. No attempt was made to try and optimize the agreement of the Monte Carlo and experiment for the E-531 Monte Carlo, but some of the default parameters were changed to improve the predictions.

The suppression of s quark pair production compared with u or d quarks (variable PAR(2) in the Monte Carlo) was reduced from 0.3 to 0.2. This was based on the finding of a group that compared the Monte Carlo results with their experimental results [48], and on the recommendation of G. Ingelman[3]. To improve the multiplicities and momentum spectra G. Ingelman also recommended changing the fragmentation 'stopping point' (PAR(23)) from 1.1 to 0.2. Another recommendation was to lower the minimum allowable energy of a colour singlet jet system (PAR(22)) from 1.0 to 0.5. Normally the Monte Carlo had a minimum Q^2 cut of 1.0 GeV/c^2 and a minimum W^2 cut of 5.0 GeV/c^2. However some experimental events had values that were less than these. Thus, to be able to reproduce the experimental results the minimum Q^2 was reduced to 0.1 GeV/c^2 and the minimum W^2 was set to 3.0 GeV/c^2. In order to save running time the Monte Carlo program did not do any first order QCD corrections as these corrections were small and could be safely ignored. All the above changes did not necessarily optimize the Monte Carlo predictions, but for our purposes the agreement was good enough (Section 5.3) since the main purpose of the Monte Carlo was to study the response of the spectrometer.

---

[3] Private communication.

5.2 Visible Energy

In order to calculate the value of the variables that are studied when looking at the charmed-particle production the energy of the incoming neutrino had to be known fairly accurately. There were a number of different ways that the data from the spectrometer could be used to calculate the total energy of the neutrino. Because of the inefficiencies of the spectrometer (and to a small extent its finite size), not all the neutrino energy is 'seen' in the detectors. To a first approximation, the "visible energy" in the spectrometer can be used as the neutrino energy. This energy is the sum of the energies deposited in the calorimeter plus the muon energy (if a muon is present). E_{vis} is defined as

$$E_{\mathrm{vis}} = 0.02 \cdot PH_{EPIC} + E_{\mathrm{PbG}} + E_{\mathrm{HC}} + P_{\mu} - 2.5 \cdot N_{\mathrm{muons}}$$

PH_{EPIC} is the average of the total of the pulse heights seen in each of the three electromagnetic EPIC planes, E_{PbG} is the total energy deposited in the lead glass, E_{HC} is the total energy deposited in the hadron calorimeter, P_{μ} is the sum of the tagged muon momenta, and N_{muons} is the number of tagged MUFB muons. The EPIC pulse height is multiplied by the average energy lost by each electron as it traverses the lead sheet (0.02 GeV). Each muon passing through the spectrometer deposits on average 2.5 GeV in the two calorimeters, and this energy has to be subtracted to ensure that it is not 'double counted'.

5.2.1 E_{vis} and E_{ν} Relationship

E_{vis} is the energy that is used for the calculation of the various variables that are studied when studying non-charmed neutrino interactions. Usually E_{vis} is lower than the true neutrino energy (E_{ν}) and in order to use E_{vis} it needs to be corrected for this difference. The experiment Monte Carlo calculated E_{vis} for all events using the same procedure as was done experimentally and it was, thus, possible to compare the neutrino energy to the visible energy. Figure 45 is a scatter plot of E_{ν} versus E_{vis} for all events with a negative MUFB muon. As can be seen, all the points cluster around a line offset slightly from the line $E_{\mathrm{vis}} = E_{\nu}$. For calculation

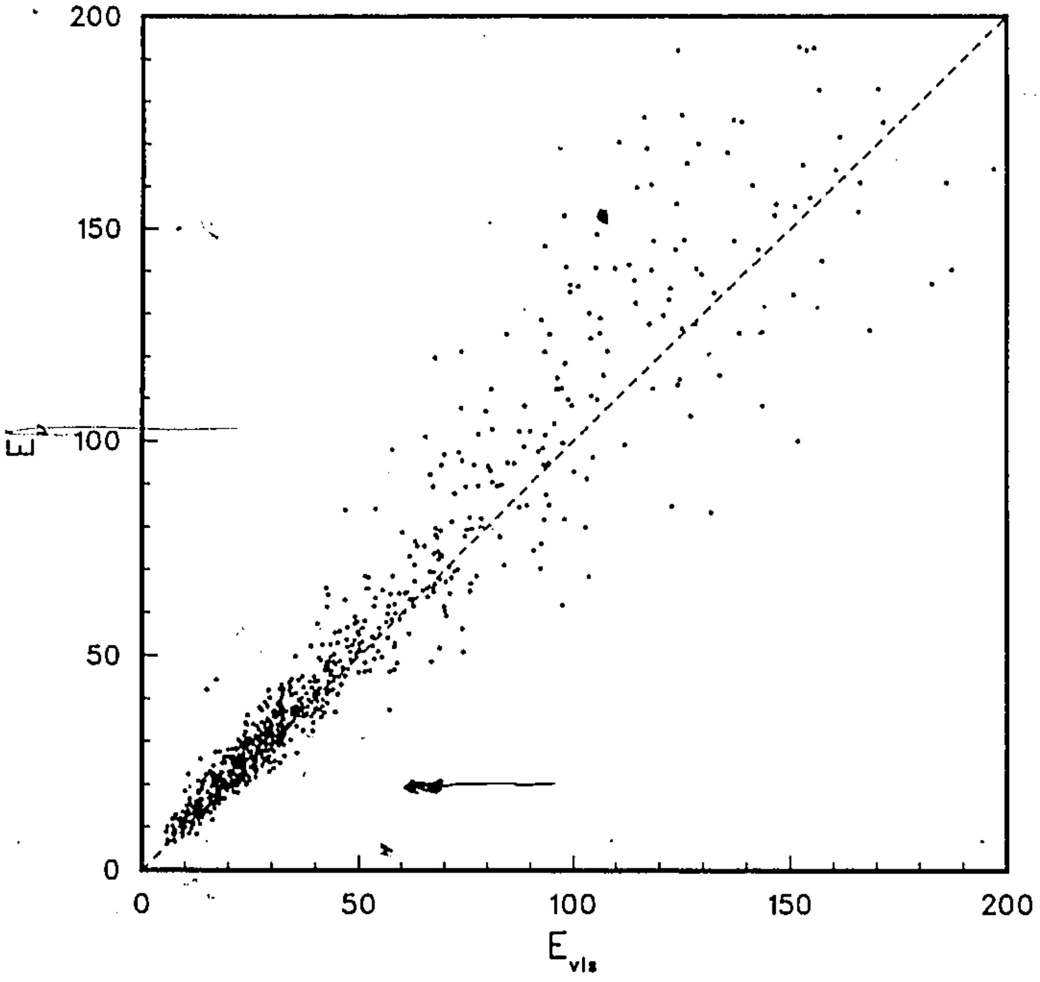

Figure 45: Scatter plot of E_ν versus E_{vis}.

purposes the plot of E_ν/E_{vis} versus E_{vis} (Figure 46) for charged current ν_μ events was used. The rise in the correction factor for the low E_{vis} is due to the large number of particles leaving the sides of the spectrometer. The drop off for large E_{vis} is due to the measurement uncertainty in the muon momenta. The drift chambers actually measure 1/P and thus the errors on all momenta are asymmetric. For most momenta, this asymmetry is not very significant. However, for very large momenta (100 GeV/c), it is important and the measured momenta will tend to be higher than the actual momenta. Events with a large $E_\nu$will obviously have a large muon momentum and the measured momentum will tend to be shifted upwards increasing E_{vis}, and resulting in an E_{vis} larger than E_ν. When computing the various variables of Section 1.5 certain problems are encountered if the neutrino energy is too low compared with the muon energy, and thus when converting E_{vis} to E_ν the neutrino energy was set equal to E_{vis} for large energies. This approximation had very little effect since very few events have large neutrino energies.

Only events with a tagged MUFB muon were considered as charged current interactions. It was estimated that the efficiency for tagging a muon as a MUFB for all found events was 72%. The inefficiency was due to: the muon paddle inefficiencies, the muon track not being reconstructed, the muons having insufficient energy to reach the MUB paddles, or the muons having too large an angle and so unable to hit the MUB paddles. Events with more than one muon of opposite charge could not be used as a charged current interaction since it was not known whether the interaction was due to a ν_μ or a $\bar{\nu}_\mu$. For events with two (or more) muons of the same sign it was assumed that the muon with the larger momentum was the "primary" muon (muon coming from the primary vertex and due to the neutrino), the second muon was then assumed to be due to the decay of a pion or kaon (or charmed particle).

The Monte Carlo also generated plots of E_ν versus E_{vis} for other types of events, such as events with positive MUFB muon and events with no identified muons. The events with a positive MUFB muon were not used for anything because there were very few events when compared with the negative-MUFB-muon events. The energy estimated for the nonidentified-muon events was very uncertain since some

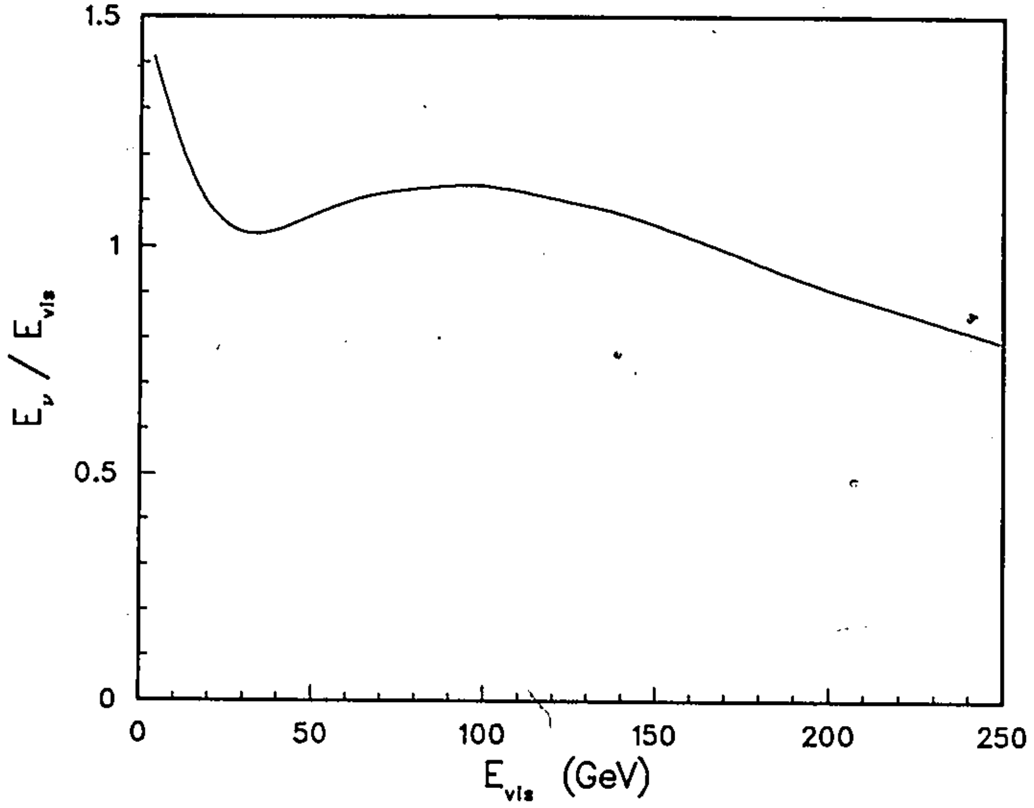

Figure 46: E_ν/E_{vis} versus $E_{\text{vis}}$for charged current ν_μ events.

energy was obviously missing, either due to an untagged muon (which did not deposit much energy in the calorimeters), or a scattered neutrino (from neutral current interactions) which was not observable. The nonidentified-muon events also included some charged current ν_e and $\bar{\nu}_e$ interactions, but it was very difficult (if not impossible) to tag these events as such. The negative MUFB events contained some "contamination" due to neutral current interactions, ν_e /$\bar{\nu}_e$ interactions with a decay resulting in a negative muon, or charged current $\bar{\nu}_\mu$ interactions in which the muon was given the wrong sign. This "contamination" was very small ($\simeq 0.3\%$) and ignored.

5.3 Comparison of Monte Carlo and Data

To check the validity of the Monte Carlo its predictions had to be compared with that observed experimentally. The Monte Carlo was run to generate the plot of the energy correction factor as a function of E_{vis}. The Monte Carlo was then run a second time and the E_{vis} corrected and used to calculate the various variables that are used in the study of neutrino interactions. Distributions of these variables were generated and then compared with that observed experimentally.

A total of 3886 neutrino and antineutrino interactions were found in the fiducial volume of the emulsion. It was not possible to calculate the values of the kinematic variables for all events. It was only for those events with muons of a single sign that all the necessary information was available. Using only the 1870 events that had a single tagged negative MUFB muon (or possibly more but all of the same sign) the values of E_{vis}, Bjorken-x, y, Q^2, and W for the events and Feynman-x for the up-down tracks were calculated and then compared with the Monte Carlo prediction.

The calculated values of E_{vis} have been plotted in Figure 47 for the 1870 events with a single tagged negative MUFB, these events are all assumed to be charged current ν_μ interactions. The actual observed data is histogrammed while the smooth curve is the Monte Carlo prediction, as can be seen the agreement between the two is quite good. The Monte Carlo distribution is slightly narrower than the experimental

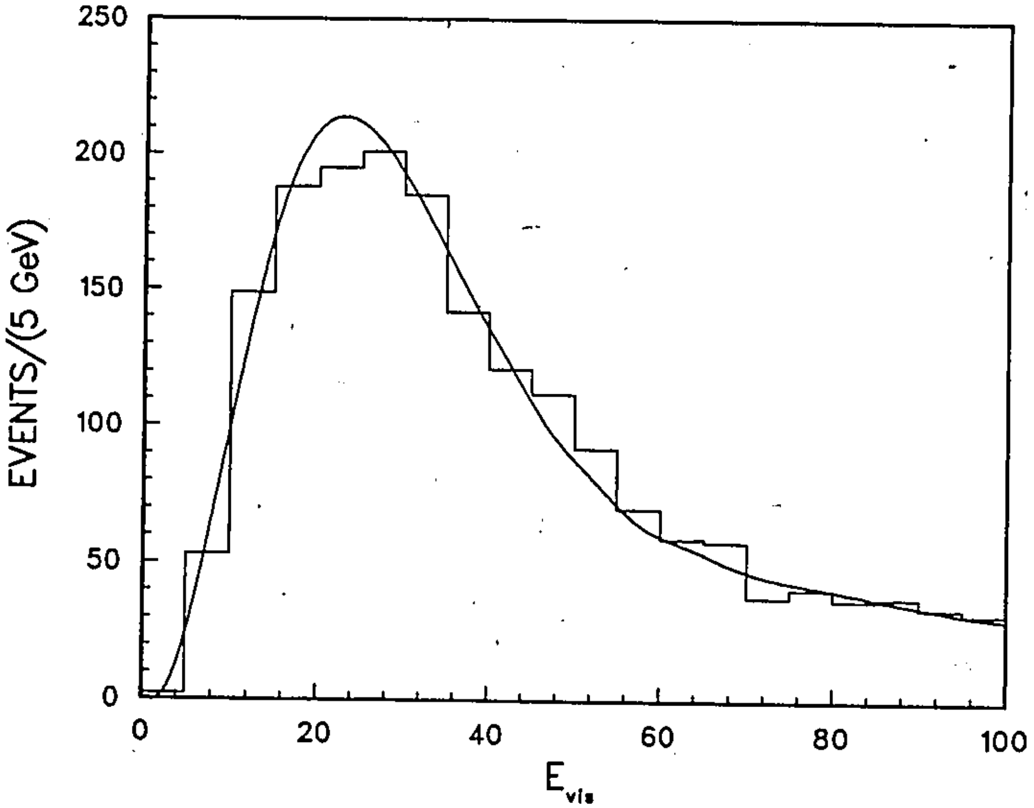

Figure 47: $E_{\mathrm{vis}}$for charged current neutrino interactions.

distribution, but this difference is very slight.

The predicted and measured Bjorken-x distributions are shown in Figure 48, (again the smooth curve is the Monte Carlo prediction). The two distributions are in excellent agreement. The average x value for the data was calculated to be 0.25. Figure 49 shows the y distributions and again the Monte Carlo and data agree very well with each other. The drop of the distribution at a low y is due to inefficiencies in the tagging, reconstruction, and finding of the neutrino interactions since the available energy for hadronic production is low. The drop for large y is because of inefficiencies in the tagging of muons since these muons will have a low energy and miss the muon paddles or have insufficient energy to reach the MUB paddles. The mean value of the y distribution was measured to be 0.44.

Figure 50 shows the distribution of the square of the momentum transfered (Q^2) while Figure 51 shows the invariant mass of the hadrons recoiling against the scattered muon from all tagged charged-current $\nu_\mu$interactions. As can be seen most of the events have $Q^2 > 3.0$ and the Monte Carlo is slightly "unstable" when $Q^2 < 3.0$, however the agreement between the Monte Carlo and the data is still quite good for all Q^2. The Monte Carlo did not generate any events with $Q^2 < 0.1$ (minimum cut), and experimentally there were only about 7 events with Q^2 less than this. The average invariant mass (W) of the charged-current $\nu_\mu$interactions was 5.3 GeV/c^2, and the distribution of the data and Monte Carlo are in good agreement. The W^2 minimum cut used in the Monte Carlo did not have a very large effect since most events had a much larger invariant mass and there was a "natural" minimum W, which was the mass of the nucleon knocked out in the interaction.

5.4 Feynman-x Distribution

Figure 52 shows the Feynman-x distribution for all the reconstructed up-down drift chamber tracks, for the found events, the histogrammed points are the data while the smooth curve is the Monte Carlo prediction. The distribution is very peaked and has a mean of 0.05 and a R.M.S. value of 0.20. The peaked shape occurs because most particles are produced with only a fraction of the available energy

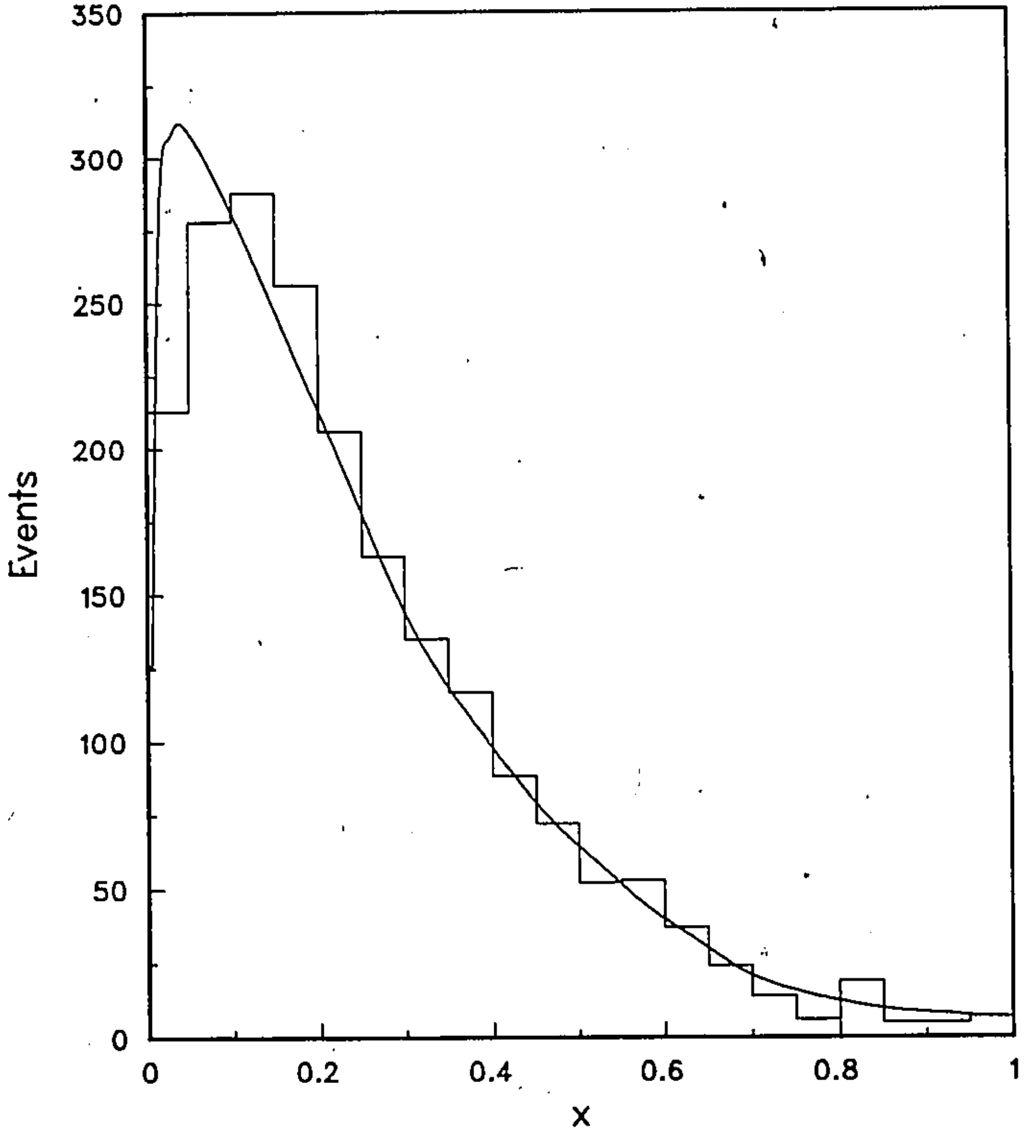

Figure 48: Bjorken-x distribution for charged-current interactions.

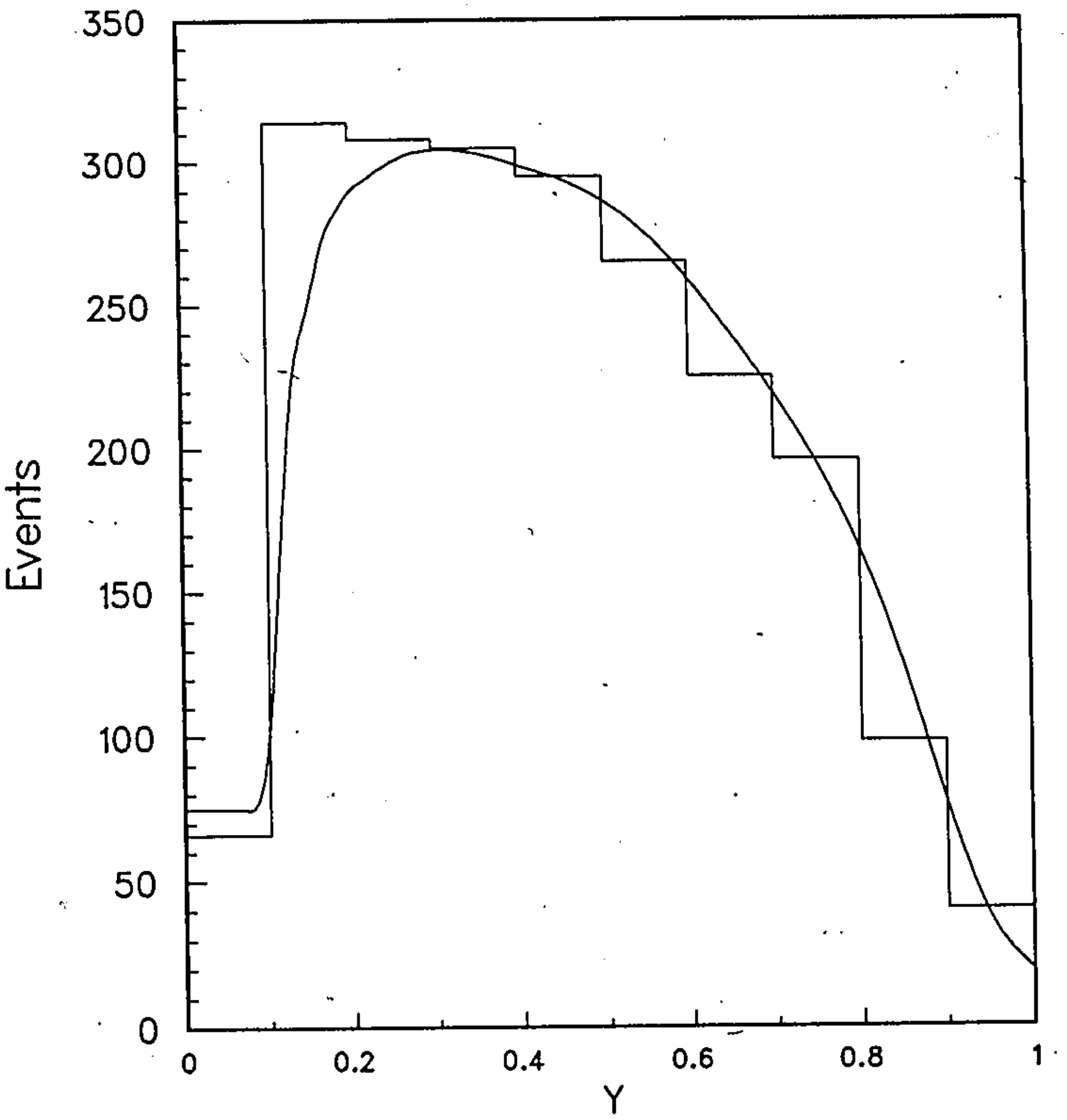

Figure 49: y distribution for charged-current interactions.

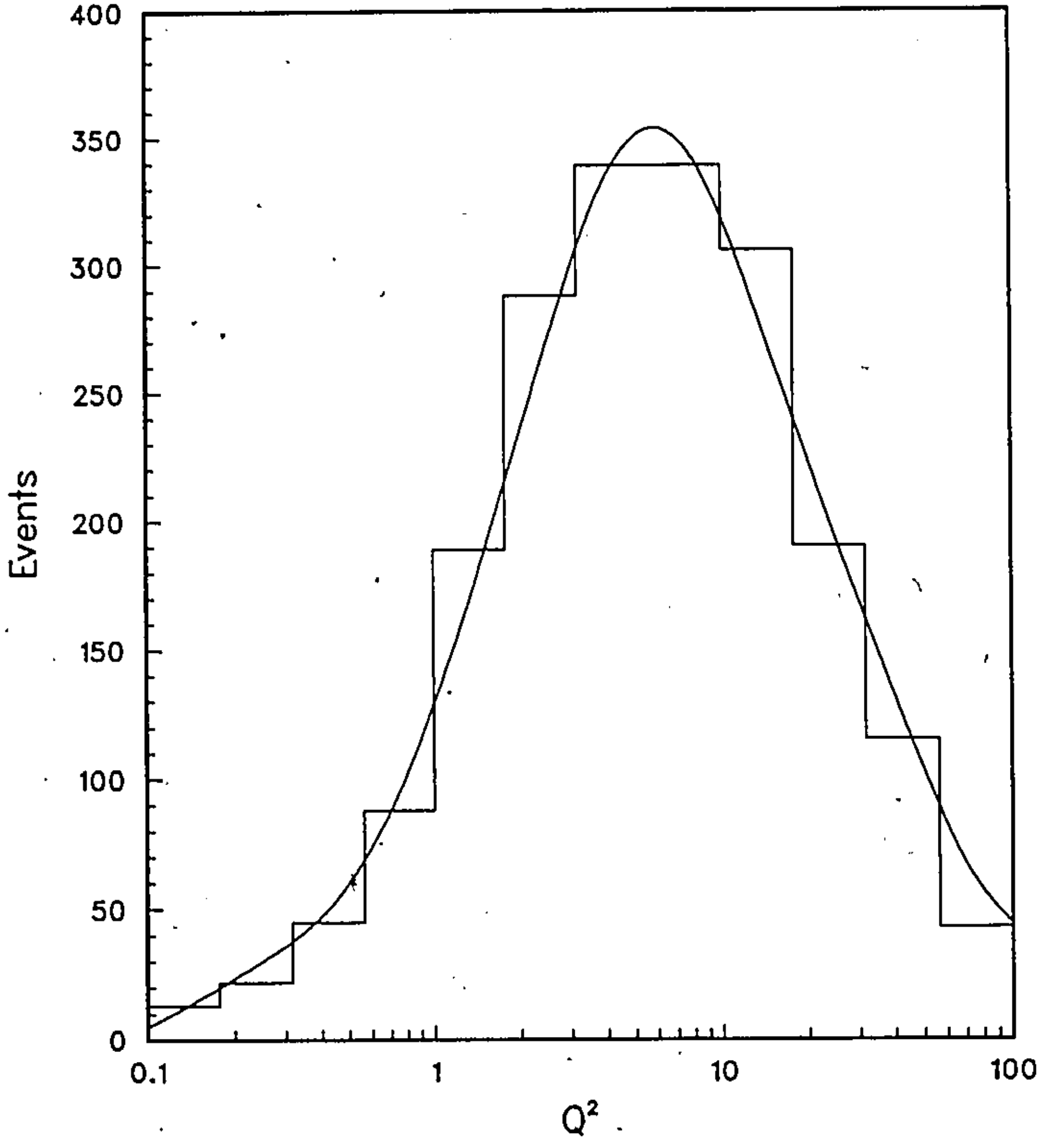

Figure 50: Q^2 distribution for charged-current interactions.

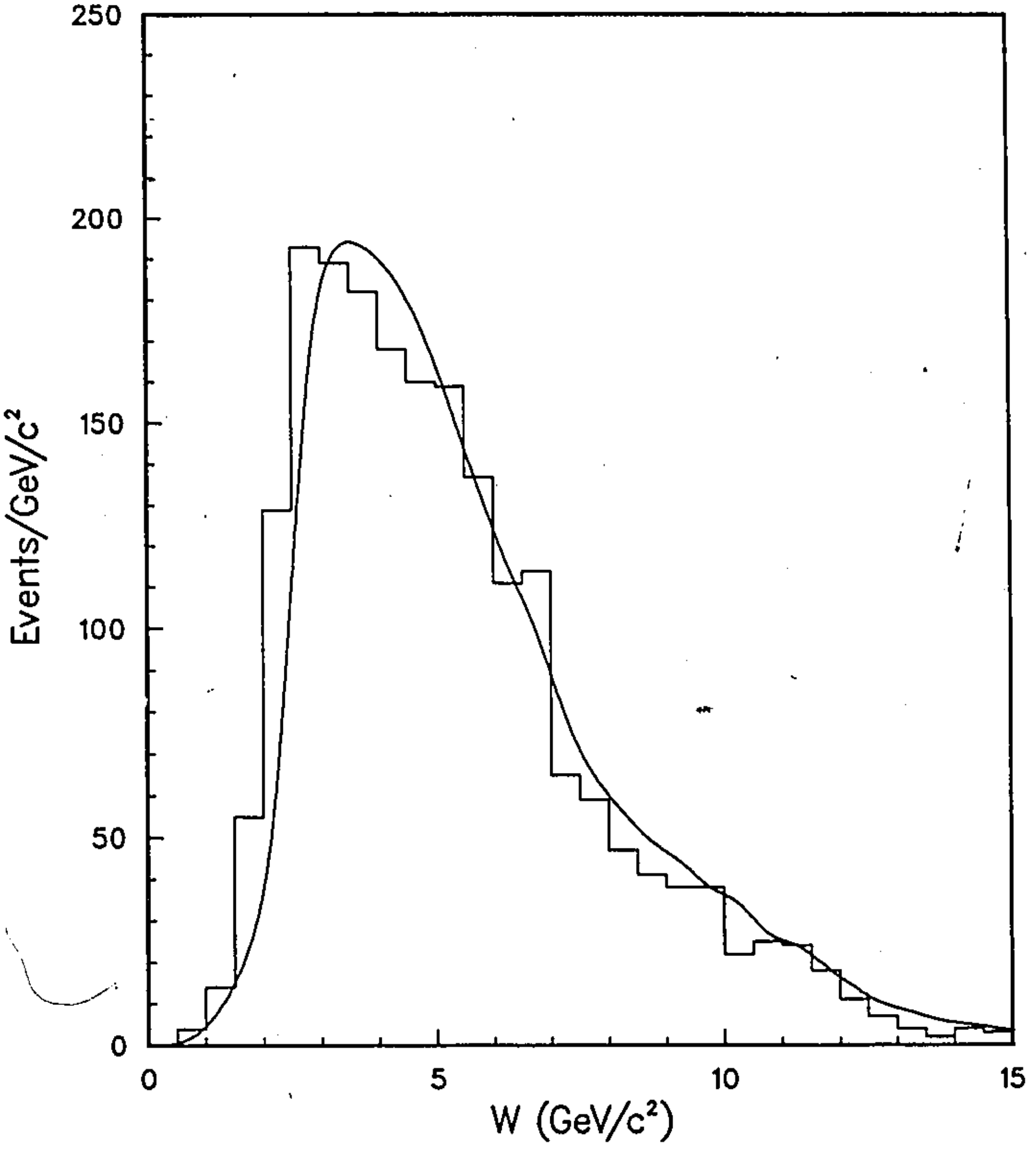

Figure 51: W distribution for charged-current interactions.

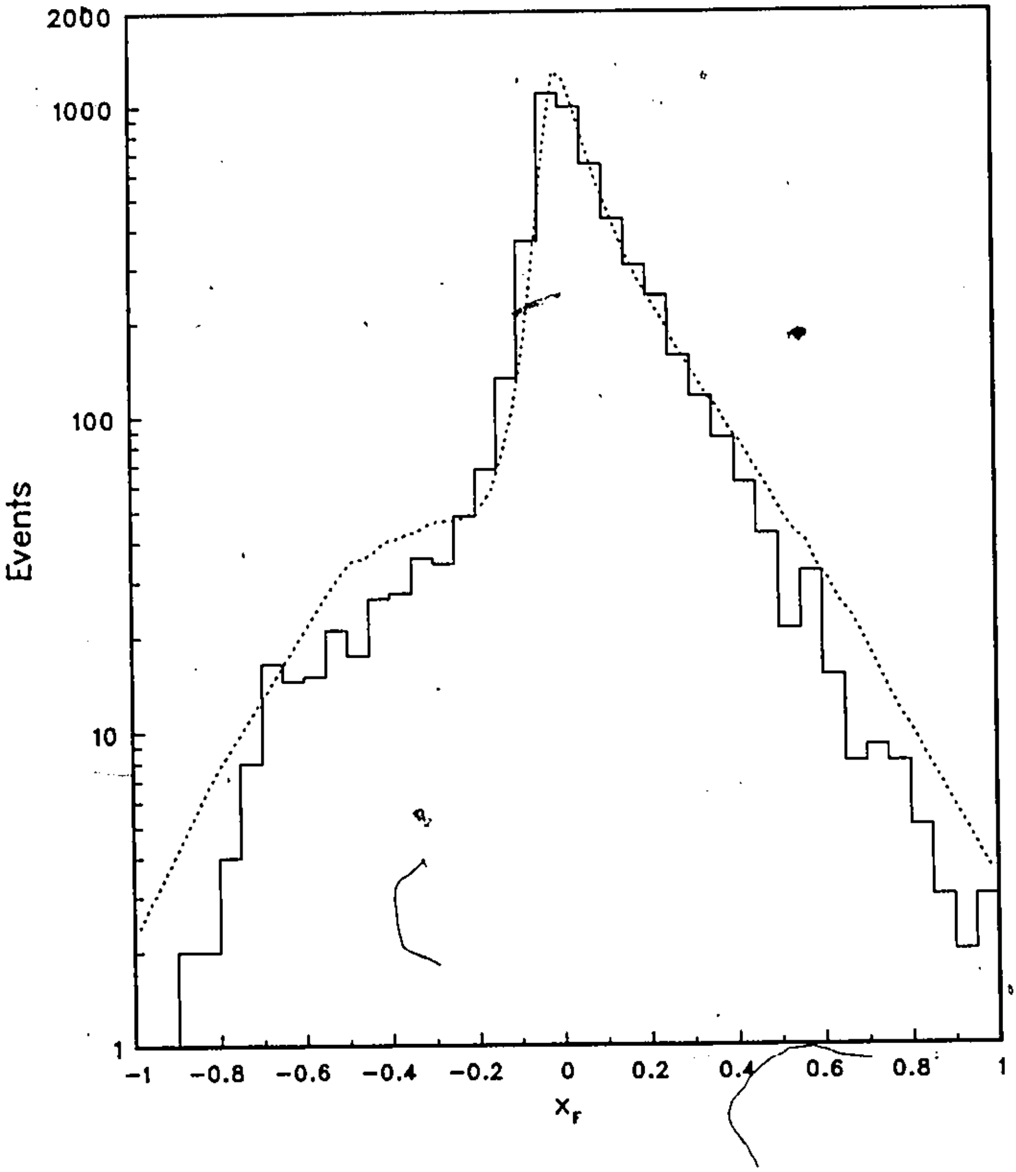

Figure 52: x_F distribution of up-down tracks.

and at a random angle in the center of mass. Most of the tracks in the distribution are pions since these are the lightest and most easily produced particles.

Chapter 6

The Production of Charmed Particles

Once the analysis of the individual charm events had been finished and a momentum assigned to each charmed particle, it was possible to study the production of charmed particles by neutrinos. Using the efficiencies obtained from the experiment Monte Carlo, it was also possible to calculate the relative production rates (or cross sections) for various modes.

6.1 E_ν for Charmed-Particle Events

For the charmed-particle interactions it was possible to calculate the neutrino energy much more accurately than by using E_{vis}. Since these events had been analyzed in great detail, all the available information could be used to determine E_ν. The neutrino energy was calculated by summing up: the energy/momentum of all the true tracks seen in the drift chambers, the excess electromagnetic energy, the charmed-particle energy, and the energy of any neutral hadrons observed in the spectrometer. When doing the sum, care was taken to ensure that no double counting was done; for example, the energy of the decay tracks was not included among the drift chamber tracks since their energy was accounted for by the charmed-particle energy. For the unfittable events, an estimate had to be made of the charmed-particle momentum, and this estimate was then used when calculating the E_ν (and the various kinematic variables). Those charm events with no identified muon were assumed to be charged-current interactions with a very low momentum (~ 0) muon. The E_ν spectrum obtained for the 122 charmed-particle interactions is shown in Figure 53.

6.2 Event Weight Calculation

Each charmed-particle event was given a decay weight to reflect the probability of finding the decay given the initial direction and momentum of the particle (Section 4.8). Using these weights it is possible to obtain information on all the found neutrino interactions with charmed-particles; usually, however, it is all neutrino interactions that are of interest, not just the found interactions. Thus, in order to study all the interactions it is necessary to apply a correction to the found events. Every charmed-particle interaction was given an overall "event weight" which reflected the probability that an event with the given "kinematics" would trigger the detector, be reconstructed, and the primary vertex found.

The "kinematics" of the events were the neutrino energy (E_ν), the values of Bjorken-x, y, Q^2, and W. These parameters are not independent of each other, and given any three of the parameters it is possible to determine the remaining two. For charmed-particle interactions there are also the extra parameters Z and Feynman-x of the charmed particles. These two are not independent of each other and it appears that given one, then the other is also determined, although the relationship is not as obvious as for the other parameters.

The experiment Monte Carlo was used to determine the "event weight". Events were generated with the measured E_ν, Bjorken-x and y (these three were chosen because they are the most commonly used). Only the events for which a charmed particle was generated were considered. If the Bjorken-x and y were not measured (no tagged muon), then the two parameters were chosen randomly by the LEPTO routines. The various quarks were allowed to fragment using the usual LUND

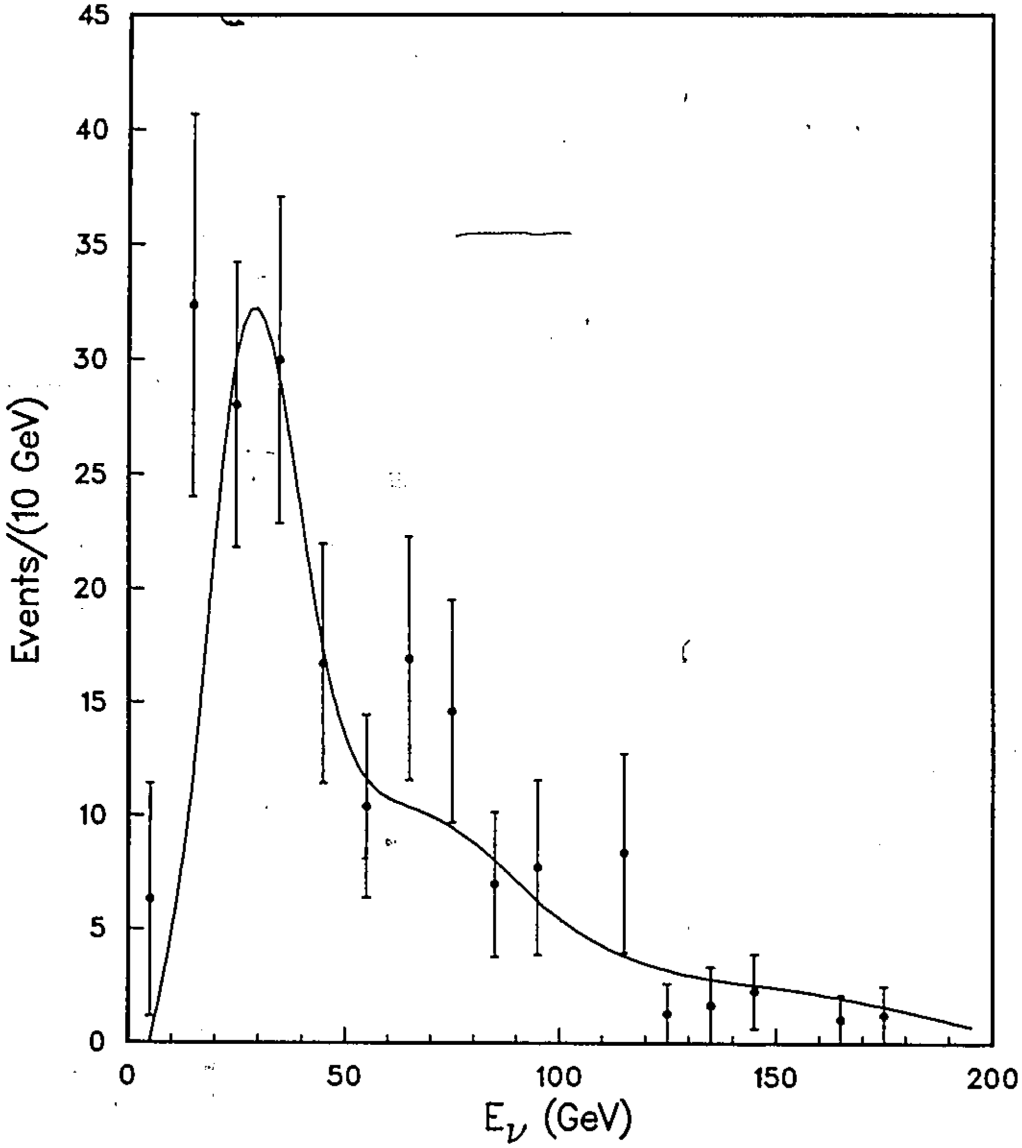

Figure 53: Neutrino energy spectrum for charm events.

procedures and only the events with a Z value within 0.05 of the measured Z were kept. It was found that for most events the generated Feynman-x of the charmed particle agreed within 0.1 of the measured value (when doing the cut on the Z value). No attempts were made to "correct" the Monte Carlo Feynman-x for this difference since it was found that the weight depended very weakly on the value of Feynman-x. The particles from the interaction were then allowed to decay and tracked through the entire spectrometer, as discussed previously (Section 5.1). The ratio of the number of events generated to the number found was used as the "event weight". For some events the Monte Carlo was unable to generate any charmed particles with the measured kinematics (usually the invariant mass (W) was to low). In order for the Monte Carlo to work the neutrino energy used had to be increased slightly, on average only a few GeV, which would not effect the event weight very much. The quasi-elastic Λ_c^+ also had to be generated differently since for these events only two particles were produced at the primary vertex (the Λ_c^+ and the muon). The Monte Carlo was also used to find an overall weight for the ordinary neutrino interactions. This was obtained using the neutrino interactions generated when the Monte Carlo randomly chose E_ν, Bjorken-x, and y.

The average weight obtained for all the charmed-particle events was 1.102. For the ordinary neutrino interactions the event weights were found to be 1.316 and 1.181 for the first and second runs, respectively. The weight differences are due to the different triggering and track reconstruction efficiencies of the two runs.

6.3 Interaction Types

A total of 3886 neutrino interactions were found in the fiducial volume of the emulsion target. Thirty-one (2.5%) of the first run events had to be dropped from the data sample, because the magnet was off at the time when they occured. Thus, the total number of "usable" events is 3855. Of these events, 1870 events had an identified negative MUFB, 150 had an identified positive MUFB, and about 6% of the remaining 1866 events had more than one identified MUFB with opposite signs. The 1866 events are a mixture of $\nu_\mu/\bar{\nu}_\mu$ $/\nu_e$ $/\bar{\nu}_e$ charged-current and neutral-current

Table 19: Number of Found Events

	Run 1	Run 2	Run 1 & 2
ν_μC.C.	950	2002	2952
$\bar{\nu}_\mu$ C.C.	40	112	152
ν_μN.C.	199	450	649
$\bar{\nu}_\mu$ N.C.	10	32	42

interactions, but it is not possible to separate the various interaction types.

The experiment Monte Carlo was used to estimate the number of charged-current ν_μ interactions which were found. It was estimated that about 77% of all the found interactions were charged-current ν_μ interactions, and 4% were $\bar{\nu}_\mu$ charged-current interactions. The total number of ν_μ and $\bar{\nu}_\mu$ charged-current interactions that were found was estimated to be 2952 and 152 events, respectively; the estimated number of ν_μ and $\bar{\nu}_\mu$ neutral current interactions was 649 and 42 events, respectively. The various numbers for the first and second runs are shown in Table 19. The remaining 60 events are all ν_e and $\bar{\nu}_e$ interactions.

6.4 Charmed-Particles Cross Sections

A total of 122 charmed-particle decays was found in the emulsion (46 during the first run, and 76 in the second run). The number of decays had to be corrected for the various efficiencies, using the decay and event weights discussed in Sections 4.8 and 6.2. The weights for all the charmed-particle events are listed in Appendix C (along with the values of the different kinematic variables). Using these weights the number of produced charm events is: 67 ± 12 during the first run and 109 ± 15 during the second run. There were also 7.0 ± 3.2 and 4.3 ± 2.2 anticharm events during the first and second runs, respectively.

Using the number of produced charmed particles and the number of charged-current interactions (along with their weighting factors), the relative charm and anticharm production rates were calculated to be[1]:

$$\begin{aligned}\frac{\sigma(\nu N \rightarrow c\,\mu^- X)}{\sigma(\nu N \rightarrow \mu^- X)} &= 4.85^{+0.67}_{-0.63}\ \% \\ \frac{\sigma(\bar{\nu} N \rightarrow \bar{c}\,\mu^+ X)}{\sigma(\bar{\nu} N \rightarrow \mu^+ X)} &= 5.75^{+2.88}_{-2.04}\ \%\end{aligned}$$

The charm production rate can be compared with the same sign dilepton rate found using the Fermilab 15-ft bubble chamber [67]; they found $\sigma(\nu N \rightarrow \mu^- \mu^+ X)/\sigma(\nu N \rightarrow \mu^- X) = (0.52 \pm 0.09)\ \%$. Using a semileptonic branching ratio of 10% for the charmed particles the two rates agree with each other within their errors.

The relative D^0 production rate is

$$\frac{\sigma(\nu N \rightarrow D^0 \mu^- X)}{\sigma(\nu N \rightarrow \mu^- X)} = 2.19^{+0.39}_{-0.35}\ \%$$

6.5 Cross Section Energy Dependence

The E_ν energy distribution of the charmed particles is shown in Figure 53 using the weighted events. The peak of the spectrum occurs around 20 GeV and the mean E_ν is 50 GeV. This should be compared with the predicted ν_μ interaction spectrum (smooth curve in Figure 53) for the charm events. As can be seen, the agreement is quite good.

The observed E_ν distribution for the charged-current ν_μ interactions is obtained using the measured E_{vis} for each event and 'correcting' it to obtain a neutrino energy. The relative charmed-particle cross section as a function of energy is calculated by taking the ratio of the number of weighted charmed events over the corrected number of charged-current ν_μ interactions. The correction for the ν_μ interactions is obtained from the Monte Carlo using the number of neutrino interactions over the number of events tagged as ν_μ charged-current interactions. The relative charmed-particle cross section is shown in Figure 54. The smooth curves are the theoretical predictions calculated by R. Brock [68] (after correcting for them for the semileptonic branching ratios of charm).

---

[1] Using just the decay weight give fairly similar results

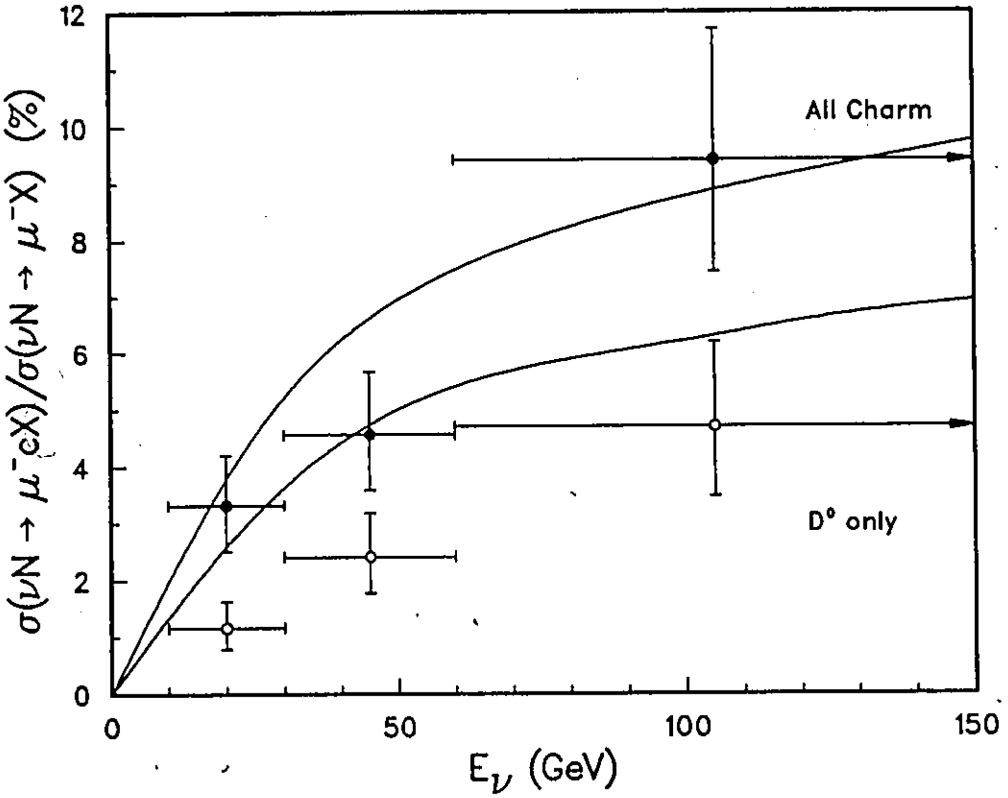

Figure 54: Charmed-particle cross section.

6.6 Neutral Current Production of Charm

A total of 2 first run events and $6\frac{1}{2}$ second run charmed events did not have an identified muon (the half event corresponds to an event with no muon and both the D^0 and $\bar{D}^0$solutions are possible). The weighted number of events are 3.0 ± 2.2 and 12.4 ± 5.1 for the two runs. These numbers correspond to a muon tagging efficiency for charmed events of $91.2 \pm 3.3\%$.

Assuming that these events with no tagged muon were due to the neutral current production of a charmed particle, it is possible to set an upper limit to this production. In order to do this calculation properly the relative efficiencies to find a neutral current charm event and an 'ordinary' neutral current interaction has to be determined. Since the exact neutral current process that could produce a charmed particle is not known some arbitray mechanism has to be used. The experiment Monte Carlo is used to generate some charm particles and ordinary interactions, and once the event has been generated the outgoing muon is 'turned' into a neutrino (it is ignored completely as if it did not exist). As before the charm events are all generated with a neutrino energy equal to that measured for the 'no-muon' events, to obtain individual event weights.

Using this procedure a total of 22.7 weighted events did not have a muon, and the neutral current events have a weight of 1.825 and 1.540 for first and second run events, respectively. Thus, the following limit is obtained

$$\frac{\sigma(\nu N \rightarrow \nu c X)}{\sigma(\nu N \rightarrow \nu X)} < 3\ \% \quad (90\ \%\ \text{C.L.})$$

The limit is actually smaller than this since the muon tagging efficiency is only 90%, and not all events are expected to have an identified muon. If this 'background' is subtracted the limit can be reduced to about 2%. This charm changing neutral current limit is comparable to the results of previous experiments. These experiments found (using a 10% charm semileptonic branching ratio) $\sigma(\nu_\mu N \rightarrow \nu_\mu c X)/\sigma(\nu_\mu N \rightarrow \nu_\mu X) < 1.8\ \%$ (90 % C.L.) [69], < 2.6 (90 % C.L.) [70], and $\sigma(\bar{\nu}_\mu N \rightarrow \bar{\nu}_\mu \bar{c} X)/\sigma(\bar{\nu}_\mu N \rightarrow \bar{\nu}_\mu X) < 4\ \%$ (90 % C.L.) [71].

6.7 Production of Charm Pair

In this experiment one event was found in which a D^0 and a $\bar{D}^0$ pair was produced [10]. The D^0 and $\bar{D}^0$ had momenta 13 GeV/c and 48 GeV/c, respectively, and carried about 90% of the events visible energy (68 ± 8 GeV). The energy of the incoming neutrino is larger than this since the scattered lepton carries off some energy, and if the scattered lepton is a neutrino it can carry off almost any amount of energy (if it is a muon or electron then its energy is limited since a high-energy charged lepton should have been observed). For calculation purposes it is assumed that the incoming neutrino energy is 68 GeV. It is probably not much larger since there are very few high energy neutrinos.

Assuming the double charm event was produced by a neutral current interaction, the production rate of $c\bar{c}$ events is[2]

$$\frac{\sigma(\nu N \to \nu c \bar{c} X)}{\sigma(\nu N \to \nu X)} = 0.13^{+0.31}_{-0.11}\ \%$$

The muon tagging efficiency is estimated to be very large (90%) for charmed-particle events and so it is unlikely that the double charm event was a charged current interaction. Assuming, however, that the muon was missed and this event is a charged current interaction, the production rate is

$$\frac{\sigma(\nu N \to \mu^- c \bar{c} X)}{\sigma(\nu N \to \mu^- X)} = 0.04^{+0.09}_{-0.03}\ \%$$

Instead of calculating a production rate it is possible to calculate a limit, which is

$$\frac{\sigma(\nu N \to c \bar{c} \mu^- X)}{\sigma(\nu N \to \mu^- X)} < 0.12\ \% \qquad (90\%\ \text{C.L.})$$

This process is expected to be the main source of same-sign dilepton events which have been observed in a number of neutrino experiments. The production of $c\bar{c}$ pairs produced in second-order QCD diagrams is expected to have a same-sign rate $\lesssim 10^{-4}$ [72]. A CERN experiment [73] reported a rate of $\sigma(\nu_\mu N \to \mu^- \ell^- X)/\sigma(\nu_\mu N \to \mu^- X) = (0.34 \pm 0.18) \times 10^{-4}$, while a Fermilab experiment [74] reported an upper

---

[2] All the rates and limits calculated in this section have combined the data of the neutrino and antineutrino events

limit of $0.76 \times 10^{-}4$ (90% C.L.) to this ratio. Using a 10% charm semileptonic branching ratio, our charged-current $c\bar{c}$ production limit of 12×10^{-4} (90% C.L.) is comparable with these rates and expectation. There are some experiments [75] with same-sign dilepton rates larger than the above values; these rates, however, have large errors and are still consistent with the above results.

The rate of the double charm production relative to the single charm production is

$$\frac{\sigma(\nu N \to c\,\bar{c}\,X)}{\sigma(\nu N \to c\,X)} = 0.83^{+1.93}_{-0.69}\ \%$$

Another limit of interest is the ratio of the double charm over single charm charged-current production rates. A total of 187 ± 19 single charm events were generated, and assuming that the one double charm event was produced in a charged-current interaction, the following limit can be set.

$$\frac{\sigma(\nu N \to c\,\bar{c}\,\mu^- X)}{\sigma(\nu N \to c\,\mu^- X)} < 3\ \% \qquad (90\%\ \text{C.L.})$$

6.8 Wrong Sign Charm Events

A "wrong sign" charm event is a charged-current event in which a charm particle was produced by an $\bar{\nu}_\mu$ (or an anticharm by a ν_μ), and thus for charged-charmed-particle decays the charmed particle and muon would have the same sign (such as $\nu_\mu N \to D^-\mu^- X$). For neutral decays a $\bar{D}^0$ would be found in an event with a negative muon. We have no events for which the muon and charmed-particle have the same sign, or an event in which the only possible solution is a $\bar{D}^0$ (D^0) with a μ^- (μ^+) coming from the primary vertex. It is almost impossible to obtain only a $\bar{D}^0$ solution and not D^0 since often the Cabibbo favored decay modes of the two are very similar.

"Wrong sign" events could be double charm events or beauty events in which not all the particles were seen or identified, such as

$$
\begin{array}{lcl}
\nu_\mu N & \rightarrow & \mu^- \, (c) \, \bar{c} \, X \\
\nu_\mu N & \rightarrow & \mu^- \, (\bar{b}) \, X \\
 & & \quad\;\; \downarrow \\
 & & \quad\;\; \bar{c}
\end{array}
$$

where the particles in brackets were not seen.

As was already mentioned we did not observe any "wrong sign" decays directly, however there were some charged decays for which the sign could not be determined directly (the sign of all the decay tracks was not known). Some D^0 decay will also work as $\bar{D}^0$, for example the decay $D^0 \rightarrow X\bar{K}^0$ will always work as $\bar{D}^0 \rightarrow XK^0$. The total weighted number of charm events that could work as an anticharm event were 10.4 ± 4.0 first run events and 25.5 ± 6.7 second run events (there were also 1.6 ± 1.6 and 2.5 ± 1.8 anticharm events that worked as charm events). Thus, the probability of assigning the wrong sign to an event is $(16 \pm 7)\%$ and $(26 \pm 7)\%$ in the first and second run, respectively. Using the fact that no events were observed to have been produced with a wrong sign, and the tagging efficiencies above, the following limits are obtained

$$\frac{\sigma(\nu N \rightarrow \bar{c}\,\mu^- X)}{\sigma(\nu N \rightarrow \mu^- X)} < 0.12\ \% \qquad (90\%\ \text{C.L.})$$

$$\frac{\sigma(\nu N \rightarrow \bar{c}\,\mu^- X)}{\sigma(\nu N \rightarrow c\,\mu^- X)} < 3\ \% \qquad (90\%\ \text{C.L.})$$

6.9 Beauty Production Limits

When searching for charm decays, it should also have been possible to find beauty decays. The efficiency for finding beauty decays is higher than that for finding charm due to the larger multiplicity of the decays. As a conservative estimate it is assumed that the charm and beauty finding efficiencies are equal. An event is considered as a beauty candidate if its invariant mass is greater than 2.1–2.3 GeV/c² for mesons and baryons, respectively, which well below the B mass of about 5.2 GeV/c². This

Table 20: Relative Charm Production Rates

Particle	Unweighted Number	Weighted Number	Rate (%)
D^0	51.5	79	$45.5^{+6.1}_{-5.1}$
D^+	39	58	$33.5^{+5.9}_{-8.1}$
D_s^+	5.5	9	$5.1^{+4.2}_{-2.5}$
Λ_c^+	14.5	28	$15.9^{+8.1}_{-4.3}$
$\bar{D}^0$	5.5	8	70^{+36}_{-13}
D^-	2	2	20^{+30}_{-12}
D_s^-	1	1	10^{+25}_{-8}

cut retains at least 90% of the beauty events (based on applying a similar cut to the charm events). No beauty candidate events were found, and thus

$$\frac{\sigma(\nu N \to b\,\mu^- X)}{\sigma(\nu N \to c\,\mu^- X)} < 2\ \% \qquad (90\%\ \text{C.L.})$$

Assuming that the branching ratio of $b \to c$ is 100%, then the limit on $\bar{b}$ production is also equal to the limit on wrong sign production, since any anti-charm event could be due to the decay of a $\bar{b}$. Thus, the following limit is obtained

$$\frac{\sigma(\nu N \to \bar{b}\,\mu^- X)}{\sigma(\nu N \to c\,\mu^- X)} < 3\ \% \qquad (90\%\ \text{C.L.})$$

6.10 Relative Production Rates of Charmed Particles

There are no simple arguments that will predict the relative production rates for the different charmed-particle species. Using the weights for the various events, the relative rates for the different charmed-particle species are shown in Table 20. These calculations assumed that all the ambiguous events were $D^\pm$, and the effect of the short lived contamination (17%) among the ambiguous events was included in the error.

A total of 3 unweighted events was tagged as quasi-elastic Λ_c^+. The weighted number of events is 9.1 ± 5.8 which corresponds to a quasi-elastic Λ_c^+ production rate of

$$\frac{\sigma(\nu n \to \Lambda_c^+ \mu^-)}{\sigma(\nu N \to \mu^- X)} = 0.25^{+0.25}_{-0.15}\ \%$$

6.11 Bjorken x Distribution

The Bjorken x distribution is shown in Figure 55 for all the charm events with an identified muon. Parts (a)–(d) show the distributions for the D^0, D^+, D_s^+, and Λ_c^+ (and their anti-particles). There is no obvious difference among the various distributions. Figure 55(e) shows the distribution for all charmed-particles. The mean of the distribution is 0.17 which is less than the mean for ordinary charged-current neutrino interactions (0.23). The Bjorken-x values for charmed-particles are expected to be lower than for ordinary neutrino interactions, since the charmed-particles are produced off the d valence quarks and s sea quarks and the sea quarks generally carry a smaller fraction of the particles' momentum.

Using the d and s quark distributions as determined by other experiments [76], the relative number of strange and down quarks in the nucleon can be determined. The valence and sea quark distributions are given by $\sqrt{x}(1-x)^{3.5}$ and $(1-x)^7$, respectively. Thus the Bjorken x distribution is given by

$$\frac{dN}{dx} = N(A_d\sqrt{x}(1-x)^{3.5} + A_s(1-x)^7)$$

where A_d and A_s are the number of d and s quarks that produced a charm particle, and N a normalization factor. Rearranging this equation and including the effect of the Cabibbo angle the equation becomes:

$$\frac{dN}{dx} = N(\sqrt{x}(1-x)^{3.5} + f(1-x)^7)$$

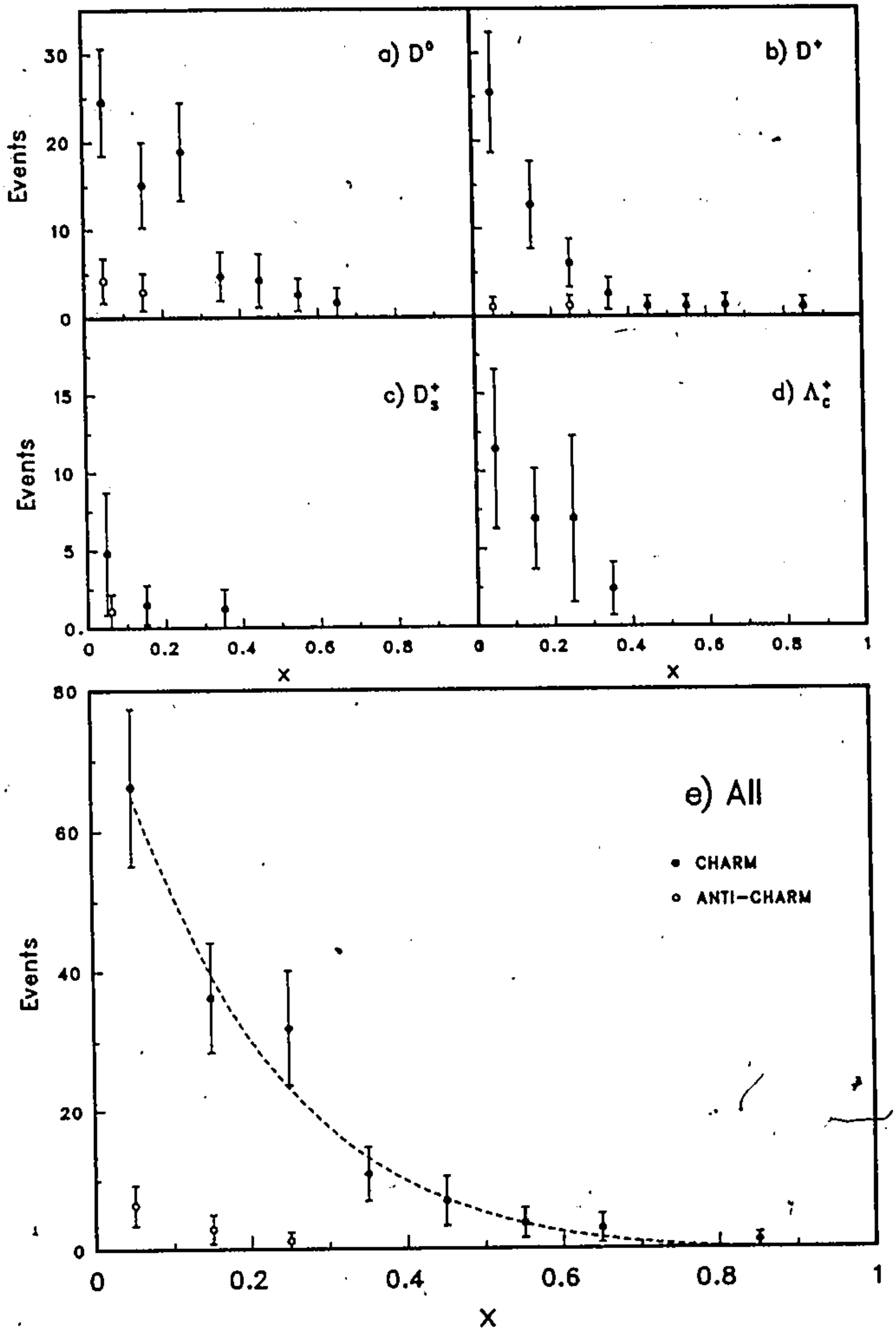

Figure 55: Charmed-particle Bjorken x distribution.

where N is a new normalization factor, and $f = N_s/(N_d \tan^2 \theta_c)$, N_s and N_d are the relative number of strange and down quarks in the nucleon. In this derivation it is implicitly assumed that if a charm quark is produced from a d quark, then the original d was one of the valence quarks. By varying N and f and minimizing the χ^2 it was possible to fit the above equation. The fitted values for all charm events were $N = 74 \pm 15$ and $f = 0.99 \pm 0.33$, and the predicted distribution is the smooth curve in Figure 55(e); the χ^2 is 2.9 for 7 degrees of freedom. The distribution for only the Ds (D^0, $\bar{D}^0$, and $D^{\pm}$) looks very similar and has fitted values of $N = 57 \pm 13$ and $f = 1.11 \pm 0.40$. Using the Cabibbo angle of $\theta_c = 13.4°$ the number of strange-sea quarks is $5.6 \pm 1.9\%$ of the total number of down quarks. Our calculated value for f can be compared to other experimnets. The 15-ft bubble chamber at Fermilab found [67] that in neon $f = 0.76 \pm 0.29$, which is in excellent agreement with our value.

6.12 Y Distribution

The Y distribution for the charm events with an identified muon is shown in Figure 56; again (a)–(d) show the D^0, D^+, $D_s^+$and Λ_c^+ distributions, while (e) shows all the charm events. The mean of the distribution is 0.53 compared with 'ordinary' interactions which have a mean of 0.44. This difference is also expected since charmed-particles are heavy, and a large fraction of the available energy is needed in order to produce charm. The distribution appears to peak slightly at high y values. However, the uncertainties in the plot are quite large and the distribution is consistent with being flat. There is a deficiency of events at large y (close to 1.0) due to an inability of the spectrometer to tag low-momentum muons, and so charm events with a large y will be found but the kinematic variables cannot be calculated accurately.

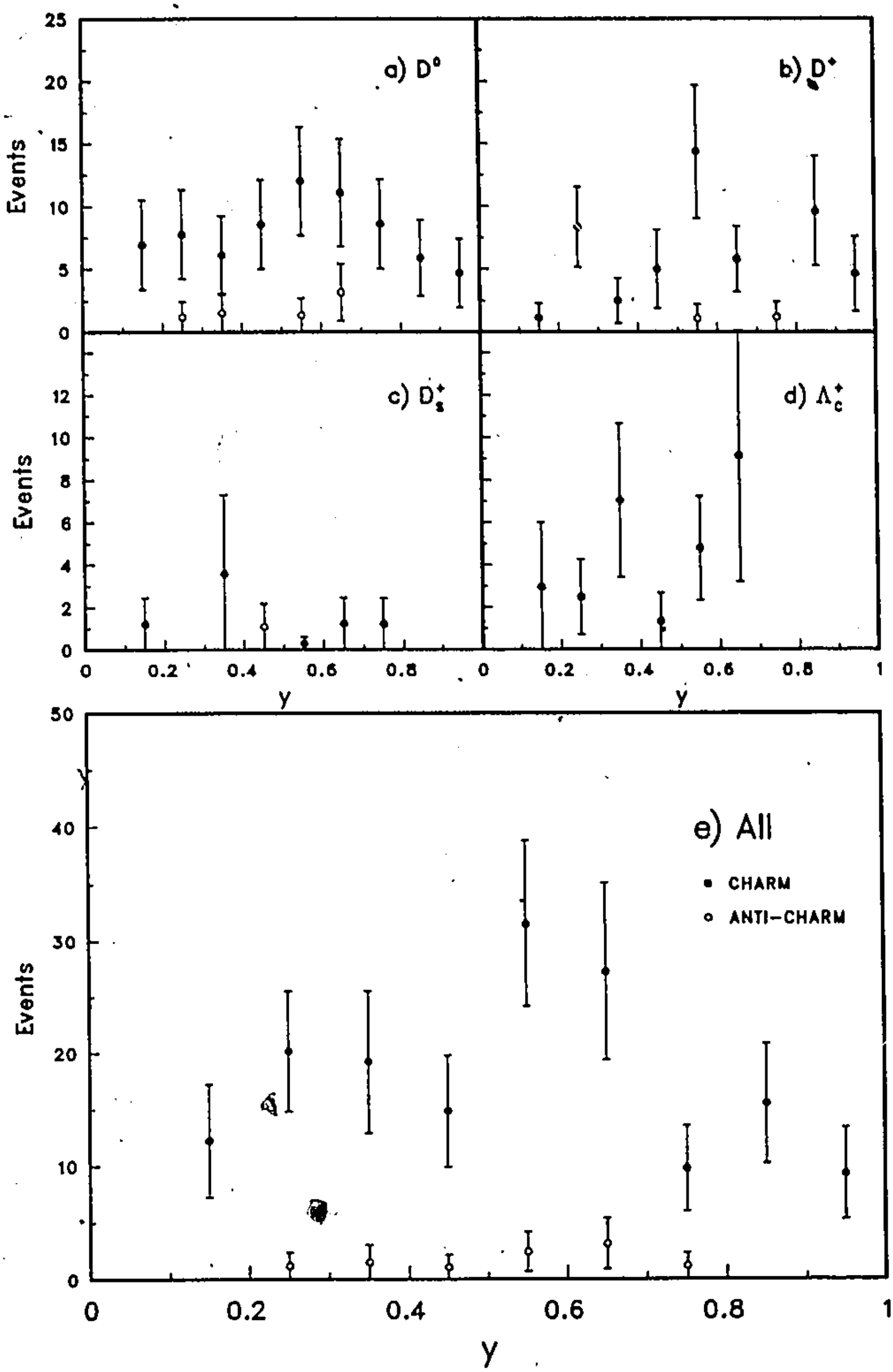

Figure 56: Charmed-particle y distribution.

6.13 Q^2 and W Distribution

Figures 57 and 58 show the Q^2 and hadronic mass (W) distributions. The Q^2 distributions appears to be very similar to the 'ordinary' interactions, shown by the smooth curve in Figure 57(e). However, the errors in the plot are very large and it is not possible to observe any differences. The mean hadronic mass of the charm events is 6.0 GeV/c^2 which is almost one GeV/c^2 larger than the mean for the ordinary interactions (5.2 GeV/c^2). The peak of the ordinary events is at about 2.5 to 3.0 GeV/c^2, while the charm event distribution has a peak at about 5 GeV/c^2. Again there is no noticeable difference between the various charm species.

6.14 Momentum and Z Distributions

Figure 59 shows the momentum distribution of all the charmed-particles. The mean of the distribution of all charmed particles is 14 GeV/c. It is very difficult to determine the peak of the distribution, but it appears to be at about 5 to 10 GeV/c. The Λ_c^+ appear to have a lower momentum than the charmed mesons; this could be due to a difference in the production of charmed baryons and mesons, or because only low momentum Λ_c^+ can be identified as such. The reason for the lower momentum is probably a combination of the two possibilities.

The Z distribution of the charm events is shown in Figure 60. The mean of the distribution is 0.61, and as can be seen it peaks at a very high Z value. This is expected since the charmed particles are predominantely current fragments and as such will carry off most of the available energy. The Z distribution for the Λ_c^+ is, however, very flat. This occurs because the Λ_c^+ is a mixture of current and target fragments. The Λ_c^+ has the struck quark in it, and in order to conserve baryon number some of the original target quarks must be part of the charmed baryon, or a diquark pair ($qq\bar{q}\bar{q}$) must be produced, all this will tend to reduce the Λ_c^+ energy.

It is possible to compare the Z distribution for the charmed particles with that observed by other experiments. The distribution was fitted to the form of Peterson

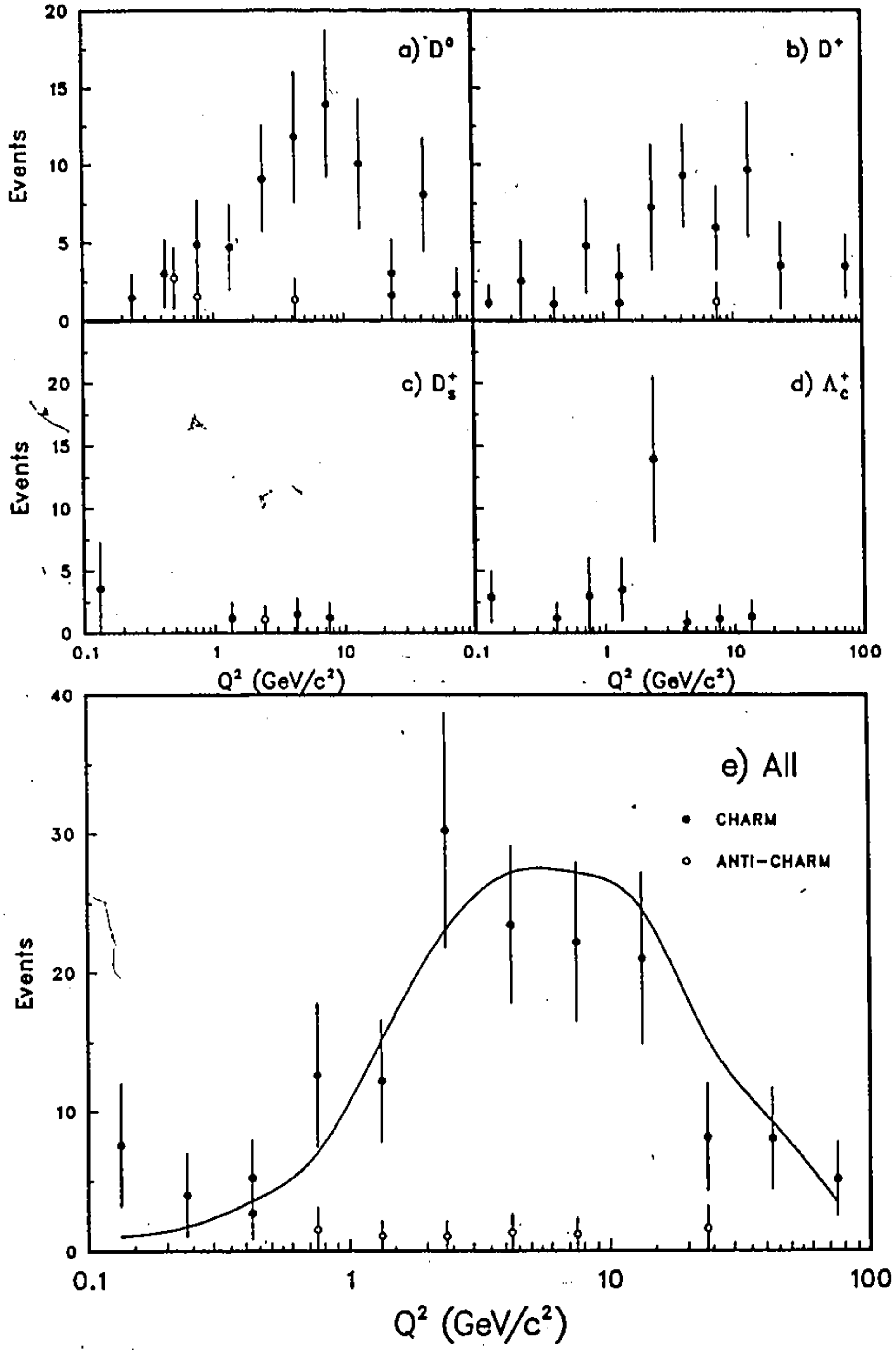

Figure 57: Q^2 distribution for charm events.

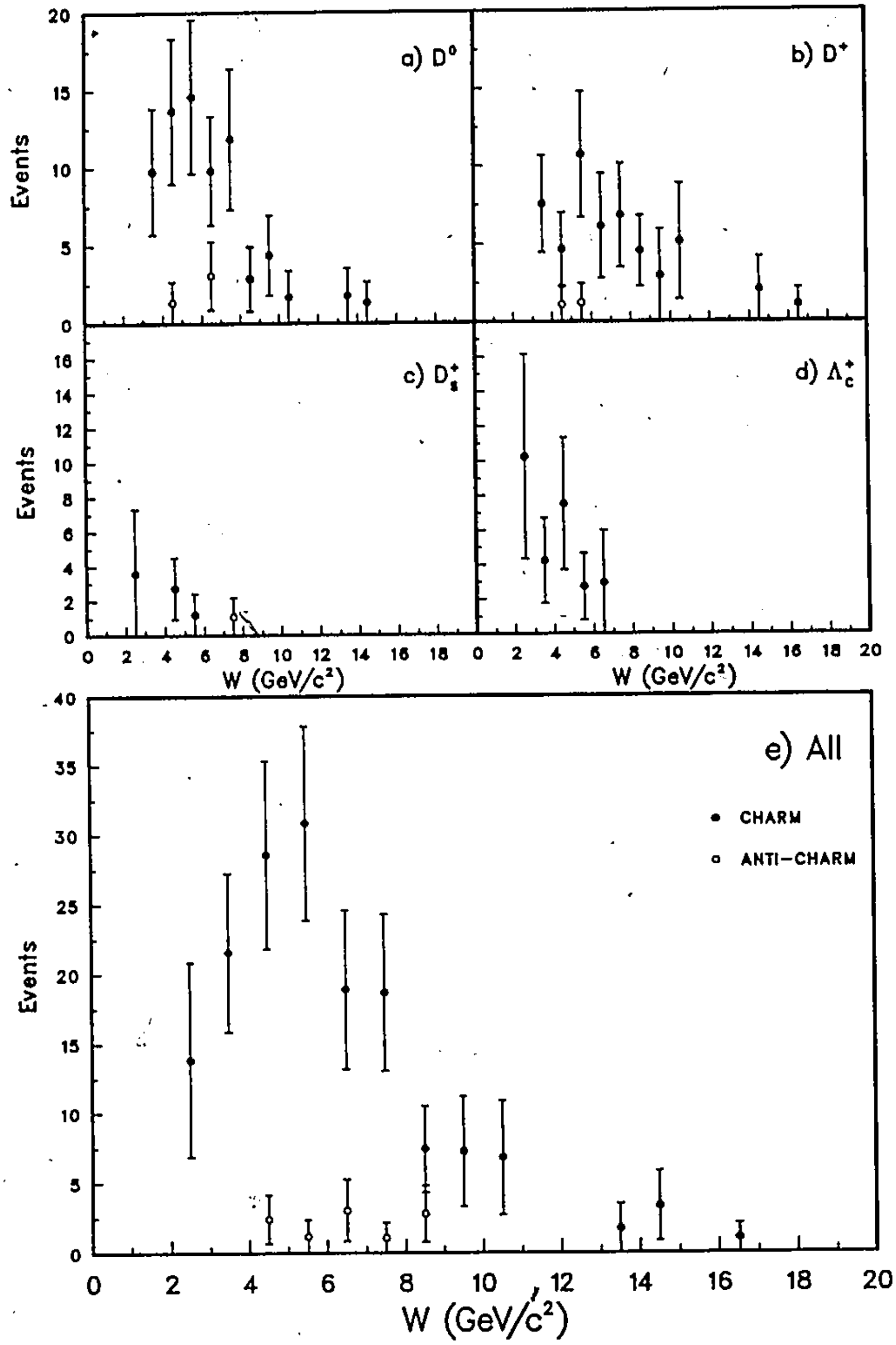

Figure 58: Hadronic mass distribution for charm events.

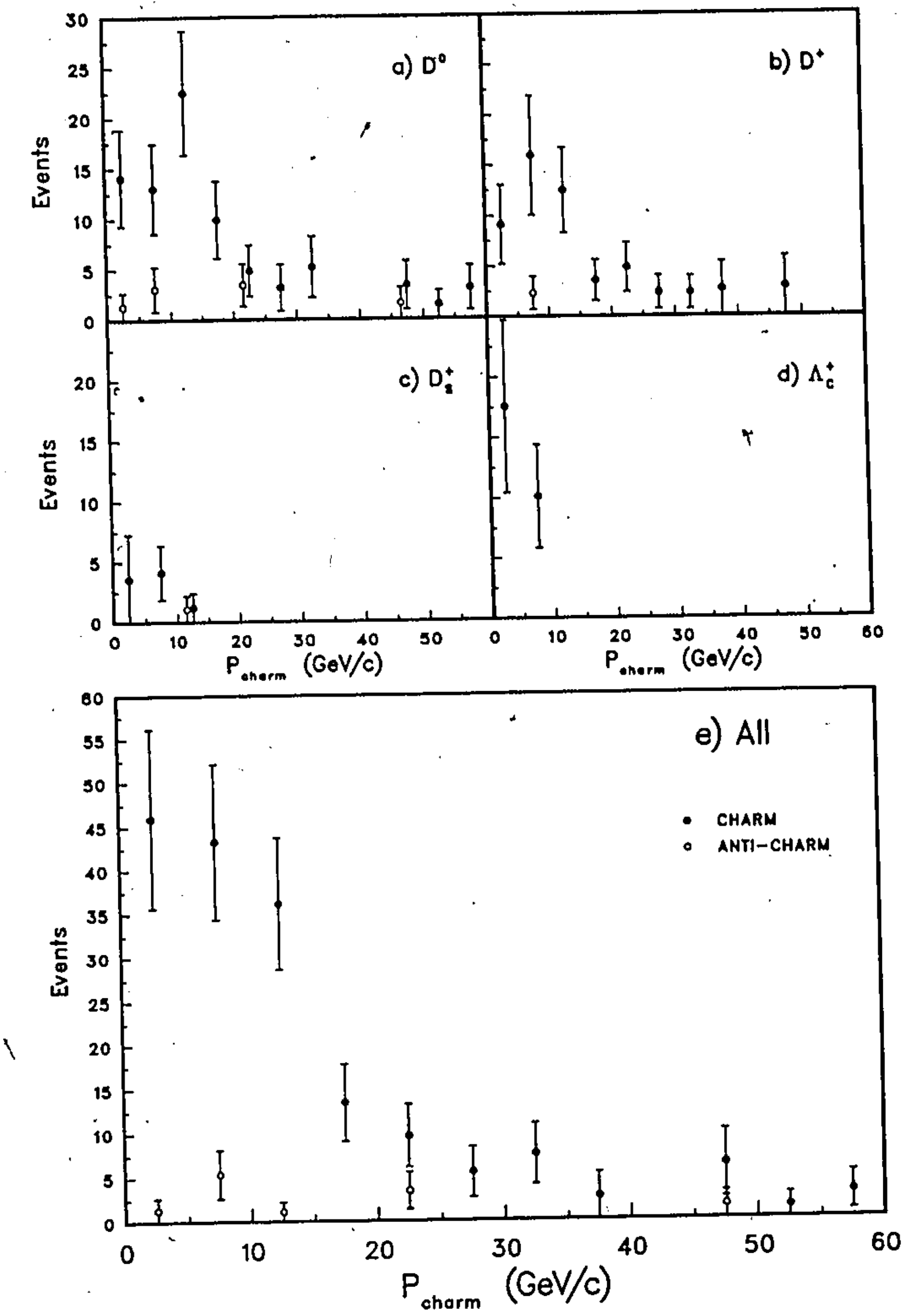

Figure 59: Charmed-particle momentum distribution.

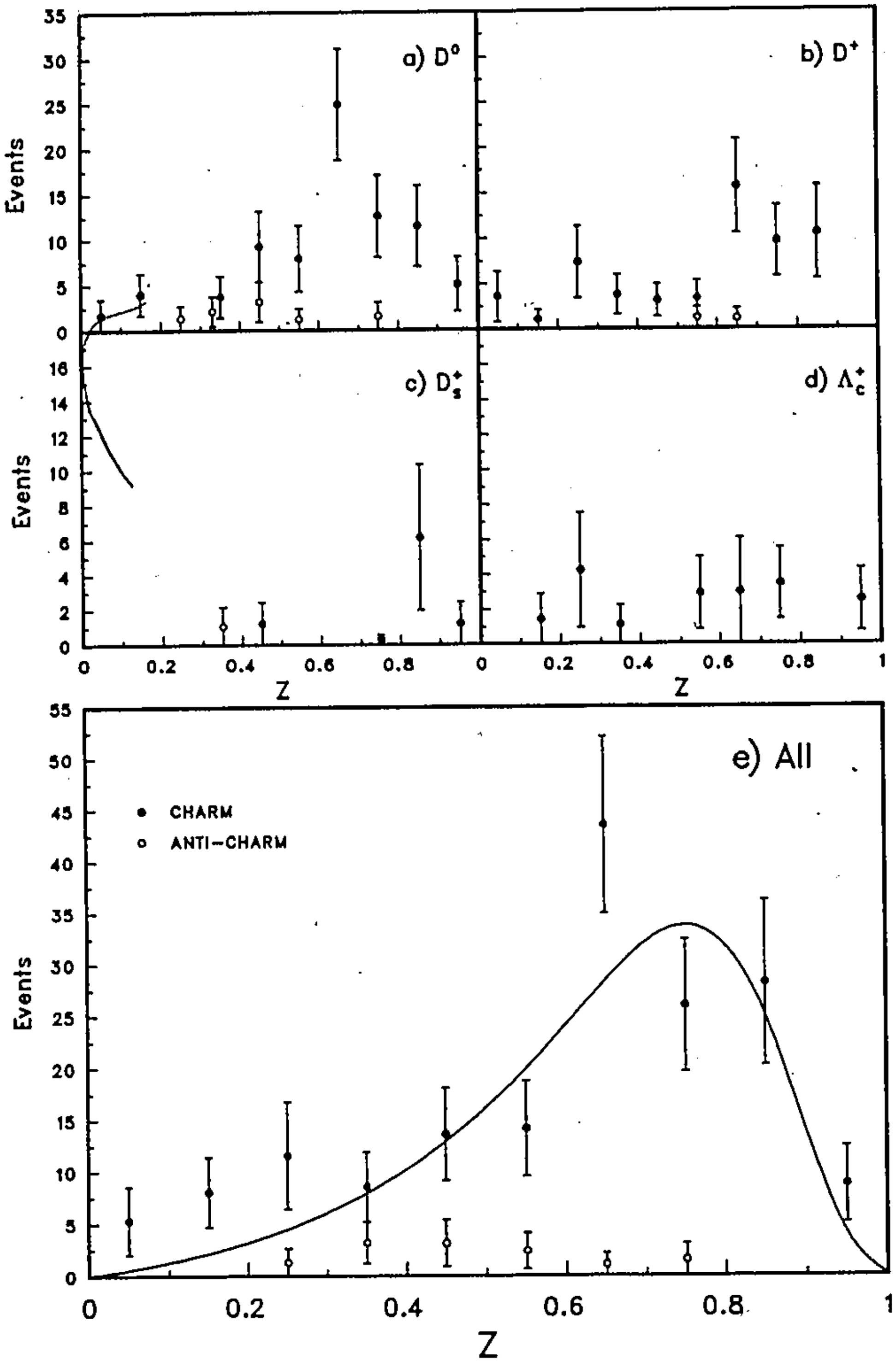

Figure 60: Z distribution.

et al.[77], which is

$$D_c^h(Z) = \frac{N}{Z[1-(1/Z)-\epsilon/(1-Z)]^2}$$

N and ϵ were varied and the fitted values were those which minimized the χ^2. For all charm events combined together the fitted values were $\epsilon = 0.081 \pm 0.014$ and $N = 10.9 \pm 1.6$, and the fragmentation function is the smooth curve in Figure 60(e). The χ^2 of the fit is 15.0 for 9 degrees of freedom. If only the charmed and anticharmed mesons are used (excluding identified Λ_c^+), then the fitted values are: $\epsilon = 0.106 \pm 0.018$ and $N = 12.6 \pm 1.9$; the distribution and curve look very similar to those for all charmed particles. For this curve the χ^2 is 11.0 which is slightly better, as expected since the Λ_c^+ fragmentation is noticeably different from the mesons.

The calculated values of ϵ do not agree very well with the world average of the e^+e^-data [78] for the fragmentation of the D^* which is $\epsilon = 0.29 \pm 0.04$. However, we do agree with Lang et al. [79], within 2.6 standard deviations, who found $\epsilon = 0.40^{+0.25}_{-0.11}$, and with the CDHS collaboration [80] who found $\epsilon = 0.22^{+0.11}_{-0.08}$. Also, our value for ϵ agrees very well with the prediction of Peterson et al. which was $\epsilon \sim 0.15$. Our average Z value of 0.6 also agrees with the e^+e^-average [78] of 0.58 ± 0.02.

6.15 Feynman x Distribution

Figure 61 shows the Feynman-x distribution for the charmed-particles. This distribution peaks at high x_F value, and almost all of the particles have a positive x_F, implying that they were all produced in the forward direction in the center of mass. The mean value of the distribution for charmed particles is $< x_F >= +0.23$. This is quite different from the pions (up-down tracks) produced in ordinary interactions which were found to peak very sharply around an x_F of zero.

The charmed-particles x_F distribution is also different from the x_F distributions of strange particles as observed in other experiments [81,82]. These experiments found that the x_F distribution for kaons produced by neutrinos had a mean of +0.10, with a symmetric distribution peaked at the same value. The difference can

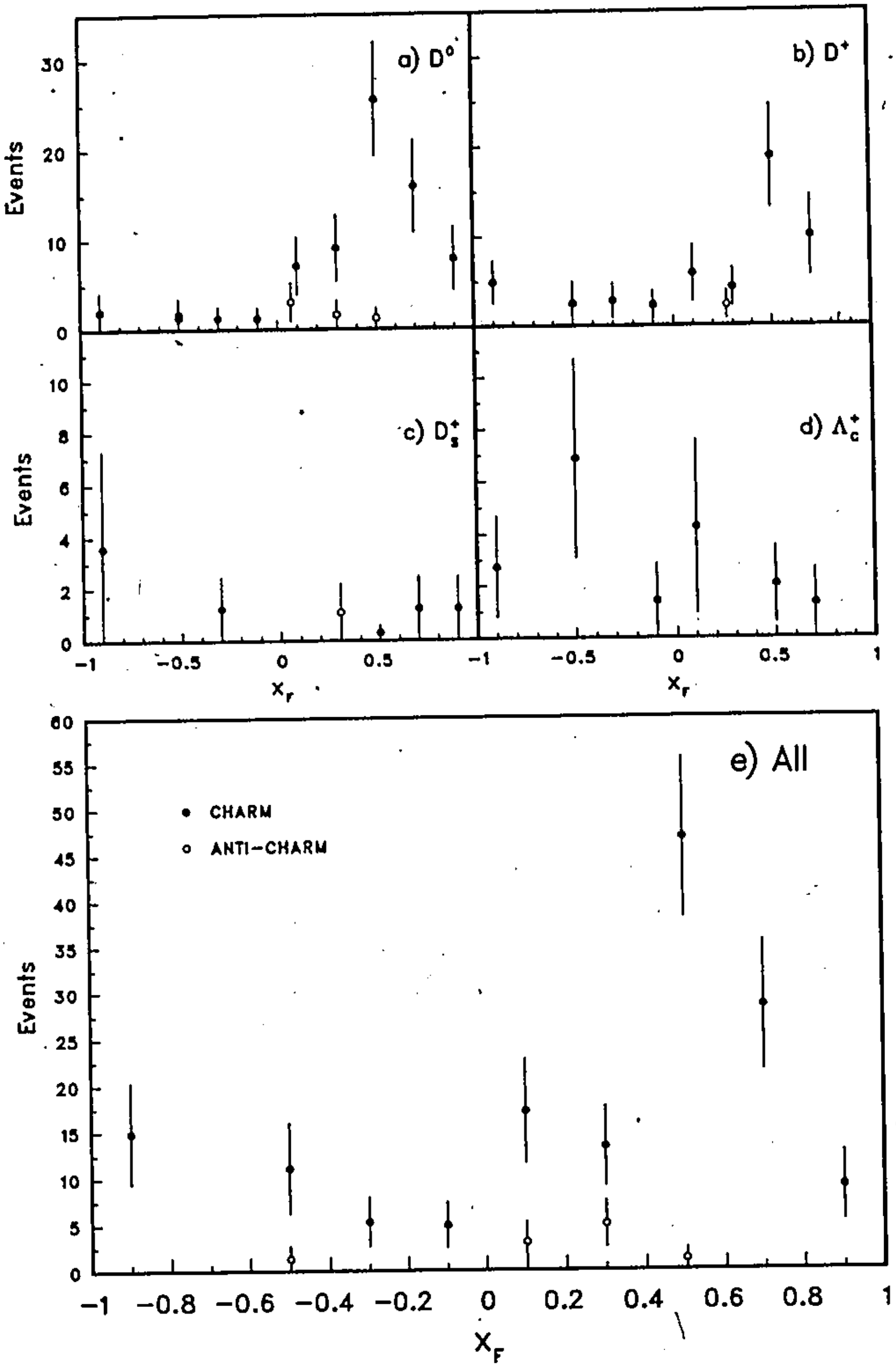

Figure 61: x_F distribution for charmed-particles.

be seen more by using the asymmetry parameter

$$A = \frac{N_F - N_B}{N_F + N_B}$$

where N_F and N_B are the number of particles in the positive and negative x_F regions respectively. Using the charmed particles data we find $A = 0.523 \pm 0.094$ which is much larger than the value quoted by the Fermilab 15-ft bubble chamber collaboration [81] who found $A = 0.16 \pm 0.02$ for the K^0. The production of charmed particles is, thus, very different from strange particle production.

The Feynman-x distribution for the Λ_c^+'s is seen to be flat (as is the Z distribution), and noticeably different from most of the charmed mesons. The mean x_F for the 11.5 $\Lambda_c^+$was found to be -0.22 (The half event is the ambiguous D_s^+/Λ_c^+ event, the three missing events are the quasi-elastic Λ_c^+ events), and the asymmetry $A = -0.13 \pm 0.31$. The asymmetry parameter is very uncertain because of the low number of tagged Λ_c^+ events. In references [81] and [82] the distributions for the Λ^0 were found to have a mean of about -0.30 with the peak of the distributions at about the same point; the asymmetry parameters were found to be -0.71 ± 0.02 and -0.59 ± 0.08. Thus, the asymmetry appears to be much more negative for the Λ^0 than for the Λ_c^+ , although the statistics are too low. The flat distribution comes about for the same reasons as the Z distribution of the Λ_c^+; the Λ_c^+ are a mixture of target and current fragments with the events close to $x_F = -1$ being target fragments.

6.16 Transverse Momentum Distribution

The p_{out} and $p_\perp^2$ distributions are shown in Figures 62 and 63. The p_{out} distribution is a falling distribution with a mean value of 0.33 GeV/c for the charmed-particles. The distribution of the D_s^+ and Λ_c^+ appear to be almost flat; unfortunately, the statistics are too low to tell if this is significant. In comparing the p_{out} and the $p_\perp$ distributions it is found that $< p_{\text{out}}^2 >= 0.17$, and $< p_\perp^2 >= 0.36$ (for events below 2.0 $(\text{GeV/c})^2$), and thus $< p_{\text{out}}^2 > \simeq \frac{1}{2} < p_\perp^2 >$ as expected.

The $p_\perp^2$ distribution was fitted to $e^{-Bp_\perp^2}$ by minimizing the χ^2 of the fit. The

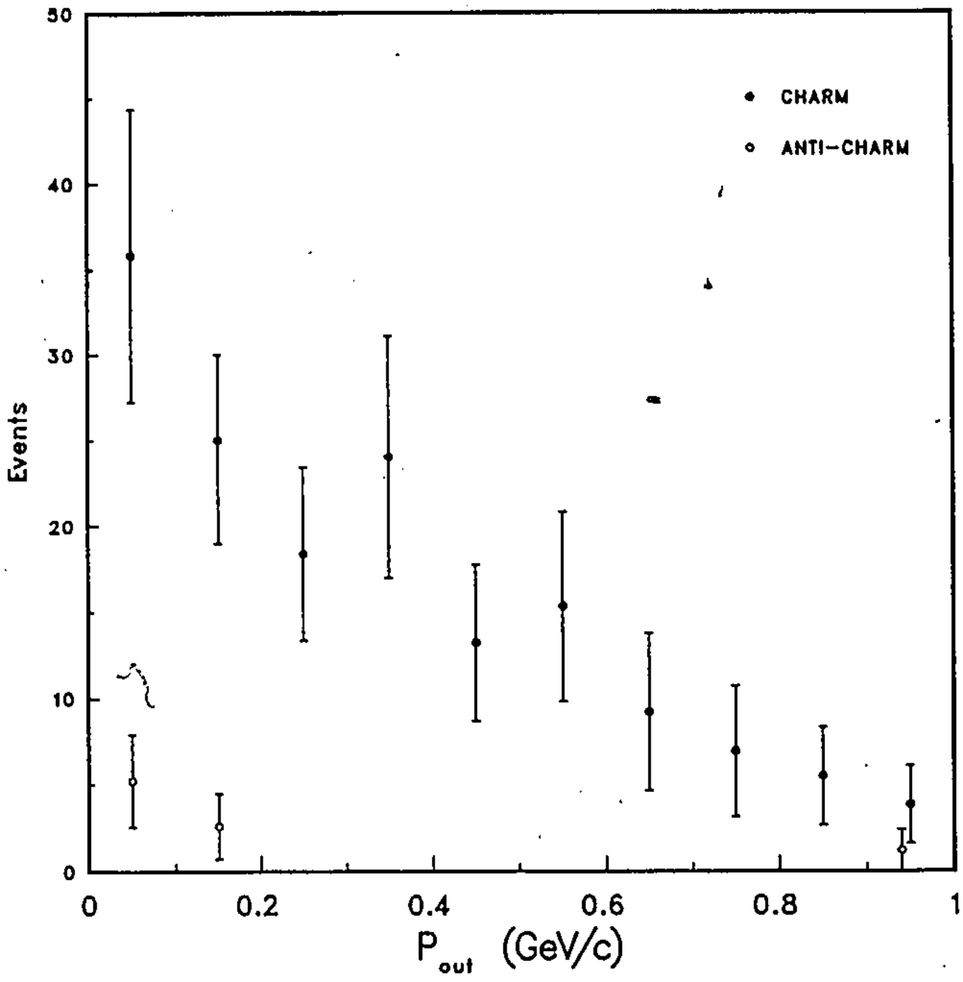

Figure 62: p_{out} distribution.

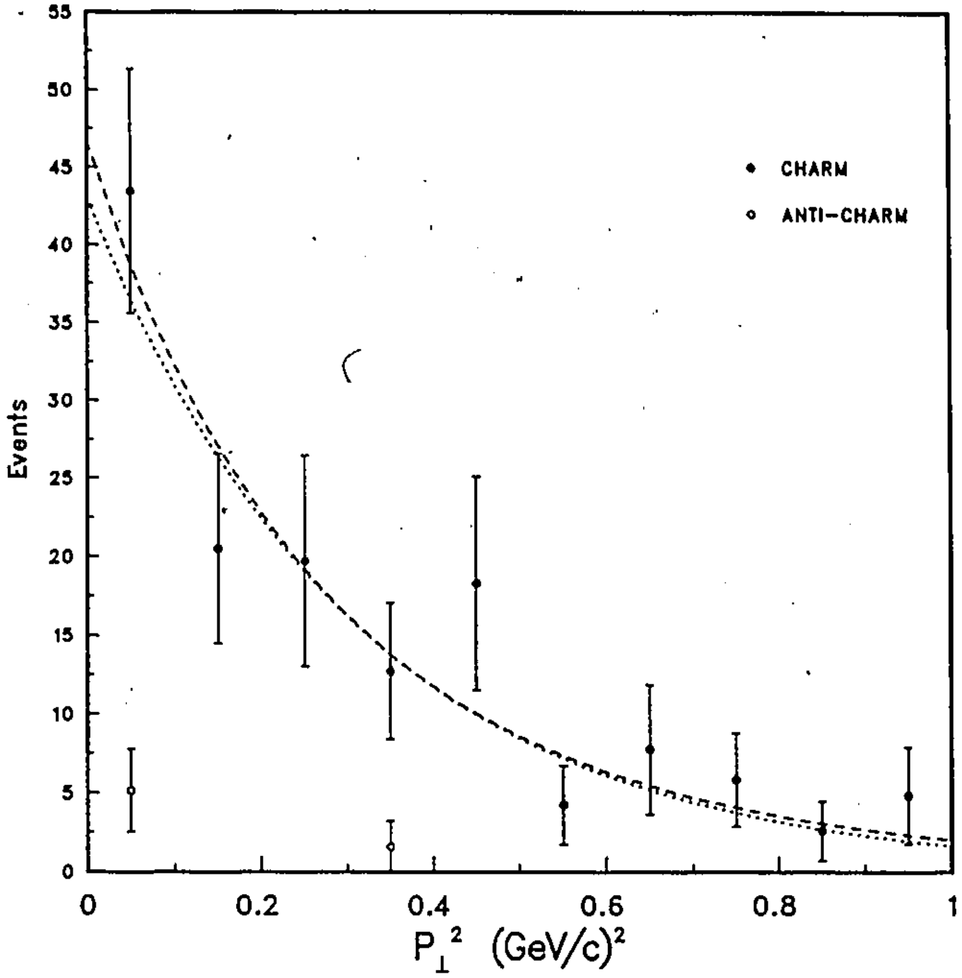

Figure 63: $p_\perp^2$ distribution.

value of B was determined to be $B = 3.25 \pm 0.37$ (GeV/c)$^{-2}$ with a χ^2 of 6.6 for 9 degrees of freedom; the resulting distribution is the dotted curve in Figure 63. This result can be compared with a study of the production of strange particles by neutrinos which gave [81] $B = 4.68 \pm 0.18$ (GeV/c)$^{-2}$ for the K^0 and 4.53 ± 0.21 (GeV/c)$^{-2}$ for the Λ^0. Thus, the $p_\perp^2$ distribution appears to drop off much more rapidly for charmed particles than for strange particles. However, the mean $p_\perp^2$ value found for the strange particles was $< p_\perp^2 >= 0.269$ (GeV/c)^2, which can be compared with our value of $< p_\perp^2 >= 0.36$ (GeV/c)^2. The reason why for the larger value of the mean $p_\perp^2$ for charmed particles is an excess of events at large $p_\perp^2$. In fact for the strange particles the exponential fit was done only for events below 0.5 (GeV/c)^2. The charmed-particle sample has too few events for this to really be noticeable.

Bosetti et al. [83] found that the $p_\perp^2$ distribution of ordinary particles could be described best by a function of the form e^{-Bm_T}, where $m_T^2 = p_\perp^2 + m^2$; they used a value of $B = 6$ (GeV/c)$^{-1}$. Using this form and fitting our data for the charmed particles, by varying B and m^2 and minimizing the χ^2, the following values were obtained: $B = 7.78 \pm 0.37$ (GeV/c)$^{-1}$ and $m^2 = 1.08 \pm 0.13$. The resulting distribution is the dashed curve in Figure 63, and it has a χ^2 of 6.3 for 9 degrees of freedom. Thus, with our limited statistics it is not possible to tell which function is best able to describe the charmed particle $p_\perp^2$ distribution.

6.17 Charm-Muon Angular Distribution

The angle ϕ_μ is defined as the opening angle between the muon and charmed-particle directions projected onto the X-Y plane. The distribution of ϕ_μ is shown in Figure 64 and, as would be expected, the distribution is found to peak at 180°. The muon and charm quark are expected to move back to back in the C.M. frame. There is no evidence for a resonant charm-muon production which would be shown by a peak in the ϕ_μ distribution at zero.

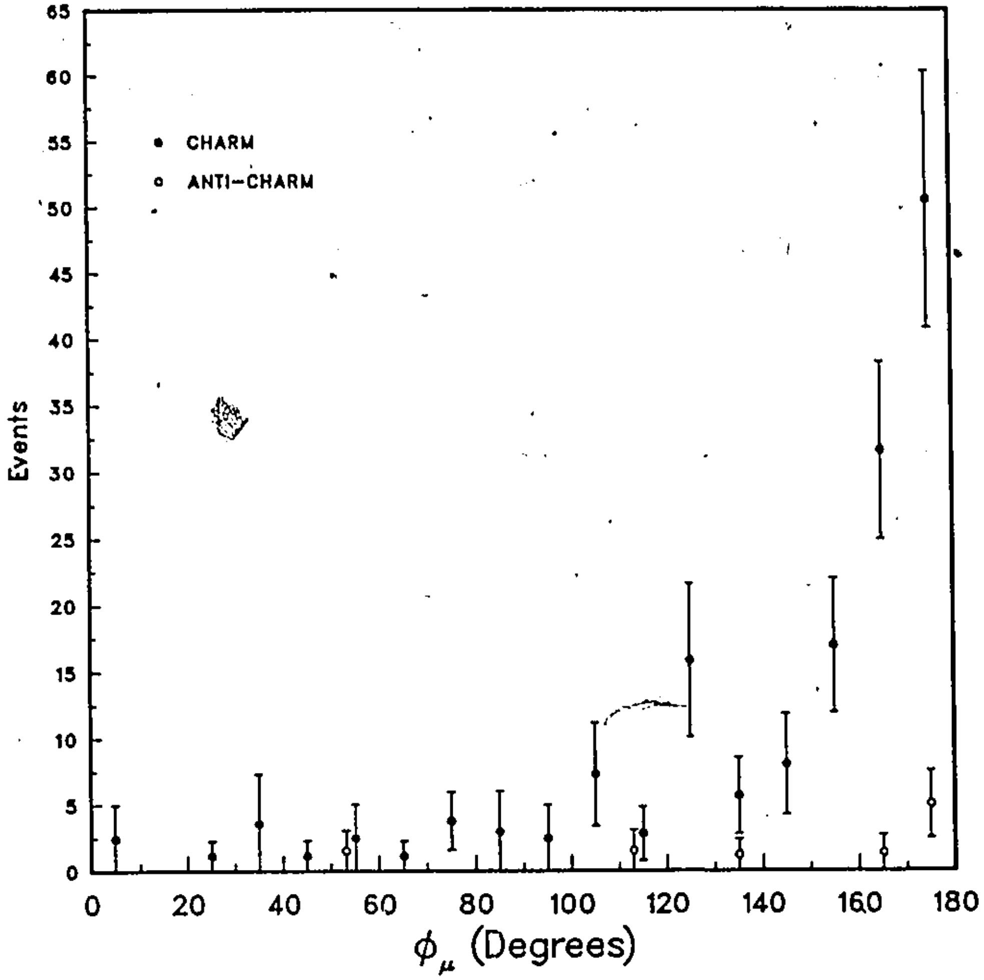

Figure 64: ϕ_μ distribution.

Chapter 7

Summary of Experimental Results

In the exposure of the E-531 emulsion target to the Fermilab wide-band neutrino beam a total of 3886 neutrino interactions were found; thirty-one events occurred while the spectrometer magnet was off and ,therefore, could not be used. It was estimated that 77% of these interactions were charged current ν_μ interactions. Of these about 4% (120 events) produced at least one charmed particle; there was also one neutral current interaction which produced two charmed particles. Thus, a total of 122 charmed particles were found in the emulsion target.

Using these charmed particles it was possible to calculate the relative production rates and limits for various modes. Some of these cross section ratios are listed below:

$$\frac{\sigma(\nu N \to c\,\mu^- X)}{\sigma(\nu N \to \mu^- X)} = 4.85^{+0.67}_{-0.63}\ \%$$

$$\frac{\sigma(\bar\nu N \to \bar c\,\mu^+ X)}{\sigma(\bar\nu N \to \mu^+ X)} = 5.75^{+2.88}_{-2.04}\ \%$$

$$\frac{\sigma(\nu N \to D^0\,\mu^- X)}{\sigma(\nu N \to \mu^- X)} = 2.19^{+0.39}_{-0.35}\ \%$$

$$\frac{\sigma(\nu N \to \nu\, c\, X)}{\sigma(\nu N \to \nu X)} < 3\ \% \qquad (90\%\ \text{C.L.})$$

Of the 122 found charm decay candidates 105 could be fitted to charmed particle decays, and used to calculated the charmed particles lifetimes. Using these events the following lifetimes were obtained:

$$\begin{aligned}
D^0 &= 4.3^{+0.7}_{-0.5}\,{}^{+0.1}_{-0.2} \times 10^{-13} \text{ seconds} \\
D_s^{\pm} &= 2.6^{+1.6}_{-0.9} \times 10^{-13} \text{ seconds} \\
\Lambda_c^{+} &= 2.0^{+0.7}_{-0.5} \times 10^{-13} \text{ seconds} \\
D^{\pm} &= 11.1^{+4.4}_{-2.9} \times 10^{-13} \text{ seconds}
\end{aligned}$$

Appendix A

E-531 Collaboration

(Second Run)

N. Ushida
Department of Physics, Aichi University of Education, Igaya-cho, Kariya-shi, Aichi 448, Japan.

T. Kondo
Fermi National Accelerator Laboratory, Batavia, Illinois 60510, U.S.A.

S. Tasaka
Faculty of Education, Gifu University, Gifu 501-11, Japan.

I. G. Park and J. S. Song
Department of Physics, Gyeongsang National University, Jinju 620, Korea.

T. Hara, Y. Homma and Y. Tsuzuki
College of Liberal Arts, Kobe University, Tsurukabuto, Nada-ku, Kobe 657, Japan.

G. Fujioka, H. Fukushima, Y. Takahashi, S. Tatsumi and C. Yokoyama
Department of Physics, Kobe University, Rokkodai-cho, Nada-ku, Kobe 657, Japan.

K. Fujiwara and K. Taruma
Graduate School of Science and Technology, Kobe University, Rokkodai-cho, Nada-ku, Kobe 657, Japan.

S. Y. Bahk , C. O. Kim and J. N. Park
Department of Physics, Korea University, Seoul 132, Korea.

D. C. Bailey , S. Conetti, P. Mercure, J. Trischuk and M. Turçotte
Department of Physics, McGill University, Montreal, Quebec H3A 2T8, Canada.

S. Aoki, K. Chiba, H. Fuchi, K. Hoshino, K. Kodama, R. Matsui, M. Miyanishi M. Nakamura, K. Nakazawa, K. Niu, K. Niwa, M. Ohashi, H. Sasaki, Y. Tomita, N. Torii, O. Yamakawa, and Y. Yanagisawa
Department of Physics, Nagoya University, Furo-cho, Chikusa-ku, Nagoya 464, Japan.

G. J. Aubrecht II, S. Errede , A. Gauthier, M. J. Gutzwiller , S. Kuramata, G. Oleynik, N. W. Reay, K. Reibel, R. A. Sidwell, and N. R. Stanton
Physics Department. The Ohio State University, Columbus, Ohio 43210, U.S.A.

K. Moriyama and H. Shibata
Physics Department, Okayama University, Tsushimanaka, Okayama 700, Japan.

O. Kusumoto, Y. Noguchi, T. Okusawa, M. Teranaka and J. Yamato
Physics Department, Osaka City University, Sugimoto, Sumiyoshi-ku, Osaka 558, Japan.

H. Okabe and J. Yokota
Science Education Institute of Osaka Prefecture, Karita, Sumiyoshi-ku, Osaka 558, Japan.

S. G. Frederiksen, C. J. D. Hébert, J. Hébert, and B. McLeod
Department of Physics, University of Ottawa, Ottawa, Ontario K1N 6N5, Canada.

M. Kazuno, H. Shibuya
Physics Department, Toho University, Funabashi-shi, Chiba 274, Japan.

I. A. Lovatt, J. F. Martin, D. Pitman, J. D. Prentice, B. J. Stacey, and T.-S. Yoon
Physics Department, University of Toronto, Toronto, Ontario M5S 1A7, Canada

Y. Maeda
Faculty of Education, Yokohama National University, Tokiwadai, Hodogaya-ku, Yokohama 240, Japan.

Appendix B

Summary of Decay Hypotheses

This appendix summarizes the fitted decay modes and solutions for the various charmed-particle decays.

The 'Run' and 'Rec.' (Record) are the event numbers as recorded on the magnetic data tapes.

For the various event hypotheses, an underlined particle implies that the particle has been identified as such; the particles in brackets were unseen but were implied in the 0C solution. The events that have a decaying 'C' particle, an 'X' particle in the decay hypothesis, and/or no calculated lifetime were the unfittable events for which no hypothesis was determined. The momentum solution had to be estimated and was very uncertain. The 'NB' for one event stands for neutral baryon; for this event the decaying particle is not known very well.

'C.L.' stands for the fit confidence level (if known) for the constrained events.

'P_μ' is the momentum of the primary muon (if identified) and its is the sign of the muon; 'P_T' is the transverse momentum of all the charged decay tracks with respect to the direction of the charmed particle; 'P_c' is the fitted charm momentum used in the lifetime and charm kinematic calculations.

'D.L.' is the measured decay length of the decaying particle, and 'τ' is the lifetime of the particle.

The mass is the calculated mass of the constrained events.

#	Run	Rec.	Hypothesis	C.L.	P_μ (GeV/c)	P_T (GeV/c)	P_c (GeV/c)	D.L. (μm)	r (10^{-13} s)	Mass (GeV/c²)
1.	476	4449	$\Lambda_c^+ \rightarrow \underline{p}\,\underline{\pi}^+\underline{\pi}^-(\bar{K}^0)$	–	−52	?	2.7	27.7	0.79 0.08	
				–		?	4.8		0.44 0.05	
2.	478	2638	$D^0 \rightarrow \underline{\pi}^-\pi^-\underline{\pi}^+\underline{\pi}^+K^-\pi^+\pi^0$	?	−4	?	7.5	126	1.03 0.08	1897 26
3.	486	6857	$D^{*+} \rightarrow D^0\pi^+$ $D^0 \rightarrow K^-\pi^-\underline{\pi}^+\pi^+(\pi^0)$	?	?	?	12.9	256	1.24 0.09	
4.	493	177	$D^0 \rightarrow \pi^+\underline{\pi}^-K_L^0$	?	−17	?	11.3	324	1.77 0.13	1819 80
5.	493	1235	$D^+ \rightarrow \pi^+\pi^+\pi^-K_L^0$	?	−7	?	11.9	2203	11.5 1.2	2061 156
			$D_s^+ \rightarrow \pi^+\pi^+K^-K_L^0$	?			11.7		12.7 0.8	2246 166
			$\Lambda_c^+ \rightarrow \pi^+\pi^+K^-n$	?			13.3		12.6 1.9	2330 123
6.	498	4985	$\Lambda_c^+ \rightarrow \underline{\pi}^+\underline{\pi}^-\underline{\pi}^+\Lambda^0$	?	−14	?	8.4	180	1.63 0.05	2274 41
7.	499	4713	$\Lambda_c^+ \rightarrow \pi^+\underline{\Sigma}^0$	?	−97	?	4.2	366	6.60 0.19	2269 17
8.	512	5761	$D^+ \rightarrow K^-\pi^+\underline{\pi}^+\pi^0$	?	−62	?	10.4	457	2.77 0.05	1829 35
			$D_s^+ \rightarrow K^-K^+\underline{\pi}^+\pi^0$	?			10.3		3.00 0.05	2011 33
9.	513	8010	$\bar{D}^0 \rightarrow K^+\pi^+\underline{\pi}^-\underline{\pi}^-\pi^0$	?	+12	?	9.2	27	0.18 0.02	1766 48
10.	518	4935	$D^0 \rightarrow \pi^+K^-\pi^0\pi^0$	?	−4	?	30.1	116	0.24 0.02	1935 132

#	Run	Rec.	Hypothesis	C.L.	P_μ (GeV/c)	P_T (GeV/c)	P_c (GeV/c)	D.L. (μm)	τ (10^{-13} s)	Mass (GeV/c^2)
11.	522	2107	$D^+ \rightarrow \pi^+\underline{\pi}^+K^-(\pi^0)$	–	−40	?	23.5	13600	36.0 1.8	
							31.7		26.7 1.3	
			$D_s^+ \rightarrow K^+\underline{\pi}^+K^-(\pi^0)$	–			22.5		40.9 1.9	
							32.7		28.1 1.1	
			$\Lambda_c^+ \rightarrow p\underline{\pi}^+K^-(\pi^0)$	–			22.5		46.0 2.5	
							31.5		32.9 1.3	
12.	522	3061	$D^0 \rightarrow \pi^-\pi^+\underline{\mu}^+K^-(\nu_\mu)$	–	−59	?	35.5	5479	9.58 0.36	
							58.5		5.72 0.22	
13.	527	3682	$D_s^- \rightarrow \underline{\pi}^+\underline{\pi}^-\pi^-\pi^0$	?	+37	?	12.2	670	3.70 0.09	2026 56
14.	529	271	$D^+ \rightarrow \pi^+\pi^0(\bar{K}^0)$	–	−45	?	55.4	2547	2.9 0.1	
			$D_s^+ \rightarrow K^+(\bar{K}^0)$	–			43.1		4.0 0.1	
			$D_s^+ \rightarrow K^+\pi^0(\bar{K}^0)$	–			38.4		4.5 0.1	
15.	529	3013	$D^0 \rightarrow K^-\pi^+\pi^0$	?	?	?	12.9	626	3.02 0.18	1856 79
16.	529	3013	$\bar{D}^0 \rightarrow K^+K^-$	?	?	?	47.7	3307	4.59 0.19	1832 124
17.	533	7152	$D^+ \rightarrow \pi^+\pi^0(\bar{K}^0)$	–	−8	?	40.1	5246	8.1 0.1	
			$D_s^+ \rightarrow K^+(\bar{K}^0)$	–			34.8		10.2 0.1	

#	Run	Rec.	Hypothesis	C.L.	P_μ (GeV/c)	P_T (GeV/c)	P_c (GeV/c)	D.L. (μm)	τ (10^{-13} s)	Mass (GeV/c^2)
18.	546	1339	$D^+ \to K^-\pi^+\underline{\mu}^+(\nu_\mu)$	–	−6	?	16.6	2150	8.06 0.22	
			$D_s^+ \to \pi^-\pi^+\underline{\mu}^+(\nu_\mu)$	–			13.3		10.94 0.16	
							36.8		2.95 0.02	
19.	547	2197	$D^0 \to \pi^+\pi^-\underline{\pi}^+K^-\pi^0$	?	−38	?	23.6	4056	10.70 0.34	1861 39
20.	547	3192	$D^+ \to \pi^+K^-\pi^+$	?	−15	?	9.4	185	1.23 0.08	1717 260
			$D^+ \to \pi^+K^-\pi^+\pi^0$	?			9.7		1.19 0.07	2036 291
			$D_s^+ \to \pi^+\pi^-\pi^+\pi^0$	?			10.8		1.15 0.07	2209 323
21.	547	3705	$D^{*+} \to D^0\pi^+$ $D^0 \to K^-\pi^+\underline{\pi}^+\pi^-$	?	−96	?	13.5	748	3.44 0.21	1947 99
22.	549	4068	$\Lambda_c^+ \to \underline{p}\,K^-\underline{\pi}^+(\pi^0)$	–	−10	?	1.9	20.6	0.77 0.07	
							2.5		0.63 0.07	
23.	556	152	$D^{*+} \to D^0\pi^+$ $D^0 \to \pi^-K^-\underline{\pi}^+\underline{\pi}^+\pi^0$	?	−10	?	15.4	41	0.17 0.01	1855 43
24.	567	2596	$\Lambda_c^+ \to \underline{p}\,K_L^0$	?	−6	?	5.8	175	2.30 0.08	2204 207
25.	577	5409	$D^{*+} \to D^0\pi^+$ $D^0 \to \pi^+\underline{\pi}^-(\bar{K}^0)$	?	−26	?	11.3	67	0.37 0.04	
26.	580	4508	$D^- \to \pi^-\underline{K}^+\underline{e}^-(\bar{\nu}_e)$	–	+6	?	9.5	2307	15.20 0.40	
							10.0		14.37 0.36	

#	Run	Rec.	Hypothesis	C.L.	P_μ (GeV/c)	P_T (GeV/c)	P_c (GeV/c)	D.L. (μm)	τ (10^{-13} s)	Mass (GeV/c^2)
27.	597	1851	$D_s^+ \to \underline{K}^+\underline{\pi}^-\underline{\pi}^+K_L^0$	?	?	?	9.3	130	0.97 0.09	2057 110
28.	597	6914	$D^0 \to \underline{e}^+K^-(\nu_e)$	–	−47	?	29.8	4374	9.13 0.44	
							62.7		4.33 0.21	
29.	598	1759	$D^+ \to K^-K^+\underline{\pi}^+\pi^0$	?	−10	?	17.4	1802	6.45 0.13	1862 25
			$\Lambda_c^+ \to K^-p\,\underline{\pi}^+\pi^0$	?			17.9		7.63 0.14	2179 38
30.	602	2032	$\Lambda_c^+ \to \underline{p}\,\pi^+\pi^-(\bar{K}^0)$	–	−19	?	6.3	282.5	3.40 0.10	
31.	610	4088	$\Lambda_c^+ \to \underline{\Lambda^0\pi}^+\underline{\pi}^-\underline{\pi}^+$	?	−7	?	4.7	221	3.60 0.19	2374 62
32.	635	4949	$NB \to \underline{p}\,\pi^-\underline{K}_s^0$	?	−84	?	4.64 0.51	4390	77.2 0.9	2450 15
			$NB \to \underline{p}\,K^-\underline{K}_s^0$				4.64 0.51		83.4 0.9	2647 11
33.	638	5640	$\bar{D}^0 \to \pi^-K^+\pi^0\pi^0$	?	+33	?	22.4	183	0.51 0.05	1825 68
34.	638	9417	$D_s^+ \to \underline{K}^+K^-\pi^+\pi^0$	?	−8	?	6.0	153	1.72 0.09	2050 45
35.	650	6003	$\Lambda_c^+ \to \underline{\Lambda^0\pi}^+\pi^-\underline{\pi}^+$	?	−14	?	5.7	40.6	0.54 0.03	2131 63
36.	654	3711	$D^0 \to \pi^+\underline{\pi}^+K^-\pi^-\underline{\pi}^-\underline{\pi}^+$	?	−4	?	19.2	6.5	0.020 0.003	1923 46
37.	656	2631	$D^+ \to \pi^+K^-\pi^+\pi^0$	?	−126	?	32.6	570	1.09 0.05	1933 73
			$D_s^+ \to K^+K^-\pi^+\pi^0$	?			32.4		1.19 0.05	2099 73
			$\Lambda_c^+ \to p\,K^-\pi^+$	?			31.7		1.36 0.06	2317 76

#	Run	Rec.	Hypothesis	C.L.	P_μ (GeV/c)	P_T (GeV/c)	P_c (GeV/c)	D.L. (μm)	τ (10^{-13} s)	Mass (GeV/c^2)
38.	661	2729	$D^{*+} \rightarrow D^0\pi^+$ $D^0 \rightarrow \underline{\pi}^+\underline{\pi}^-\underline{K}^0_s\pi^0$	?	−23	?	12.4	734	3.66 0.19	1835 41
39.	661	6517	$D^0 \rightarrow K^-\underline{\mu}^+(\nu_\mu)$	?	−19	?	22.8	2647	7.20 0.37	
							38.7		4.24 0.22	
40.	663	7758	$D^+ \rightarrow K^-\pi^+\underline{e}^+(\nu_e)$	–	−108	?	114.3	13000	7.08 0.44	
			$D_s^+ \rightarrow \pi^-\pi^+\underline{e}^+(\nu_e)$	–			96.8		8.36 0.47	
41.	665	2113	$C^+ \rightarrow \underline{\pi}^+\underline{\pi}^-\underline{\pi}^+(X^0)$	–	−24	?	3.1	33		
42.	666	5294	$D^0 \rightarrow K^-\pi^-\underline{\pi}^+\pi^+$	?	−96	?	55.2	653	0.73 0.04	1865 101
43.	670	12	$\Lambda_c^+ \rightarrow \underline{p}X^+X^-(X^0)$	–	−5	?	2.4	56		
44.	670	7870	$D^{*-} \rightarrow \bar{D}^0\pi^-$ $\bar{D}^0 \rightarrow K^+\underline{\pi}^-(\pi^0)$	–	+39	?	6.8	187	1.71 0.12	
45.	671	2642	$C^+ \rightarrow \underline{\pi}^+\underline{\pi}^-X^+(X^0)$	–	−17	?	3.1	2350		
46.	671	7015	$D_s^+ \rightarrow \underline{K}^+\underline{K}^0_s$	–	−7	?	2.8	65	1.57 0.12	2055 94
47.	1018	792	$D^{*+} \rightarrow \pi^+D^0$ $D^0 \rightarrow K^-\underline{\pi}^+(\pi^0)$	0.62	−10	0.11 0.06	9.50 0.30	2106 112	13.86 0.84	
48.	1026	133	$D^0 \rightarrow K^-\underline{\mu}^+(\nu_\mu)$	–	−45	0.42 0.04	14.2 0.2	2054 2	9.00 0.13	
49.	1028	277	$D_s^+ \rightarrow \underline{K}^-K^+\pi^+$	1.00	−9	0.02 0.18	7.19 0.05	246 5	2.25 0.05	1968 11
			$\Lambda_c^+ \rightarrow \underline{K}^-p\pi^+$	0.18			7.25 0.05		2.58 0.06	2261 10

#	Run	Rec.	Hypothesis	C.L.	P_μ (GeV/c)	P_T (GeV/c)	P_c (GeV/c)	D.L. (μm)	τ (10^{-13} s)	Mass (GeV/c^2)
50.	1028	4410	$D^0 \to K^-\pi^+(\pi^0)$	–	−62	0.46 0.03	4.0 0.1	705 20	10.8 0.5	
			$D^0 \to \pi^-\pi^+(\bar{K}^0)$	–			4.4 0.1		9.9 0.4	
51.	1046	2977	$D^+ \to \pi^+\pi^-\pi^+\pi^0$	0.75	?	0.73 0.16	10.7 0.2	154 5	0.90 0.03	1872 71
			$D_s^+ \to \pi^+\pi^-\pi^+\pi^0$	0.53			11.0 0.2		0.92 0.03	1872 71
			$\Lambda_c^+ \to p\,\pi^-\pi^+\pi^0$	0.73			10.8 0.3		1.09 0.05	2266 67
52.	1053	1113	$C^+ \to X^+(X^0)$	–	?	0.65	10.0	7490 10		
53.	1050	2844	$D^+ \to \underline{\pi}^+\pi^+\underline{\pi}^-\pi^0\pi^0$	0.23	−15	0.36 0.04	23.0 0.5	1292 4	3.50 0.08	1914 33
			$D_s^+ \to \underline{\pi}^+\pi^+\underline{\pi}^-\pi^0\pi^0$	0.18			24.6 0.6		3.45 0.08	1914 33
54.	1057	2341	$D^0 \to \pi^+K^-\pi^0$	0.61	−38	0.73 0.05	32.0 3.1	120 2	0.23 0.02	2118 234
55.	1066	119	$D^0 \to \underline{\pi}^+K^-(\pi^0)$	–	−8	0.23 0.01	3.50 0.01	383.4 0.3	6.81 0.02	
			$D^0 \to \underline{\pi}^+\pi^-(\bar{K}^0)$	–			3.78 0.01		6.31 0.02	
56.	1068	5090	$D^+ \to \underline{\pi}^+K^-\pi^+(\pi^0)$	–	−12	0.42 0.01	13.7 0.8	827 3	3.76 0.22	
			$D_s^+ \to \underline{\pi}^+\pi^-\pi^+(\pi^0)$	–			12.8 0.6		4.25 0.20	
57.	1070	4557	$D^0 \to K^-\underline{\pi}^-\underline{\pi}^+\underline{\pi}^+(\pi^0)$	–	−15	0.44 0.04	5.83 0.20	338 15	3.61 0.20	
58.	1070	5521	$D^0 \to K^-\pi^+\pi^+\pi^-\pi^0$	0.16	−11	0.16 0.01	17.8 0.3	2128 10	7.4 0.1	1876 17

#	Run	Rec.	Hypothesis	C.L.	P_μ (GeV/c)	P_T (GeV/c)	P_c (GeV/c)	D.L. (μm)	τ (10^{-13} s)	Mass (GeV/c^2)
59.	1073	192	$D^+ \to \pi^+\pi^+\pi^-(\bar{K}^0)$	–	−16	0.18 0.02	6.8 0.5	927 1	8.50 0.63	
			$D^+ \to \pi^+\pi^+K^-(\pi^0)$	–			6.0 0.4		9.63 0.64	
				–			4.7 0.3		12.30 0.79	
			$D_s^+ \to \pi^+\pi^+\pi^-(\pi^0)$	–			4.4 0.3		13.85 0.94	
			$D_s^+ \to K^+\pi^+\pi^-(\bar{K}^0)$	–			6.0 0.4		10.16 0.68	
			$D_s^+ \to K^+\pi^+K^-(\pi^0)$	–			5.6 0.3		10.88 0.58	
				–			4.7 0.3		12.97 0.83	
60.	1080	2521	$D^+ \to \pi^+K^-\pi^+\pi^0$	0.40	−45	0.22 0.14	22.5 0.7	188 4	0.52 0.02	1704 133
			$D_s^+ \to \pi^+K^-K^+\pi^0$	0.61			20.6 1.0		0.60 0.03	1884 115
			$D_s^+ \to K^+K^-\pi^+\pi^0$	0.72			17.7 0.4		0.70 0.02	2015 161
			$D_s^+ \to K^+K^-\pi^+$	0.12			20.7 0.4		0.60 0.02	1802 135
			$\Lambda_c^+ \to \pi^+K^-p$	0.18			18.5 2.0		0.77 0.09	2147 129
			$\Lambda_c^+ \to \pi^+K^-p\,\pi^0$	0.72			18.3 2.0		0.78 0.09	2317 137
			$\Lambda_c^+ \to p\,K^-\pi^+$	0.07			14.0 0.4		1.02 0.04	2493 196
61.	1080	7420	$D^+ \to \underline{\pi}^-\underline{\pi}^+\pi^+\pi^0\pi^0$	0.67	−4	0.33 0.06	25.0 0.6	354 1	0.88 0.02	1828 58
			$D_s^+ \to \underline{\pi}^-\underline{\pi}^+\pi^+\pi^0\pi^0$	0.21			26.7 0.7		0.87 0.02	1828 58
			$\Lambda_c^+ \to \underline{\pi}^-\underline{\pi}^+p\,\pi^0\pi^0$	0.26			26.6 0.7		1.01 0.03	2175 45

#	Run	Rec.	Hypothesis	C.L.	P_μ (GeV/c)	P_T (GeV/c)	P_c (GeV/c)	D.L. (μm)	τ (10^{-13} s)	Mass (GeV/c^2)
62.	1086	3828	$D^0 \rightarrow K^-\pi^+(\pi^0)$	–	−42	0.45 0.05	7.48 0.05	34.0 0.5	0.28 0.00	
			$D^0 \rightarrow \pi^-\pi^+(\bar{K}^0)$	–			8.01 0.06		0.26 0.00	
63.	1089	5646	$\Lambda_c^+ \rightarrow \underline{K}^-\pi^+\underline{p}$	0.12	−11	0.10 0.03	5.22 0.03	275 5	4.01 0.08	2422 252
64.	1090	1701	$C^0 \rightarrow X^+X^-(X^0)$	–	?	0.20 0.01	4.00	353 24		
65.	1099	1180	$\bar{D}^0 \rightarrow \underline{\pi}^+\underline{\pi}^-(K^0)$	–	+11	0.20 0.01	2.84 0.02	654 20	14.32 0.45	
66.	1099	3226	$D^{*+} \rightarrow \underline{\pi}^+D^0$ $D^0 \rightarrow \underline{\pi}^-\pi^+K^-\pi^+$	0.32	−10	– –	4.41 0.02	486 20	6.9 0.3	1866 109
67.	1100	113	$D^0 \rightarrow \pi^+K^-\pi^0\pi^0$	0.66	−43	0.41 0.04	13.3 0.4	128 2	0.60 0.02	1861 57
68.	1105	4668	$D^+ \rightarrow \pi^+\pi^0K_L^0$	0.68	−19	0.79 0.02	12.5 0.6	321 2	1.60 0.08	1885 53
			$D_s^+ \rightarrow K^+\pi^0K_L^0$	0.05			11.7 0.5		1.80 0.08	2035 40
			$\Lambda_c^+ \rightarrow \pi^+\pi^0n$	0.76			13.0 0.8		1.88 0.12	2275 53
69.	1118	4569	$D^0 \rightarrow \underline{K}^-\pi^+\underline{\pi}^-\underline{\pi}^+\pi^0$	0.45	−13	0.17 0.02	8.5 0.2	1589 50	11.7 0.4	1862 15
70.	1122	7258	$\bar{D}^0 \rightarrow \pi^+\pi^-\pi^-\pi^+$	0.95	+111	0.02 0.03	21.5 0.2	1301 55	3.8 0.2	1877 25
71.	1131	423	$D^0 \rightarrow K^-\pi^+\pi^0$	0.02	−18	0.59 0.04	10.7 0.1	304 18	1.76 0.11	1976 65
72.	1148	5847	$D^0 \rightarrow \pi^-\underline{\pi}^+K_L^0$	0.36	−67	0.42 0.03	14.9 0.6	425 24	1.8 0.1	2150 201
73.	1158	5775	$C^\pm \rightarrow \underline{K}\,\underline{\pi}\,X\,(X^0)$	–	−16	?	1.0	9190		

#	Run	Rec.	Hypothesis	C.L.	P_μ (GeV/c)	P_T (GeV/c)	P_c (GeV/c)	D.L. (μm)	τ (10^{-13} s)	Mass (GeV/c^2)
74.	1161	1632	$D^0 \rightarrow \pi^+ K^- \pi^0$	0.59	−37	0.36 0.02	15.6 0.4	2521 110	10.0 0.5	1805 84
75.	1162	971	$C^+ \rightarrow X^+ (X^0)$	–	?	0.44	10.0	789 44		
76.	1166	3069	$D^0 \rightarrow \pi^+ \underline{K}^- \pi^- \pi^+$	0.15	−10	0.09 0.17	9.2 0.1	201 12	1.4 0.1	1925 29
77.	1169	1620	$D^0 \rightarrow \pi^+ \pi^+ K^- \pi^-$	0.59	−11	0.13 0.07	49.2 1.5	4199 5	5.3 0.2	1943 89
			$D^0 \rightarrow \pi^+ \pi^+ \pi^- K^-$	0.39			48.9 1.4		5.3 0.2	1964 85
78.	1194	807	$D^+ \rightarrow K^- \underline{\pi}^+ \pi^+$	0.32	−31	0.12 0.06	22.7 0.3	14015 759	38.50 2.15	1900 39
			$D_s^+ \rightarrow K^- \underline{\pi}^+ K^+$	0.09			22.3 0.3		41.32 2.31	2035 36
			$\Lambda_c^+ \rightarrow \pi^- \underline{\pi}^+ p$	0.41			23.2 0.4		45.98 2.61	2282 35
79.	1195	4860	$\Lambda_c^+ \rightarrow \underline{\pi}^+ \Lambda^0 (\pi^0)$	–	−3	0.45 0.04	4.9 0.2	182 17	2.83 0.29	
80.	1198	1114	$C^+ \rightarrow X^+ (X^0)$	–	−5	0.99	8.0	82 1		
81.	1198	3153	$\Lambda_c^+ \rightarrow \underline{p} \pi^+ \pi^- K_L^0$	0.09	−9	0.05 0.10	7.1 0.8	82 9	0.88 0.14	2259 35
82.	1198	3877	$D^+ \rightarrow \pi^+ K^- \underline{\pi}^+ \pi^0$	0.26	−71	0.28 0.06	15.5 0.5	2280 148	9.17 0.66	1783 57
			$D_s^+ \rightarrow K^+ K^- \underline{\pi}^+ \pi^0$	0.99			13.1 0.3		11.44 0.79	1975 48
			$\Lambda_c^+ \rightarrow p \pi^- \underline{\pi}^+ \pi^0$	0.10			9.9 0.1		17.53 1.15	2513 67
83.	1203	1250	$D^0 \rightarrow \underline{\mu}^+ K^- (\nu_\mu)$	–	−63	0.27 0.08	5.4 0.3	25 2	0.29 0.03	
							3.1 0.2		0.50 0.05	

#	Run	Rec.	Hypothesis	C.L.	P_μ (GeV/c)	P_T (GeV/c)	P_c (GeV/c)	D.L. (μm)	τ (10^{-13} s)	Mass (GeV/c^2)
84.	1205	1433	$D^0 \rightarrow \underline{\mu}^+ K^- (\nu_\mu)$	–	−59	0.26 0.04	11.7 0.1	197 20	1.05 0.11	
							5.20 0.04		2.36 0.24	
85.	1207	1167	$D^0 \rightarrow K^- \pi^+ \underline{\pi}^+ \pi^-$	0.07	−9	0.11 0.04	20.0 0.1	1077 58	3.4 0.2	1873 25
86.	1208	1779	$C^+ \rightarrow X^+ X^- X^+ (X^0)$	–	−100	?	8.0	33800 1800		
87.	1208	2921	$D^0 \rightarrow \pi^+ K^- (\pi^0)$	–	−37	0.46 0.02	7.0 0.1	459 23	4.1 0.2	
			$D^0 \rightarrow \pi^+ \pi^- (\bar{K}^0)$	–			7.6 0.1		3.8 0.2	
88.	1208	2964	$D^{*+} \rightarrow D^0 \pi^+$ $D^0 \rightarrow K^- \pi^+ \pi^0 \pi^0$	0.05	−6	0.36 0.04	18.9 0.3	3477 100	11.4 0.4	1865 97
89.	1211	376	$D^0 \rightarrow \pi^+ \underline{\pi}^- \pi^0 \pi^0$	0.14	−18	0.32 0.03	15.2 0.3	452 15	1.85 0.07	1838 34
90.	1215	4119	$\Lambda_c^+ \rightarrow \underline{\pi}^+ \underline{p} K^-$	0.13	−9	0.16 0.07	3.23 0.02	62.8 0.2	1.48 0.01	2253 50
91.	1218	1980	$C^+ \rightarrow \underline{K}^+ X^- \underline{\pi}^+ (X^0)$	–	−42	0.45 0.04	9.0	4460 240		
92.	1222	281	$D_s^+ \rightarrow K^+ K^- \underline{\pi}^+$	0.13	−45	0.04 0.02	9.31 0.04	1051 28	7.42 0.20	1961 19
93.	1226	2884	$C^+ \rightarrow X^+ X^- X^+ (X^0)$	–	−20	?	1.0	518 5		
94.	1233	1678	$D^0 \rightarrow K^- \pi^+ (\pi^0)$	–	−3	0.08 0.09	11.0 0.1	437 28	2.5 0.2	
95.	1250	2883	$C^+ \rightarrow X^+ (X^0)$	–	−5	0.84	1.0	5150 35		

#	Run	Rec.	Hypothesis	C.L.	P_μ (GeV/c)	P_T (GeV/c)	P_c (GeV/c)	D.L. (μm)	τ (10^{-13} s)	Mass (GeV/c²)
96.	1256	2092	$D^+ \to \pi^+\pi^+K^-\pi^0\pi^0$	0.11	−38	0.23 0.01	16.1 0.6	3965 216	15.36 1.01	1709 82
			$D_s^+ \to \pi^+\pi^+K^-\pi^0K_L^0$	0.08			15.3 0.8		17.04 1.29	1940 93
			$D_s^+ \to K^+\pi^+K^-\pi^0\pi^0$	0.44			15.9 0.6		16.40 1.09	1938 71
			$D_s^+ \to K^+\pi^+\pi^-\pi^0K_L^0$	0.03			15.4 0.8		16.93 1.27	1873 88
			$\Lambda_c^+ \to p\,\pi^+\pi^-\pi^0\pi^0$	0.39			16.0 0.6		18.86 1.25	2236 62
97.	1261	5401	$D^+ \to K^-\pi^+\underline{\mu}^+(\nu_\mu)$	–	−12	0.21 0.07	14.8 1.3	3896 211	16.42 1.69	
							10.3 0.5		23.59 1.72	
			$D_s^+ \to \pi^-\pi^+\underline{\mu}^+(\nu_\mu)$	–			19.8 1.9		12.94 1.43	
							10.1 0.4		25.36 1.70	
98.	1263	3857	$D^- \to \pi^-\pi^-K^+\pi^0$	0.09	+9	–	6.5 0.4	94 1	0.90 0.06	2150 172
			$F^- \to \pi^-\pi^-\pi^+\pi^0$	0.97			8.7 0.1		0.71 0.01	1975 125
99.	1263	5821	$D^+ \to \pi^+\pi^+K^-$	0.10	−6	0.05 0.04	14.1 0.3	1281 59	5.67 0.29	1935 29
			$D_s^+ \to \pi^+K^+K^-$	0.12			14.1 0.3		5.97 0.30	2028 27
			$\Lambda_c^+ \to \pi^+p\,K^-$	0.78			14.5 0.3		6.72 0.34	2273 23
100.	1269	3706	$D^0 \to K^-\pi^+\pi^0\pi^0$	0.33	?	0.12 0.01	25.8 0.8	760 40	1.8 0.1	1676 70
			$\bar{D}^0 \to \pi^-K^+\pi^0\pi^0$	0.89			19.5 0.3		2.4 0.1	1780 57
101.	1269	5327	$D^0 \to K^-\pi^+(\pi^0)$	–	−31	0.52 0.03	6.8 1.0	994 5	9.2 1.3	
							4.4 0.3		14.1 1.0	
			$D^0 \to \pi^-\pi^+(\bar{K}^0)$	–			4.3 0.1		14.3 0.3	

#	Run	Rec.	Hypothesis	C.L.	P_μ (GeV/c)	P_T (GeV/c)	P_c (GeV/c)	D.L. (μm)	τ (10^{-13} s)	Mass (GeV/c^2)
102.	1271	7264	$D^0 \rightarrow \pi^- \underline{\pi}^+ \pi^- \pi^+ (\bar{K}^0)$	–	−27	0.50 0.10	4.4	18.0 0.5	0.3	
			$D^0 \rightarrow K^- \underline{\pi}^+ \pi^- \pi^+ (\pi^0)$				3.9		0.3	
			$D^0 \rightarrow \pi^- \underline{\pi}^+ K^- \pi^+ (\pi^0)$	–			3.8		0.3	
103.	1276	2132	$D^0 \rightarrow \underline{\pi}^+ K^- \pi^0$	0.78	−29	0.22 0.06	28.8 0.7	1332 74	2.88 0.17	1825 44
104.	1277	2257	$\Lambda_c^+ \rightarrow \underline{\pi}^- \underline{\pi}^+ \underline{p} (K_L^0)$	–	−9	0.16 0.05	3.67 0.10	18 3	0.37 0.06	
105.	1286	4471	$C^+ \rightarrow X^+ X^- X^+ (X^0)$	–	−9	?	6.0	165 1		
106.	1296	1709	$D^{*+} \rightarrow D^0 \pi^+$ $D^0 \rightarrow \pi^+ \pi^- \pi^+ K^-$	0.65	?	0.06 0.09	3.8 0.1	112 8	1.8 0.1	1868 73
107.	1296	2462	$D^+ \rightarrow \pi^+ \pi^- \pi^+ (\bar{K}^0)$	–	−63	0.29 0.01	9.6 0.2	2891 92	18.78 0.71	
			$D_s^+ \rightarrow \pi^+ \pi^- \pi^+ (\pi^0)$	–			8.5 0.2		22.36 0.88	
			$D_s^+ \rightarrow \pi^+ \pi^- K^+ (\bar{K}^0)$	–			9.8 0.2		19.40 0.73	
			$D_s^+ \rightarrow K^+ \pi^- \pi^+ (\bar{K}^0)$	–			9.9 0.3		19.20 0.84	
			$\Lambda_c^+ \rightarrow \pi^+ \pi^- p (\bar{K}^0)$	–			11.7 0.2		18.81 0.68	
				–			10.6 0.3		20.76 0.88	
108.	1296	3516	$D^0 \rightarrow \pi^+ K^- \underline{\pi}^- \pi^+$	0.82	−19	0.04 0.13	4.62 0.02	273 19	3.7 0.3	1903 95
109.	1303	4151	$D^0 \rightarrow \pi^- \pi^+ K_L^0$	0.37	−9	0.80 0.53	13.2 0.8	15.3 1.0	0.07 0.01	1890 60
110.	1304	4693	$D^0 \rightarrow K^- \pi^+ \underline{\pi}^- \underline{\pi}^+ \pi^0$	0.02	−3	0.18 0.02	12.4 0.3	374 1	1.88 0.04	1996 68

#	Run	Rec.	Hypothesis	C.L.	P_μ (GeV/c)	P_T (GeV/c)	P_c (GeV/c)	D.L. (μm)	τ (10^{-13} s)	Mass (GeV/c^2)
111.	1305	5297	$D^+ \rightarrow K^-\pi^+\pi^+\pi^0$	0.80	−5	0.55 0.37	32.2 2.0	164 17	0.32 0.04	1899 107
			$D_s^+ \rightarrow K^-K^+\pi^+\pi^0$	0.75			31.9 2.0		0.34 0.04	2041 100
			$D_s^+ \rightarrow \pi^-\pi^+\pi^+\pi^0$	0.43			33.6 2.0		0.32 0.04	1852 216
			$\Lambda_c^+ \rightarrow K^-p\pi^+\pi^0$	0.66			31.3 2.0		0.40 0.05	2285 91
112.	1310	3118	$C^+ \rightarrow \underline{\pi}^+X^-X^+(X^0)$	–	−7	?	2.0	3841 3		
113.	1311	3060	$D^+ \rightarrow \pi^+\pi^-\pi^+(\bar{K}^0)$	–	−7	0.47 0.03	9.4 0.5	944 10	6.26 0.34	
			$D^+ \rightarrow \pi^+K^-\pi^+(\pi^0)$	–			8.6 0.4		6.84 0.33	
			$D_s^+ \rightarrow \pi^+\pi^-\pi^+(\pi^0)$	–			8.1 0.3		7.66 0.30	
			$D_s^+ \rightarrow \pi^+K^-\pi^+(\bar{K}^0)$	–			9.8 0.5		6.33 0.33	
			$D_s^+ \rightarrow K^+\pi^-\pi^+(K^0)$	–			9.9 0.6		6.27 0.39	
			$D_s^+ \rightarrow K^+K^-\pi^+(\pi^0)$	–			8.8 0.4		7.05 0.33	
114.	1317	3892	$D^0 \rightarrow K^-\pi^+$	0.66	−7	0.21 0.17	58.3 1.0	1058 54	1.13 0.06	1600 250
115.	1318	3525	$D^0 \rightarrow \underline{\pi}^+\pi^-K^-\underline{\pi}^+$	0.01	−6	0.29 0.06	10.9 0.1	129 14	0.74 0.08	1839 15
116.	1322	1554	$D^+ \rightarrow K^-\pi^+\pi^+$	0.14	−36	0.07 0.07	20.1 0.4	1791 74	5.56 0.25	1976 56
			$D_s^+ \rightarrow \pi^-\pi^+\pi^+$	0.56			23.8 0.5		4.95 0.23	1905 59
117.	1322	1734	$D^0 \rightarrow K^-\pi^+$	0.18	?	0.08 0.21	26.2 0.3	3006 3	7.13 0.08	1932 124

#	Run	Rec.	Hypothesis	C.L.	P_μ (GeV/c)	P_T (GeV/c)	P_c (GeV/c)	D.L. (μm)	τ (10^{-13} s)	Mass (GeV/c^2)
118.	1329	3624	$D^0 \rightarrow K^- K^+ \pi^0$	0.64	−8	0.63 0.03	15.1 0.3	2107 113	8.7 0.5	1846 27
119.	1334	3546	$D^0 \rightarrow K^- \underline{\pi}^+ (\pi^0)$	–	−7	0.81 0.02	8.3 0.8	1306 11	9.8 1.0	
			$D^0 \rightarrow \pi^- \underline{\pi}^+ (\bar{K}^0)$	–			7.7 0.7		10.5 1.0	
120.	1340	1667	$D_s^+ \rightarrow K^- K^+ \pi^+ \pi^0$	0.82	−5	0.37 0.07	13.6 0.3	134 9	0.65 0.05	1968 33
121.	1364	1946	$C^+ \rightarrow X^+ (X^0)$	–	−20	0.43	10.0	661 20		
122.	1371	503	$D^0 \rightarrow K^- \pi^+ \pi^0$	0.59	−67	0.67 0.12	22.4 1.3	157 10	0.44 0.04	1987 123

Appendix C

Charmed-Particle Kinematic Parameters

This appendix summarizes the various kinematic variables that were calculated for all the charmed-particles found in the emulsion.

The 'Run' and 'Rec.' correspond to the event numbers as recorded on the magnetic data tapes.

The 'ID' of the particles is the type of particle that the decay was assumed to be in the calculation of the various parameters. The weight 'D.W. $\pm\Delta D.W.$' was the decay weight estimated for the various events, and 'E.W.' was the event weight that was assigned to each event.

In the Comment column those events with a *charm* or $\overline{charm}$ tag were decays that could work as a charm decay or an anti-charm decay. The 'Q.E.' events were the quasi-elastically produced Λ_c^+.

E_{had} corresponds to the total hadronic energy in the event and is equal to ν plus the mass/energy of the struck nucleon.

The remaining variables were discussed and defined in Section 1.5.

#	Run	Rec.	ID	D.W.	$\Delta D.W.$	E.W.	E_ν	ν	Comment
1	476	4449	Λ_c^+	1.178	0.092	1.095	74.00	21.37	
2	478	2638	D^0	1.473	0.169	1.172	12.30	7.89	
3	486	6857	D^0	1.531	0.142	1.081	22.90	21.06	
4	493	177	D^0	1.516	0.148	1.030	46.90	29.66	$\overline{\mathit{charm}}$
5	493	1235	D^+	1.101	0.063	1.013	47.10	40.11	$\overline{\mathit{charm}}$
6	498	4985	Λ_c^+	1.104	0.069	1.201	22.60	9.09	
7	499	4713	Λ_c^+	2.731	0.443	1.080	117.30	20.21	
8	512	5761	D^+	1.093	0.061	1.050	77.40	14.90	
9	513	8010	$\bar{D}^0$	1.493	0.156	1.037	35.40	23.35	
10	518	4935	D^0	1.629	0.124	1.079	44.90	40.99	$\overline{\mathit{charm}}$
11	522	2107	D^+	1.196	0.086	1.015	85.30	45.30	
12	522	3061	D^0	1.666	0.098	1.006	138.80	79.98	
13	527	3682	D_s^-	1.076	0.081	1.013	69.70	32.66	
14	529	271	D^+	2.828	0.513	1.027	99.30	53.85	
15	529	3013	D^0	1.487	0.117	1.033	68.00	67.96	
16	529	3013	$\bar{D}^0$	1.487	0.117	1.042	68.00	67.96	
17	533	7152	D^+	2.640	0.371	1.006	69.40	61.07	
18	546	1339	D^+	1.130	0.071	1.079	33.00	26.59	
19	547	2197	D^0	1.603	0.126	1.032	68.30	29.84	
20	547	3192	D^+	1.088	0.053	1.026	35.40	20.47	$\overline{\mathit{charm}}$
21	547	3705	D^0	1.692	0.182	1.268	112.90	16.75	
22	549	4068	Λ_c^+	1.254	0.101	1.141	27.20	16.78	
23	556	152	D^0	1.552	0.135	1.106	30.20	20.40	
24	567	2596	Λ_c^+	2.556	0.386	1.164	14.60	9.10	
25	577	5409	D^0	1.516	0.148	1.037	44.00	18.36	$\overline{\mathit{charm}}$
26	580	4508	D^-	1.091	0.059	1.105	24.40	18.19	
27	597	1851	D_s^+	1.084	0.086	1.262	15.80	11.66	
28	597	6914	D^0	1.660	0.098	1.011	117.00	69.38	
29	598	1759	D^+	1.221	0.132	1.116	32.90	23.00	
30	602	2032	Λ_c^+	1.122	0.074	1.130	30.10	11.23	
31	610	4088	Λ_c^+	1.145	0.086	1.934	11.80	4.39	Q.E.
32	635	4949	NB	1.536	0.116	1.040	111.20	27.87	
33	638	5640	$\bar{D}^0$	1.599	0.127	1.009	86.20	52.87	*charm*
34	638	9417	D_s^+	1.101	0.112	1.117	21.90	13.70	
35	650	6003	Λ_c^+	1.128	0.078	1.254	22.20	8.50	
36	654	3711	D^0	1.581	0.131	1.034	50.30	46.01	$\overline{\mathit{charm}}$
37	656	2631	D^+	1.225	0.110	1.024	171.60	46.60	
38	661	2729	D^0	1.527	0.142	1.063	40.10	16.84	$\overline{\mathit{charm}}$
39	661	6517	D^0	1.626	0.097	1.013	63.80	45.28	
40	663	7758	D^+	2.008	0,510	1.011	238.10	126.99	
41	665	2113	D^+	1.074	0.061	1.248	33.50	9.11	

#	Run	Rec.	ID	D.W.	$\Delta D.W.$	E.W.	E_ν	ν	Comment
42	666	5294	D^0	1.750	0.140	1.005	226.10	126.10	
43	670	12	D^+	1.079	0.061	1.508	10.30	5.60	
44	670	7870	$\bar{D}^0$	1.464	0.173	1.039	59.10	20.64	
45	671	2642	D^+	1.074	0.061	1.385	22.40	5.45	
46	671	7015	D_s^+	2.725	0.603	1.315	11.10	4.11	
47	1018	792	D^0	1.200	0.046	1.099	21.50	11.98	
48	1026	133	D^0	1.746	0.190	1.107	70.20	24.75	
49	1028	277	Λ_c^+/D_s^+	1.036	0.041	1.109	19.10	10.01	
50	1028	4410	D^0	1.237	0.048	1.012	99.40	36.90	$\overline{charm}$
51	1046	2977	D^+	1.027	0.039	1.188	15.30	12.56	
52	1050	2844	D^+	1.115	0.079	1.040	47.50	32.57	
53	1053	1113	D^+	2.342	0.364	1.038	39.10	36.56	
54	1057	2341	D^0	1.761	0.219	1.014	88.90	50.44	$\overline{charm}$
55	1066	119	D^0	1.712	0.158	1.017	67.30	59.43	$\overline{charm}$
56	1068	5090	D^+	1.053	0.048	1.025	32.40	20.35	
57	1070	4557	D^0	1.217	0.049	1.060	27.10	11.95	
58	1070	5521	D^0	1.751	0.201	1.016	41.30	29.81	
59	1073	192	D^+	1.031	0.038	1.106	24.10	7.71	
60	1080	2521	D^+	1.104	0.068	1.013	78.60	33.15	
61	1080	7420	D^+	1.117	0.070	1.010	44.50	40.33	
62	1086	3828	D^0	1.731	0.125	1.047	55.30	13.63	$\overline{charm}$
63	1089	5646	Λ_c^+	1.046	0.044	1.059	25.80	14.81	
64	1090	1701	D^0	1.240	0.052	1.276	6.70	5.76	
65	1099	1180	$\bar{D}^0$	1.274	0.054	1.052	24.40	13.29	*charm*
66	1099	3226	D^0	1.490	0.089	1.100	15.60	5.50	
67	1100	113	D^0	1.745	0.188	1.102	57.70	14.22	
68	1105	4668	D^+	2.486	0.357	1.021	40.10	20.87	
69	1118	4569	D^0	1.161	0.047	1.036	32.40	19.58	
70	1122	7258	$\bar{D}^0$	1.192	0.045	1.010	147.50	36.39	*charm*
71	1131	423	D^0	1.154	0.047	1.041	33.40	15.22	
72	1148	5847	D^0	1.194	0.046	1.023	90.30	23.63	$\overline{charm}$
73	1158	5775	D^+	1.110	0.040	1.032	86.40	70.01	$\overline{charm}$
74	1161	1632	D^0	1.194	0.046	1.022	62.00	24.96	
75	1162	971	D^+	2.276	0.285	1.325	12.10	11.36	
76	1166	3069	D^0	1.201	0.047	1.137	22.90	12.59	
77	1169	1620	D^0	1.356	0.091	1.031	64.60	53.36	$\overline{charm}$
78	1194	807	D^+	1.036	0.038	1.008	66.50	35.25	
79	1195	4860	Λ_c^+	2.716	0.477	1.739	8.60	5.42	Q.E.
80	1198	1114	D^+	2.442	0.379	1.013	36.40	31.73	
81	1198	3153	Λ_c^+	1.105	0.075	1.081	18.50	9.41	
82	1198	3877	D^+	1.021	0.038	1.012	99.20	27.77	

#	Run	Rec.	ID	D.W.	$\Delta D.W.$	E.W.	E_ν	ν	Comment
83	1203	1250	D^0	1.716	0.127	1.203	72.10	9.60	
84	1205	1433	D^0	1.209	0.045	1.040	71.90	13.08	
85	1207	1167	D^0	1.192	0.046	1.064	41.90	32.47	
86	1208	1779	D^+	1.020	0.036	1.068	140.40	40.40	
87	1208	2921	D^0	1.208	0.046	1.011	83.90	46.86	$\overline{\textit{charm}}$
88	1208	2964	D^0	1.144	0.047	1.016	33.40	27.55	
89	1211	376	D^0	1.194	0.046	1.015	42.60	24.42	$\overline{\textit{charm}}$
90	1215	4119	Λ_c^+	1.068	0.056	1.116	13.30	3.95	
91	1218	1980	D^+	1.022	0.036	1.068	55.00	13.33	
92	1222	281	D_s^+	1.053	0.157	1.156	55.30	9.85	
93	1226	2884	D^+	1.037	0.037	1.324	29.70	10.09	$\overline{\textit{charm}}$
94	1233	1678	D^0	1.197	0.046	1.205	15.90	12.45	$\overline{\textit{charm}}$
95	1250	2833	D^+	2.442	0.377	1.011	71.30	66.06	$\overline{\textit{charm}}$
96	1256	2092	D^+	1.046	0.051	1.018	76.90	38.44	
97	1261	5401	D^+	1.028	0.038	1.119	30.70	19.07	
98	1263	3857	D^-	1.053	0.047	1.043	21.00	11.99	
99	1263	5821	D^+	1.028	0.036	1.008	36.40	30.81	
100	1269	3706	$D^0/\bar{D}^0$	1.194	0.044	1.021	58.80	57.86	
101	1269	5327	D^0	1.349	0.066	1.112	39.50	8.25	$\overline{\textit{charm}}$
102	1271	7264	D^0	1.349	0.064	1.098	33.00	5.97	$\overline{\textit{charm}}$
103	1276	2132	D^0	1.192	0.046	1.016	73.80	45.23	
104	1277	2257	Λ_c^+	1.212	0.120	1.761	14.10	4.75	Q.E.
105	1286	4471	D^+	1.015	0.035	1.154	20.00	10.57	$\overline{\textit{charm}}$
106	1296	1709	D^0	1.244	0.051	1.246	12.40	11.56	
107	1296	2462	D^+	1.027	0.037	1.021	79.50	17.00	
108	1296	3516	D^0	1.230	0.051	1.050	28.50	9.98	$\overline{\textit{charm}}$
109	1303	4151	D^0	1.745	0.188	1.037	29.50	20.57	$\overline{\textit{charm}}$
110	1304	4693	D^0	1.351	0.100	1.192	20.60	18.12	
111	1305	5297	D^+	1.058	0.051	1.004	166.60	161.39	
112	1310	3118	D^+	1.034	0.040	1.256	16.00	8.86	$\overline{\textit{charm}}$
113	1311	3060	D^+	1.007	0.035	1.058	23.00	15.54	
114	1317	3892	D^0	1.301	0.067	1.006	125.50	118.88	
115	1318	3525	D^0	1.197	0.046	1.049	22.40	16.03	
116	1322	1554	D^+	1.327	0.198	1.053	62.20	26.49	
117	1322	1734	D^0	1.758	0.211	1.118	31.10	30.16	
118	1329	3624	D^0	1.194	0.045	1.014	38.00	29.60	
119	1334	3546	D^0	1.732	0.127	1.066	18.10	11.48	$\overline{\textit{charm}}$
120	1340	1667	D_s^+	1.146	0.162	1.058	21.90	16.58	
121	1364	1946	D^+	2.342	0.362	1.066	34.30	13.89	
122	1371	503	D^0	1.243	0.054	1.058	92.30	25.63	

#	Run	Rec.	ID	E_{had}	Q^2	W	x	y
1	476	4449	Λ_c^+	22.31	12.458	5.343	0.310	0.289
2	478	2638	D^0	8.83	0.383	3.914	0.026	0.642
3	486	6857	D^0	22.00				
4	493	177	D^0	30.60	4.374	7.225	0.079	0.632
5	493	1235	D^+	41.05	4.204	8.485	0.056	0.852
6	498	4985	Λ_c^+	10.03	1.765	4.022	0.103	0.402
7	499	4713	Λ_c^+	21.15	2.567	6.023	0.068	0.172
8	512	5761	D^+	15.84	0.704	5.306	0.025	0.193
9	513	8010	$\bar{D}^0$	24.29	0.881	6.622	0.020	0.660
10	518	4935	D^0	41.93	17.773	7.752	0.231	0.913
11	522	2107	D^+	46.24	16.774	8.317	0.197	0.531
12	522	3061	D^0	80.92	38.614	10.604	0.257	0.576
13	527	3682	D_s^-	33.60	2.704	7.715	0.044	0.469
14	529	271	D^+	54.78	13.747	9.394	0.136	0.542
15	529	3013	D^0	68.90				
16	529	3013	$\bar{D}^0$	68.90				
17	533	7152	D^+	62.00	2.531	10.631	0.022	0.880
18	546	1339	D^+	27.53	15.307	5.959	0.307	0.806
19	547	2197	D^0	30.78	0.770	7.493	0.014	0.437
20	547	3192	D^+	21.41	4.461	5.905	0.116	0.578
21	547	3705	D^0	17.69	14.665	4.203	0.466	0.148
22	549	4068	Λ_c^+	17.72	2.546	5.464	0.081	0.617
23	556	152	D^0	21.33	8.028	5.582	0.210	0.675
24	567	2596	Λ_c^+	10.04	0.682	4.159	0.040	0.624
25	577	5409	D^0	19.30	6.176	5.402	0.179	0.417
26	580	4508	D^-	19.13	7.348	5.262	0.215	0.745
27	597	1851	D_s^+	12.60				
28	597	6914	D^0	70.32	81.356	7.058	0.624	0.593
29	598	1759	D^+	23.94	9.023	5.920	0.209	0.699
30	602	2032	Λ_c^+	12.17	0.121	4.675	0.006	0.373
31	610	4088	Λ_c^+	5.33	2.238	2.625	0.271	0.372
32	635	4949	NB	28.81	23.235	5.475	0.444	0.251
33	638	5640	$\bar{D}^0$	53.81	19.715	8.969	0.199	0.613
34	638	9417	D_s^+	14.64	9.582	4.127	0.372	0.626
35	650	6003	Λ_c^+	9.44	2.359	3.806	0.148	0.383
36	654	3711	D^0	46.95	32.120	7.427	0.372	0.915
37	656	2631	D^+	47.54	57.020	5.601	0.652	0.272
38	661	2729	D^0	17.78	3.624	5.375	0.115	0.420
39	661	6517	D^0	46.22	10.799	8.667	0.127	0.710
40	663	7758	D^+	127.93	15.473	14.963	0.065	0.533
41	665	2113	D^+	10.05	1.364	4.077	0.080	0.272

#	Run	Rec.	ID	E_{had}	Q^2	W	x	y
42	666	5294	D^0	127.04	48.961	13.738	0.207	0.558
43	670	12	D^+	6.54	0.155	3.854	0.015	0.544
44	670	7870	$\bar{D}^0$	21.58	0.411	6.263	0.011	0.349
45	671	2642	D^+	6.39	1.648	5.077	0.161	0.243
46	671	7015	D_s^+	5.05	0.107	2.913	0.014	0.370
47	1018	792	D^0	12.91	4.879	4.300	0.217	0.557
48	1026	133	D^0	25.68	11.797	5.963	0.254	0.352
49	1028	277	Λ_c^+/D_s^+	10.95	3.605	4.009	0.192	0.524
50	1028	4410	D^0	37.84	2.856	8.205	0.041	0.371
51	1046	2977	D^+	13.50				
52	1050	2844	D^+	33.51	17.663	6.663	0.289	0.686
53	1053	1113	D^+	37.50				
54	1057	2341	D^0	51.38	34.172	7.838	0.361	0.567
55	1066	119	D^0	60.36	22.584	9.481	0.202	0.883
56	1068	5090	D^+	21.29	9.973	5.397	0.261	0.628
57	1070	4557	D^0	12.89	0.935	4.731	0.042	0.441
58	1070	5521	D^0	30.74	6.275	7.112	0.112	0.722
59	1073	192	D^+	8.65	0.176	3.896	0.012	0.320
60	1080	2521	D^+	34.08	5.083	7.619	0.082	0.422
61	1080	7420	D^+	41.27	0.687	8.714	0.009	0.906
62	1086	3828	D^0	14.57	3.387	4.806	0.132	0.247
63	1089	5646	Λ_c^+	15.75	8.900	4.449	0.320	0.574
64	1090	1701	D^0	6.70				
65	1099	1180	$\bar{D}^0$	14.23	3.286	4.749	0.132	0.545
66	1099	3226	D^0	6.44	1.012	3.193	0.098	0.352
67	1100	113	D^0	15.16	0.915	5.165	0.034	0.246
68	1105	4668	D^+	21.81	0.199	6.314	0.005	0.520
69	1118	4569	D^0	20.52	10.701	5.191	0.291	0.604
70	1122	7258	$\bar{D}^0$	37.33	0.407	8.295	0.006	0.247
71	1131	423	D^0	16.16	1.896	5.250	0.066	0.456
72	1148	5847	D^0	24.57	1.356	6.626	0.031	0.262
73	1158	5775	D^+	70.95	75.692	7.527	0.576	0.810
74	1161	1632	D^0	25.90	2.891	6.698	0.062	0.403
75	1162	971	D^+	12.30				
76	1166	3069	D^0	13.53	12.791	3.425	0.541	0.550
77	1169	1620	D^0	54.30	2.659	9.921	0.027	0.826
78	1194	807	D^+	36.19	4.516	7.910	0.068	0.530
79	1195	4860	Λ_c^+	6.36	2.401	2.944	0.236	0.631
80	1198	1114	D^+	32.66	2.516	7.612	0.042	0.872
81	1198	3153	Λ_c^+	10.35	2.845	3.963	0.161	0.509
82	1198	3877	D^+	28.71	4.938	6.935	0.095	0.280

#	Run	Rec.	ID	E_{had}	Q^2	W	x	y
83	1203	1250	D^0	10.54	8.731	3.190	0.484	0.133
84	1205	1433	D^0	14.02	2.754	4.763	0.112	0.182
85	1207	1167	D^0	33.40	19.486	6.509	0.320	0.775
86	1208	1779	D^+	41.34	67.497	3.042	0.890	0.288
87	1208	2921	D^0	47.80	3.680	9.231	0.042	0.559
88	1208	2964	D^0	28.49	5.327	6.877	0.103	0.825
89	1211	376	D^0	25.36	9.485	6.103	0.207	0.573
90	1215	4119	Λ_c^+	4.89	0.549	2.785	0.074	0.297
91	1218	1980	D^+	14.27	2.317	4.858	0.093	0.242
92	1222	281	D_s^+	10.78	1.215	4.261	0.066	0.178
93	1226	2884	D^+	11.03	6.173	3.696	0.326	0.340
94	1233	1678	D^0	13.39	2.691	4.644	0.115	0.783
95	1250	2833	D^+	67.00	24.635	10.015	0.199	0.927
96	1256	2092	D^+	39.38	7.754	8.081	0.107	0.500
97	1261	5401	D^+	20.01	16.633	4.479	0.464	0.621
98	1263	3857	D^-	12.93	1.596	4.669	0.071	0.571
99	1263	5821	D^+	31.75	2.921	7.472	0.050	0.846
100	1269	3706	$D^0/\bar{D}^0$	58.80				
101	1269	5327	D^0	9.19	3.852	3.539	0.249	0.209
102	1271	7264	D^0	6.91	0.211	3.448	0.019	0.181
103	1276	2132	D^0	46.17	45.149	6.377	0.532	0.613
104	1277	2257	Λ_c^+	5.69	1.413	2.897	0.158	0.337
105	1286	4471	D^+	11.50	5.265	3.932	0.265	0.528
106	1296	1709	D^0	12.50				
107	1296	2462	D^+	17.94	0.501	5.684	0.016	0.214
108	1296	3516	D^0	10.92	0.392	4.386	0.021	0.350
109	1303	4151	D^0	21.51	7.968	5.616	0.206	0.697
110	1304	4693	D^0	19.06	4.740	5.492	0.139	0.879
111	1305	5297	D^+	162.33	24.105	16.729	0.080	0.969
112	1310	3118	D^+	9.80	3.742	3.711	0.225	0.554
113	1311	3060	D^+	16.48	5.665	4.939	0.194	0.676
114	1317	3892	D^0	119.82	9.014	14.666	0.040	0.947
115	1318	3525	D^0	16.97	8.055	4.788	0.268	0.716
116	1322	1554	D^+	27.42	5.016	6.753	0.101	0.426
117	1322	1734	D^0	31.10				
118	1329	3624	D^0	30.53	8.839	6.901	0.159	0.779
119	1334	3546	D^0	12.42	1.213	4.607	0.056	0.634
120	1340	1667	D_s^+	17.52	3.260	5.363	0.105	0.757
121	1364	1946	D^+	14.83	0.680	5.127	0.026	0.405
122	1371	503	D^0	26.57	2.067	6.852	0.043	0.278

#	Run	Rec.	ID	Z	x_F	P_{out}	$P_\perp$	ϕ_μ
1	476	4449	Λ_c^+	0.207	−1.043	0.067	0.068	172.4
2	478	2638	D^0	0.981	0.894	0.817	0.854	125.8
3	486	6857	D^0	0.615				
4	493	177	D^0	0.388	0.222	0.096	0.126	166.5
5	493	1235	D^+	0.312	−0.132	0.771	2.268	162.0
6	498	4985	Λ_c^+	0.958	0.749	0.541	0.542	150.7
7	499	4713	Λ_c^+	0.237	−0.592	0.656	0.664	121.3
8	512	5761	D^+	0.707	0.540	0.269	0.854	42.9
9	513	8010	$\bar{D}^0$	0.401	0.130	1.010	1.063	118.2
10	518	4935	D^0	0.741	0.689	0.480	0.731	161.7
11	522	2107	D^+	0.603	0.446	0.909	1.755	164.0
12	522	3061	D^0	0.592	0.549	0.430	0.493	170.7
13	527	3682	D_s^-	0.378	0.209	0.090	0.196	171.7
14	529	271	D^+	0.897	0.716	3.531	3.533	123.5
15	529	3013	D^0	0.191				
16	529	3013	$\bar{D}^0$	0.701				
17	533	7152	D^+	0.611	0.565	0.777	0.791	103.5
18	546	1339	D^+	0.791	0.710	0.203	0.227	170.6
19	547	2197	D^0	0.800	0.764	0.383	0.465	154.0
20	547	3192	D^+	0.505	0.297	0.256	0.502	166.9
21	547	3705	D^0	0.815	0.662	0.359	0.782	170.3
22	549	4068	Λ_c^+	0.189	−1.247	0.400	0.442	128.1
23	556	152	D^0	0.760	0.683		0.246	179.9
24	567	2596	Λ_c^+	0.686	0.149	0.555	0.673	83.3
25	577	5409	D^0	0.627	0.455	0.036	0.653	175.9
26	580	4508	D^-	0.546	0.337	0.070	0.256	171.6
27	597	1851	D_s^+	0.812				
28	597	6914	D^0	0.663	0.541	0.187	1.153	175.9
29	598	1759	D^+	0.775	0.665	0.236	0.662	172.8
30	602	2032	Λ_c^+	0.596	0.135	0.330	0.498	147.7
31	610	4088	Λ_c^+	1.189	0.889	0.322	0.323	164.5
32	635	4949	NB	0.187	−1.356	0.372	0.395	155.4
33	638	5640	$\bar{D}^0$	0.422	0.321	0.043	0.576	175.8
34	638	9417	D_s^+	0.460	−0.202	0.232	0.490	169.3
35	650	6003	Λ_c^+	0.724	−0.032	0.926	1.059	106.4
36	654	3711	D^0	0.420	0.266	0.006	0.608	179.7
37	656	2631	D^+	0.686	0.056	0.408	3.000	163.7
38	661	2729	D^0	0.741	0.649	0.140	0.143	172.2
39	661	6517	D^0	0.677	0.616	0.530	0.845	135.2
40	663	7758	D^+	0.831	0.799	0.432	2.158	105.3
41	665	2113	D^+	0.397	−0.395	0.078	0.365	74.4

#	Run	Rec.	ID	Z	x_F	P_{out}	$P_\perp$	ϕ_μ
42	666	5294	D^0	0.441	0.402	0.175	0.576	176.1
43	670	12	D^+	0.543	−0.473	0.021	0.075	173.3
44	670	7870	$\bar{D}^0$	0.342	0.057	0.136	0.308	51.4
45	671	2642	D^+	0.663	−0.375	0.298	0.463	131.3
46	671	7015	D_s^+	0.852	−1.364	0.333	0.686	38.0
47	1018	792	D^0	0.810	0.681	0.460	0.481	155.4
48	1026	133	D^0	0.582	0.416	0.742	0.779	151.1
49	1028	277	Λ_c^+/D_s^+	0.745	0.409	0.281	0.287	161.8
50	1028	4410	D^0	0.125	−0.345	0.012	0.013	175.6
51	1046	2977	D^+	0.878				
52	1050	2844	D^+	0.734	0.675	0.147	0.186	175.4
53	1053	1113	D^+	0.278				
54	1057	2341	D^0	0.641	0.584	0.127	0.144	176.9
55	1066	119	D^0	0.067	−0.586	0.018	0.064	173.3
56	1068	5090	D^+	0.658	0.517	0.126	0.312	172.4
57	1070	4557	D^0	0.511	0.133	0.523	0.710	75.8
58	1070	5521	D^0	0.602	0.514	0.028	0.393	178.6
59	1073	192	D^+	0.762	0.454	0.164	0.604	25.9
60	1080	2521	D^+	0.601	0.494	0.525	0.525	152.4
61	1080	7420	D^+	0.649	0.589	0.310	0.427	65.5
62	1086	3828	D^0	0.581	0.164	0.155	1.336	176.0
63	1089	5646	Λ_c^+	0.384	−0.563	0.051	0.385	177.2
64	1090	1701	D^0	0.766				
65	1099	1180	$\bar{D}^0$	0.253	−0.593	0.067	0.067	165.1
66	1099	3226	D^0	0.870	0.689	0.120	0.120	169.2
67	1100	113	D^0	0.947	0.924	0.308	0.309	158.8
68	1105	4668	D^+	0.603	0.410	0.677	1.032	144.7
69	1118	4569	D^0	0.443	0.136	0.160	0.303	172.0
70	1122	7258	$\bar{D}^0$	0.587	0.488	0.977	1.163	134.4
71	1131	423	D^0	0.717	0.608	0.035	0.095	176.8
72	1148	5847	D^0	0.636	0.531	0.420	0.679	160.1
73	1158	5775	D^+	0.030	−3.017	0.043	0.051	152.3
74	1161	1632	D^0	0.630	0.542	0.222	0.260	162.0
75	1162	971	D^+	0.895				
76	1166	3069	D^0	0.744	0.380	0.120	0.695	177.1
77	1169	1620	D^0	0.938	0.931	0.335	0.340	152.9
78	1194	807	D^+	0.648	0.573	0.353	0.374	161.6
79	1195	4860	Λ_c^+	0.997	0.310	0.017	0.487	176.9
80	1198	1114	D^+	0.259	0.004	0.328	0.354	91.4
81	1198	3153	Λ_c^+	0.792	0.410	0.138	0.165	170.0
82	1198	3877	D^+	0.468	0.196	0.806	1.270	156.4

#	Run	Rec.	ID	Z	x_F	P_{out}	$P_\perp$	ϕ_μ
83	1203	1250	D^0	0.486	−1.109	0.047	0.636	175.1
84	1205	1433	D^0	0.667	0.441	0.100	0.102	174.2
85	1207	1167	D^0	0.619	0.523	0.228	0.287	168.3
86	1208	1779	D^+	0.203	−4.793	0.041	0.225	177.9
87	1208	2921	D^0	0.158	−0.122	0.222	0.223	133.9
88	1208	2964	D^0	0.688	0.623	0.113	0.164	171.6
89	1211	376	D^0	0.625	0.505	0.161	0.508	168.0
90	1215	4119	Λ_c^+	0.993	−0.479	0.695	0.760	104.0
91	1218	1980	D^+	0.690	0.509	0.054	0.612	177.9
92	1222	281	D_s^+	0.962	0.864	0.782	0.935	118.0
93	1226	2884	D^+	0.210	−2.575	0.106	0.110	147.0
94	1233	1678	D^0	0.895	0.823	0.572	0.607	128.5
95	1250	2833	D^+	0.067	−0.539	0.052	0.400	9.3
96	1256	2092	D^+	0.416	0.270	0.224	0.231	163.5
97	1261	5401	D^+	0.725	0.455	0.270	0.995	161.3
98	1263	3857	D^-	0.654	0.295	0.191	1.200	173.7
99	1263	5821	D^+	0.466	0.291	0.342	0.816	161.9
100	1269	3706	$D^0/\bar{D}^0$	0.392				
101	1269	5327	D^0	0.642	0.138	0.056	0.147	176.4
102	1271	7264	D^0	0.745	0.350	0.307	0.328	141.9
103	1276	2132	D^0	0.633	0.525	0.659	0.684	164.8
104	1277	2257	Λ_c^+	0.896	−0.298	0.225	0.314	166.2
105	1286	4471	D^+	0.594	−0.044	0.585	1.157	77.0
106	1296	1709	D^0	0.366				
107	1296	2462	D^+	0.605	0.420	0.020	0.270	168.7
108	1296	3516	D^0	0.498	0.019	0.604	0.625	122.8
109	1303	4151	D^0	0.646	0.381	0.057	1.540	178.7
110	1304	4693	D^0	0.689	0.569	0.225	0.454	115.3
111	1305	5297	D^+	0.199	0.122	0.353	0.357	120.4
112	1310	3118	D^+	0.309	−1.214	0.116	0.163	163.7
113	1311	3060	D^+	0.598	0.382	0.002	0.030	179.9
114	1317	3892	D^0	0.495	0.466	0.417	0.600	151.5
115	1318	3525	D^0	0.688	0.531	0.173	0.288	167.4
116	1322	1554	D^+	0.830	0.770	0.835	0.923	140.2
117	1322	1734	D^0	0.875				
118	1329	3624	D^0	0.516	0.353	0.979	0.979	126.4
119	1334	3546	D^0	0.717	0.529	0.583	0.583	127.9
120	1340	1667	D_s^+	0.824	0.739	0.497	0.576	153.7
121	1364	1946	D^+	0.732	0.554	0.590	0.997	59.3
122	1371	503	D^0	0.870	0.826	0.854	0.856	139.9

References

[1] J.J. Aubert *et al.*, Phys. Rev. Lett. **33**, 1404 (1974); J.-E. Augustin *et al.*, Phys. Rev. Lett. **33**, 1406 (1974).

[2] B.J. Bjorken and S.L. Glashow, Phys. Rev. Lett. **11**, 255 (1964).

[3] M.K. Gaillard, B.W. Lee, and J.L. Rosner, Rev. Mod. Phys. **47**, 277 (1975).

[4] S.L. Glashow, J. Iliopoulos and L. Maiani, Phys. Rev. D **2**, 1285 (1970).

[5] G. Goldhaber *et al.*, Phys. Rev. Lett. **37**, 255 (1976).

[6] N. Ushida *et al.*, Lett. Nuovo Cimento **23**, 577 (1978); H. Fuchi *et al.*, Phys. Lett. **85B**, 135 (1979); D. Allasia *et al.*, Phys. Lett. **87B**, 287 (1979); J. Sandweiss *et al.*, Phys. Rev. Lett. **44**, 1104 (1980); H.C. Ballagh *et al.*, Phys. Lett. **89B**, 423 (1980); M.I. Adamovich *et al.*, Phys. Lett. **89B**, 427 (1980).

[7] H. Fuchi *et al.*, Phys. Lett. **85B**, 135 (1979).

[8] S.Y. Bahk, Ph.D. Thesis, Korea University, 1984; M.J. Gutzwiller, Ph.D. thesis, The Ohio State University, 1981; M. Miyanishi, Ph.D. thesis, Nagoya University, 1983; D. Pitman, Ph.D. thesis, University of Toronto, 1983; H. Shibuya, Ph.D. thesis, Nagoya University, 1982; Y. Takahashi, Ph.D. thesis, Kobe University, 1983.

[9] T. Hara, Ph.D. thesis, Osaka City UNiversity, 1982.

[10] D.C. Bailey, Ph.D. thesis, McGill University, 1983.

[11] S. Errede, Ph.D. thesis, The Ohio State University, 1981.

[12] N. Ushida *et al.*, Phys. Rev. Lett. **45**, 1049 (1980); **48**, 844 (1982).

[13] N. Ushida *et al.*, Phys. Rev. Lett. **45**, 1053 (1980); **51**, 2362 (1983).

[14] N. Ushida *et al.*, Phys. Rev. Lett. **47**, 1694 (1981).

[15] N. Ushida *et al.*, Nucl. Instrum. Methods Phys. Res., Sect. A **224**, 50 (1984).

[16] N. Ushida *et al.*, Phys. Lett. **121B**, 287 (1983).

[17] N. Ushida *et al.*, Phys. Lett. **121B**, 292 (1983).

[18] M. Kobayashi and T. Maskawa, Prog. of Theor. Phys. **49**, 652 (1973).

[19] M. Auguilar-Benitez *et al.* (Particle Data Group), Phys. Lett. **170B**, 1 (1986).

[20] N. Schmitz, Rapporteur's talk in: *Proceedings of the 1979 International Symposium on Lepton and Photon Interactions at HIgh Energies*, eds. T.B.W. Kirk and H.D.I. Abarbanel (Fermilab, U.S.A., 1979) p. 359 .

[21] C.G. Wohl *et al.* (Particle data group), Rev. Mod. Phys. **56**, S1 (1984).

[22] N. Armenise *et al.*, Phys. Lett. **86B**, 115 (1979).

[23] D. Allasia *et al.*, Nucl. Phys. **B176**, 13 (1980).

[24] M.I. Adamovich *et al.*, Phys. Lett. **89B**, 427 (1980); **99B**, 271 (1981).

[25] W. Bacino *et al.*, Phys. Rev. Lett. **45**, 329 (1980).

[26] H.C. Ballagh *et al.*, Phys. Lett. **89B**, 423 (1980); Phys. Rev. D **24**, 7 (1981).

[27] B. Adeva *et al.*, Phys. Lett. **102B**, 285 (1981).

[28] M. Fuchi *et al.*, Lett. Nuovo Cimento **31**, 199 (1981).

[29] K. Abe *et al.*, Phys. Rev. Lett. **48**, 1526 (1982).

[30] E. Albini *et al.*, Phys. Lett. **110B**, 339 (1982).

[31] R. Ammar *et al.*, Phys. Lett. **94B**, 118 (1980).

[32] R.A. Sidwell, N.W. Reay, and N.R. Stanton, Annu. Rev. Nucl. Part. Sci. **33**, 539 (1983).

[33] G. Giacomelli, in Proceedings of the 1985 CERN-JINR School of Physics, September 1985, Vol. 2, p. 266.

[34] E. Leader and E. Predazzi, *An Introduction to Gauge Theories and the 'New Physics'* (Cambridge University Press, New York, 1982).

[35] E.D. Commins and P.H. Bucksbaum, *Weak Interactions of Leptons and Quarks* (Cambridge University Press, New York, 1983).

[36] C. Baltay *et al.*, Phys Rev. Lett. **39**, 62 (1977); C. Baltay, in *Proceedings of the 1979 JINR-CERN School of Physics, September 1979*,(Hungarian Academy of Sciences, Budapest, 1980) p. 72.

[37] A.J. Malensek, FN-341, 2941.000 (October 12, 1981); numbers based on experimental data of: H.W. Atherton *et al.*, CERN 80:07, (1980).

[38] I.A. Lovatt, M.Sc. Thesis, University of Toronto, 1982.

[39] A. Bodek, in *Proceedings of the Calorimeter Workshop*, (Fermilab, May 1975, edited by M. Atac, 1975) p. 229.

[40] R.L. Ford and W.R. Nelson, SLAC-210, UC-32 (1978).

[41] B. Ronne, "Kinematical Analysis of Bubble Chamber Pictures", *Proceedings of the 1964 Easter School for Physicists*, Vol. I p. 87 (1964).

[42] A. Gauthier, Ph.D. Thesis, Ohio State University, 1987.

[43] G.H. Trilling, Phys. Rep. **75**, 57 (1981).

[44] Nagoya Group, Translated by H. Shibuya, E-531 Internal Memo (1981).

[45] H.Fukushima, Translated by Y. Noguchi, E-531 Internal Memo (1981).

[46] W. T. Eadie *et al.*, *Statistical Methods in Experimental Physics* (Nort-Holland, New York, 1971), Sect. 8.3 and 8.5; A. G. Frodesen, O. Skjeggestad, and H. Tofte, *Probability and Statistics in Particle Physics* (Columbia Univ. Press, New York, 1979), Chap. 9.

[47] R. Brock *et al.*, Phys. Rev. D **25**, 1753 (1982).

[48] D. Allasia *et al.*, Phys. Lett. **154B**, 231 (1985).

[49] W. Krenz *et al.*, Phys. Lett. **73B**, 493 (1978).

[50] N. Ushida *et al.*, Phys. Rev. Lett. **56**, 1771 (1986).

[51] I.A. Lovatt, Ph.D. Thesis, University of Toronto, 1986.

[52] N. Ushida *et al.*, Phys. Rev. Lett. **56**, 1767 (1986).

[53] M. Turcotte, Ph.D. Thesis, McGill University, 1986.

[54] J.C. Anjos *et al.*, Phys. Rev. Lett. **58**, 311 (1987).

[55] J.C. Anjos *et al.*, Phys. Rev. Lett. **58**, 1818 (1987).

[56] L. Cremaldi (representing the TPS collaboration), Talk at the Division of Particle and Fields Meeting, Salt Lake City, Utah (1987).

[57] M. Aguilar-Benitez *et al.*, Phys. Lett. **122B**, 312 (1983); A. Badertscher *et al.*, Phys. Lett. **123B**, 471 (1983); K. Abe *et al.*, Phys. Rev. D **30**, 1 (1984); M.I. Adamovich *et al.*, Phys. Lett. **140B**, 123 (1984); J.M. Yelton *et al.*, Phys. Rev. Lett. **52**, 2019 (1984); M. Aguilar-Benitez *et al.*, Phys. Lett. **146B**, 266 (1984); R. Bailey *et al.*, Z. Phys. C **28**, 357 (1985); H. Yamamoto *et al.*, Phys. Rev. D **32**, 2901 (1985); R. Bailey *et al.*, Phys. Lett. **139B**, 320 (1984); C. Jung *et al.*, Phys. Rev. Lett. **56**, 1775 (1986).

[58] R.M. Baltrusaitis *et al.*, Phys. Rev. Lett. **54**, 1976 (1985).

[59] E. Vella *et al.*, Phys. Rev. Lett. **48**, 1515 (1982).

[60] H. Albrecht *et al.*, Phys. Lett. **158B**, 525 (1985).

[61] R.M. Baltrusaitis *et al.*, Phys. Rev. Lett. **56**, 2136 (1986).

[62] R.H. Schindler *et al.*, Phys. Rev. D **24**, 78 (1981); ~~R.H.~~ Schindler, thesis, SLAC Report No. SLAC-219 (1979), unpublished.

[63] B. Andersson, G. Gustafson, G. Ingelman and T. Sjöstrand, Phys. Rep **97**, 31 (1983); T. Sjöstrand, Comput. Phys. Commun. **27**, 243 (1982); JETSET Version 6.2.

[64] R. Brun *et al.*, CERN Report DD/EE/84-1, GEANT 3.0 .

[65] D.H. Perkins, *Introduction to High Energy Physics* (Addison-Wesley Publishing Company, Don Mills, Ontario, 1982).

[66] M. Glück, E. Hoffmann, and E. Reya, Z. Phys. C **13**, 119 (1982).

[67] N.J. Baker *et al.*, Phys. Rev. D **32**, 531 (1985).

[68] R. Brock, Phys. Rev. Lett. **44**, 1027 (1980).

[69] H. Deden *et al.*, Phys. Lett. **67B**, 474 (1977).

[70] M. Holder *et al.*, Phys. Lett. **74B**, 277 (1978).

[71] V. Efremenko *et al.*, Phys. Lett. **88B**, 181 (1979).

[72] J.R. Cudell, F. Halzen, and K. Hikasa, Phys. Lett. B **175**, 227 (1986).

[73] J.G.H. de Groot *et al.*, Phys. Lett. **86B**, 103 (1979).

[74] C. Baltay *et al.*, Phys. Rev. Lett. **55**, 2543 (1985).

[75] M. Holder *et al.*, Phys. Lett. **70B**, 396 (1977); T. Trinko *et al.*, Phys. Rev. D **23**, 1889 (1981); A. Haatuft *et al.*, Nucl. Phys. **B222**, 365 (1983).

[76] M. Jonker *et al.*, Phys. Lett. **107B**, 241 (1981); H. Abramowicz *et al.*, Z. Phys. C **15**, 19 (1982).

[77] C. Peterson, D. Schlatter, I. Schmitt, and P.M. Zerwas, Phys. Rev. D **27**, 105 (1983).

[78] J. Chapman, *Proc. of the 12th SLAC Summer Institute on Particle Physics*, 373 (1984).

[79] K. Lang *et al.* (Presented by W.H. Smith), *Proc. of the 12th SLAC Summer Institute on Particle Physics*, 503 (1984).

[80] B. Renk, Ph.D. thesis, Dortmund Univ. (1984).

[81] N.J. Baker *et al.*, Phys. Rev. D **34**, 1251 (1986).

[82] D. Allasia *et al.*, Nucl. Phys. **B224**, 1 (1983).

[83] P.C. Bosetti *et al.*, Nucl. Phys. **B149**, 13 (1979).